The People's Democratic Republic of Algeria

Ministry of Higher Education and Scientific Research

Amar Telidji University - Laghouat

Faculty of Sciences

Doctoral thesis

Specialty: Material Physics

Publicly presented on30/05/2022
by:

ABDELHAKEM Abdelhafidh

THEME

Numerical Modelling of the Effect of a Magnetic Field on Dynamic Configuration During the Solidification Process of a Metallic Alloy

Thesis committee:

TEGGAR Mohamed	**President**	Pr, Amar Telidji University, Laghouat
HACHANI Lakhdar	Supervisor	Pr, Amar Telidji University, Laghouat
BENSENOUCI Ahmed	**Examiner**	HDR, Amar Telidji University, Laghouat
LAOUER Abdelghani	**Examiner**	HDR, Mohamed Seddik Benyahia University, Jijel
BOUHEZZA Aicha	**Examiner**	HDR, 20 august 1955 University, Skikda

Acknowledgement

First of all, I thank the Almighty ALLAH, for having given me the courage, the faith and the patience to be able to complete this work.

sincere respect and thanks to my supervisor Prof. HACHANI Lakhdar for having guided me from the beginning to the end of this work despite his impediments, and for his precious remarks, as well as for the inspiration, help, and time that he devoted to me.Thank you for everything Lakhdar!

My thanks and appreciations go toward to Prof. Yves Fautrelle and Dr. Kader ZAIDAT for their advices and supports throughout my work and especially for their assistances in publishing my articles.

My sincere gratefulness is dedicated to the thesis committee members, President Prof. TEGGAR Mohamed, the examiners: Associate Prof. BENSENOUCI Ahmed, Associate Prof. LAOUER Abdelghani and Associate Prof. BOUHEZZA Aicha for taking time to assess this work and to attend the PhD defense.

I also thank all the staff of the LPM laboratory, the director LEFKAIER Iben khaldoun and all the permanent, PhD students, and other, who allowed me to achieve my thesis work in a good condition, and especially to Dr. SARI Ibrahim, without forgetting KHELFI Safia, all my wishes of success for your PhD.

cannot forget my family and all my friends who have always supported me during these years of study.

Thanks to all those I could have forgotten but who also brought a contribution to the achievement of this thesis.

SUMMARY

Figures List

Tables List

NOMENCLATURE

Symbol	Designation
B_0	Amplitude of the magnetic field, *(T)*
A_0	Amplitude of the vector potential, *(T.m)*
$\langle C \rangle$	Average concentration *(wt.%)*
D_l	Chemical diffusion in the liquid*(m^2/s)*
D_s	Chemical diffusion in the solid*(m^2/s)*
ΔT_c	Chemical undercooling, (*K*).
CR	Cooling rate*(K/s)*
$\vec{j}$	Current density, *($A\ m^{-2}$).*
I	Current, *(A).*
ρ	Density *($Kg.m^{-3}$)*
μ	Dynamic viscosity*($kg.m^{-1}.s^{-1}$)*
$\vec{E}$	Electric fields, (*$V\ m^{-1}$*).
σ	Electrical conductivity, *($\Omega^{-1}m^{-1}$).*
C_E	Eutectic concentration*(wt.%)*
T_E	Eutectic temperature*(K)*
f	Frequency, (*Hz*).
Γ	Gibbs Thomson coefficient, (*m K*).
ΔT_r	Gibbs-Thomson undercooling, (*K*)
g	Gravity*(m/s^2)*
ϕ	Heat flux*(W)*
C_0	Initial concentration*(wt.%)*
I_v	Ivantsov function.
ν	Kinematic viscosity*(m^2/s)*
L	Latent heat *($J.kg^{-1}$)*
C_l	Liquid concentration *(wt.%)*
ρ_l	Liquid density*($Kg.m^{-3}$)*
m	Liquidus slope *(K.wt%)*
T_l	Liquidus temperature *(K)*
$\vec{F}$	Lorentz force, (*N*).
ω	Magnetic field pulsation, (*Hz*).
$\vec{B}$	Magnetic induction, *(T).*
μ	Magnetic permeability, *($H.m^{-1}$).*
$\vec{A}$	Magnetic vector potential, *(T).*
f_l	Mass fraction in the liquid
f_s	Mass fraction in the solid
T_m	Melting temperature*(K)*
k	Partition coefficient
K	Permeability*(m^2)*
λ_2	Secondary interdendritic spacing*(m)*
C_s	Solid concentration *(wt.%)*
ρ_s	Solid density*($Kg.m^{-3}$)*

T_s	Solidus temperatures*(K)*
β_C	Solutal expansion coefficient*($wt.\%^{-1}$)*
C	Solute concentration*(wt.%)*
Cp	Specific heat*($J.kg^{-1}.K^{-1}$)*
Ω	Suppersaturation.
T	Temperature*(K)*
DT	Temperature difference *(K)*
λ_l	Thermal conductivity in liquid$W.m^{-1}.K^{-1}$
λ_s	Thermal conductivity in solid$W.m^{-1}.K^{-1}$
α	Thermal diffusivity*(m^2/s)*
β_T	Thermal expansion coefficient *(K^{-1})*
ΔT_T	Thermal undercooling, (*K*).
t	Time*(s)*
R_{tip}	Tip radius, (m)
V_{tip}	Tip velocity, (m s^{-1})
u	Velocity component along x*(m/s)*
v	Velocity component along y *(m/s)*
w	Velocity component along z*(m/s)*
$\vec{V}$	Velocity vector*(m/s)*
k^*	Wave number in narrow liquid domain, (m^{-1})

DIMENSIONLESS NUMBER

Symbol	Designation
Pr	Prandtl Number
Ra	Rayleigh number
Re	Reynolds number

SUBSCRIPTS

Symbol	Designation
l	Liquid
s	Solid
x, y, z	Coordinates
exp	Experimental
num	Numerical
L, H, W	Length, height and width of the cavity

INTRODUCTION

Solidification of metal alloys is a multi-scale/multi-phase/multi-physics process. One of the major fundamental scientific challenges in developing a solidification model lies in the requirement to bridge the length scales, i.e., to incorporate and account for small scale physical phenomena in large scale models or vice versa [1,2]. In the last decades, numerous numerical models of solidification processes have been proposed [3], but no one single model has been able to span the entire range of the length scales from the process level of industrial interest (~ m) down to the atomic scale (~Å), due to the limitation of current computational resources [4]. Using an optimistic estimate of computational advancement, a microstructure model that accounts for the evolution of the dendritic grain morphology via phase field or level set methods would not be feasible for simulating a simple 2D casting (~ m) until the year **2055** [5]. Therefore, a trend for the process-modelling of the solidification problem is to incorporate the interfacial phenomena occurring locally below the micro-structural scale into the global solidification process with a so-called ***volume averaging approach***.

Dendrites are common solidification morphology in both pure materials and alloys. Complex interplay between macroscopic heat and solute transport and microscopic interfacial phenomena results in various dendritic solidification structures. The interaction between dendritic branches and tips are responsible for the features of the grain inner structure. These features are responsible for the macroscopic properties, such as the mush permeability, as well as for the development of freckles and channel segregations.

In the present state of the art, only a few well documented experiments on liquid metal alloys have been performed. This is particularly true for medium-size experiments where natural convection is important. Various laboratory-scale solidification experiments have already been performed. The case of a pure metal was investigated by V.R. Voller [6]. Regarding the solidification of alloys, a reference experiment was carried in this work [7]. It consisted in solidifying a rectangular vertical Pb-Sn ingot and demonstrated the appearance of solute macrosegregation related to natural convection. J.R. Sarazin [8], investigated the solidification of a vertical cylindrical Pb-Sn rod. The cooling rate was a few degrees Kelvin per minute. Channel segregates were observed both on the side and inside of the ingot. Similar experiments with the same type of alloy and geometry have been carried out by S.N. S.N. Tewari and R. Shah [9], and M.I. Bergman et *al.*,[10]. Macrosegregation in the solidified ingot was observed as well as channel segregations for a sufficient cooling rate, typically 2-5 K/min. Another, more detailed experiment was carried out by G. Quillet et *al.*, [11]. It consisted of a

preliminary benchmark solidification experiment on a Sn-10*wt*.%Bi alloy. However, considering the various experiments achieved so far various data are missing from the point of view of the modeller, such as the exact initial conditions, the dendrite arm spacing, the detailed composition maps, the detailed thermal field, the eutectic fraction, etc.

The benchmark experiment developed in the SIMAP/EPM laboratory, named **AFRODITE**, is the key tool for the validation of the models by comparison with detailed measurements obtained with thoroughly controlled initial and thermal boundary conditions. In its principle, the experiment is similar to the well-known Hebditch and Hunt experiment (1974), with a special emphasis on obtaining reproducible quantitative measurements, [12]. It is unfortunately not possible to visualize the processes that have built up the final segregation maps. We postulate that results given by AFRODITE are the post-mortem signature of interactions that happens at the mesoscales between fluid flow and the dendrites primary and secondary arms. In addition to characteristic similar to other benchmark set-ups, in AFRODITE a linear electromagnetic motor is placed at bottom of cavity, which makes it possible to stir the alloy during solidification. In particular, it was found that for the case with the Lorentz force acting in a direction opposite to the flow caused by the gravity, the structure of the samples consisted mainly of the equiaxed grains. Also, AFRODITE can control cooling rate at lateral walls of cavity and record data of real-time temperature distribution. These features make AFRODITE a good reference for testing performance of macroscopic equiaxed solidification model under convective flow.

Indeed, the objective of this thesis is to develop a 3D two-phase columnar solidification model that accounts for the growth of columnar grains, their motion and the formation of macrosegregation. Developed numerical model is used to simulate the AFRODITE solidification experiment to test the performance of model and to study the effect of electromagnetic stirring on the whole solidification process. Finally, numerical simulations are applied to predict the macrosegregation mechanism with particular emphasis on the dominant factors that have a direct effect on this phenomenon, namely the direction of electromagnetic stirring.

The thesis consists of fourth chapters.

The first chapter is a bibliography. It summarizes the various basic notions related to the phenomenon of solidification and establishes the basis on which the rest of the work will be

built. It also allows making a brief state of the art on the studied topic, the equation models, and the interest for a validation experiment in solidification.

The second chapter provides the state of the art of numerical modelling of liquid-solid phase change of pure materials and metallic alloys. The different approaches most commonly used, are reviewed and detailed. Elementary and theoretical notions, definitions, and reminders necessary for the understanding of this work are also included. The last part in this chapter is devoted to the description of some models developed in many international laboratories specialized in this field.

The third chapter presents a three-dimensional multiscale columnar solidification model in which some approximations regarding solute transport at microscopic scale are put together in a new way and incorporated into macroscopic transport equations. Through simulation for solidification case of Sn-10*wt*.% Pb alloy in a parallelepiped cavity that mimics the Hachani et *al*.,[13], experiment. Emphasis is given to the main factors that have a direct effect on the development and morphology of segregated channels, namely, the remelting phenomenon, dendrite fragmentation, and the solidification front instabilities the role of remelting in the model on the calculation results is investigated.

In the fourth chapter the proposed solidification model is extended through simulation of the same alloy solidification (Sn-10*wt*.%Pb), performed with AFRODITE benchmark experiment with presence of both natural convection and electromagnetic stirring (forced convection) in the opposite direction. The influence of stirring direction on distribution of grain nature and number density and macrosegregation morphology, namely segregated channels, is investigated.

Introduction- References

[1] C. Beckermann, C.Y. Wang, *JOM*, 46 (1994) 42-7.

[2] M. Rappaz, Int. Met. Rev., 34 (1989) 93-123.

[3] W. Boettinger, S.R. Coriell, L. Greer, A. Karma, W. Kurz, M. Rappaz, R. Trivedi, *Acta Mater.*, 48 (2000) 43-70.

[4] V.R. Voller, F. Porte-Agel, *J. Comp. Physics*, 179 (2002), 698-703.

[5] V.R. Voller, *5th Int. Conf. on CFD in the Process Industries, CSIRO*, Melbourne, Australia, (2006) 1-4.

[6] C. Gau and R. Viskanta, *J. Heat Trans.-T. ASME*, 108 (1986) 174-81.

[7] D.J. Hebditch, J.D. Hunt, *Metall. Trans.*, 5 (1974) 1557-63.

[8] J.R. Sarazin, A. Hellawell, *Metall. Trans. A*, 19 (1988) 1861-71.

[9] S.N. Tewari, R. Shah, *Metall. Trans. A*, 23 (1992) 3383–92.

[10] M.I. Bergman, D.R. Fearn, J. Bloxham, M.C. Shannon, *Metall. Mater. Trans. A*, 28 (1997) 859–66.

[11] G. Quillet, A. Ciobanas, P. Lehmann, Y. Fautrelle, *Int. J. Heat Mass Transfer*, 50 (2007) 654 66.

[12] L. Hachani, B. Saadi, X.D. Wang, A. Nouri, K. Zaidat, A. Belgacem-Bouzida, L. Ayouni Derouiche, G. Raimondi, Y. Fautrelle, *Int. J. Heat Mass Transfer*, 55 (2012) 1986-96.

[13] L. Hachani, K. Zaidat, Y. Fautrelle, *Int. J. Heat Mass Transfer*, 85 (2015) 438-454.

CHAPTER I

Introduction to Solidification: Fundamental Aspects

1. Generalities on metal alloys solidification

This chapter is devoted to an overall study of the basic solidification concepts, in particular the description of the different structures (columnar or equiaxed) resulting from the solidification process. Indeed, this study will be focused on the two most important mechanisms that govern the solidification phenomenon: the germination-growth of the microstructure as well as the transition between the two types of structures, namely the CET (transition-columnar-equiaxial). The appearance of specific structures is the result of interaction between different mechanisms: heat and mass transfer, chemistry, and thermodynamics occur at different time and space scales. Kinetic aspects play a dominant role in solidification kinetics. Since the cooling process may be faster than the actual mass and/or heat transfer, solidification is usually an unbalanced process. It is well known that the solute has a relatively faster diffusivity in liquid phases compared to that in solid, which it is significantly low, it is difficult to reach equilibrium in a short cooling time. In addition, the latent heat released due to the phase change takes more time to transfer. The system seeks to achieve a thermodynamic equilibrium, and competition between these factors results in significant differences in the final structure and grain size.

1.1.Cooling curve of a pure materials

First, let's look at the solidification of a pure metal subjected to a slow cooling in a crucible. If we measure the temperature of a given point as a function of time, we obtain a cooling curve of the metal. This curve is divided into three parts: an almost parabolic decrease, a plateau, and a final decrease (see Fig.I.1). This plateau is all the more marked as the mass of metal is large and the cooling is slow. It corresponds to the period of coexistence of the liquid and the solid metal. This thermal behavior allows defining the melting temperature T_m of the metal.

Fig.I.1 shows also the typical cooling curve of metal. It is divided into three distinct parts as mentioned above. In the first (from the start to point **A**), a decrease in temperature corresponding to the cooling of the liquid metal. It ends at the melting temperature when the first solid crystal germs are formed. The second part is the isothermal stage (from **A** to **B**) in which the temperature remains constant and equal to the melting temperature and where both solid and liquid phases of the material coexist.

In the beginning, the first solid germs are barely formed; these germs then grow until the liquid phase disappears completely around the measuring point; the metal is then completely solidified. This isothermal stage becomes significantly larger as the cooling is slow and the

mass to be solidified is large. As solidification is an exothermic phenomenon, heat is rejected along with this level. The third part (beyond point **B**) is a decrease in the temperature corresponding to the cooling of the solid metal. The heat extracted during the two temperature decreases (of the liquid, then of the solid) are sensible heats, while the heat rejected during the isothermal stage is a latent heat corresponding to the phase change (solidification). In this first typical evolution, the undercooling of the liquid is absent. In reality, the cooled liquid remains in the liquid state even below the melting temperature T_m. The first stable and enough large solids germ to grow are formed only at point **A'**. This undercooling can be attenuated by the presence of impurities, the roughness of the crucible walls, or even stirring. As soon as these first stable nuclei are formed, the temperature stable nuclei, the temperature increase by the rejection of latent heat and return to the melting temperature. This is the phenomenon of recalescence. The solidification then follows the same path as previously.

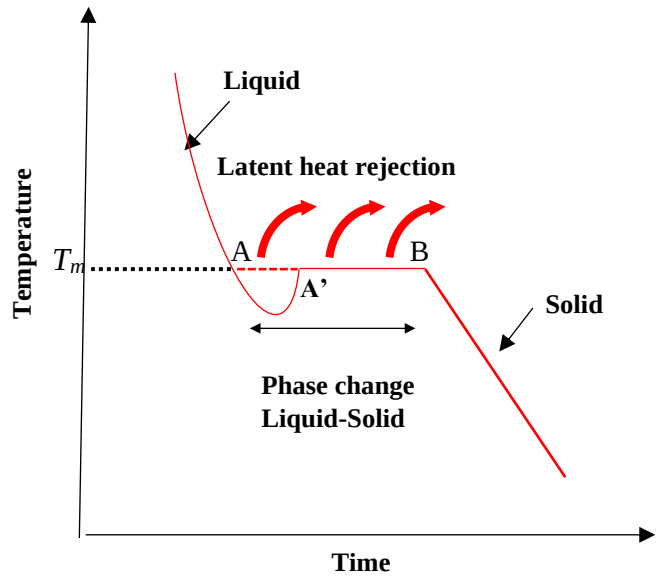

Fig.I.1 *:Typical evolution of the temperature of a pure material during its solidification (in the absence and presence of liquid undercooling). Tm is the temperature of melting temperature.*

1.2.Solidification, binary phase diagram and segregation

During the solidification process at a local scale, the concentration of the solid formed $C_s^*$is different from the liquid C_l^*at the solid-liquid interface. The solid concentration C_s^* at the interface is related to the liquid concentration C_l^* through the distribution coefficient $k = C_s^*/C_l^*$ (Kurz and Fischer [1], Flemings [2], Lesoult [3]). If the melt is completely mixed during the solidification process, the solid-liquid interface concentration is the equilibrium concentration

($k = C_s^{eq}/C_l^{eq}$). In the case of thermodynamic equilibrium, the liquid concentration is given by the phase diagram through the liquidus line, and the solid concentration is given by the solidus line.

This is only effective when the temperature in the entire system, and the liquid and solid concentrations are uniforms during the solidification process. In fact, under perfect mixing conditions on a system scale, solidification will never occur. But on a local micro-scale, a balance can be achieved. For a binary phase diagram under constant pressure, the solid and liquid concentrations only depend on the temperature

$$\boldsymbol{C_s^{eq} = C_s(T)} \quad \textbf{(I.1)}$$

$$\boldsymbol{C_l^{eq} = C_l(T)} \quad \textbf{(I.2)}$$

For simplicity, the liquid and solid curves are replaced by lines. Such a binary phase diagram is shown in (Fig. I.2), where the partition coefficient *k* is defined by a value less than 1.

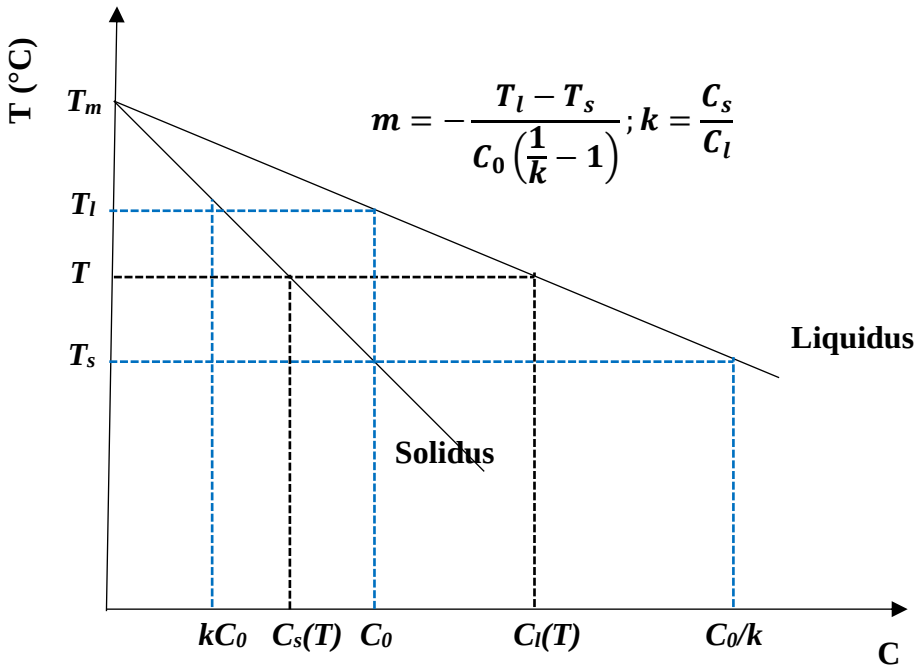

Fig.I.2: *A schema representing of linearized phase diagram for a binary alloy with k<1*

If we assumed that the solidus and liquidus curves are lines, the distribution coefficient *k* is constant. The liquidus line is defined by the following formula:

$$\boldsymbol{T_l = T_m + mC_l} \quad \textbf{(I.3)}$$

Where *m* is the liquidus slope, which is negative here.

The solidification interval at initial concentration C_0 (Fig. I .3), is defined as:

$$\Delta T = T_l - T_s = mC_0\left(1 - \frac{1}{k}\right) \quad \textbf{(I.4)}$$

If the assumption of perfect diffusion in the liquid and the solid is kept, the initial alloy concentration C_0 can be expressed as:

$$C_0 = f_l C_l + (1 - f_l)C_s \quad \textbf{(I.5)}$$

A relationship can be extracted from Equ. 5, which gives us the ratio of the two phases (liquid and solid) in equilibrium at each temperature

$$f_l = \frac{C_0 - C_s}{C_l - C_s} \quad , \quad f_s = \frac{C_l - C_0}{C_l - C_s} \quad \textbf{(I.6)}$$

This relationship is called the lever rule. In the case of the real solidification process, the relations (1) to (4) only apply to the solid-liquid interface, where the balance between C_s and C_l can be achieved. The solid concentration, in reality, is not uniform (there is no perfect diffusion), and it is very sensitive to the positions of the successive solid-liquid interface and the growth state of the solid front (plane, cell or dendritic). The solid-liquid interface morphology is the result of optimization of solute and heat exchange at the interface. Three

zones can be defined during the solidification of the alloy: solid zone, mushy zone and liquid zone. The simplified scheme of the mushy zone is considered to be a closed system between dendritic branches, where solid and liquid coexist.

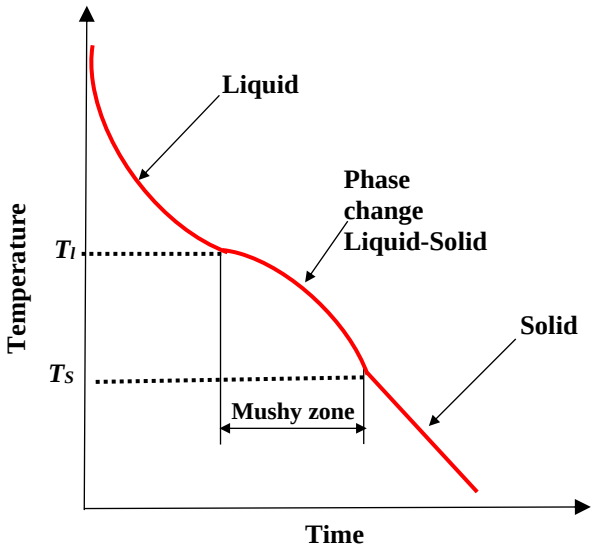

Fig.I.3: *Schematic cooling curve of an alloy.*

If it is generally believed that the liquid far from the solid-liquid interface is well mixed and has the same concentration everywhere, this is not the case in the mushy region. At the solid-liquid interface, the equilibrium represented by the phase diagram is achieved. Conversely, between two dendrites, the solute concentration will change (Flemings [2], Allen [4]). The solute concentration between the dendrites will be higher than the concentration at the solid-liquid interface (in accordance with the phase diagram shown in Fig.I.2). The interdendritic liquid melt is supercooled (the temperature is lower than T_l specified in the phase diagram), so it is very important to calculate this undercooling. Brody and Flemings [5] proposed the idea of adjusting the interdendritic space to minimize the undercooling. In this way, the undercooling is negligible, the liquid will be "completely mixed", and its concentration is given by the thermodynamic equilibrium. Under this assumption, the liquid concentration in the mushy zone is directly controlled by temperature. Even if the undercooling is not always as low as Flemings [2] confirmed, Allen's work [4] still confirms this hypothesis. Theoretically, solidification starts at the liquidus temperature and ends at the solidus temperature. In fact, solidification starts near the liquidus temperature (minus the undercooling) and usually ends at the eutectic temperature. This defines the temperature interval and concentration, corresponding to the presence of a mushy zone.

If we consider (contrary to the diffusion assumption) that solid is formed layer by layer, each solid layer will have a different concentration. Considering the liquid fraction transformation $f_l \rightarrow f_l - df_l$, the Gulliver–Scheil law can be written in differential form:

$$(\boldsymbol{C_l - C_s})\boldsymbol{df_l} = (\mathbf{1} - \boldsymbol{k})\boldsymbol{C_l df_l} \qquad \textbf{(I.7)}$$

If $k > 1$ k the solubility of the solute in the solid is greater than that in the liquid, so the solid will have lower and lower solute concentrations in each layer until only the pure solvent solidifies.

If $k<$ The solute is rejected at the solid-liquid interface, so the redistribution of solute will occur in the liquid before the interface. The solid is enriched in each layer until equilibrium is reached. The solid alloy retains traces of major segregation. These segregations are arranged in the order of the size of the space between dendrites, which means hundreds of micrometers, the so-called micro-segregation. When diffusion is accelerated, these concentration variations can be eliminated by heat treatment. However, in some alloys, the composition may vary greatly in the size of the ingot, which is called macrosegregation. Gulliver-Schill's law can be used to predict macro segregation. In the case where the distribution coefficient is less than 1, the

macrosegregation is caused by the solute rejected during the solidification process. Macrosegregation can take different forms (Lesoult [3]): the segregated channels (also called freckles) are striped, with varying composition, and thermal tearing (cracks) (Fig.I.4) [6, 7]. The occurrence of these defects is directly related to the effect of convection on the mushy zone [Prescott and Incropera 8]. These channels or freckles are visible in steel ingots containing high carbon or other elements (S, Mg, Mo) [2], aluminum-copper alloys [2], and transparent alloys [9] (Fig.I.5).) And Pb-Sn alloy [Sarazin and Hellawell 10, Bergman et al. 11].

(a) **(b)**

Fig.I.4: *a) X-ray photography showing segregated channel in a Sn-3wt.% Pb ingot (10×6×1 cm) [6]. b) in Ni supper-alloy (9 mm diameter) [7].*

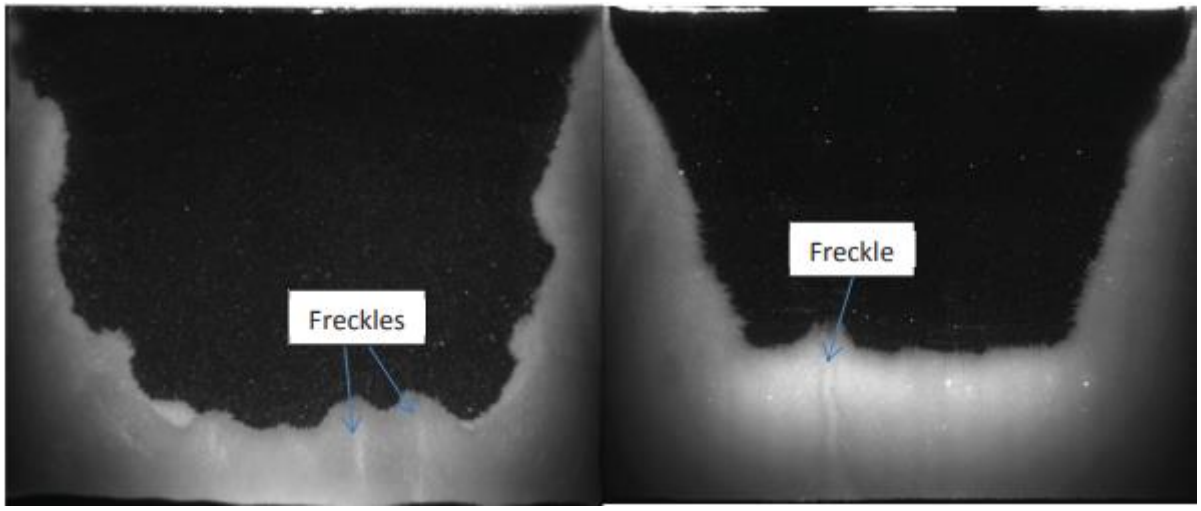

Fig.I.5: *Freckles in ammonium chloride-water mushy zone [9].*

1.3. Microsegregation and solid fraction

It has been seen previously that during the solidification of a binary alloy with a nominal composition of C_0, solutes will be rejected at the solid-liquid interface (for k <1). In the case of thermodynamic equilibrium, consider infinite diffusion in liquid and solid. The first solid crystal appears at temperature T_l, and the last solidified solid will appear at temperature T_s. The lever rule gives the liquid composition in equilibrium:

$$\boldsymbol{C_l = \frac{C_0}{1-(1-k)f_s}} \quad \textbf{(I.8)}$$

Where f_s represents the solid fraction. The solid fraction is communally "1" when the system is entirely solid and "**0** "when is totally liquid. Using Eq. 3, for $C_l = C_0$ the solid fraction can be expressed as function of temperature:

$$\boldsymbol{f_s = \left(\frac{1}{1-k}\right)\left(\frac{T_l-T}{T_m-T}\right)} \quad \textbf{(I.9)}$$

Where T_m is the melting temperature of the pure solvent. However, in reality, solidification is an unbalanced process, mainly due to chemical diffusion. Gulliver [12] and Scheil [13] proposed a model that considers the solute rejection in a simple way: assuming there is no diffusion in solid and infinite diffusion in liquid. The liquid concentration C_l and the solid fraction f_s become:

$$\boldsymbol{C_l = \frac{C_0}{(1-f_s)^{(1-k)}}} \quad \textbf{(I.10)}$$

$$\boldsymbol{f_s = 1 - \left(\frac{T_m-T}{T_m-T_l}\right)^{\left(\frac{1}{k-1}\right)}} \quad \textbf{(I.11)}$$

Moreover, it is well known that the solute diffusion in solid metals is not zero. Brody and Flemings [5] in their model considered it, by introducing the Fourier number $\alpha = \frac{D_s t_s}{(\lambda_{2,f})^2}$

Where D_s is the diffusion coefficient in the solid, t_s the solidification time and $\lambda_{2,f}$ the secondary dendrite arm spacing at the end of the solidification. This model was modified by Clyne and Kurz [14]. They used a new coefficient $\boldsymbol{\alpha'}$because the Brody and Flemings models are not effective for too large solid diffusivity. Considering this new factor, the liquid concentration and solid fraction can be written as follows:

$$\alpha' = \alpha[1 - exp(-1)] - \frac{1}{2}exp(-\frac{1}{2}) \quad \textbf{(I.12)}$$

$$C_l = C_0[1 - f_s(1 - 2k\alpha')]^{\left(\frac{k-1}{1-2k\alpha'}\right)} \quad \textbf{(I.13)}$$

$$f_s = \frac{1}{2k\alpha'}\left[1 - \left(\frac{T_m - T}{T_m - T_l}\right)^{\left(\frac{1-2k\alpha'}{k-1}\right)}\right] \quad \textbf{(I.14)}$$

Using Eq. 12 – Eq. 14, for α' equal to "0" the Scheil model can be retrieved and for α'equal to "0.5" the lever rule case can be described. The exact solution of the Brody- Flemings model was found by Kobayashi [15].

In the case of multicomponent alloys solidification, the models presented (lever rule, Scheil and Clyne-Kurz) can be adapted by taking into account the concentration of each element, considering $C_{l,i}$ the liquid concentration, $C_{0,i}$ the initial concentration and k_i the partition coefficient, for each alloy element i . Eq. 8, Eq. 10 and Eq. 13 become then:

$$C_{l,i} = \frac{C_{0,i}}{1-(1-k_i)f_s} \quad \textbf{(I.15)}$$

$$C_{l,i} = \frac{C_{0,i}}{(1-f_s)^{(1-k_i)}} \quad \textbf{(I.16)}$$

$$C_{l,i} = C_{0,i}[1 - f_s(1 - 2k_i\alpha')]^{\left(\frac{k_i-1}{1-2k_i\alpha'}\right)} \quad \textbf{(I.17)}$$

2. Macrosegregation

Segregation refers to non-uniformity of chemical composition. It can be classified into macro, meso and micro- segregation. Microsegregation results from the solute enrichment in the interdendritic liquid during solidification. While macrosegregation results from the local microsegregation and the relative movement of liquid and, possibly, solid phases. s. It ranges in scale from several millimeters to centimeters or even to several meters. These concentration variations will have a negative impact on the properties of the alloy, and even lead to total rejection of the solidified product. Macrosegregation occurs in all solidification processes: continuous casting, iron casting, aluminum and copper alloy mold casting, single crystal superalloys and ingot casting for semiconductor growth. Indeed, due to the low diffusion rate of the solute in the solid state and the large to cross, once the solidification is completed, the macrosegregation cannot be corrected by heat treatment. Both the experimental investigations and numerical simulations show that he main cause of macrosegregation is related to the relative

movement of the melt rich in solute and solid phase. Almost all phase diagrams, show that most alloying elements have a lower solubility in the solid phase than in the liquid phase. During the solidification process, solute elements are rejected from the solid into the liquid. Therefore, the solute concentration in the liquid phase continues to increase, and the solute concentration in the solid decreases at the same time. This segregation occurs on the microstructure scale (often usually caused by dendrites), and inhomogeneities happen in the concentration distribution in the arms of the dendrites, which is called microsegregation.

Ludwig et *al.* [16] present the four mechanisms described by J.A. Dantzig and M. Rappaz [17], responsible for macrosegregation, considering idealised scenarios. The macrosegregation is measured by means of mixture concentration, C_{mix}, as:

$$\boldsymbol{C_{mix} = \frac{f_l \rho_l \bar{C}_l + f_c \rho_c \bar{C}_c + f_e \rho_e \bar{C}_e}{f_l \rho_l + f_c \rho_c + f_e \rho_e},} \quad \textbf{(I.18)}$$

with f_l, f_c and f_e being the volume fractions of the liquid, columnar and equiaxed phases ρ_l, ρ_c and ρ_e the corresponding densities, and $\bar{C}_l$, $\bar{C}_c$ and $\bar{C}_e$ the corresponding species concentrations averaged over the volume element. Note that the volume fractions, densities, and average concentrations are supposed to be constant in the volume element, but may change over time.

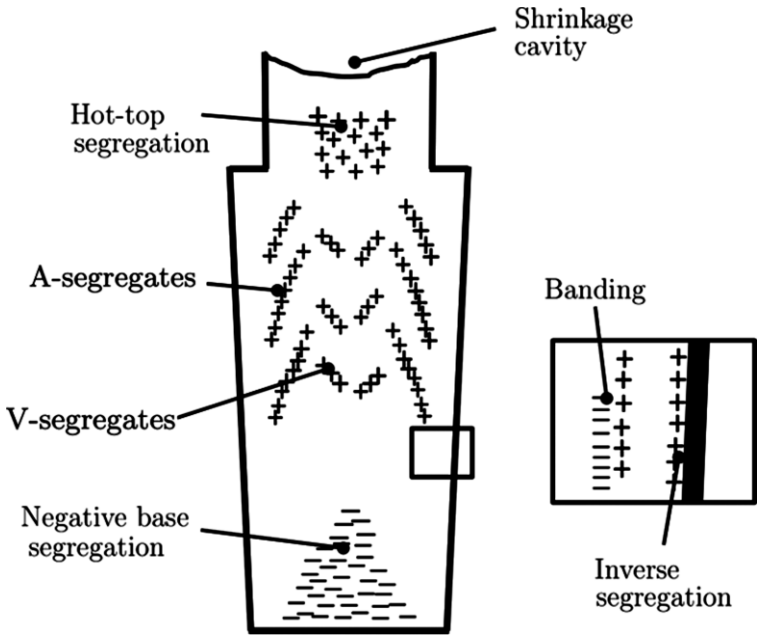

Fig.I.6: *Schematic of the different types of macrosegregation that can be found in large ingots. Positive segregation is denoted by + symbols (regions enriched in solute) and negative by - (regions depleted). Similar figures can be found in other macrosegregation reports, [25].*

The first examinations of macrosegregation phenomena in steel ingots were carried out many decades ago and although our understanding of the processes leading to segregation has improved considerably, the same patterns can still be observed in ingots made today. [18,19]. These, shown in Fig.I.6, include A-segregation, V-segregation and negative base segregation.

Up to the mid-1960s, solute buildup at the tips of advancing solid interface was believed to be the predominant underlying cause of macrosegregation phenomena in ingots by a number of authors, [18,20-23]). However, this premise has since been demonstrated to be erroneous by numerous theoretical and experimental investigations. It is now well recognised that the majority of solute is rejected sideways from a growing dendrite, enriching the mushy zone, and that build up in front of dendrite tips is negligible in this regard, [24].

All types of macrosegregation are derived from the same basic mechanism: that of mass transfer during solidification. The movement of enriched liquid and depleted solid, as shown in Fig.I.6, can occur through a number of processes:

- Convective flows due to density gradients caused by temperature and composition variations in the liquid, Fig.I.7(a). The thermal and solutal buoyancy contributions can either favourase or oppose each other depending on whether local temperature and concentration fields cause liquid density to increase or decrease. The convection due to the coupled action of temperature and solute is known as thermosolutal convection.
- Movement of equiaxed grains or solid fragments which have either nucleated heterogeneously in the melt, become detached from dendrites due to remelting/ stress, or have separated from the mould wall after pouring, Fig.I.7(b). Equiaxed grains in steels are denser than the surrounding liquid and will hence tend to sink. This mechanism, along with convective fluid flow, is a dominant macrosegregation process in large ingots.
- Flow to account for solidification shrinkage and thermal contraction of the liquid and solid on cooling, Fig.I.7(c).
- Deformation of the solid network due to thermal stresses, shrinkage stresses and metallostatic head (i.e., the pressure provided by the liquid metal above), Fig.I.7(d).
- Imposed flows due to pouring, applied magnetic fields, stirring, rotation etc.

The complex interplay between these mechanisms makes accurate modelling of macrosegregation phenomena a formidable challenge, often involving complicated

mathematical treatments. Thus, before such models are discussed, some qualitative explanations of how these mechanisms lead to macrosegregation defects are given below [113].

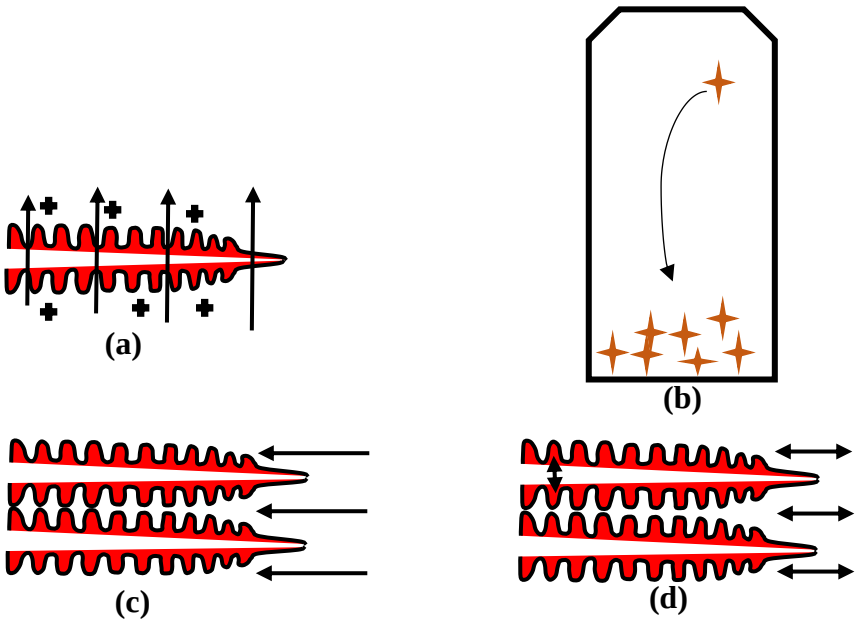

Fig.I.7: *Schematic of the processes which lead to mass transport during ingot solidification. (a) Convective flows in the interdendritic liquid (+ symbols denote enrichment in solute, whilst – denote depletion), (b) grain sedimentation (more generally solid movement), (c) liquid flow to feed solidification shrinkage and (d) mushy-zone deformation. Note that the columnar solid in (a), (c) and (d) has grown from the mould wal*

2.1. A-Segregation

A-segregates arise due to the flow of solute-rich interdendritic fluid via thermosolutal convection. They are characterised in the final solidified microstructure as channels of enriched solid, often with near-eutectic composition. Their formation mechanism can be described as follows: for example in steels the enriched interdendritic liquid will often be less dense than the bulk liquid, and will hence tend to rise. As the liquid moves towards the bulk liquid and the top of the ingot, it will increase in temperature, but its composition will remain nearly constant due to slow mass diffusion. This hotter enriched liquid then causes delayed growth or remelting of the solid around it, creating persistent solute-enriched channels. A-segregates are also commonly referred to as ‘channel segregates’ or ‘freckles’ when they arise in directionally-solidified castings (when the melt is cooled from below, for instance during the casting of single crystal nickel- based superalloy turbine blades).

The prevalence of A-segregation has meant it is perhaps the most investigated of all macrosegregation phenomena, not only in steels, but also many other systems. Some of the earliest studies which identified the importance of mushy zone fluid flow on macrosegregation were made by the Japanese steel industry in the 1950s, and focused on A-segregates. Kawai [26], was one of the first to attribute their formation in ingots to the gravity-induced flow of enriched mushy-zone liquid, whilst others confirmed that liquid density changes due to composition were of critical importance (by reducing the Si content and increasing Mo levels, it was found that A-segregation could be minimised), [27,28]. Later on, Suzuki et *al.* found that A-segregates started to form in the mushy zone when the fraction solid was between 0.3 and 0.35, and persisted until the fraction solid was as high as 0.7, [29].

Similar results were found by investigations of the NH_4Cl-H_2O system, a favourite of researchers because its transparent liquid allows the mushy zone to be directly observed during solidification. Particularly noteworthy NH_4Cl-H_2O studies were carried out by McDonald and Hunt and Copley et *al.*, and demonstrated that increased solidification times (and alloy freezing ranges) increased the severity of channel segregation, [30-35]. The Pb-Sn system was also the subject of a considerable research effort, [36-40]. Streat and Weinberg not only examined compositional and liquid-density effects in Pb-Sn, but also the extent of fluid drags within the mushy-zone network (i.e., the permeability, discussed below) on channel formation. The nucleation and stability of channel segregates were like- wise investigated experimentally and theoretically in a number of studies, [41-43].

A-segregation is of particular concern to the manufacturers of pressure vessels required for nuclear power generation. Such vessels are created by removing the core of the ingot after casting to create a shell, which is then forged and machined to finish. Welds may then be made to attach nozzles or end sections, and there is a concern that A-segregates could impinge on these welds. The enriched material within A-segregates is commonly associated with increased hardness and decreased toughness relative to bulk, which could lead to reduced weld integrity [44]. Fig.I.8 (a) shows the A-segregation present in material taken from a low-alloy steel ingot (0.2C–1.3Mn–0.7Ni–0.5Mo) after forging. Fig.I.8(b) and 8(c) show the difference in microstructure following slow cooling from austenisation at 940 °C at 0.1 °C s^{-1}; the hardness of the positively-segregated material was ~ 80HV2 higher than the bulk material in this untempered state [45].

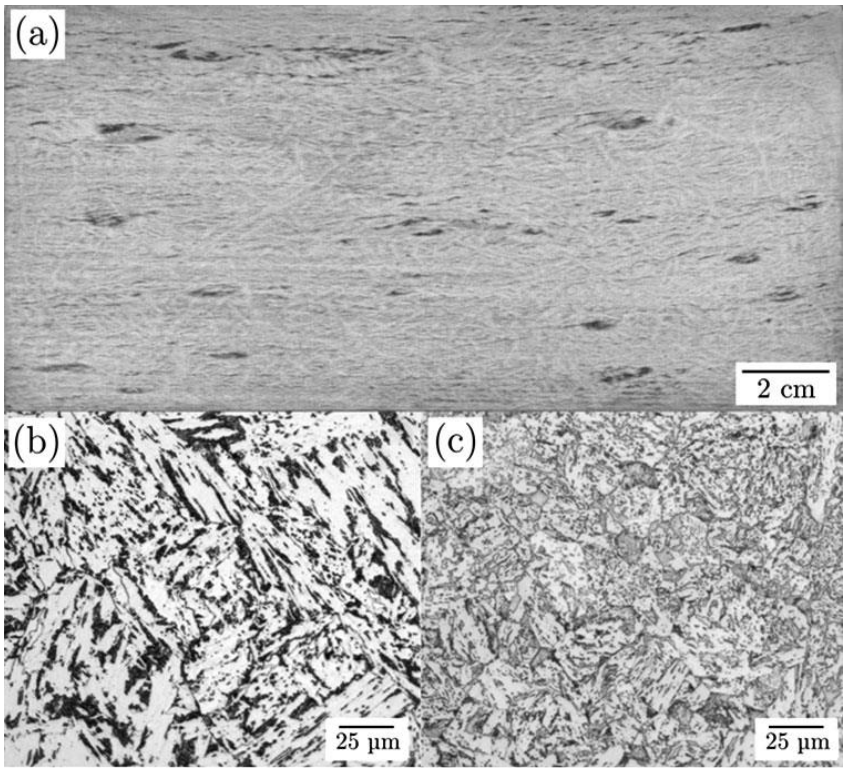

Fig.I.8: *(a) Low-alloy steel plate taken from forged ingot, macroetched in 5% nitric acid. A-segregates (in cross-section) are seen as ellipses of dark material; the remnants of primary dendrite arms also appear as lightly-etched bands. The plate normal is aligned with the vertical axis of the ingot. (b) and (c) show the effect on microstructure of slow cooling from austenisation at 940°C at 0.1°C s^{-1}. The bulk material in (b) shows a Widmannstätten ferrite structure, whilst the enriched material in (c) is a mixture of bainite, retained austenite, and martensite. Both were etched in 2% nital and imaged with an optical microscope. [45].*

2.2. Negative Base Segregation

It has been proposed that negative base segregation can arise in ingots due to two processes:

(i) the settling of solute depleted (negatively-segregated) equiaxed grains at the bottom of the ingot under the action of gravity and

(ii) the general rise of solute-enriched liquid upwards. There has been some dispute over which of these mechanisms is predominant: early investigations by Marburg and others suggested that the flow of enriched liquid upwards was the dominant factor, citing the appearance of negative segregation in ingots which apparently contained no equiaxed zone [20, 22]. But in reality, it is rarely the case that steel ingots undergo fully columnar solidification, and more recent modelling investigations have tended to lend greater significance to grain sedimentation [46].

It has been found that the equiaxed zone in a low-alloy steel ingot may extend to well over half its height [46,47], and that the equiaxed grains at the very base of the ingot are more globular in form than those found further up the ingot (globular grains are rounder and not so branched, equiaxed grains typically start growing in this form before becoming dendritic) [46,48,49]. Disconnected grains can form through a number of mechanisms, which include heterogeneous nucleation in the melt and dendrite-arm detachment. The predominant mechanism is usually detachment due to the action of convective flows or shrinkage stresses. Note that if the density of enriched liquid is higher than the bulk, as is possible, then flow in the mushy zone will be generally downwards, and this may reduce the severity of both negative base segregation and any positive segregation (enrichment) at the ingot top.

2.3. V-Segregation

During the final stages of ingot solidification, the centre of the casting is usually occupied by a network of loosely-connected equiaxed grains. It is thought that V-segregates arise due to the fissuring of such networks under action of metallostatic head (i.e., the weight of material above) and solidification shrinkage, see Fig.I.9, which leads to the formation of open shear planes that can fill with any remaining liquid [25,50,51]. This remaining liquid will have been enriched throughout solidification by convective flows from the mushy zone, and also by solidification in the final cavity, and it solidifies to produce positively-segregated solid. Indeed, the solidification of enriched material at the end of solidification generally produces the often-referred-to centreline segregation.

Despite being regularly observed, V-segregation is generally not well understood other than through the mechanism given above. Theoretical treatments and models of V-segregate formation in ingots have yet to be produced and are likely to prove challenging as they would need to account for phenomena including equiaxed grain sedimentation, mushy zone deformation and fluid flow. Nevertheless, the total lack of literature on V-segregation in ingots is perhaps indicative of a further issue - the disinterest of manufacturers in the subject. It is often the case that the centres of ingots are removed after casting (as highlighted above) or that the effects of V-segregation are insignificant for end applications. Not only would modelling of V-segregation be a great challenge, but it may not prove to be particularly useful.

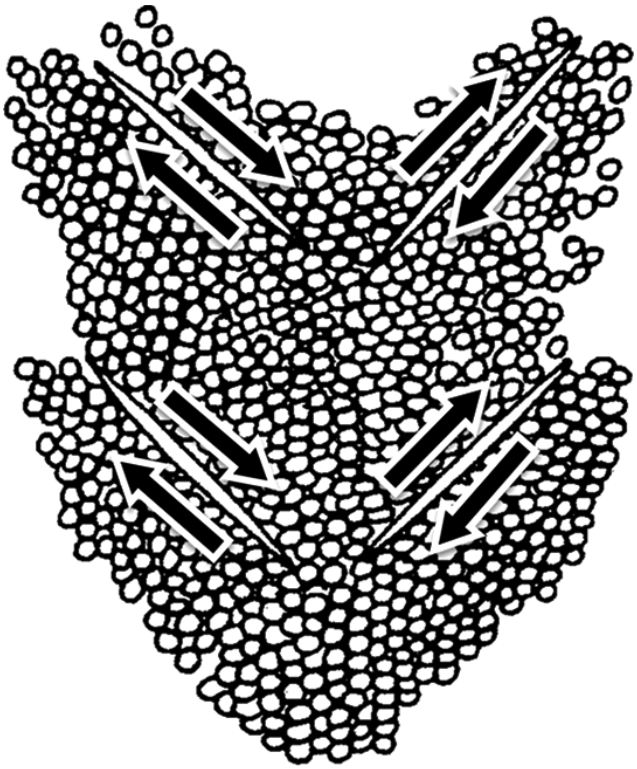

Fig.I.9: *Schematic showing formation of V-segregates through shearing on preferred planes during settling and compression of equiaxed grains. Adapted from Flemings, [25].*

2.4. Modelling Macrosegregation

In order to modelate the phenomenon of macrosegregation, the liquid flow through the mushy zone is considered to be the main source of the segregation at macro scale, and the mushy zone is the area where solid is supposed to grow in a rigid arrangement. The macrosegregation in this case can be explained by the approach of Flemings et *al.* [52]. They considered the Local Solute Redistribution Equation (LSRE) based on the local solute balance on the small volume elements inside the mushy zone, as shown in Fig (I.11). Just like in the standard Scheil model, the local solute diffusion in the solid phase is ignored. Therefore, the liquid composition in the mushy zone inside the volume element is considered to be uniform and in equilibrium. The solute concentration in liquid $\boldsymbol{C_l}$ is controlled by the temperature and the liquidus slope given by the phase diagram. Consider the solute advection caused by liquid flow, the inside and outside of the volume element, and the different densities of solids and liquids. Eq.I.19, [52]:

$$\frac{\boldsymbol{df_s}}{\boldsymbol{dC_l}} = \frac{\boldsymbol{(1-f_s)}}{\boldsymbol{C_l}} \frac{\boldsymbol{(1-\beta)}}{\boldsymbol{(1-k)}} \left(\boldsymbol{1} - \frac{\boldsymbol{u_n}}{\boldsymbol{v_T}}\right) \qquad \textbf{(I.19)}$$

where u_n is the liquid flow velocity in the direction normal to the isotherms, v_T is the isotherm velocity and β is the solidification shrinkage, expressed as the ration between the density difference (solid and liquid) and the solid density.

$$\boldsymbol{\beta = \frac{\rho_s - \rho_l}{\rho_s}} \quad \textbf{(I.20)}$$

In one dimension, the mass conservation equation indicates that the liquid velocity required to feed the solidification shrinkage should be:

$$\boldsymbol{u_{n\backslash shrink} = v_T\left(1 - \frac{\rho_s}{\rho_l}\right) = -v_T\left(\frac{\beta}{1-\beta}\right)} \quad \textbf{(I.21)}$$

It must be noted that the liquid flow caused by solid shrinkage is opposite to the isotherm velocity, that is, the same direction as the temperature decreases and the solid fraction increases. In Eq. 21, if the alloy density decreases during the solidification ($\beta < 0$), the liquid flow due to solid shrinkage $u_{n\backslash shrink}$ can have the same sign as v_T

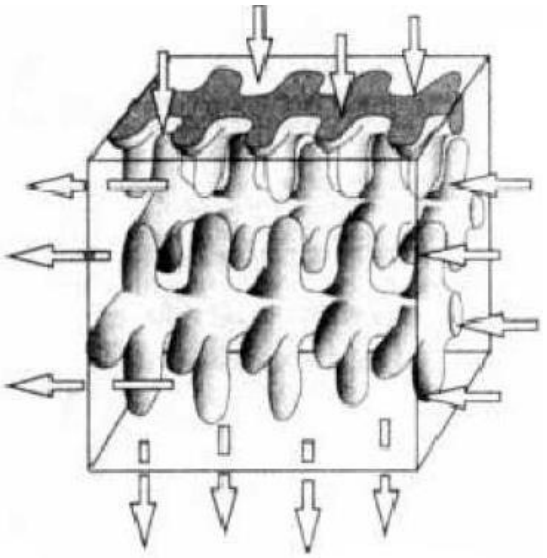

Fig.I.10: *Schematic of volume element in mushy zone considered when developing conservation equations, [53].*

In Fig.I.10, more details of the liquid flow inside the mushy zone are given to make the $u_{n\backslash shrink}$ and v_T terms clearer. The solute concentration along the isotherm is constant, so the liquid flowing in or out of the volume element along the isotherm has the same solute concentration, and no macrosegregation occurs.

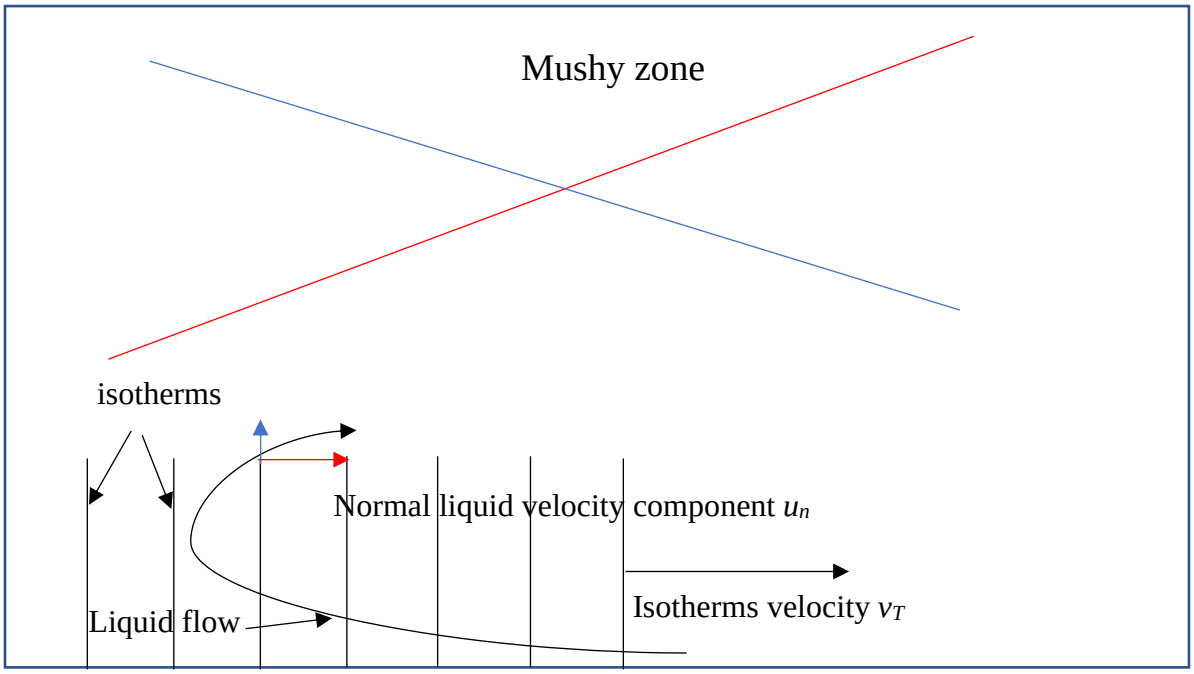

Fig.I.11: *Schema of liquid flow inside the mushy region.*

Beckerman [54] defined a flow factor ξ considering the liquid flow inside the volume element and the isotherms velocity, as follows:

$$\boldsymbol{\xi = (1-\beta)\left(1-\frac{u_n}{v_T}\right)} \qquad \textbf{(I.22)}$$

If ξ and k are assumed constant, Flemings's equation (Eq. 19) can be integrated and a modified Scheil equation can be obtained:

$$\boldsymbol{\frac{C_l}{C_0} = (1-f_s)^{\frac{k-1}{\xi}}} \qquad \textbf{(I.23)}$$

When $\xi = 1$ no macrosegregation happens and Eq. 23 gives simply the Scheil classical equation.

In two main cases, no macro segregation phenomenon will occur($\xi = 1$):

- If no shrinkage occurs ($\beta = 0$) and no liquid flow perpendicular to the isotherms exists ($u_n = 0$)
- If no liquid flow occurs, except the flow needed to feed the solidification shrinkage in a given dimension $u_n = -v_T \frac{\beta}{1-\beta}$ or $u_n = u_{n\backslash shrink}$

When the flow factor ξ is different than 1 macrosegregation phenomena always occur, since the liquid concentration C_l changes in a different way than in the Scheil classical model. Using

the Scheil modified equation (Eq.23), three different macrosegregation mechanisms can be described for $k < 1$

2.5. Remelting

During the solidification process, there is a possibility of local remelting of the solid that has formed. There are two ways in which local remelting can occur: by increase in enthalpy of a cell due to local reheating, and/or by local increase in liquid concentration due to flow of solute-rich liquid into the region. This case can happen if the liquid circulates towards the low solid fraction area at a velocity higher than the isotherm velocity ($u_n > v_T$) in the direction of temperature increase. This means that the flow coefficient is negative ($\xi < 0$).

Taking into account the Flemings equation (Eq.18), this flow will cause a decrease in solid fraction and temperature. This means that remelting will occur and segregated channels will form in the mushy zone. Once the solidification in this zone is completed, a positive macrosegregation can be seen inside these channels.

The direction and magnitude of the flow inside the mushy zone depend on many factors. The permeability of the mushy zone is the most important parameter, which can limit the flow inside the mush, [55]. Generally, permeability decreases with increasing solid fraction, so small interdendritic voids reduce permeability.

The following examples illustrate the macro separation mechanism described earlier in more detail.

3.3.Inverse segregation

Near the cooled surfaces, positive macrosegregation is often observed, Ohnaka and Matsumota [56]. This type of segregation is called reverse segregation (Fig.I.12). J. S. Kirkaldy [57] shows that this is a direct result of the second macrosegregation mechanism previously discussed. In fact, besides the cooling surfaces, the liquid velocity is zero ($u_n = 0$), so $u_{n\backslash shrink} < 0$. Therefore, the condition $u_n > u_{n\backslash shrink}$ is always valid at the cooling surface, so a positive macrosegregation is produced.

In the case where there is a gap between the cooling mold and the ingot to solidify, the solute-rich interdendritic liquid is pressed into the gap due to the metallostatic pressure. This phenomenon usually happens when there is a positive macrosegregation at the cooled surface.

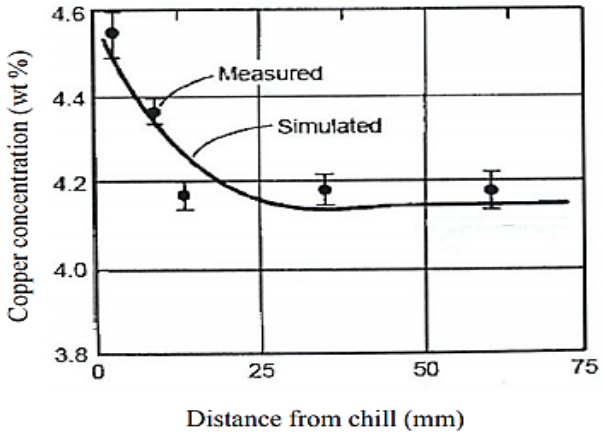

Fig.I.12: *Comparison of simulated and measured solute distribution during the unidirectional solidification of a Al-4.1 wt.% Cu ingot alloy, [56].*

3.4.Macrosegregation due to the thermosolutal convection flow

If there is convection in the mushy zone, the first two macrosegregation mechanisms can be observed simultaneously. The work of Ohnaka et al. proved this, [56] on the Horizontal solidification of Al-Cu alloy. Fig.I.13 shows a schema of the flow caused by themosolutal convection with counter-clockwise circulation roll, the flow in the bulk, and the liquid flow that penetrates into the mushy zone.

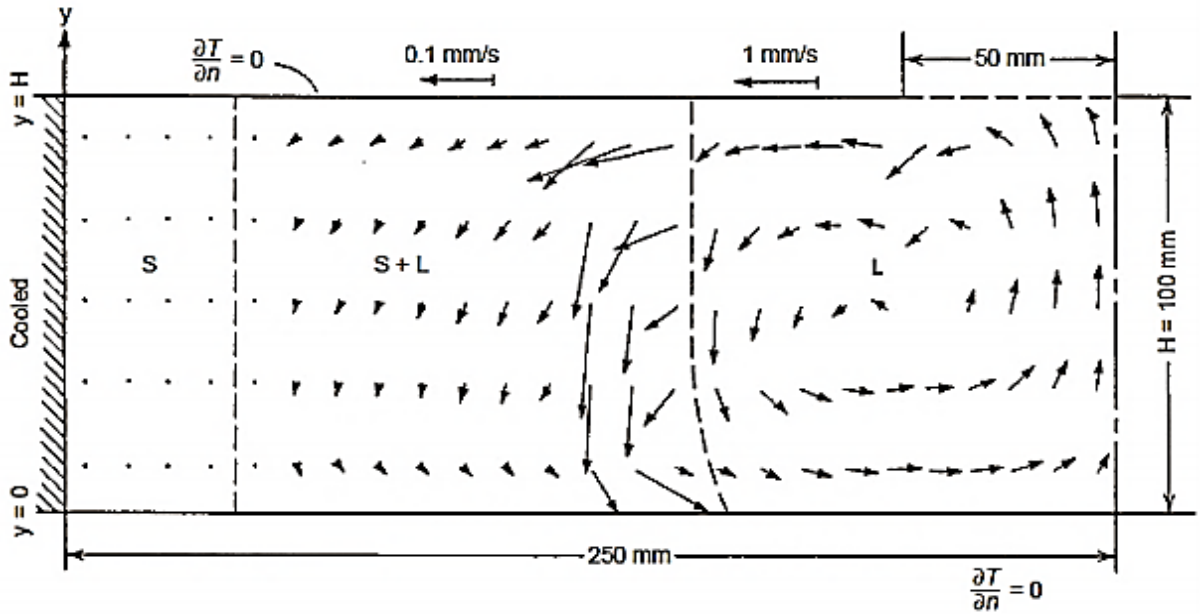

Fig.I.13: *Numerical simulation of the liquid flow (400 s after the cooling started) during the horizontal solidification of the Al-4.4 wt% Cu alloy, [56]*

In the upper part of the mushy zone, the flow is in the direction of temperature decrease,$u_n < 0$. Considering the first macrosegregation mechanism, a negative macrosegregation will happen under these conditions. Compared with the experimental results shown in Fig.I.14, the numerical simulation clearly confirmed the occurrence of negative macrosegregation in this upper region. In contrast, in the lower part of the mushy zone, the interdendritic liquid flows toward the bulk in the direction where the temperature increase $u_n > 0$. This situation will produce positive macrosegregation, as described in the second macrosegregation mechanism, which has been firmly verified by the results in Fig.I.14.

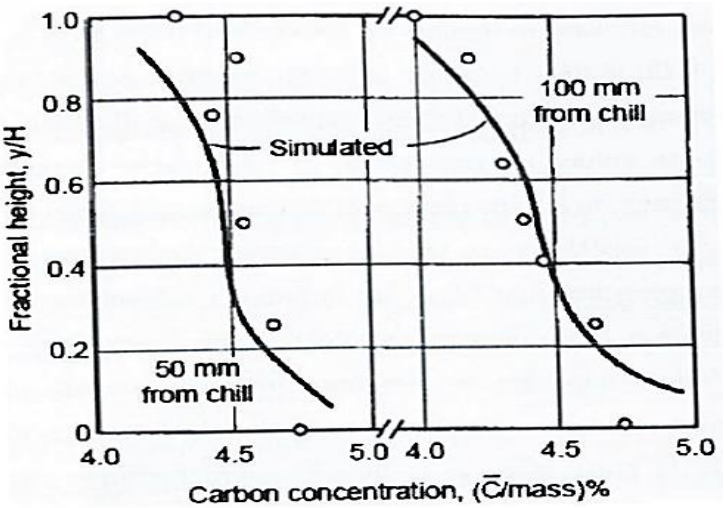

Fig.I.14: *Solute distribution in the ingot Al-4.4wt% Cu, [56]: negative macrosegregation at the top and positive at the bottom.*

Interestingly, due to the flow parallel to the isotherm lines, there is no macrosegregation in the middle-high mushy zone.

2.6. Segregated channels

The third macrosegregation mechanism brings the appearance of channels. Fig.I.15 shows this segregation defect, commonly referred to as freckles. During the monocrystal directional solidification of Ni alloys, segregated channels or freckles are often observed on the upper part. In this process, a large number of elements (such as Al and Ti) are rejected in the liquid, while heavy elements (such as Tg) are incorporated into the solid. This situation is the origin of the strong upper flow in the mushy zone. Even if there is a stable temperature gradient, convection rolls will be generated, and considering that the liquid velocity is higher than the isotherm velocity, the solid fraction will decrease as the temperature decreases (as described in the third

mechanism). This phenomenon will create conditions for the formation of channels in the mushy zone, and the solute-enriched liquid will flow out of the mush.

Fig.I.15: *Freckle of 2 mm diameter, observed in a Ni supper alloy [M. C. Schneider 58].*

The numerical results given in Fig.I.15 show these flow configurations are responsible for creating channels [58]. In this case, the size of the channel is a few millimeters thick and a few centimeters high. During the solidification process, these channels are filled with dendrites fragments, which can be seen as equiaxed crystals in the final solidified alloy. In this way, the positive macrosegregation in these channels can be seen in the numerical simulation results (Fig.I.16).

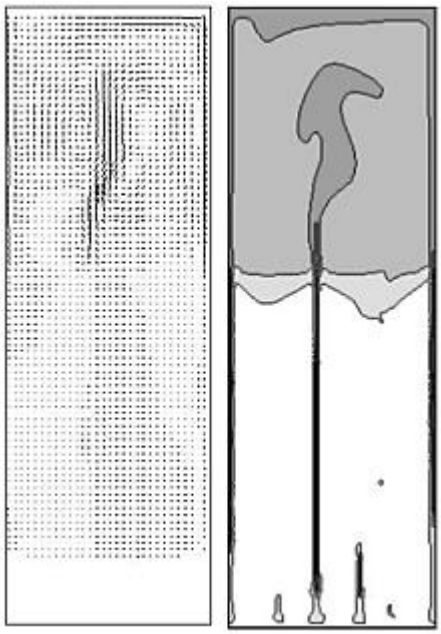

Fig.I.16*: Numerical simulation of segregated channels during the directional solidification of a Ni superalloy, [58].*

3. Solidification structure

3.1. Solid front morphology

When we fix the temperature gradient in the liquid "*G"* and the initial concentration "C_0*"*, we notice that at the low speed of pulling the solid-liquid interface is flat. If velocity "*V"* is increased beyond a critical velocity "V_C*"*, the front becomes unstable and the solid-liquid interface solid-liquid interface presents a spatial structuring. These microstructures, whose period or primary spacing "λ" is typical of the order of a few tens or hundreds of micrometers, are called cells or dendrites (Fig.I.17) [59].

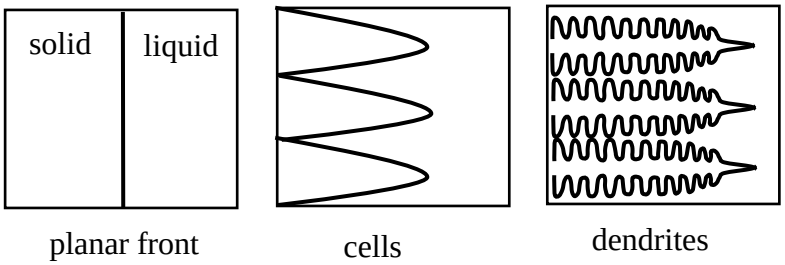

Fig.I.17: *a) Schema of different interface morphologies and resulting microstructures.*

3.2. Solid-liquid interface and its stability

The solidification mechanism of metals implies a thermo-dynamical phase change: from a disordered liquid to an ordered solid. This state change requires an atomic-level reorganisation, which initiates by forming a solid nucleus in a liquid. In order to produce a solid nucleus, a solid-liquid interface needs to be created, and its morphology depends on its stability during solidification.

3.2.1. Nucleation

Nucleation is a phenomenon out of equilibrium and requires additional energy to establish a solid-liquid interface. This energy barrier can be overcome by undercooling, and the temperature of the liquid is lower than the melting temperature. This temperature difference is called nucleation undercooling (ΔT_n). There are two types of nucleation:

- Homogeneous nucleation: direct formation of nuclei in the liquid without solid particle and solid contact (no mould contact). Even in pure liquids, impurities are always present in a small percentage. Therefore, it is difficult to speak about homogeneous nucleation in reality.
- Heterogeneous nucleation: solid particles already present in the liquid will reduce the energy barrier for nucleation, thereby overcoming the nucleation and making the growth of a nucleus easier

During solidification a nucleation rate is defined, that follows an Arrhenius type law [60]:

$$\boldsymbol{I = I_0(N - N_0)exp\left(-\frac{\Delta G_n}{k_B T}\right)} \quad \textbf{(I.24)}$$

where I_0 is a constant (for metals is equal to 10^{20} s^{-1}), N_0 is the total number of nucleation sites per volume unit, N the number of activated sites, ΔG_n the activation energy, k_B the Boltzmann constant and T the temperature. Hunt, [65] in his heterogeneous model admitted that for small undercoolings ($\frac{\Delta G_n}{k_B T} \propto a/(\Delta T)^2$, where ΔT is the system-imposed undercooling and a is a constant, $a = (\Delta T)^2 \ln(N_0 10^{20})$), the nucleation rate depends on the cooling conditions (number of activated sites, imposed undercooling) and on material properties (number of nucleation sites, nucleation undercooling).

3.2.2. Interface instability

In the case of pure metal, the origin of the destabilization of the interface is only thermal. The interface will be stable if the temperature gradient in front of the solidification front is positive (case of directed solidification) and unstable if the gradient is negative (free growth), [61].

Let us consider the case of a binary metal alloy of initial concentration C_0 of the alloy element, advancing with a planar front at a velocity V in a stationary regime. During the alloy solidification, the low solid solubility ($k < 1$) induces solute rejection in front of the interface. This solute rejection is limited to the boundary layer ($\delta_c = D_l/V$), characterised by the solute diffusion in the liquid D_l and interface velocity V. The resulting concentration profile is schematised on Fig.I.19. The solute concentration in this boundary layer decreases exponentially with the distance x from C_0/k until C_0.

$$\boldsymbol{C(x) = C_0 + \left(\frac{C_0}{k} - C_0\right) exp\left(-\frac{V_x}{D_l}\right)} \quad \textbf{(I.25)}$$

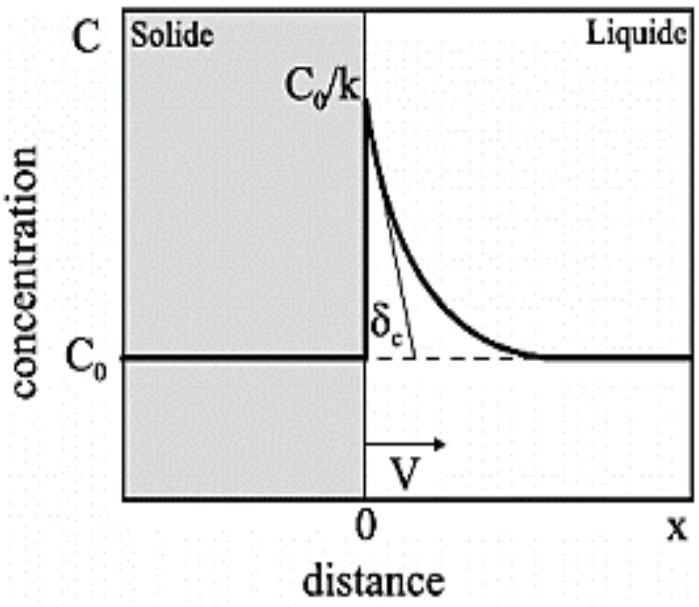

Fig.I.18: *Concentration profile at the solid-liquid interface. The solute release is located in the liquid zone adjacent to the interface, [1].*

According to the phase diagram, the equilibrium temperature of the liquid is described by the relation:

$$\boldsymbol{T_l(C(x)) = T_l + m(C_x - C_0)} \qquad \textbf{(I.26)}$$

T_l and m are respectively the liquidus temperature and the liquidus slope.

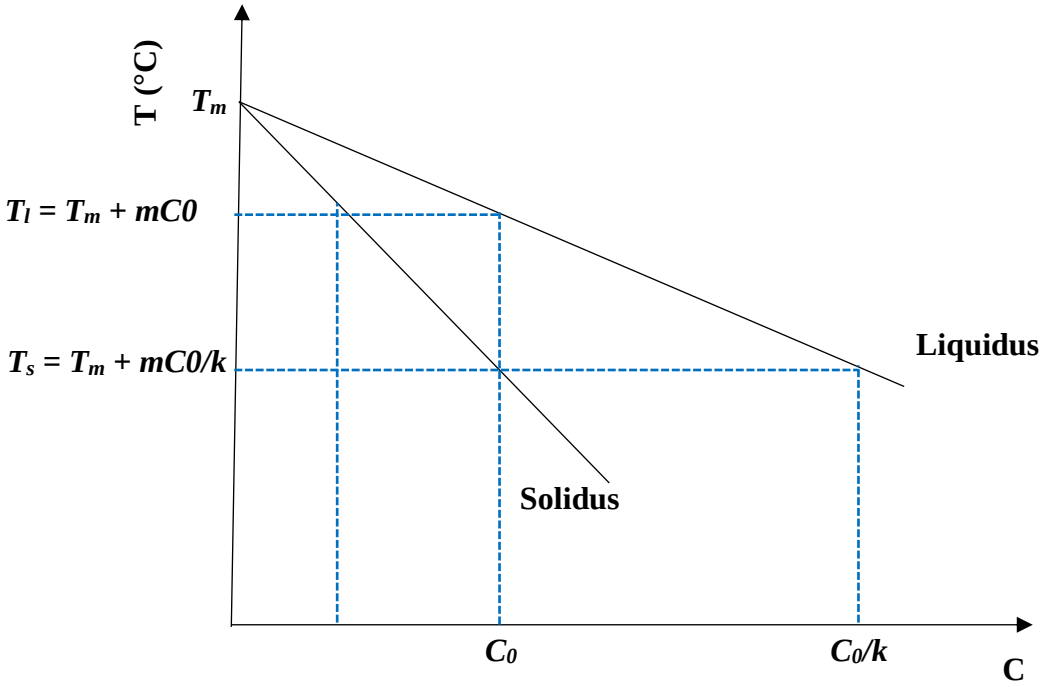

Fig.I.19: *Schema of a binary phase diagram with* $k < 1$.

The interface stability will then depend on the evolution on the temperature $T(x)$imposed by the heat flux present during the solidification.

$$\boldsymbol{T(x) = T_m + m\frac{C_0}{k} + G(x)} \quad \textbf{(I.27)}$$

Two cases can be distinguished (Fig.I.20):

(1) if $T(x)$ is larger than $T_l(C(x))$ locally, the system is stable, the solidification front stays planar.

(2) if $T(x)$ is lower than $T_l(C(x))$ locally, the system becomes unstable, the solid front destabilises. This instability condition is called constitutional undercooling because it depends only on the solute rejection in a given temperature gradient

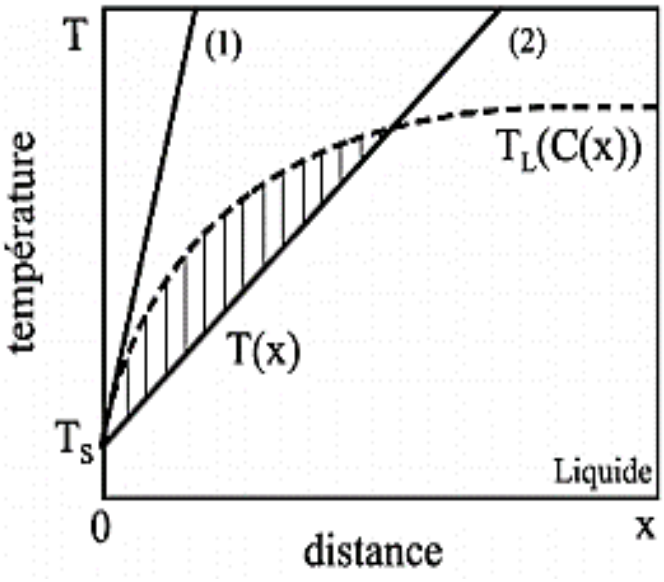

Fig.I.20: *Temperature profile at the solid - liquid interface. The system can remain in stable conditions (1) or be in constitutional undercooling (2) (hatched part) [1].*

The criterion of constitution undercooling assumes that any disturbance arising on the plane interface will develop provided that the relation:

$$\boldsymbol{G - mG_C < 0} \quad \textbf{(I.28)}$$

where G_C is the concentration gradient in the liquid at the interface that can be deduced from equation (I.25). At a fixed gradient, a plane front will be considered as unstable for velocity higher than a critical velocity:

$$\boldsymbol{V > V_C = \frac{kGD_L}{(k-1)mC_0}} \quad \textbf{(I.29)}$$

Although this analysis is based on a purely thermodynamic argument and the whole dynamic aspect of solidification is ignored, its agreement with the experiment can be considered satisfactory in the first approach. Moreover, it highlights the stabilizing effect of the temperature gradient and destabilizing effect of the concentration gradient. On the other hand, it is obvious that the constitution undercooling does not give any prediction on the size, and even less on the shape, of the microstructure that will be established at the solidification front.

3.3. Dendritic microstructure development

3.3.1. Dendritic growth models

Dendritic structures are the most commonly encountered in metallurgy. In order to control the chemical segregations associated with these microstructures, it is essential to understand the physical processes involved during dendritic growth. In this part, we propose to state the theoretical basis of the growth of a dendrite tip.

The mathematical solution to the problem of the growth of a needle-shaped crystal (parabola) in a liquid at rest and in supercooling was elaborated for a zero-surface tension by Ivantsov in 1947, [62]. The problem admits an exact solution:

$$\boldsymbol{\Omega = I_v(Pe)} \qquad \textbf{(I.30)}$$

With $\Omega = \frac{C_l^* - C_0}{C_L^*(1-k)}$) and $I_v(Pe) = Pe * exp(Pe) * E_1(Pe)$

Ω is defined as the supersaturation, *Iv(x)* corresponds to the Ivantsov function, $E_1(x)$ is the exponential integral function and *Pe* the Peclet number, which corresponds to the ratio of the characteristic dimension of the system "*R"* (the radius of curvature of the dendrite) and the distance of diffusion of the solute "*δc"*:

$$\boldsymbol{Pe = \frac{RV}{2D_l}} \textbf{ with } \boldsymbol{\delta_c = 2D_l/V} \qquad \textbf{(I.31)}$$

The solid as well as the isoconcentrations in the liquid around the tip form a system of confocal paraboloids of revolution. Nevertheless, for a given undercooling, there is a continuum of solutions of pairs (*R,V*) and only the product *RV* (with *R* radius of curvature at the top of the dendrite and *V* growth rate) is fixed. It is therefore impossible to know independently the tip radius and the growth velocity.

Experimentally, the two parameters *R* and *V* are reproducible for a given supersaturation. The problem of selection arises, which consists in finding the "*good*" solution, if it exists, among

the continuum of possible solutions. In order to the degeneracy of the Ivantsov solution, a selection criterion has been introduced by Langer and Müller-Krumbhaar in 1978 called the marginal stability criterion, [63]. The authors are interested in the stability of solutions in the presence of a non-zero surface tension. It was proposed that the operating point of the dendrite tip corresponds to the point of marginal stability, i.e. when the amplification rate of a perturbation at the tip of the dendrite is just the dendrite is just zero. The dendrite then grows with a radius of curvature close to the wavelength of the marginal stability, λ_i, of a plane front advancing under the same conditions as the dendrite tip either:

$$\boldsymbol{R = \lambda_i = 2\pi\sqrt{\frac{\Gamma}{G_c - G}}} \qquad \textbf{(I.32)}$$

Where G_c is the solute gradient in the liquid at the dendrite tip:$D_l G_c = -VC_l^*(1-k)$. In this way it is possible to calculate R or T^*independently of V , using Eqs. 31 and 32.

These results can be generalized to the case of directed growth of binary alloys to determine the evolution of the radius of curvature *R*, the temperature at the tip of the dendrite *T** and the primary spacing λ_1 as a function of the growth rate *V*. By example, Fig.I.22 and Fig.I.23 correspond to the KGT (Kurz, Giovanola, Trivedi) model, [64].

We can see (Fig.I.21) that the temperature of the dendrite tip first tends to approach the liquidus temperature then moves away from it. This behavior can be explained simply by considering that the capillary effects are not preponderant at low velocity and the fact that the size of the solutal layer in front of the tip δc (which defines in first approximation the size of the undercooled liquid zone) decreases with velocity. For the highest velocities, capillary effects are important and the temperature of the tip of the dendrite decreases due to curvature undercooling.

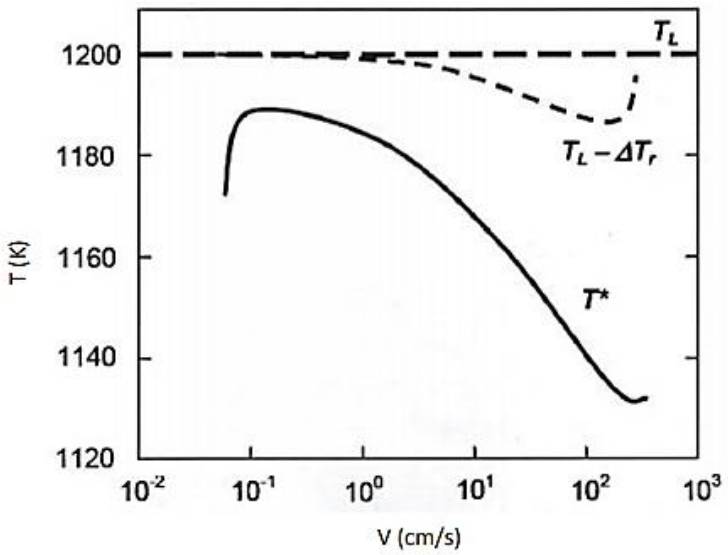

Fig.I.21: *Evolution of the dendrite tip temperature with the growth velocity for an Ag-5% Cu alloy, [65].*

The microstructures likely to be encountered can be deduced from these evolution curves (Fig.I.22). At low growth rate, the interface remains stable. At the value corresponding to the constitutional undercooling, the front destabilizes and leads to the development of cells and then dendrites. Note that at high velocity, the interface stabilizes once again, and absolute stability is reached (for more details on this phenomenon see reference, [65]).

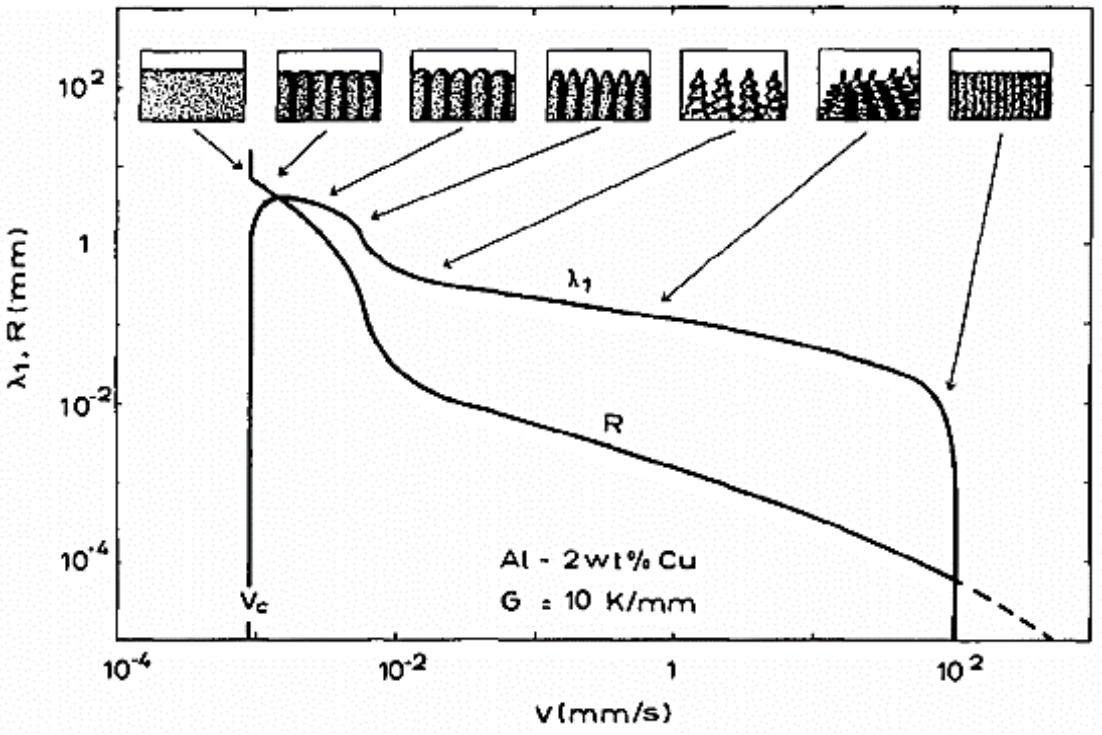

Fig.I.22: *Microstructure types assumed from the evolution curves of the dendrite tip radius and of the primary arm spacing λ_1 versus the velocity growth of a Al-2% Cu alloy, [1].*

The values predicted by the marginal stability assumption are generally in good agreement with experimental studies such as those of Huang and Glicksman, [66]. However, there is no real justification for the selection of the marginal stable state with respect to the other possible stable states. There is therefore no rigorous solution to the problem of dendritic growth problem when we consider the surface tension as being isotropic.

Studies have been conducted taking into account the anisotropy of the interfacial energy "γ" [67-70] and the resulting theories are called "microscopic solvability theories". These theories allow to predict a value of the product (VR^2) when the interfacial energy is not zero and show that there exists in this case a discrete set of couple radius of curvature, growth rate which are solutions to the dendritic growth problem. The growth rate corresponding to the most stable state is the highest and it is the one selected by the system. The selected rate corresponds to a "stability constant" σ^* which depends only on the characteristics of the material and which varies as $\varepsilon^{7/4}$ with ε the anisotropy parameter of interfacial energy.

Finally, it should be noted that numerical simulations using the phase-field modelling technique have recently progressed rapidly and, after having been able for a long time to give only a qualitative description of the selection of the microstructure and of the morphological instability, are now able to model quantitatively more and more phenomena taking place during solidification. The solidification of dendrites of pure substances has been simulated for both high and low subcooling, [71, 72]. More recently, the solidification of alloys has been treated in the case of free solidification and directional solidification, [73, 74]. Models taking into account the fluid movements, [75] or the simultaneous diffusion of heat and solute, [76]. Have also been developed.

3.3.2. Primary and secondary dendrite arms spacing

Fig.I.23 represents the main features that define the dendritic microstructure: the radius of the dendritic tip R, and the primary and secondary dendrite arms spacings λ_1 and λ_2. The microstructure (changes in these parameters) affects the properties of the material (such as mechanical properties).

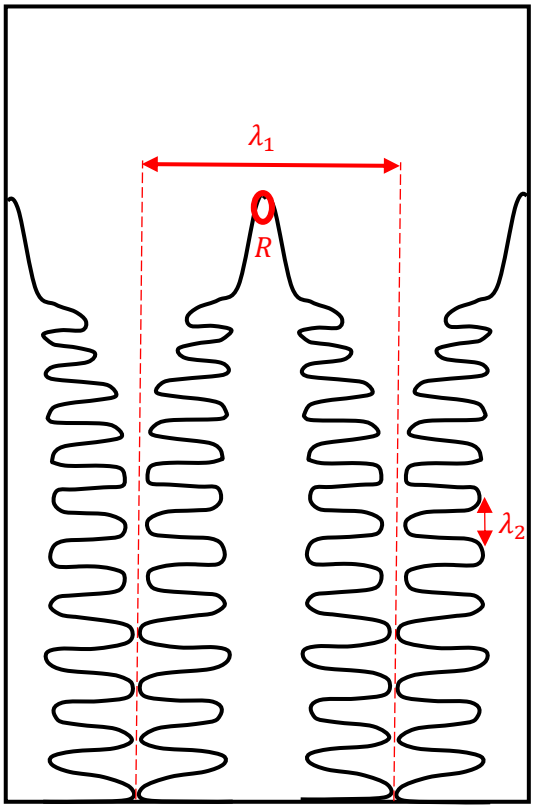

Fig.I.23: *Main characteristics of dendrites.*

The model that predicts the spacing of the main dendrite arms considers a relationship generally expressed as a function of the mushy zone thickness, the temperature gradient, and the velocity growth. Eq 34 shows an example of the model, [77]:

$$\boldsymbol{\lambda_1 = 4.3\left(\frac{D_l \Gamma \Delta T_0}{m}\right)^{\frac{1}{4}} V^{-\frac{1}{4}} G^{-\frac{1}{2}}} \quad \textbf{(I.33)}$$

Based on the work of Kattamis and Flemings, [78], Feurer and Wunderlin, [79] developed a model to calculate λ_2 , taking into account the maturation phenomenon:

$$\boldsymbol{\lambda_2 = 5.5\left(M t_f\right)^{\frac{1}{3}}} \quad \textbf{(I.34)}$$

With

$$\boldsymbol{M = \frac{\Gamma D_l \ln\frac{C_l}{C_0}}{(1-m)(C_l - C_0)}} \textbf{ and } \boldsymbol{t_f = \frac{\Delta T'}{|T|} = \frac{\Delta T'}{|GV|}} \quad \textbf{(I.35)}$$

where M is the maturation factor, t_f the solidification time, C_l is the final solute concentration in the liquid and $\Delta T'$ is the temperature difference between the dendrite tip and the solidus temperature. This can be approximated with ΔT_0.

4. Influence of crystallographic stresses

In general, crystal growth is limited by:

- The diffusion of heat and solute in the liquid.
- Capillarity
- Attachment kinetics of atoms at the interface

The relative importance of each of these factors depends on the material considered and the solidification parameters. For some materials, atom attachment kinetics may play an important role. For example, for those materials that exhibit a "no-faceted" growth morphology typical of metals, it can be assumed that the transfer of atoms from the liquid to the crystal is so fast that the attachment kinetics is not a limiting factor of the growth. When the material presents a faceted growth mode, typical of most no-metals or intermetallic compounds, the kinetic term can be important.

The materials are classified as faceted or non-faceted type according to their growth morphology (Fig.I.24). Metals as well as a certain class of molecular composites (plastic crystals or organic alloys) do not present facets, but rather a smooth solid-liquid interface, despite their crystalline nature. The kinetic attachment is not very dependent on the orientation of the considered crystal planes and there are many sites for attaching new atoms: the solid-liquid interface is rough. For dendritic structures, however, a tendency to grow anisotropically remains because of the anisotropy of the interfacial energy. This leads to the formation of primary trunks whose direction of growth is determined by crystallography and the directions of the arms correspond to low indices. On the other hand, the materials which have a complex crystalline structure and a directional character of attachment of the atoms will form crystals having plane surfaces (facets).

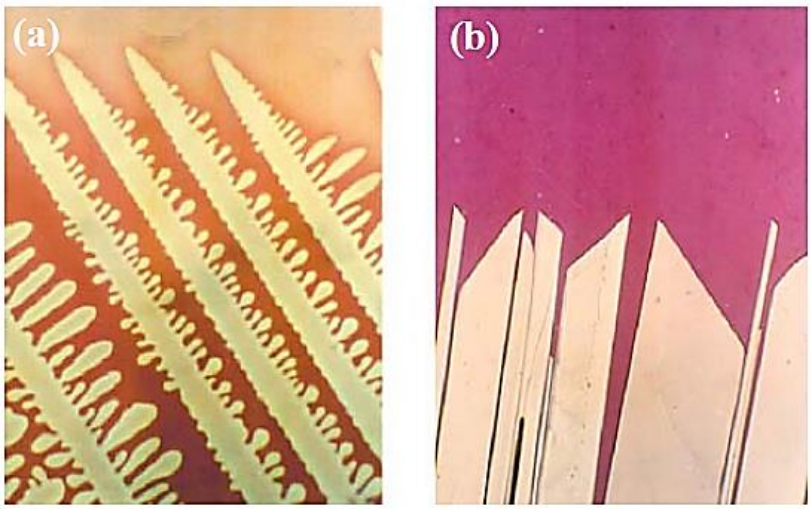

Fig.I.24: *(a) Dendrites colonnaires pour un alliage transparent ayant un comportement analogue aux alliages métalliques et (d) cristal de benzyle présentant des facettes bien développées, [80].*

By evaluating the rate of atoms attached to the interface (which depends on the diffusion of atoms in the liquid) and the rate of detachment (which depends on the number of neighbors bonding the atom to the interface), K.A. Jackson determined a factor α that predicts the facetedness or non-facetedness of materials as they grow, [80-81]:

$$\boldsymbol{\alpha = \frac{\eta}{Z}\frac{L}{kT_m} = \frac{\Delta S_f}{R}} \qquad \textbf{(I.36)}$$

With η the number of first neighbors adjacent to an atom in the interface plane, Z the total number of first neighbors of an atom in the crystal, L the latent heat of fusion, T_m the temperature of fusion and k the Boltzmann constant. ΔS_f is the entropy of fusion and R the perfect gas constant.

A coefficient α less than ≈ 2 indicates that the material tends to grow with a non-faceted morphology, while for values of $\alpha > 2$ faceted growth takes place. A list of different materials with the corresponding α coefficient value as well as their growth morphology from different phases are given in Table I-2. Thus, it can be seen that metals and "plastic" crystals are indeed in the same group.

Table.I-1: Growth morphologies and Jackson's factors.

Jackson factor α	Material	Phase	Morphology
≈1	Metals	Molten bath	Non-faceted
≈1	Crystals (plastic)	Molten bath	Non-faceted
2-3	Semiconductors	Solution	nf/faceted
2-3	Semimetals	Solution	nf/faceted
≈6	Molecular crystals	Solution	faceted
≈10	Metals	Steam	faceted
≈20	Momplex molecules	Molten bath	faceted
≈100	Polymers	Molten bath	faceted

4.1.Anisotropy of the material

4.2.1. Attachment kinetics:

For materials with facets, the local equilibrium assumption cannot be applied. A larger or smaller deviation from the equilibrium temperature called kinetic undercooling ΔT_k is always required to advance the facet. The kinetic undercooling depends on the crystallographic orientation of the facet and allows for the kinetic attachment anisotropy. The total undercooling at the interface is then written:

$$\boldsymbol{\Delta T^* = T_L - T^* = \Delta T_c + \Delta T_r + \Delta T_k} \quad \textbf{(I.37)}$$

with $\Delta T_c = m(C_0 - C_l^*)$ the chemical undercooling and $\Delta T_r = \Gamma\kappa^*$ the curvature undercooling. The kinetic undercooling term ΔT_k can be written from the Gibbs- Thomson equation (Eq.35):

$$\boldsymbol{\Delta T_k = T_m + mC_l^* - \Gamma\kappa^* - T^*} \quad \textbf{(I.38)}$$

The kinetic attachment, characterized by the kinetic undercooling ΔT_k , depends on the local orientation θ and the local normal velocity V_n of the solid-liquid interface. The relationship between ΔT_k and V_n depends on the type of atomic attachment mechanism.

On a facet, growth can be controlled by two-dimensional germination (Eq.39a), [82], by screw dislocation (Eq.39b), [83] or by ledge growth, (Eq.39c), [84]:

$$\boldsymbol{V_n = \mu_1 \exp\left(-\frac{\mu_2}{\Delta T_k}\right)} \textbf{ with } \boldsymbol{(\mu_1, \mu_2)} \textbf{ 2 constants} \quad \textbf{(I.39a)}$$

$V_n = \mu \Delta T_k^2$ **with μ the kinetic coefficient** **(I.39b)**

$V_n = \mu \Delta T_k$ **with μ the kinetic coefficient** **(I.39c)**

4.2.2. Surface tension anisotropy:

The surface tension depends on the crystallographic orientation of the interface. For a planar geometry, the surface tension can be expressed by a function of the type γ(θ), where θ is the polar angle between the normal to the interface and a crystallographic reference plane. For a weakly anisotropic rough cell interface, the Wulff diagram which represents γ(θ) has no singularity (no angular point) and γ can be written for a crystal with cubic symmetry, [85]:

$$\gamma(\theta) = \gamma_0 \left(1 + \frac{\varepsilon}{15} cos4\theta\right) \quad \textbf{(I.40)}$$

Where ε is the rough crystal anisotropy parameter (on the order of 10-2) and γ_0 is the average value of $\gamma(\theta)$.

For an anisotropic surface tension, we generalize the expression for the capillary constant Γ by replacing the surface tension γ(θ) by the surface stiffness σ(θ) which is written:

$$\sigma(\theta) = \gamma(\theta) + \frac{\partial^2 \gamma(\theta)}{\partial \theta^2} = \gamma_0 (1 - \varepsilon cos4\theta) \quad \textbf{(I.41)}$$

4.2.Influence of anisotropy in directional solidification

4.3.1. Selection of the dendritic microstructure

In dendritic free growth, many theoretical works have emphasized the crucial role played by crystal anisotropy in the microstructure selection process, [86]. It is now well established that it is the surface tension anisotropy that selects the radius of the dendrite apex as well as the velocity of the dendrite tip. This phenomenon of selection by anisotropy has been experimentally demonstrated by *Ben-Jacob et col*. In the case of viscous digitation, [87].

4.3.2. Orientation of dendritic microstructures:

A well-known fact is the variation of the orientation of the stationary microstructures as a function of the solidification rate "V" for fairly anisotropic but not faceted materials. At low velocities, the cells are oriented along the direction of the heat flow, i.e. along the direction of pulling. For higher and higher velocities, the microstructure becomes dendritic and the dendrites progressively tilt towards the growth direction they would have in free growth. An experimental and numerical study on this subject was carried out by Akamatsu et al. in a "thin blade"

configuration on the transparent binary alloy CBr4-C2Cl6 [88,89] . The results definitely establishing that the dendrite tilt angle grows with *the Peclet number* = $\lambda V/D_L$ (i.e., with the velocity insofar as the wavelength is constant in these experiments) up to a limiting value that depends only on the orientation of the crystal with respect to the pulling direction (Fig.I.25). This result was also established numerically by Okada and Saito, [90] who, like Akamatsu et al. consider only the surface tension anisotropy.

On the other hand, the inclination of the dendrites for anisotropic materials induces two noticeable effects on the microstructure: (i) the dendrites are necessarily asymmetric since the concentration field around the dendrite is itself asymmetric, (ii) a phenomenon of lateral drift, at constant velocity, of the microstructure is observed, [88]. This drift due to the anisotropy (of surface tension or of attachment kinetics) of the material cannot be interpreted only by linear models such as that of Coriell and Sekerka, [91].

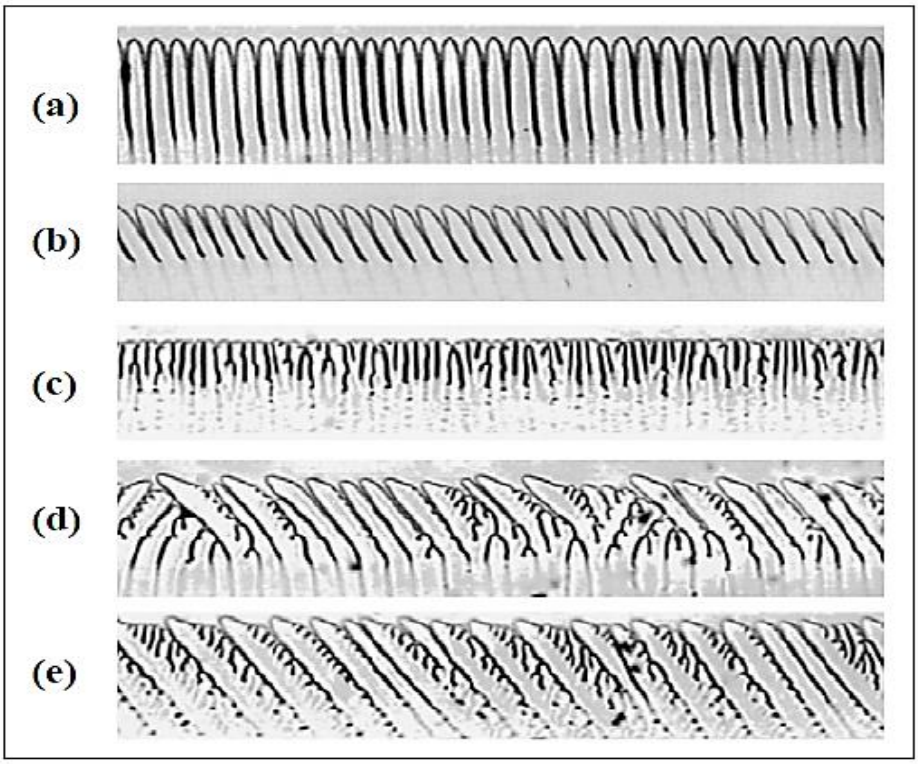

Fig.I.25: *Microstructures obtained from the same crystal for different Solidification rates [92]. (a) Symmetrical cells (V = 3.1 μm/s), (b) tilted dendrites (V = 23.9 μm/s), (c) "seaweed" structure (V = 31.1 μm/s), (d) co-existence of left and right tilted dendrites (V = 31 μm/s, after some time left tilted dendrites predominate), (e) tilted dendrites for low anisotropy (V = 31.1 μm/s).*

5. Columnar to equiaxed transition

In solidification, two growth modes can be distinguished: columnar growth (directed solidification) and equiaxed growth (or free solidification). The transition between these two growth modes is a function of the evolution of thermal and solutal conditions during solidification. This transition, called Columnar to Equiaxed Transition (CET), has a very pronounced impact on the intrinsic properties of the material since the resulting microstructure is completely different (Fig.I.26).

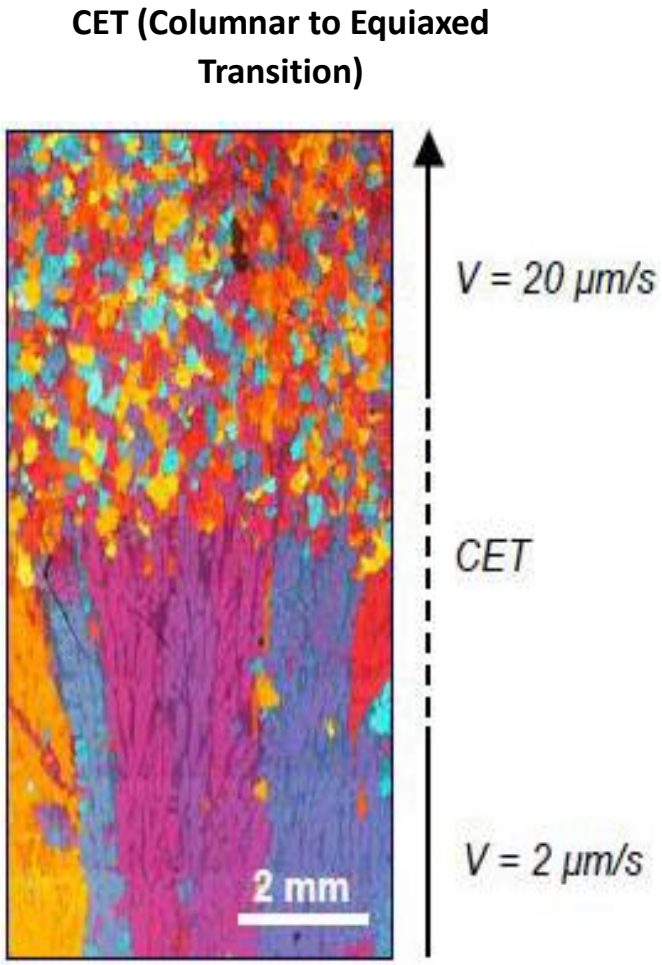

Fig.I.26: *Longitudinal section of a cylindrical bar of Al - 3.5 % wt Ni alloy refined for which the transition from a columnar to an equiaxed microstructure was obtained by applying an increase of the solidification rate. (H. Jung, L2MP)*

The existence of equiaxed grains in directional solidification is related to the fact that there is a zone of supercooled liquid between the peak temperature of the columnar dendrites T^* and the liquidus temperature T_L. If solid germs are present in this zone, they can grow and competition

between the growth of free equiaxed crystals and the advancement of the columnar front is established, which can lead to TEC. The formation of solid germs, embryos of equiaxed grains, can have two origins:

- Fragmentation: the nuclei can be represented by the dendrite's fragments separated from the mushy zone by local remelting and transported in the undercooled liquid zone by convection flow (Fig.I.27). Fragmentation is not very clear, but observation on organic alloys solidification have been made by C.J. Paradies, [93] and T. Sato, [94]. As Jackson, [95], Paradies, [93] and Sato, [94] related fragmentation to the local remelting of the finest dendrites' arms at their neck. Liu, [96] concluded that the fragmentation is mainly due to the dissolution of dendrites caused by solute variation in the mushy zone (the solute variation caused by the decrease in cooling rate). Gu and Beckermann, [97] as Hellawell, [98] associated fragmentation to the solutal dissolution of dendrites arms in segregated channels. It is worth mentioning that Pilling's work, [99] pointed out that interdendritic liquid that causes mechanical deformation cannot cause dendrites fragmentation.

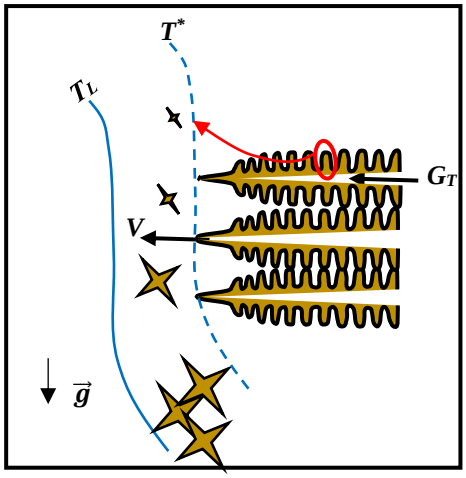

Fig.I.27: *TEC mechanism described by the Maxwell and Hellawell model in horizontal solidification*

- Inoculation: The introduction of seeding particles will form the preferential growth sites (heterogeneous nucleation) for the further equiaxed crystals and consequently favours CET even with a minimum undercooling. If the degree of undercooling necessary for heterogeneous nucleation is lower than the maximum undercooling present in the liquid, and if there are enough seeding particles, CET will be promoted.

5.1.CET blocking mechanism

5.1.1. mechanical

Considering a columnar dendritic front progress at a velocity *V* in a thermal gradient *G* (Fig. I.28), with the growing dendrite inducing an undercooled zone $\Delta T^* = T_l - T^*$ ahead of the columnar front, two cases can be distinguished:

- The undercooling ΔT^* is lower than the nucleation undercooling ΔT_n , the growth stays columnar.
- The undercooling $\Delta T^*$is higher than the nucleation undercooling ΔT_n, the equiaxed crystals will grow ahead of the columnar front, in the undercooled zone (Fig.I.28)

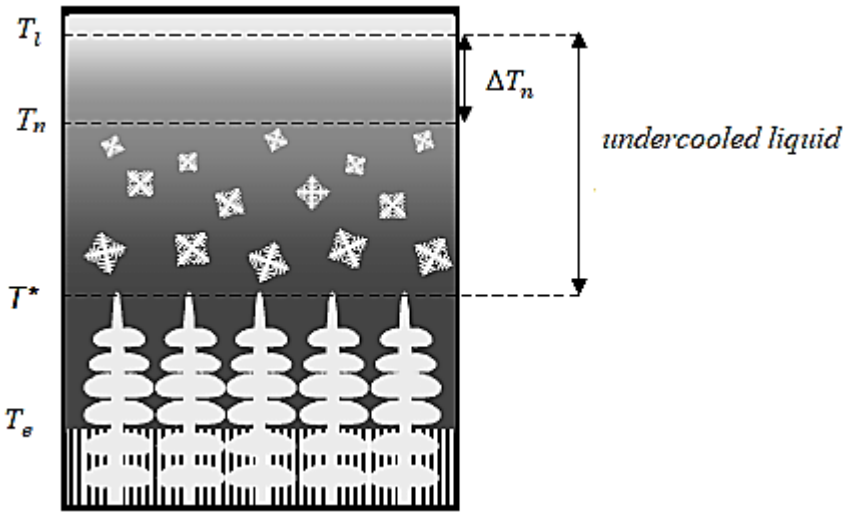

Fig.I.28: *Representation of CET, whereT_l is the liquidus temperature, T_n the nucleation temperature, T^* the dendrite tip temperature, T_e the eutectic temperature and ΔT_n the nucleation undercooling, [100].*

In fact, CET is a complex phenomenon involving many processes: nucleation, growth kinetics (equiaxial and columnar), preferential growth direction, liquid convection and the resulting solute transport. Based on a mixed model of heterogeneous nucleation and dendritic growth, analytical and numerical qualitative methods have been developed [101] to predict CET. Hunt [60] established an analytical criterion of the transition from columnar to equiaxed based on the thermal gradient at the interface. He considered the number of nucleation sites per volume N_0 and the ratio between nucleation undercooling and tissue undercooling. Define a growth criterion Φ_E:

$$\boldsymbol{\Phi_E = \frac{4\pi r^3 N_0}{3}} \qquad \textbf{(I.42)}$$

Where $\boldsymbol{r}$ is the radius of an equiaxed crystal equal to

$$\boldsymbol{r = \int_0^t V_e dt = \frac{A(\Delta T^3 - \Delta T_n^3)}{3VGC_0}} \quad \textbf{(I.43)}$$

When $\Phi_E < 0.0066$ only columnar growth occurs and when $\Phi_E > 0.0066$ only equiaxed growth happens. In Eq.43, V_e represents the growth velocity of an equiaxed crystal given by the dendrite tips, estimated using a KGT type model $V_e = A\Delta T^2/C_0$ (A is a growing constant depending on the material and ΔT the local undercooling). The cooling velocity is expressed as $\frac{dT}{dt} = -GV = \frac{d(\Delta T)}{dt}$ [1]. Combining Eq. 24 and 25 for a columnar growth (the undercooling for the columnar growth is equal to $\Delta T_{col} = (VC_0/A)^{1/2}$), a criterion based on the thermal gradient is obtained. A columnar structure occurs if

$$\boldsymbol{G > 0.617(100N_0)^{1/3}\left(1 - \frac{\Delta T_n^3}{\Delta T_{col}^3}\right)\Delta T_{col}} \quad \textbf{(I.44)}$$

and in the case of an equiaxed growth

$$\boldsymbol{G < 0.617(100N_0)^{1/3}\left(1 - \frac{\Delta T_n^3}{\Delta T_{col}^3}\right)\Delta T_{col}} \quad \textbf{(I.45)}$$

These entire criterions are valid under certain hypothesis:

- The solute transport is done only by diffusion (no convection);
- The heterogeneous nucleation sites are randomly distributed and are active immediately, which makes the nucleation undercooling ΔT_n lower than the undercooling ahead of the solidification front;
- The equiaxed crystal growth is considered to be spherical;
- The temperature gradient is stable; therefore, it is assumed that the growth rate and temperature gradient of the columnar front are constant.

Considering Eq. 45 and 46, a microstructure map can be drawn for any given system. Generally, the equiaxed growth is favoured if the solid growth velocity increases, the alloy concentration and the nucleation sites are increasing and if the nucleation undercooling or the temperature gradient decreases and columnar growth occurs at low velocities and high gradients (Fig. I.29).

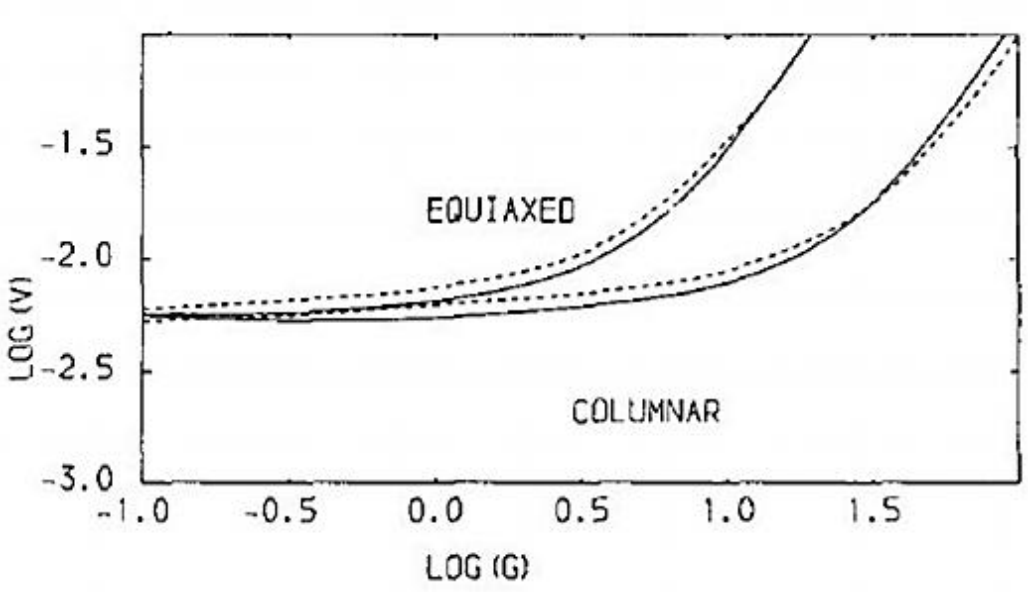

Fig.I.29: *Hunt diagram for Al-3wt.% Cu for a nucleation undercooling 0.75 K and* $N_0 = 1$ *mm^{-3}.*

Later Flood, [102] used a more complex description of the heat exchange between growth and solidification front advancement to establish a numerical model. Based on the Hunter model, Goldman completed the study of Flood's by paying more attention to nucleation, [103]. Wang considered a finite difference method to solve this problem, [104]. All these models are only valid for dendritic growth parallel to heat flux.

In order to account the solidification of super-alloys, Gäumann, [105] adapted Hunt's model, considering the growth orientation. In the same way, Gandin, [106] developed a cellular automata model to simulate growth competition between columnar grains by considering the crystallographic orientation of the grains and the temperature changes in the system. Then, the finite element method was used to combine this model with heat flux calculations, resulting in a very important numerical tool for 2D and 3D grain structure prediction, [107].

The CET is very important to the industry. It should be noted that the complexity of this phenomenon is caused by the diversity of industrial casting conditions (particle seeding, cooling rate, natural convection or forced convection, etc.). Understanding the different phenomena that occur during CET will help to fully understand the microstructure obtained in the casting.

5.1.2. solutal

This mechanism is based on the solution interaction caused by solute rejection during equiaxed growth. These equations are published from the Wang and Beckerman model, [104].

Neither convection nor the movement of free equiaxed crystals are taken into account (grains sedimentation due to gravity is also neglected). Three phases are defined within the volume element by Martorano et *al.* [108]:

- A solid volume fraction ε_s,
- A liquid interdendritic fraction ε_d,
- A liquid extra dendritic fraction ε_l,

and $\varepsilon_s + \varepsilon_d + \varepsilon_l = 1$

The grain volume fraction is expressed by $\varepsilon_g = \varepsilon_s + \varepsilon_d$. In another way the inter- and extra dendritic liquids are separated by an invisible envelope all around the grain (Fig. I.30).

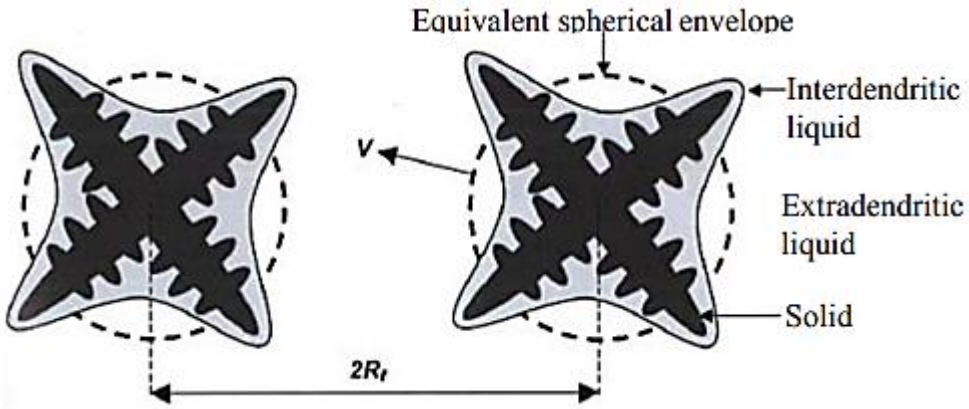

Fig.I.30: *Schema of the envelope around the equiaxed grain delimitating the inter- and extradendritic liquids, [108].*

Using these symbols, Hunter's criterion for the transition from columnar to equiaxed becomes $\varepsilon_g = 0.49$. In order to simulate equiaxed grains and their dendritic branches, a sphere with an equivalent surface S_e is defined (as shown in Fig.I.31). The distance between the two grains is $2R_f$, where R_f represents the final grain radius. The grain growth rate determined by the kinetics of free tip growth (Lipton, [60]) is added to the energy and solute conservation equations.

$$\boldsymbol{V = \frac{4\sigma^* D_l m_l (k-1) C_l^*}{\Gamma} (Iv^{-1}(\Omega))^2 = 0.4567 \left(\frac{\Omega}{1-\Omega}\right)^{1.195}} \quad \textbf{(I.46)}$$

where $\sigma^* \approx 1/(4\pi)^2$ is the stability constant, Γ is the Gibbs-Thomson coefficient, Iv^{-1} is the inverse of the Ivantsov function and Ω is the supersaturation, defined as $\Omega = \frac{C_l^* - C_l}{C_l^*(1-k)}$

Hunt's model considers C_l to be constant and equal to C_0, while Martorano's model considers the variation of C_l during equiaxed growth (but not during columnar growth). Therefore, phenomena that play a role in solute interactions are considered, such as the solutal blocking due to solute rejection by the equiaxed grains during their solidification. The rejected solute enriches the inter-dendritic liquid (Fig.I.31), so the gradient concentration as the driving force will gradually decrease. Then, the growth of the grain will slow down until it stops (the grain is not in direct contact).

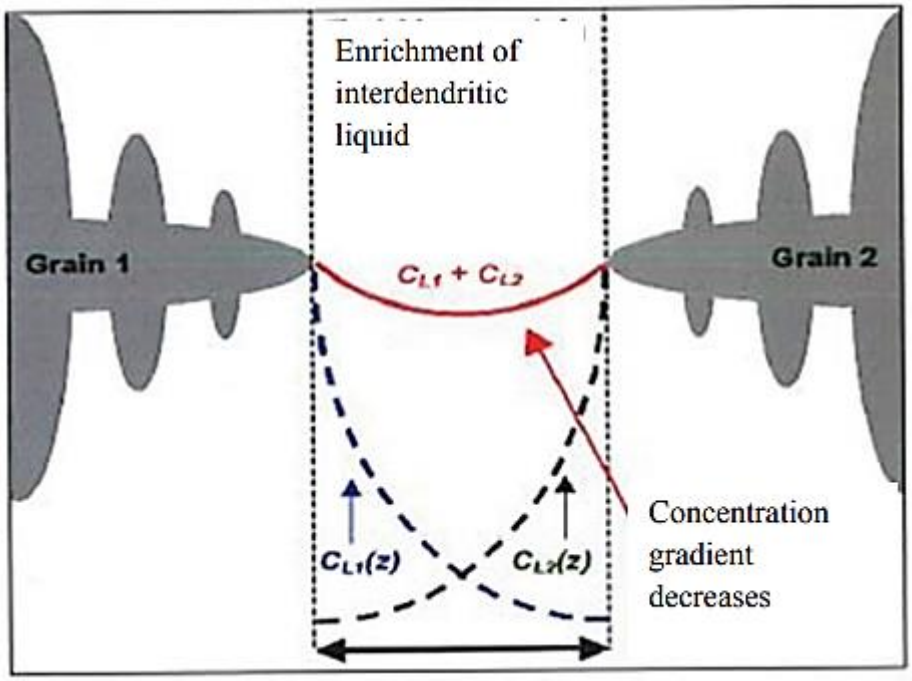

Fig.I.31: *Concentration profile between two equiaxed grains during solutal blocking, [100].*

Martorano's model proves two limited cases of CET, as shown in Fig.I.32. In the first case, the density of the equiaxed grains is relatively large (as in the case when an inoculant is introduced), so the grains practically remain spherical. A great number of spherical grains will reject a major quantity of solutes in the surrounding liquid, resulting in a sharp drop in the solutal undercooling ahead of the columnar front. The CET takes then place for volume fraction values below 0.49 (Hunt's criterion). In the second case, the grain density is relatively low, but the grain size is larger (R_f increases). Equiaxed grains become strongly dendritic, so for a large R_f value, the liquid concentration C_l stays for a period of time close to the initial concentration C_0 , and then tends to C_l^* .During this period, as predicted by Hunt's criterion., the equiaxed grains continue to grow and the CET takes place for volume fraction larger than 49%.

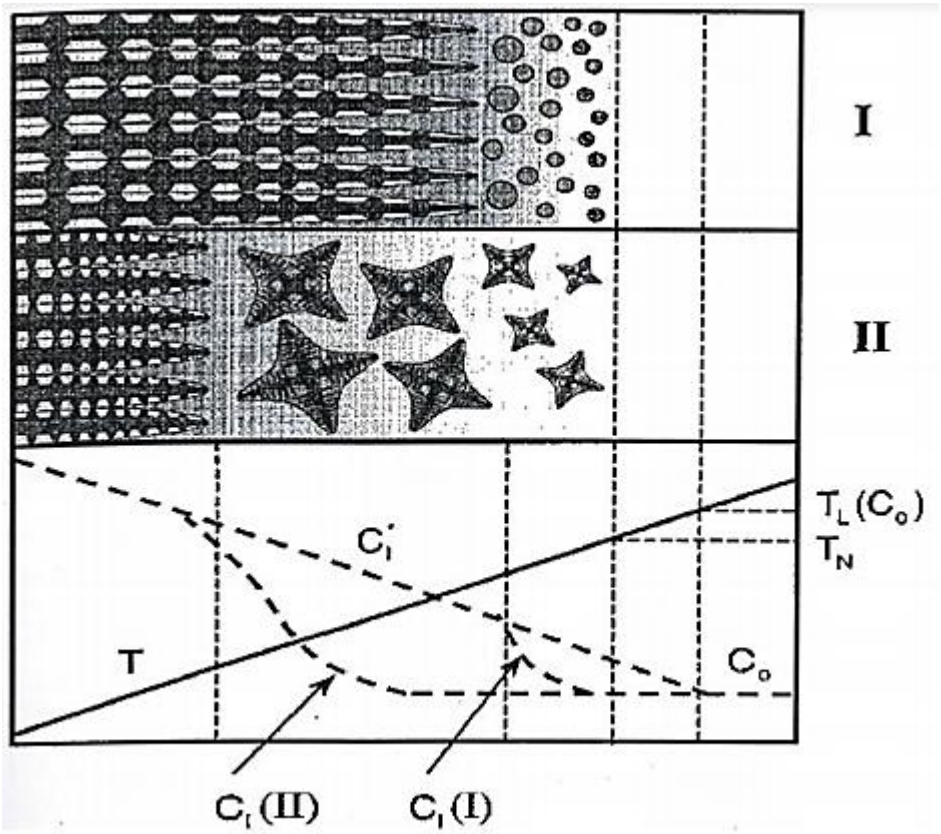

Fig.I.32: *Solutal interaction between columnar and equiaxed grains, [108]. Case I: solutal interactions in the presence of a large density grain. Case II: solutal interactions in the presence of a lower density grain*

The comparison between the Martorano's model, [108] and the two models of Gandin gives a satisfactory consistency for CET. Recently, Badillo and Beckermann, [109] developed a CET model using the phase field method. They considered the elongation of equiaxed grains along the temperature gradient during the growth process, the existence of a mixed growing regime columnar–equiaxed for large velocity growth, and also the particle deactivation potential for nucleation via solutal interactions.

A three phase Eulerian approach was developed by Ludwig and Wu, [110, 111] to model the columnar to equiaxed transition. The three phases defined during the mixed solidification are: the parent melt, the columnar dendrites and the equiaxed crystals. A binary "steel" (Fe–0.34 wt.% C) ingot casting was used as benchmark for simulation, in ordered to demonstrate the ability of the model. This model was modified and five phase regions resulted: extradendritic melt, interdendritic melt and solid dendrites in equiaxed grains, interdendritic melt and solid dendrites in columnar arrays of dendrites, [112].

All classic CET models do not consider natural convection or forced convection. These two factors have a great influence (fragment movement, equiaxed grain movement, particle movement, solute redistribution, etc...), without the effect of gravity (particles and grains Precipitation etc...).

PARTIAL CONCLUSION

In this first chapter, a bibliographical review of the fundamentals of solidification has been carried out, for pure metals as well as for metallic alloys. The emphasis was put on the segregation phenomena that interest us in this study. These fundamentals of solidification will help to understand the problems that will arise in the future, but also enable us to understand the solidification theme: equation models, analysis, and experimental research, which are supported by experimental benchmarks.

References

[1] W. Kurz and D.J. Fisher, Trans. Tech. Publication ltd., 1998.

[2] M. C. Flemings, McGraw-Hill, INC., 1974.

[3] L. G. Lesoult, Techniques de l'ingénieur, M58, pp. 1-26.

[4] D. J. Allen and J. D. Hunt, Met. Trans. A, 1979, vol. 10A, pp. 1389.

[5] H. D. Brody and M. C, TMS of AIME, 1966, vol. 236, pp. 615.

[6] L. Hachani, B. Saadi, X. D. Wang, A. Nouri, K. Zaidat, A. Belgacem-Bouzida, L. Ayouni-Derouiche, G. Raimondi, Y. Fautrelle, Int. J. Heat and Mass Transfer, 2012, vol.55, pp. 1986.

[7] A. F. Giamei and B. H. Kear, Metall. Trans., 1970, vol.1, pp. 2185.

[8] P. Prescot and F. Incropera, Advances in heat transfer, 1996, vol. 28, pp. 231.

[9] A. Kharicha, M. Stefan-Kharicha, A. Ludwig and M. Wu, Metall. Mater. Trans. A, 2013, vol. 44, pp. 661.

[10] J. R. Sarazin and A. Hellawell, Met. Trans. A, 1988, vol. 19A, pp.1861.

[11] M. I. Bergman, D. R. Fearn, J. Bloxham, and M. C. Shannon, Met. Trans. A, 1997, vol. 28A, pp.859.

[12] G. H. Gulliver, London, Griffin, 1922.

[13] E. Scheil, Z. Metallforschung, 1942, vol. 34, pp. 70.

[14] T. W. Clyne and W. Kurz, Met. Trans., 1981, vol. 12A, pp. 965.

[15] S. Kobayashi, J. Crystal Growth, 1988, vol. 88, pp. 87.

[16] A. Ludwig, M. Wu and A. Kharicha, Metall. Mater. Trans. A,2015, vol. 46, pp. 4854.

[17] J. A. Dantzig and M. Rappaz, EPFL, London, 2009.

[18] Heterogeneity Sub-Committee of the British Iron and Steel Institute: J. Iron Steel Inst., 113 (1926), 39.

[19] A. Hultgren, J. Iron Steel Inst., 120 (1929), 69.

[20] E. Marburg: JOM, (1953), 157.

[21] G. Derge, AIME, NY,Physical Chemistry of Steelmaking Committee: Basic Open-Hearth Steelmaking, ed., (1964).

[22] Joint Committee of the Iron and Steel Institute and the British Iron and Steel Federation: J. Iron Steel Inst., 35 (1937), 12.

[23] L. Northcott and V. Dickin: J. Inst. Met., 70 (1944), 301.

[24] W. Kurz and D. J. Fisher, Trans Tech Publications LTD, Switzerland, (1986).

[25] M. C. Flemings, McGraw-Hill, NY, (1974).

[26] M. Kawai, Tetsu-to-Hagané, 42 (1956), 14.

[27] C. E. Smeltzer, Iron Age, 184 (1959), 188.

[28] K. Suzuki and T. Miyamoto, Trans. Iron Steel Inst. Jpn., 21 (1981), 235.

[29] K. Suzuki and T. Miyamoto, Tetsu-to-Hagané, 63 (1977), 45.

[30] R. J. McDonald and J. D. Hunt, Trans. TMS AIME, 245 (1969), 1993.

[31] R. J. McDonald and J. D. Hunt, Metall. Trans., 1 (1970), 1787.

[32] S. M. Copley, A. F. Giamei, S. M. Johnson and M. F. Hornbecker, Metall. Trans., 1 (1970), 2193.

[33] A. Ohno, Tetsu-to-Hagané, 54 (1968), 401.

[34] S. Asai, T. Sahara and I. Muchi, Tetsu-to-Hagané, 63 (1977), 1512.

[35] A. F. Giamei and B. H. Kear, Metall. Trans., 1 (1970), 2185.

[36] N. Streat and F. Weinberg, Metall. Trans., 3 (1972), 3181.

[37] N. Streat and F. Weinberg, Metall. Trans., 5 (1974), 2539.

[38] N. Streat and F. Weinberg, Metall. Trans. B, 7B (1976), 417

[39] H. Fredriksson and S. O. Nilsson, Metall. Trans. B, 9B (1978), 111.

[40] K. M. Fisher and J. D. Hunt, Proc. Int. Conf. on Solidification, The Metals Society, London, (1977), 325.

[41] A. Sample and A. Hellawell, Metall. Trans. B, 13B (1982), 495.

[42] A. Sample and A. Hellawell, Metall. Trans. A, 15A (1984), 2163.

[43] J. R. Sarazin and A. Hellawell, Metall. Trans. A, 19A (1988), 1861.

[44] C. Maidorn and B. Blind, Nucl. Eng. Des., 84 (1985), 285.

[45] E. J. Pickering, unpublished work.

[46] G. Lesoult, Mater. Sci. Eng. A, 413–414 (2005), 19.

[47] B. Crawshaw and A. D. Choudhury, Proc. Conf, The Iron and Steel Institute, London, UK, (1967), 377.

[48] H. Combeau, M. Zaloznik, S. Hans and P. E. Richy, Metall. Mater. Trans. B, 40B (2009), 289.

[49] I. Vannier, H. Combeau and G. Lesoult, Mater. Sci. Eng. A, 173 (1993), 317.

[50] S. Onodera and Y. Arakida, Tetsu-to-Hagané, 45 (1959), 16.

[51] B. Gray, J. Iron Steel Inst., 182 (1956), 366.

[52] M. C. Flemings and G. E. Nereo: “Macrosegregation, part 1”, Trans. Met. Soc. AIME, 1967, vol. 239, pp. 1449.

[53] M. C. Flemings, ISIJ Int., 40 (2000), 833.

[54] C. Beckermann, ASM Handbook, 2008, vol. 15, pp. 348.

[55] D. R. Poirier: , Metall. Trans. B, 1987, vol. 18, pp. 245.

[56] I. Ohnaka and M. Matsumoto, J. Iron Steel Inst. Jpn., 1987, vol. 73, pp. 1698.

[57] J. S. Kirkaldy and W. V. Youdelis, TMS AIME, 1958, vol. 212, pp. 833.

[58] M. C. Schneider, J. P. Gu, C. Beckermann, W. J. Boettinger and U. R. Kattner, Metall. Mater. Trans. A, 1997, vol. 28, pp. 1517.

[59] Th. Campanella, PhD, École Polytechnique Federale de Lausanne, 2003.

[60] J. D. H unt, Mater. Sci. Eng. V, 1984, vol. 65, pp. 75.

[61] W. Kurz, D.J. Fisher, trans tech publications ltd, p46, 1998

[62] G.P. Ivantsov, Doklady Akademii Nauk SSSR 58, p567, 1947

[63] J.S. Langer, H. Müller-Krumbhaar, Acta Met. 26, p1681, 1978

[64] W. Kurz, B. Giovanola, R. Trivedi, Acta Met. 34, p823, 1986

[65] G.W. Young, S.H. Davis, Phys. Rev. B34, p3388,1986D.S. Riley, S.H. Davis, IMA J. Appl. Math. 45, p267, 1991

[66] S.C. Huang, M.E. Glicksman, Acta Metallurgica 29, p701, 1981

[67] D.A. Kessler, J. Koplik, H. Levine, Adv. Phys. 37, p255, 1988

[68] E. Brener, V.I. Melnikov, Adv. Phys. 40, p53, 1991

[69] Y. Pomeau, M. Ben Amar, ed. C. Godrèche, Cambridge, p365, 1991

[70] W. Kurz, R. Trivedi, Acta. Metall. Mater. 38, p1, 1990

[71] A. Karma, W.-J Rappel, Phys. Rev. E 57, pp4323-4349, 1998

[72] A. Karma, Y.H. Lee, M. Plapp, Phys. Rev. E 61, pp3996-4006, 2000

[73] B. Echebarria et col., Phys. Rev. E 70, 061604, 2004

[74] R. Folch, M. Plapp, Phys. Rev. E 72, 011602, 2005

[75] C. Beckerman et col., J. Comput. Phys. 154, pp468-496, 1999

[76] J.C. Ramirez et col., Phys. Rev. E 69, 051607, 2004

[77] W. Kurz and D. J. Fisher, Acta Met., 1986, vol. 29, pp. 11.

[78] T. Z. Kattamis and M. C. Fleming, Trans. TMS-AIME, vol. 233, 1965, pp. 992.

[79] U. Feurer and R. Wunderlin, Trans. Tech. Publication LTD. Aedermannsdorf, Switzerland, 1986.

[80] K.A. Jackson, J. of Cryst. Growth 264, pp519-529, 2004

[81] K.A. Jackson, American Society for Metals, Cleveland, p174, 1958

[82] M.I. Volmer, J. Marder, *Z. Phys. Chem*. A154, p97, 1931

[83] W. Hillig, D. Turnbull, *J. Chem. Phys.* 24, p914, 1956

[84] W.A. Tiller, Cambridge Univ. Press., UK, 1991

[85] L.D. Landau, E. Lifshitz, Pergamon Press, London, 1980

[86] J.S. Langer, Ecole D'été Les Houches, Hollande, 1986

[87] E. Ben-Jacob, P. Garik, *Nature* 343, p523,1990

[88] S. Akamatsu, T. Ihle, *Physical Review E* 56 (4), pp4479-4485, 1997

[89] S. Akamatsu, G. Faivre, T. Ihle, *Physical Review E* 51B (5), pp4751-4773, 1995

[90] T. Okada, Y. Saito, *Phys. Rev. E* 54(1), p650, 1996

[91] S.R. Coriell, R.F. Sekerka, *J. Crystal Growth* 34, p157, 1976

[92] S. Akamatsu, G. Faivre, Physical Review E 58 (3), pp3302-3315, 1998

[93] C. J. Paradies, R. N. Smith and M. E. Glicksman, Metall.Mater. Trans. A., 1997, vol. 28, pp. 875.

[94] T. Sato, W. Kurz and K. Ikawa, Trans. of the Japan institute of metals, 1987, vol. 28, pp. 1012.

[95] K. A. Jackson, J. D. Hunt, D. R. Uhlmann and T. P. Seward, TMS AlME, 1966, vol. 236, pp. 149.

[96] S. Liu, S.-Z. Lu and A. Hellawell, J. Crystal Growth, 2002, vol. 234, pp. 740.

[97] J. P. Gu, C. Beckermann and A. F. Giarnei, Metall. Mater. Trans. A, 1997, vol. 28, pp. 1533.

[98] A. Hellawell, J. R. Sarazin and R. S. Steube, Phil. Trans. R. Soc. Lond. A, 1993, vol. 345, pp. 507.

[99] J. Pilling and A. Hellawell, Metal. Mater. Trans. A, 1996, vol. 27, pp. 229.

[100] Guillaume Reinhard, PhD, Université Paul Cezanne Aix-Marseille III 2006.

[101] J. Lipton, W. Reinemann and W. Kurz,Arch. Eisenhunttenwes, 1984, vol. 55, pp. 195.

[102] S. C. Flood and J. D. Hunt, J. Crystal Growth, 1987, vol. 82, pp. 552.

[103] M. Gäumann, R. Trivedi and W. Kurz, Mater. Sci. Eng., 1997, vol. A226-228, p p. 763.

[104] C. Y. Wang and C. Beckermann, Met. Trans. A, 1993, vol. 24, pp. 2787.

[105] M. Gäumann, C. Bezenvon, P. Canalis and W. Kurz, Acta Mater., 2001, vol. 49, pp. 1051.

[106] Ch.-A. Gandin and M. Rappaz, Acta Metall. Mater., 1994, vol. 42, pp. 2233.

[107] Ch.-A. Gandin, J.-L. Desbiolles, M. Rappaz and Ph. Thevoz, Metall. Mater. Trans. A, 1999, vol. 30A, pp. 3153.

[108] M. A. Martorano, C. Beckermann, Ch.-A Gandin,Metall. Mater. Trans. A, 2003, vol. 25, pp. 1657.

[109] A. Badillo, C. Beckermann, Acta Mater. 2006, vol. 54, pp. 2015-2026.

[110] A. Ludwig and M. Wu, Mat. Sci. and Eng., 2005, vol. A 413–414, pp. 109.

[111] M. Wu and A. Ludwig, Metall. Mater. Trans. A, 2006, vol. 37, pp. 1613.

[112] M. Wu and A. Ludwig, Int. J. Cast Metals Research, 2009, vol. 22, pp. 323.

[113] Edward John PICKERING, ISIJ International, Vol. 53 (2013), No. 6, pp. 935–949

CHAPTER II

State of the Art of numerical modelling of Solidification Phenomenon

Preamble

This chapter will be essentially dedicated to identify the numerical models most used in simulation of solidification phenomenon of pure metals and metal alloys involving segregation.

In view of this review of the literature about the physical phenomena that play a significant role in the process of directional solidification and about the different numerical simulation approaches that are used by the scientific community to simulate them, we can conclude that this field of study is very rich and that it is still very current. Indeed, many physical phenomena relevant to solidification and segregation have been studied and highlighted. They have been studied independently or coupled way, in various configurations. Some of these studies are between twenty and thirty years old, while others are still very recent. Through all these monotonous efforts, it appears that complete 3D industrial simulations of solidification processes remain a real challenge today, with very high costs and computation times, even prohibitive, because of the multi-scale aspect of the problem and the complexity of the phenomena that come into play depending on the studied configuration. Moreover, even simulations performed on different configurations: 3D, 2D or 2D axisymmetric, require significant computational potential. One can legitimately think that the physical phenomena presented will still be studied in the future, in configurations that have not yet been treated or considering couplings of phenomena that have not yet been studied. We can thus envisage that many simulations of directed solidification will still be carried out in the years to come.

Moreover, it also appears from this literature review that there is still no real consensus on the most efficient numerical approaches for modelling directed solidification. Indeed, two approaches are mainly used, namely the deformable mesh methods and the enthalpic methods. These approaches have both intrinsic advantages and disadvantages, without one of the two approaches having really taken precedence over the other in practice. It is therefore relevant and necessary to consider improving one or the other of these approaches, in order to meet the need for performance and optimization, necessary to reduce the computational costs of future simulations. On the other hand, although it has already been studied in several publications, the integration of impurities segregation phenomena in directed solidification models remains difficult and may require, in the case of enthalpic methods, to propose an implementation with a volume source term of rejection at the interface.

1. The numerical approaches

1.1. The enthalpic approach

Enthalpic methods are part of the uni-domain approaches in which the same unique system of equations is solved everywhere in the domain containing both phases: solid and liquid phases which are represented by a single fluid. In order to properly take into account, the phase change, two major ingredients are essential. First, the rejection or absorption of the latent heat of fusion, noted ΔH_f , must be taken into account in the energy conservation equation. As a reminder, ΔH_f is the energy (in the form of heat) rejected (or absorbed) by a body during phase change at constant temperature and pressure. This can be done in several ways. Either by reformulating the energy equation based on the enthalpy, this is the case of the enthalpic formulation and the h-source method; or by keeping the energy conservation equation based on temperature but modifying the formulation of the heat capacity, this is the case of the of the apparent capacity. Then, the velocities inside the solid phase must be forced to be zero. Here again, different methods and formulations are available: the switch-off method, the method of variable viscosity and the Darcy method.

1.1.1. Consideration of latent heat

This section is devoted to the different techniques used to take into account the rejection (or absorption) of the latent heat of solid-liquid phase change. This latent heat can be included in different ways in the energy conservation equation. In all the following formulations of the energy equation, the heat dissipation due to viscous effects is considered negligible.

1.1.1.1. Enthalpic formulation

This formulation consists in solving the energy equation as follows, [2, 3]:

$$\boldsymbol{\rho}\left(\frac{\partial \boldsymbol{h}}{\partial \boldsymbol{t}} + \boldsymbol{u}.\boldsymbol{\nabla h}\right) = \boldsymbol{\nabla}.(\boldsymbol{\lambda \nabla T}) \qquad \textbf{(II.1)}$$

where ρ , h, t, u, λ and T are, respectively, density, enthalpy, time, velocity, thermal conductivity and temperature. The enthalpy, which is here the sum of the sensible enthalpy and the latent heat, is entirely convected by the velocity field. It is expressed as follows, [4]:

$$\boldsymbol{h(T)} = \int_{\boldsymbol{T_{ref}}}^{\boldsymbol{T}} (\boldsymbol{C_p} + \boldsymbol{\delta_{Tm}} \boldsymbol{\Delta H_m}) \boldsymbol{dT} \qquad \textbf{(II.2)}$$

$$\boldsymbol{\delta_{Tm}(T) = \frac{e^{-\left(\frac{T-T_m}{\Delta T/4}\right)^2}}{\sqrt{\pi}\Delta T/4}} \quad \textbf{(II.3)}$$

where C_p is the heat capacity and δ_{T_m} is a Dirac distribution centred on the temperature of fusion $T_{m,}$ generally considered as distributed over a temperature interval ΔT around T_m. The pasty zone containing the two phases is then included between the temperature solid, T_{sol}, and the liquid temperature, T_{liq}, respectively defined by $T_{sol} = T_m - \Delta T/2$ and $T_{liq} = T_m + \Delta T/2$. Assuming that the liquid fraction, f_l, varies linearly from 0 to 1 within the pasty zone between T solidus and T liquidus i.e.:

$$\boldsymbol{f_l = \frac{T-T_{sol}}{T_{liq}-T_{sol}} = \frac{T-T_m+(\Delta T/2)}{\Delta T}} \quad \textbf{(II.4)}$$

and the latent heat is rejected/absorbed linearly in proportion to f_l, the enthalpy is then expressed as:

$$h = \begin{cases} C_{p_s}(T - T_{ref}) & if\ T < T_{sol} \\ C_{p_s}(T_m - T_{ref}) + f_l \Delta H_m & if\ \ T_{sol} < T < T_{liq} \\ C_{p_s}(T_m - T_{ref}) + \Delta H_m + C_{p_l}(T - T_m) & if\ T_l < T \end{cases} \quad \textbf{(II.5)}$$

where C_{ps} and C_{pl} are respectively the heat capacities of the solid and liquid phases

1.1.1.2. H-source formulation

In this formulation, the two types of enthalpy, which are the sensible enthalpy "h_{sen}" and the latent enthalpy of phase change "h_m" and whose sum is the total enthalpy h, are expressed separately as follows:

$$\boldsymbol{h = h_{sen} + h_{lat} = \int_{T_{ref}}^{T} C_p dT + \rho f_l(T)\, \Delta H_m} \quad \textbf{(II.6)}$$

This allows us to reformulate the energy conservation equation, so that only temperature is involved as an unknown, in the following form:

$$\boldsymbol{\rho C_p \left(\frac{\partial T}{\partial t} + u.\nabla T\right) = \nabla.(\lambda \nabla T) - \rho \Delta H_m (\frac{\partial f_l}{\partial t} + u.\nabla f_l)} \quad \textbf{(II.7)}$$

The $u.\nabla f_l$ term is negligible when the solid phase is assumed to be fixed or if the phase change is considered to be isothermal, [5]. Expressions of the liquid fraction f_l, other than that given by Eq.II.4, have been proposed. They are no longer expressed in parts but with error functions (*er*), [6] or by polynomials, [7] or in power law, [8]. And are continuously derivable. Although they

are most often devoid of physical considerations, they facilitate the physical considerations, they facilitate the solution of Eq.II.6 and improve the convergence of the numerical schemes.

1.1.1.3. Formulation of the Apparent Capacity

This allows us to reformulate the energy conservation equation, so that only temperature is involved as a variable, in the following form:

$$\boldsymbol{C_{p_{app}}\left(\frac{\partial T}{\partial t}+u.\nabla T\right)=\nabla.(\lambda\nabla T)} \quad \textbf{(II.8)}$$

The phase change and the latent heat are taken into account by changing the definition of the heat capacity *Cp* which is formulated as an apparent capacity noted here Cp_{app}. It is defined within the mushy zone as follows [9]:

$$\boldsymbol{C_{p_{app}}=\frac{\Delta H_m}{T_{liq}-T_{sol}}+C_{p_s}} \quad \textbf{(II.9)}$$

A detailed comparison between these different methods of taking into account latent heat in enthalpic methods, accompanied by their different implementations, has been carried out by Franquet *et al* [5,10]. The influence of the spatial and temporal discretization applied with the different approaches on the quality of the predicted results is also detailed in this work. It is shown that the enthalpic formulation is, in general, the most accurate and robust. The h-source formulation can give results at least as accurate as the previous one, provided that it is well parameterized with adequate choices of time step and mesh size. The Apparent Capacity formulation is on the other hand the least accurate, because the conservation of the total energy is not ensured and the calculated temperature fields are approximate. Its accuracy can be slightly improved and give hardly acceptable results when the mushy zone is spread over a wide enough temperature range (T_{liq} - T_{sol}), but this is even further away from the cases of quasi-isothermal phase change.

1.1.2. Solid phase braking

With the uni-domain approach, the phase change problem is treated within the same and unique domain where the two phases, solid and liquid, are assimilated to a single fluid. However, during the phase change, more precisely during the transition from liquid to solid at the interface, the velocities become zero. Different techniques have been presented and used to force these velocities of the solid phase to be zero. The three main techniques used in enthalpic

formulations for solidification models are presented here. Before detailing them, the system of equations modelling the hydrodynamic part in these enthalpic models is presented. We should recall that, since in these models the solid and liquid parts are seen as a single phase, the modelling of the hydrodynamics must necessarily include a treatment of the solid part. The considered phase thus describes the two solid and liquid states of the material. The system of PDEs consists of the conservation of mass equation (Eq.II.10) and the conservation of momentum equations (Eq.II.11). For an incompressible Newtonian fluid, when the flow in the melt is created by buoyancy forces and with physical properties considered as constant between the two phases (this is not a general rule and a variation of these properties can be taken into account), these equations are:

$$\boldsymbol{\nabla . u = 0} \qquad \textbf{(II.10)}$$

$$\boldsymbol{\frac{\partial \rho u_i}{\partial t} + \rho u . \nabla u_i = -\frac{\partial P}{\partial x_i} + \mu \nabla^2 u_i + F_{buoyancy} + F_{braking}} \qquad \textbf{(II.11)}$$

where *i* varies from 1 to 2 in 2D modelling and from 1 to 3 in 3D modelling; and where *u, t, p,* and μ are respectively velocity, time, pressure, density and dynamic viscosity. The density is considered as constant, the Boussinesq approximation is used to take into account its variations in the buoyancy term. This term inducing convective flows is expressed as follows:

$$\boldsymbol{F_{buoyancy} = \rho g \beta_T (T - T_m)} \qquad \textbf{(II.12)}$$

where g, T, β_T and T_m are respectively the force of gravity, the temperature, the coefficient of thermal expansion and the melting temperature. This buoyancy term occurs only along the vertical direction y carrying gravity. The term *F* braking is used to induce a strong damping when the liquid fraction f_l tends to zero (in the solid phase) and must be zero when it is 1 (in the liquid phase). Several ways to express this term exist, they are detailed below.

1.1.2.1. Darcy method

In this formulation (also known as the porosity method), the mushy zone separating the totally liquid and totally solid regions is considered as a saturated porous medium. The permeability in this medium must change from a total permeability in the liquid to a zero permeability in the solid (or almost zero), in order to progressively reduce the velocities from their finite values in the liquid to zero in the solid. The braking term, $F_{braking}$ in Eq.II.11, corresponds to a Darcy term and is expressed by:

$$\boldsymbol{F_{braking} = -Au} \quad \textbf{(II.13)}$$

where A is a parameterizable porosity function that must be defined to force the momentum conservation equation to match the Carman-Kozeny law for flows in porous media. In a medium with porosity ϵ_0, this law allows to express the pressure gradient ∇P, it is given by:

$$\boldsymbol{\nabla P = -B_0 \frac{(1-\epsilon_0)^2}{\epsilon_0^3} u_a} \quad \textbf{(II.14)}$$

where u_a is the apparent velocity of the liquid in the porous medium and B_0 is a constant taking into account the properties of the porous medium. In practice, Voller *et al* [11] equate the liquid fraction f_l with the porosity of the mushy zone ϵ_0, and give a definition of the function A:

$$\boldsymbol{A = B_1 \frac{(1-f_l)^2}{f_l^3+B_2} u_a} \quad \textbf{(II.15)}$$

where B_1 and B_2 are numerical constants. B_2 has a small value and is used to avoid division by zero when the liquid fraction f_l is zero. Voller *et al* [4] report that this definition of A corresponds well to cases of phase change with a mushy zone, and note that this correspondence is even more affirmed if the constant B_1 is based on experimental observations and takes into account the morphology of the mushy zone. However, for cases of isothermal phase change, where this approach is purely numerical, any function increasing from zero to a large value when the liquid fraction f_l decreases from 1 to 0 is sufficient. This braking term takes a zero value in the liquid region, so the momentum equations of a simple fluid are recovered. In the mushy zone, the value of A increases so that the value of the braking term begins to dominate the transient, convective and diffusive terms, the momentum conservation equation then approaches Darcy's law. Finally, when the local liquid fraction tends to 0, this term dominates all the other terms of Eq.II.11 and forces the calculated velocities to have values close to 0.

1.1.2.2. The variable viscosity method

In this method, originally proposed by Gartling *et al* [12], the viscosity μ is assumed to be a function of temperature thus during the phase change and in the solid region, μ takes a high value. This has the effect of slowing down the solid phase and having negligible calculated velocities there. The Gartling formulation ($\mu = \mu(T)$) is adapted to enthalpic methods in order to have the viscosity as a function of the latent heat of a control volume ΔH_v. This amounts to defining the viscosity as a function of the liquid fraction f_l contained in the control volume. The variable viscosity is therefore defined as follows [11,13]:

$$\boldsymbol{\mu = \mu_l + B_3(\Delta H_m - \Delta H_v) \leftrightarrow \mu = \mu_l + B_4(1 - f_l(T))} \quad \textbf{(II.16)}$$

where μ_l is the viscosity of the liquid phase and B_3 and B_4 are purely numerical constants of an order of magnitude much greater than μ_l (of the order of 10^5). With this definition, when a numerical element is entirely liquid, its latent heat of phase change ΔH_v is equal to ΔH_m (or the liquid fraction of this element is 1), the viscosity μ associated with it is equal to μ_l. When this element undergoes a phase change, ΔH_v becomes lower than ΔH_m (f_l also becomes lower than 1), μ increases. Finally, at the end of the phase change of this considered phase, i.e., $\Delta H_v = 0$, and consequently ($f_l = 0$), the value of μ takes its maximum value $\mu_l + B_3 \Delta H_m$ (or $\mu_l + B_4$). The influence of this maximum value of viscosity, also noted μ_s as viscosity of the solid phase, has been studied by Kasibhatla *et al* [14]. They show that the larger μ_s is (of the order of 10^5 Pa.s), is the better estimation corresponding with the experimental results, but this implies additional computational costs.

1.1.2.3. Switch-off technique

With this method, the calculated velocities in the solid are simply replaced by zero, [15]. The only difficulty is to identify the solid and liquid regions within the domain. This is done, for each element, by using the calculated values of ΔH_v (the latent heat of phase change of the considered element) [11]. It is then a matter of applying a condition on ΔH_v to know if the calculated velocity at this element is overwritten by a zero velocity or kept. The calculated velocities can be overwritten as soon as the phase change at the element starts i.e. $u = 0$ as soon as $\Delta H_v > 0$, or once the element is fully solid i.e. $u = 0$ only if $\Delta H_v = \Delta H_m$, or when partial solidification is reached i.e. $u = 0$ as soon as $\Delta H_v > H_0$ where H_0 is a value of the latent heat of fusion arbitrarily set such that: $0 < H_0 < \Delta H_m$. Among these three approaches, the porosity method is the one most used by the community for its efficiency and ease of implementation. It's important to mention that this approach is also the case in the modules dealing with solid-liquid phase change in commercial CFD codes (Comsol, Fluent, Star-CCM...).

1.2. The multi-domain approach

With the multi-domain approach, both solid and liquid phases are treated separately each with its own computational domain. These two domains are separated by a moving boundary which is the solid-liquid front. Unlike enthalpic methods, where the interface is diffuse and therefore not representative of isothermal phase changes, the multidomain approach allows the explicit

description of the front and its follow-up during the resolution. The front plays the role of both thermal and hydrodynamic boundary conditions at both domains. In this section we present the so-called Stefan formulation, which takes into account the case of convective exchanges within the liquid phase, for a solid-liquid phase change. To get an idea of the problematic presented here and treated throughout this work, let us consider the case of a solid-liquid phase change in a rectangular cavity differentially heated (heated rectangular cavity). During the phase change, the solid-liquid interface moves within this same cavity as illustrated in Fig. II.1.

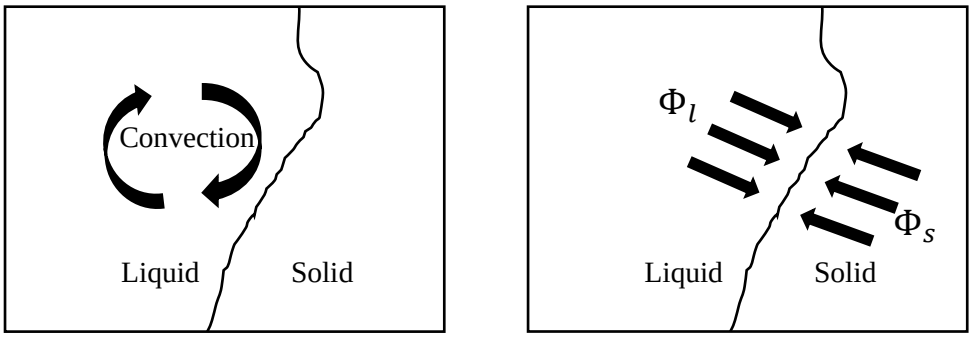

Fig.II.1 :*Schematic representation of a horizontal directional solidification process in a differentially heated cavity.*

In the solid phase, the only conservation equation to solve is the energy conservation equation:

$$\frac{\partial T}{\partial t} = \frac{\lambda_s}{\rho C_{p_s}} \nabla^2 T \qquad \textbf{(II.17)}$$

with T the temperature in the solid and where λ_s and C_{p_s} are respectively the thermal conductivity and the heat capacity of the solid phase. The properties of the solid have been considered here as constant.

In the liquid phase, the energy conservation equation additionally contains a convective term and is coupled to the conservation equations for momentum and mass. For an incompressible Newtonian fluid with the same density as the solid, under the Boussinesq approximation and neglecting thermal dissipation due to viscous effects, these equations are:

- The momentum conservation equation:

$$\frac{\partial u_i}{\partial t} + u.\nabla u_i = -\frac{1}{\rho}\frac{\partial P}{\partial x_i} + \nu\nabla^2 u_i + g\beta_T\left(T_{liq} - T_m\right) \text{ for } i = 1 and\ 2 \qquad \textbf{(II.18)}$$

where T_{liq} is the temperature of the liquid and ν the kinematic viscosity

- The energy conservation equation

$$\frac{\partial T_{liq}}{\partial t} + \boldsymbol{u}.\nabla \boldsymbol{T_{liq}} = \frac{\lambda_l}{\rho C_{p_l}} \nabla^2 \boldsymbol{T_{liq}} \quad \textbf{(II.19)}$$

where λ_l and C_{p_l} are the thermal conductivity and heat capacity of the liquid phase, respectively.

- The mass conservation equation:

$$\nabla.\boldsymbol{u} = \boldsymbol{0} \quad \textbf{(II.20)}$$

The Stefan condition [16] giving the energy balance at the solid-liquid interface is expressed as:

$$\rho \Delta \boldsymbol{H_m} \boldsymbol{v_f}.\boldsymbol{n} = (\boldsymbol{\phi_l} - \boldsymbol{\phi_s}).\boldsymbol{n} \quad \textbf{(II.21)}$$

where v_f is the velocity of the solid-liquid front, ϕ_l and ϕ_s are the heat fluxes from the liquid and solid regions respectively (Fig. II.1), and *n* is the normal vector to the front.

This condition allows us to estimate the displacement velocities of the solid-liquid front i.e. the way in which the two solid and liquid domains are deformed. One of the main advantages of this multi-domain approach, besides having an explicit, and non-diffuse interface, is that once coupled to a resolution method with a deformable (adaptive) mesh, one can constantly modify the proportions of the two domains as a function of the front velocity. This gives several advantages to the multi-domain approach with adaptive mesh compared to the enthalpic method. First, the separation of the two domains in the former allows the use of different meshes between the two domains, either in mesh type or in refinement; where the enthalpic method requires a unique and sufficiently refined mesh wherever the interface is likely to pass within the domain. Although approaches with sliding mesh, allowing a fine mesh at the interface and a coarse mesh elsewhere in the domain, have been domain, have been proposed with the enthalpic method [17]; however, this is limited to quasi-1D cases where the mesh sliding velocity must be well adjusted to match the geometrical and thermal with the geometrical and thermal configuration, but also that the rewriting of the conservation equations and thus additional modelling efforts are required.

The other advantage is that there is no longer a need for a solid phase braking term in the multi-domain approach. A condition of adhesion to the wall is considered directly at the front for the liquid domain, while in the enthalpic for the liquid domain, whereas in the enthalpic methods the damping of the velocities to the solid zone is done in a progressive way through

the mushy zone whose thickness is generally not negligible. Avnaim *et al* [13], in a comparison between the enthalpic and multi-domain approaches, report that the presence and width of the mushy zone, which is inseparable from the enthalpic approach, had a non-negligible effect on the convective loop within the liquid, thus affecting the dynamics of the global heat transfer and consequently the evolution of the solid-liquid front. They also report that the multidomain approach gives results more consistent with the experimental results of validation than the enthalpic method. It should be noted that the adaptive mesh adds additional steps during the resolution (the calculation of the new node positions and the interpolation of the different fields between these nodes), and this represents additional computational costs compared to the enthalpic approach.

2. The numerical models

In order to simulate the directional solidification process with its multiphysics phenomena represented in the segregation phenomenon, fragmentation, heat and mass transfer, the focus will be on some of the most efficient models developed in many international laboratories specialized in this field.

2.1. Numerical models based on enthalpy approach

2.1.1. Two-phase model

The simulation of alloy solidification in presence of convection requires the solution of coupled conservation equations for mass, momentum, energy, and concentration, with the necessity to take into account a phase transition governed by a phase diagram. The approach used in the present simulations is based on a two-phase volume averaging technique. The system at macroscopic scales, for the thermodynamic temperature equation (uniquely defined for the liquid and the solid phase), momentum equation for the liquid phase formulated with its intrinsic velocity $\vec{V} = f_l \overrightarrow{v_l}$ and equation for the average concentration $\langle C \rangle = f_s C_s + f_l C_l$. Moreover, the solid phase is immovable and its description does not require any momentum equation. Furthermore, spatial variations in the average concentration due to mass convection are related to concentration in the liquid phase. Here, the subscripts "*l*" and "*s*" are related to the solid and liquid phase, respectively, and f_l and f_s are the liquid and solid volume fractions.

The flow between the dendrites in the mushy zone is taken into account by adding a Darcy term in the momentum conservation equations with a permeability *K* given by a Kozeny-

Carman law based on the secondary dendrite arm spacing λ_2 $\left(K = \frac{f_l^3}{(1-f_l)^2}\frac{\lambda_2^2}{180}\right)$. This secondary arm spacing changes during the maturation or the ripening of the dendrites. In the calculations, however, we have used a constant value, $\lambda_2 = 90\mu m$, obtained by postmortem analyses of the solidified sample, [16]. The thermal conductivity λ is locally calculated as $\lambda = f_s\lambda_s + f_l\lambda_l$,. Under the assumptions of thermodynamic and chemical equilibrium, along with an instantaneous diffusion of the solute in both phases, the concentrations in the liquid and solid phases within the mushy zone are related via the lever rule, i.e.,$C_s = k_p C_l$, with k_p denoting the partition coefficient. We also assume that, within the mushy zone, the solute concentration in the liquid and the thermodynamic temperature are related via a linearized phase diagram with a liquidus slope m_L ($T = T_m + m_L C_l$). The density of the solid phase is considered as constant and the Boussinesq assumption is used for the liquid density in the buoyancy term. Finally, the no-slip condition is assigned to all the walls. These walls are also assumed to be thermally insulated, except for the two-narrow vertical endwalls (at x = 0 and x = 100 mm), on which uniform temperatures are imposed. [18]

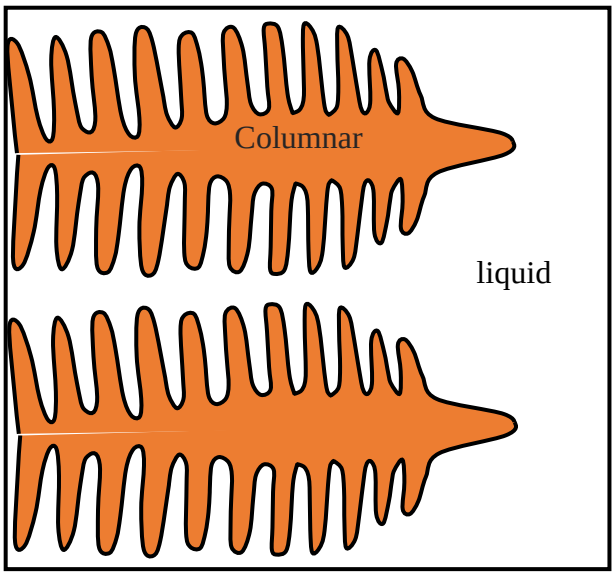

Fig.II.2:*Schematic representation of two-phases(solid-liquid)*

2.1.1.1 the gouverning equations

We formulated mass, momentum, species, and enthalpy conservation equations for both liquid and solid phases:

- **the conservation equations of mass**

$$\frac{\partial}{\partial t}(f_l\rho_l) + \nabla.(f_l\rho_l\vec{u}_l) = M_{sl} \quad \textbf{(II.22)}$$

$$\frac{\partial}{\partial t}(f_s\rho_s) + \nabla.(f_s\rho_s\vec{u}_s) = M_{ls} \quad \textbf{(II.23)}$$

M_{ls} is the mass transfer rate from liquid to solid, and ($M_{sl} = -M_{ls}$) that from solid to liquid. The unit of M_{ls} is $kg/m^3/s$. A positive M_{ls} characterizes solidification; otherwise, it characterizes melting. The terms ρ_l and ρ_s are the densities and $\vec{u}_l$ and $\vec{u}_s$ are the velocities of the liquid and solid phases.

- **the momentum conservation equations**

$$\frac{\partial(f_l\rho_l\vec{u}_l)}{\partial t} + \nabla.(f_l\rho_l\vec{u}_l \times \vec{u}_l) = -f_l\nabla P + \nabla.\bar{\bar{\tau}}_l + f_l\rho_l\vec{g} + \vec{U}_{sl} \quad \textbf{(II.24)}$$

$$\frac{\partial(f_s\rho_s\vec{u}_s)}{\partial t} + \nabla.(f_s\rho_s\vec{u}_s \times \vec{u}_s) = -f_s\nabla P + \nabla.\bar{\bar{\tau}}_s + f_s\rho_s\vec{g} + \vec{U}_{ls} \quad \textbf{(II.25)}$$

with

$$\bar{\bar{\tau}}_l = \mu_l f_l(\nabla.u_l + (\nabla.u_l)^T) \quad \textbf{(II.26)}$$

$$\bar{\bar{\tau}}_s = \mu_s f_s(\nabla.u_s + (\nabla.u_s)^T) \quad \textbf{(II.27)}$$

u_l, u_s are velocity vectors of the liquid and solid phases. $\vec{U}_{ls} = -\vec{U}_{sl}$ is the momentum exchange rate between both phases. The unit of $\vec{U}_{ls}$ is $kg/m^2/s^2$. The term p is the pressure, and g is the gravity. "$\bar{\bar{\tau}}_l$" and "$\bar{\bar{\tau}}_s$" are the stress–strain tensors, × is the dyadic product.

- **the Species conservation equations**

$$\frac{\partial(f_l\rho_l C_l)}{\partial t} + \nabla.(f_l\rho_l\vec{u}_l C_l) = \nabla.(f_l\rho_l D_l\nabla C_l) + C_{sl} \quad \textbf{(II.28)}$$

$$\frac{\partial(f_s\rho_s C_s)}{\partial t} + \nabla.(f_s\rho_s\vec{u}_s C_s) = \nabla.(f_s\rho_s D_s\nabla C_s) + C_{ls} \quad \textbf{(II.29)}$$

where $C_{ls} = -C_{sl}$ (5 2 Csl) is the species exchange rate between both phases. As C_l and C_s represent mass fractions, they are dimensionless. Thus C_{ls} has the unit of $kg/m^3/s$. The terms D_l and D_s are the diffusion coefficients of the solute in the liquid and solid phases.

- **the enthalpy conservation equations**

$$\frac{\partial(f_l\rho_l h_l)}{\partial t} + \nabla.(f_l\rho_l\vec{u}_l h_l) = \nabla.(f_l k_l\nabla.T_l) + Q_{sl} \quad \textbf{(II.30)}$$

$$\frac{\partial(f_s\rho_s h_s)}{\partial t} + \nabla.(f_s\rho_s\vec{u}_s h_s) = \nabla.(f_s k_s\nabla.T_s) + Q_{ls} \quad \textbf{(II.31)}$$

where $Q_{ls} = -Q_{sl}$ is the energy exchange rate between both phases. The unit of h_l and h_s is *J/kg*. Thus, Q_{ls} has the unit of $J/m^3/s$. The terms k_l and k_s are the heat conductivities of the liquid and solid phases. The relationship between the enthalpy h_l (or h_s) and the temperature T_l (or T_s) is determined via:

$$\boldsymbol{h_l = \int_{T_{ref}}^{T_l} c_{pl}\, dT + h_l^{ref}} \textbf{ and } \boldsymbol{h_s = \int_{T_{ref}}^{T_s} C_{ps}\, dT + h_s^{ref}} \qquad \textbf{(II.32)}$$

where c_{pl} and $c_{ps}$are the specific heat capacities of the liquid and solid phases, and h_l^{ref} and h_s^{ref} are the enthalpies at the reference temperature T_{ref}.

In addition to the conservation equations of mass, momentum, species, and enthalpy for both liquid and solid, the conservation of grains is:

$$\boldsymbol{\frac{\partial}{\partial t} n + \nabla.(\vec{u}_s n) = N} \qquad \textbf{(II.33)}$$

n is the grain density and *N* the grain production (nucleation rate). The unit of *n* is m^2. Thus, *N* has the unit of $m^{-2}s^{-1}$. *N* is positive with nucleation and negative with grain dissolution (total remelting). [19]

2.1.1.2 Auxiliary Quantities

The following auxiliary quantities are used: mixed concentration C_{mix}, average grain diameter ds and viscosity of the solid phase μ_s.

- **The mixed concentration**

$$\boldsymbol{C_{mix} = \frac{C_l \rho_l f_l + C_s \rho_s f_s}{\rho_l f_l + \rho_s f_s}} \qquad \textbf{(II.34)}$$

- **average grain diameter**

To estimate the average grain diameter, we assume the morphology of the growing grains to be almost spherical, allowing the volume fraction of solid to be related to the grain density and the average grain volume by

$$\boldsymbol{f_e = n \frac{4\pi}{3} \left(\frac{d_s}{2}\right)^3} \qquad \textbf{(II.35)}$$

- **viscosity of the solid phase**

the momentum of the solid phase is also treated like that of a fluid. Hence, the solution of the corresponding conservation equation requires the definition of viscosity of the solid phase, This

viscosity may be caused by collisions between individual rigid grains. It should increase with increasing solid volume fraction and crystal size because of stronger crystal interactions. Ishii and Zuber [19] found for the viscosity of a solid/liquid mixture.

$$\boldsymbol{\mu_{mix} = \mu_l \left(1 - \frac{f_s}{f_s'}\right)^{-2.5 f_s'}} \quad \textbf{(II.36)}$$

with f_s' representing a critical solid volume fraction above which the equiaxed crystals merge to form a rigid solid structure. Assuming the validity of a mixing rule for viscosity,[20] $\mu_{mix} = \mu_l f_l + \mu_s f_s$, Eq.II.36 can be used to derive an expression for the viscosity of the solid phase

$$\boldsymbol{\mu_s = \frac{\mu_l}{f_s}\left(\left(1 - \frac{f_s}{f_s'}\right)^{-2.5 f_s'} - (1 - f_l)\right)} \quad \textbf{(II.37)}$$

we assume that f_s' is the packing limit $f_s' = 0.637$. For $f_s > f_s'$, μ_s is infinitely large. This forces the macroscopic velocity gradients in the solid to vanish. For example, if the rigid solid structure is attached to a wall, the solid velocity will then be uniformly equal to the velocity of the wall due to the nonslip condition [19].

2.1.2. Three-phase model

Over the last few decades, the authors created two distinguished approaches of this model (two-phase model), one for equiaxed solidification [21-24] and one more for hypermonotectic solidification [25-27]. The two models depend on an Eulerian-Eulerian approach. This part of the chapter will be focused on the extension of the two-phase solidification model to a three-phase model for a mixed columnar and equiaxed solidification with taking into consideration columnar-to-equiaxed transition (CET).

For the additional (columnar) phase, another set of conservation equations for mass, enthalpy, and species must be solved. However, no additional momentum equation is solved because the columnar phase is considered stationary. The most challenging point is the proper definition of the closure laws of the phase exchanges and interactions: for example, the competitive growth of two solid phases and the mechanical interaction between them. Allows free growth and movement of equiaxed phases that nucleate everywhere in bulk melt. The stationary columnar phase is considered to start from the mold wall and therefore preferentially grow in the direction of heat flow. During the solidification process, the two phases grow competitively. When the tips of the growing columnar dendrites are blocked by equiaxed grains, the so-called columnar to equiaxed transition (CET). Early studies reported two main "blocking" mechanisms: one is when the local volume fraction of the equiaxed grain envelope

exceeds a certain limit through "mechanical blocking", [28], and the other is when the local constitutional undercooling disappears. " Chemical blocking", [29, 30], as well detailed previously in the first chapter. The proposed three-phase model is characterized0 by the fact that it clearly tracks the columnar tip front and includes the above two CET mechanisms (mechanical and chemical). However, we also consider the influence of melt convection and equiaxed grain transport on the occurrence of CET, [31].

The three-phase model is built on a general assumption that the three considered phases are the parent melt as the primary phase, as well as the solidifying columnar dendrites and globular equiaxed grains as two different secondary phases. Their corresponding phase fractions is given by f_l, f_c, and f_e with $f_l + f_e + f_c = 1$. With a Eulerian approach, the three phases are considered as spatially coupled and interpenetrating continua. For all three phases, the mass, momentum, species, and enthalpy conservation equations are solved. An extra conservation equation is created and solved for the number density of the equiaxed grains. Nucleation of the equiaxed grains, diffusion-controlled growth of both columnar and equiaxed phases, interphase exchanges, and interactions such as mass transfer during solidification, drag force, solute partitioning at the liquid/solid interface, and release of latent heat are taken into account. Both the primary and equiaxed phases are moving phases, for which the corresponding Navier-Stokes equations are solved. The columnar phase is assumed to stick to the wall and solidify from the wall toward the bulk melt. Thus, no momentum equation for the columnar phase is considered. Ideal morphologies for both solid phases are assumed: spheres for equiaxed (globular) grains and cylinders for columnar (cellular) dendrites. The grain size of equiaxed grains and the diameter of the columnar trunks are explicitly calculated, while a constant value for the primary arm spacing of columnar dendrites is assumed. No feeding flow is included. The Boussinesq approach is employed to model thermosolutal convection, grain sedimentation, and sedimentation induced melt convection, and Grain fragments brought, [32].

2.1.2.1 Nucleation of equiaxed grains and grain transport

The density number of equiaxed grains (m^{-3}), n, is calculated with:

$$\frac{\partial}{\partial t}\boldsymbol{n} + \boldsymbol{\nabla}.(\vec{\boldsymbol{u}}_{\boldsymbol{e}}\boldsymbol{n}) = \boldsymbol{N_e} \qquad \textbf{(II.38)}$$

where $\vec{u}_e$ is the (volume averaged) velocity of the equiaxed phase. The nucleation rate (m^{-3} s^{-1}), *Ne*, is modeled with a three-parameter heterogeneous nucleation law [21,22].

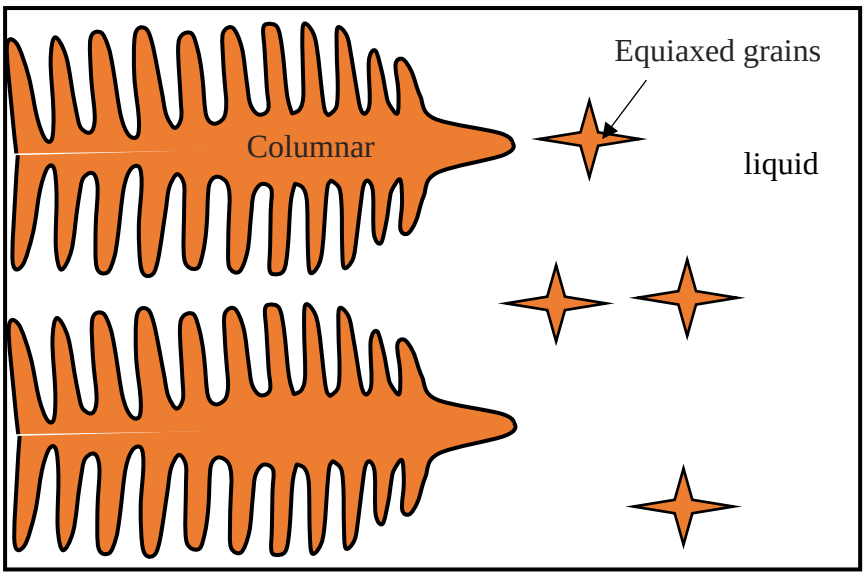

Fig.II. 3: *Schematic representation of three phases in M. Wu and A. Ludwig model [32].*

2.1.2.2 Mass conservation and grain growth kinetics

Mass conservation equations (Eq.II.10) is written as follows in a three-phase model:

$$\frac{\partial}{\partial t}(f_l \rho_l) + \nabla.(f_l \rho_l \vec{u}_l) = M_{el} + M_{cl} \quad \textbf{(II.39)}$$

$$\frac{\partial}{\partial t}(f_e \rho_e) + \nabla.(f_e \rho_e \vec{u}_e) = M_{le} + M_{ce} \quad \textbf{(II.40)}$$

$$\frac{\partial}{\partial t}(f_c \rho_c) + \nabla.(f_c \rho_c \vec{u}_c) = M_{lc} + M_{ec} \quad \textbf{(II.41)}$$

where ρ_l, ρ_e, ρ_c, are the densities and $\vec{u}_l$, $\vec{u}_e$, $\vec{u}_c$ the velocities of the different phases. The source terms M_{lc} (=-M_{cl}) is the mass transfer rate ($kg/m^3.s$) from liquid to columnar phase, and M_{le} (=-M_{ce}) from liquid to equiaxed phase by solidification (positive) or melting (negative), and M_{ce} (=-M_{ec}) from columnar to equiaxed phase by the mechanism of fragmentation (positive) or by attaching (negative). The fragmentation is ignored, so we chose M_{ce} = 0.

Considering the diffusion on the micro-scale to control the kinetics of grain growth. For equiaxed solidification, the ideal spherical shape is considered so that the grain growth velocity in the radius direction can be solved analytically, [33]:

$$v_{Re} = \frac{dR_e}{dt} = \frac{D_l}{R_e}\frac{C_l^* - C_l}{C_l^* - C_s^*} = \frac{D_l}{R_e(1-k)}\left(1 - \frac{C_l}{C_l^*}\right) \quad \textbf{(II.42)}$$

Where, C_l^* and C_s^* are the equilibrium concentrations adjacent to the solid/liquid interface, and from the phase diagram $C_l^* = (T - T_m)/m$ yields. D_l is the diffusion coefficient in the liquid and $R_e = \frac{d_e}{2}$ is the radius of the grain. With Eq.II.42, considering the overall surface area of the spherical grains and the influence of pingement by an Avrami-factor "F_l", we can estimate the volume-averaged mass transfer rate for globular equiaxed solidification:

$$\boldsymbol{M_{le} = v_{Re}(n\pi d_e^2)\rho_e F_l} \quad \textbf{(II.43)}$$

There are two cases that can be distinguished for columnar solidification: (i) tip areas (ii) growing columnar trunks behind the tip region. A diffusion-controlled growth model around cylindrical dendrite trunks is employed for the volume elements that have already been pasted by the tip front. The growth velocity in radial direction of such a cylindrical trunk is approximated with the similar analytical method of W. Kurz and D.J. Fisher, [33] As follows:

$$\boldsymbol{v_{Rc} = \frac{dR_c}{dt} = \frac{D_l}{R_c}\frac{C_l^* - C_l}{C_l^* - C_s^*} ln^{-1}\left(\frac{R_f}{R_c}\right)} \quad \textbf{(II.44)}$$

where now $R_c = \frac{d_c}{2}$ is the average radius of a cylindrical dendrite trunk and $R_f = \frac{\lambda_1}{2}$ is half of the primary dendrite spacing λ_1. Hence, we can define the volume averaged mass transfer rate for those volume elements by considering the total surface area of columnar dendrite trunks per volume $S_A = \pi d_c/\lambda_1$ and an Avrami-factor "F_l":

$$\boldsymbol{M_{lc} = v_{Rc}\left(\frac{\pi d_c}{\lambda_1^2}\right)\rho_c F_l} \quad \textbf{(II.45)}$$

For the elements containing the growing columnar tips, the mass transfer rate "M_{lc}" for columnar solidification is written by considering both the tip growth velocity, v_{tip}, and radial growth velocity, "v_{Rc}":

$$\boldsymbol{M_{lc} = v_{Rc} n_c(\pi d_c l)\rho_l F_l + v_{tip} n_c(\pi R_{tip}^2)F_l} \quad \textbf{(II.46)}$$

The first term on the left-hand side of Eq. II.46 denotes the mass transfer rate due to the growth in radial direction and the second term that of the growth in tip direction. $n_c = 4f_c/(\pi d_c^2 l)$ is the number density of the columnar trunks. The dendrite tip velocity "v_{tip}" and the tip radius "R_{tip}" are calculated according to [33,34].

2.1.2.3 Momentum conservation

The momentum equations for both moving equiaxed phase and the parent melt are:

$$\frac{\partial(f_l\rho_l\vec{u}_l)}{\partial t} + \nabla.(f_l\rho_l\vec{u}_l \times \vec{u}_l) = -f_l\nabla P + \nabla.\bar{\bar{\tau}}_l + \vec{F}_{Bl} + \vec{U}_{cl} + \vec{U}_{el} \quad \textbf{(II.47)}$$

$$\frac{\partial(f_e\rho_e\vec{u}_e)}{\partial t} + \nabla.(f_e\rho_e\vec{u}_e \times \vec{u}_e) = -f_e\nabla P + \nabla.\bar{\bar{\tau}}_e + \vec{F}_{Be} + \vec{U}_{le} + \vec{U}_{ce} \quad \textbf{(II.48)}$$

where "$\bar{\bar{\tau}}_l$" and "$\bar{\bar{\tau}}_e$" are the stress–strain tensors. With the Boussenisq approximation, the thermal-solutal buoyancy force $\vec{F}_{Bl}$ acting on the liquid and the buoyancy force $\vec{F}_{Be}$ acting on the free moving equiaxed grains are applied, [24]. Each of the momentum exchange terms $\vec{U}_{le}$, $\vec{U}_{lc}$ and $\vec{U}_{ce}$ includes two parts: the part due to phase transformation and the part due to drag force, for example, $\vec{U}_{le} = \vec{U}_{le}^{p} + \vec{U}_{le}^{d}$ and $\vec{U}_{lc} = \vec{U}_{lc}^{p} + \vec{U}_{lc}^{d}$. A. Ludwig and M. Wu [21,22], provide the details about the way of how to deal with these momentum exchange terms between the liquid and equiaxed phases. The same concept is employed for the momentum exchange between the liquid and the columnar phase. However, a mushy zone permeability as described in [35] to calculate the liquid-columnar drag force, it was used. A simple approach is used for momentum exchange between the columnar and equiaxed phases. It assumed that when the local volume fraction of the columnar phase is greater than a critical value of $f_c^{free} = 0.2$, an infinite drag force coefficient between both solid phases applies, capturing the equiaxed grains. When the volume fraction of the columnar phase is less than this critical value, there is no drag force between both solid phases exists and thus the movement of the equiaxed grains is unaffected by the columnar front. The choice of this critical value for $f_c^{free} = 0.2$ is taken arbitrary. Therefore, further parameter study on the effect of this value on the final result is necessary.

2.1.2.4 Species conservations

The volume averaged concentration C_l in the liquid phase, C_e in the equiaxed phase and C_c in the columnar phase are obtained by solving the species concentration equations:

$$\frac{\partial(f_l\rho_l C_l)}{\partial t} + \nabla.(f_l\rho_l\vec{u}_l C_l) = \nabla.(f_l\rho_l D_l\nabla C_l) + C_{cl} + C_{el} \quad \textbf{(II.49)}$$

$$\frac{\partial(f_e\rho_e C_e)}{\partial t} + \nabla.(f_e\rho_e\vec{u}_e C_e) = \nabla.(f_e\rho_e D_e\nabla C_e) + C_{le} + C_{ce} \quad \textbf{(II.50)}$$

$$\frac{\partial(f_c\rho_c C_c)}{\partial t} + \nabla.(f_c\rho_c\vec{u}_c C_c) = \nabla.(f_c\rho_c D_c \nabla C_c) + C_{lc} + C_{ec} \quad \textbf{(II.51)}$$

where D_l, D_e, D_c are the diffusion coefficients. The diffusive species exchange at the phase interface is neglected. However, during solidification (and melting), the species partitioning at the phase interface is taken into account, [21,22]. As we ignore any phase exchange between equiaxed and columnar phases, we set $C_{ce} \equiv 0$.

2.1.2.5 Enthalpy conservation

We solve the enthalpy conservation equation for each phase:

$$\frac{\partial(f_l\rho_l h_l)}{\partial t} + \nabla.(f_l\rho_l\vec{u}_l h_l) = \nabla.(f_l k_l \nabla.T_l) + Q_{cl} + Q_{el} \quad \textbf{(II.52)}$$

$$\frac{\partial(f_e\rho_e h_e)}{\partial t} + \nabla.(f_e\rho_e\vec{u}_e h_e) = \nabla.(f_e k_e \nabla.T_e) + Q_{le} + Q_{ce} \quad \textbf{(II.53)}$$

$$\frac{\partial(f_c\rho_c h_c)}{\partial t} + \nabla.(f_c\rho_c\vec{u}_c h_c) = \nabla.(f_c k_c \nabla.T_c) + Q_{lc} + Q_{ec} \quad \textbf{(II.54)}$$

where the enthalpies are defined via $h_l = \int_{T_{ref}}^{T_l} c_{pl}\, dT + h_l^{ref}$ and $h_e = h_c = \int_{T_{ref}}^{T_e} C_{ps}\, dT + h_e^{ref}$ with specific heat c_{pl} and c_{ps} of the liquid and the solid phase respectively . T_{ref} and h_e^{ref} are defined so that the enthalpy difference between liquid and any solid, $h_l - h_e$ and $h_l - h_c$, is equal to the latent heat of fusion. Further details to treat the latent heat can be found in several works, namely [21,22]. By solving Eqs. II. (52)-(54), three different temperatures are obtained, T_l , T_e and T_c. The thermal equilibrium condition ($T_l \approx T_e \approx T_c$) is satisfied by applying a quite large volumetric heat transfer coefficient of 10^8 ($Wm^{-3}\,K^{-1}$) between the phases.

2.1.2.6 Auxiliary quantities

A mixture concentration for the description of macrosegregations, C_{mix}, is defined by:

$$C_{mix} = \frac{C_l\rho_l f_l + C_e\rho_e f_e + C_c\rho_c f_c}{\rho_l f_l + \rho_e f_e + \rho_c f_c} \quad \textbf{(II.55)}$$

The average diameter of the equiaxed grains d_e is calculated from the following relation

$$f_e = n\frac{4\pi}{3}\left(\frac{d_e}{2}\right)^3 \quad \textbf{(II.56)}$$

The average diameter of the columnar dendrite trunks d_c is calculated by relating the cross-section area of a single columnar trunk $\pi\left(\frac{d_c}{2}\right)^2$ to the maximal available area of each trunk when the dendrites are ranked in hexagon. Thus, we get:

$$\boldsymbol{f_c = \frac{3}{4}\frac{d_c^2}{\lambda_1^2}} \qquad \textbf{(II.57)}$$

In the case the dendrites are ranked in square, the prefactor of Eq.II.57 would be π/4 instead of 3/4. The average dendrite arms spacing, λ_1, is assumed to be constant, [31].

2.1.2.7 Columnar tip front tracking and tip front 'blocking' mechanism

Columnar tip front tracking is based on the concept that columnar dendrite trunks extend into the bulk melt from the wall. However, no growth-favoured crystalline orientation is taken into account.

- The columnar status marker "i_c" is assigned to each control volume, indicating whether it has the columnar tip front ($i_c = 1$), columnar dendrite trunks ($i_c = 2$), or no trunks or tips ($i_c = 0$). Except for the boundary (wall) elements which have ($i_c = 1$), all control volumes are initialized with $i_c = 0$.
- An "equivalence" cylinder with a radius of "R_{ref}" and a height of "l_{ref}" is considered for each control volume. The cylinder volume is set to be equal to that of the corresponding control volume, i.e., $l_{ref}^3 = \Delta V$. The "*equivalence*" cylinder is considered to be oriented parallel to the local heat flow direction because no preferred crystal growth orientation is determined.
- With a growth velocity "v_{tip}" calculated from the LGT model [34], the columnar front grows parallel to the "equivalence" cylinder. Starting as soon as the front enters the control volume, the integral $l = \int v_{tip} dt$ is evaluated to track the real position of the front.
- For ($l > l_{ref}$), the columnar tip front has grown from the "equivalent" cylinder. In this case, all adjacent control volumes that are still "empty" ($i_c = 0$) will be "reached" by the. Therefore, the columnar status markers of these volumes are set to ($i_c = 1$), and the marker of the considered volume is set to ($i_c = 2$).
- A mass transfer to the columnar phase from the liquid is only considered for those control volumes $i_c \neq 0$.

- In order to model the 'mechanical blocking' mechanism by Hunt [28] as soon as the local volume fraction of equiaxed f_e increases over the critical threshold of $f_{e,CET} = 0.49$, the tip growth velocity is set to zero, $v_{tip} \equiv 0$. This event defines the CET known in the literature. The above CET process automatically leads to the so-called "soft blocking" mechanism proposed by Martorano et *al.* [30], because v_{tip} disappears when the local constitutional undercooling disappears.

2.1.3. Five-phase model

Wang and Beckermann [36,37] have outlined a general multiphase approach for dealing with the dendritic morphology in equiaxed or columnar solidification. With the idea similar to the Rappaz and Thevoz model, [38,39] they defined a grain envelope to separate the extra dendritic melt from the interdendritic melt. Because columnar dendrites and equiaxed grains have different morphologies, different formulations and morphological parameters must be considered. Their principal approach is to implement the above idea into a previously-developed 3-phase mixed columnar-equiaxed solidification model by the authors [31,32]. Melt convection, grain sedimentation, columnar tip front tracking, interaction between equiaxed grains and columnar dendrites, columnar-to-equiaxed transition, and other elements of the previous 3-phase mixed columnar-equiaxed solidification model are all taken into account [40].

In this model, five-phase regions have been identified to address mixed columnar-equiaxed solidification with dendritic morphology, and the volume fractions of the five phases are specified as follows: extradendritic melt, f_l, interdendritic melt in the equiaxed grain, f_l^e , and solid dendrite in the equiaxed grain, f_s^e, interdendritic melt in the columnar trunk, f_l^c , and solid dendrite in the columnar trunk, f_s^c, as shown in Fig. II.5.

The interdendritic liquid and solid dendrite in the equiaxed grain combine to generate a 'hydrodynamic' *e*-phase that moves at an average velocity, whereas the interdendritic liquid and solid dendrite in the columnar stem combine to form a 'hydrodynamic' *c*-phase that moves at a predetermined velocity. A grain boundary, also known as the grain envelope, separates the interdendritic and extra dendritic liquids. The extra dendritic melt is considered as a third 'hydrodynamic' phase, "l- phase", which has a velocity. The velocity of the corresponding 'hydrodynamic' phase is used to determine the transport of mass, species, and energy in each phase region. The whole physical domain is divided by the columnar tip front into two: in front

of the columnar tip, the number of 'hydrodynamic' phases is 2, i.e., '*l*- and e-phases, thus there are only 3 phases existing behind the columnar tip front, all the 3 'hydrodynamic' phases (*l*-, e- and c-phases) and all the 5 phase zones (f_l, f_l^e, f_s^e, f_l^c, f_s^c) might be involved. The columnar tip front is tracked explicitly, [40].

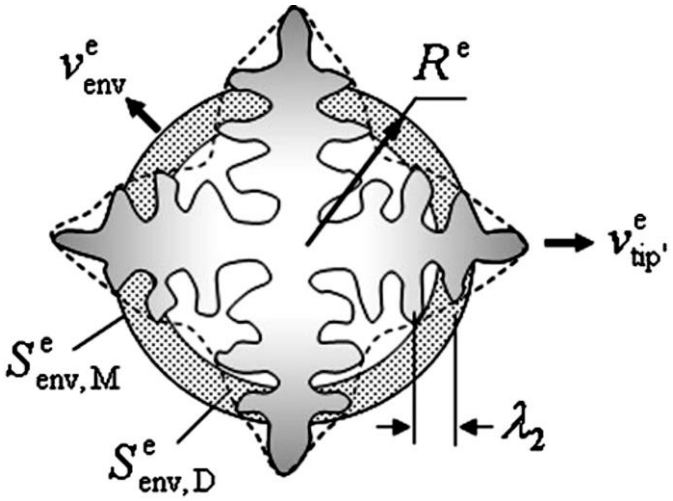

***Fig.II. 4*:** *The shape of the equiaxed dendritic grain is simplified as a sphere with the equivalent volume of the fictitious grain envelope connecting the primary and secondary dendrite tips [40]*

The basic idea of the five-phase approach was mainly based on an improved model for equiaxed dendritic solidification published previously, [43]. As can be seen in Fig. II. 4, the grain envelope (dashed line) is defined as a fictitious surface connecting the primary and secondary dendrite tips. The averaged concentration of the interdendritic melt is C_l^e, while the concentration of the extradendritic melt is C_l. When the grain envelope expands, both species transfer and species diffusive flux due to the growth of the envelope are taken into account, [41]. Solidification occurs only at the solid-liquid interface, i.e., the interface between the interdendritic melt and solid dendrites, where a thermodynamic equilibrium condition applies. The interdendritic melt and solid adjacent to the solid-liquid interface has the equilibrium concentrations C_l^* and C_s^*, dictated by the local temperature according to thermodynamics. It is the concentration difference ($C_l^* - C_l^e$) that serves as driving force for the solidification of the interdendritic melt. Latent heat is released, and solute partitioning ($k = {C_s^*}/{C_l^*}$) occurs at the solid-liquid interface.

The local growth velocity of the fictitious grain envelope (dashed line, Fig. II.4) is unknown. What is known from the classical tip growth kinetics is the primary tip growth velocity $v^e_{tip\prime}$, e.g. by the LGK model, [42]. Therefore, it further simplifies the shape of the equiaxed dendritic grain as an 'equivalent sphere', with its volume equivalent to the volume enclosed in the fictitious grain envelope. By defining a shape factor Φ^e_{env},[41] it can obtain the growth velocity of the equivalent sphere from the primary tip growth velocity:

$$\boldsymbol{v^e_{env,S} = \Phi^e_{env}.\, v^e_{tip\prime}} \quad \textbf{(II.58)}$$

In order to calculate the species diffusive flux at the envelope between the interdendritic and extradendritic melts, however, the real surface area of the envelope $S^e_{env,D}$ is required. This area $S^e_{env,D}$ is actually correlated to the surface area of the equivalent sphere $S^e_{env,S}$ by another factor Φ^e_{sph}, which is called sphericity,

$$\boldsymbol{S^e_{env,D} = S^e_{env,S}/\Phi^e_{sph}} \quad \textbf{(II.59)}$$

Both Φ^e_{env} and $\Phi^e_{sph}$are two morphological parameters, dependent purely on the shape of the grain envelope. If the shape of the grain envelope is preserved and constant, then they can be determined previously. For example, in the RT model, [38,39] an ideal sphere envelope connecting the primary dendrite tips is assumed, both Φ^e_{env} and $\Phi^e_{sph}$are equal to one. For an octahedral envelope considered by Nielsen *et al.*,[43] Φ^e_{env} is $\frac{1}{\sqrt[3]{\pi}}$ and $\Phi^e_{sph}$is $\frac{\sqrt[3]{\pi}}{\sqrt{3}}$. For a general case (Fig.II.4), both morphological parameters might be smaller than the values mentioned above. By using the above two morphological parameters the nature of the arbitrary shape of the grain envelope with a simplified equivalent sphere can be approximated [40].

The dendrite trunk is wrapped in a theoretical dendrite envelope for columnar growth, as seen in Fig.II.5 (dash line). It encloses the primary dendrite tip and secondary dendrites near the primary dendrite tip, as well as the secondary and tertiary dendrites in the trunk region (away from the primary dendrite tip). The cross section of the dendrite trunk can be approximated by a quadrate or cloverleaf, while the longitudinal section of the envelope around the primary dendrite tip is parabolic. As a result, the region around the main dendrite tip is treated differently from the columnar dendrite trunk region.

For the columnar trunks, the dendrite envelope is further simplified as a step-wise growing cylinder with the cross-section area equivalent to the enclosed area of the dendrite

envelope. The growth rate of the cylinder in the radial direction can be derived from the growth velocity of the secondary dendrite tip $v^c_{tip''}$.

$$\boldsymbol{v^c_{env,C} = \Phi^c_{env}.\, v^c_{tip''}} \quad \textbf{(II.60)}$$

where Φ^c_{env} is a shape factor. The diffusion area of the columnar envelope $S^c_{env,D}$ is calculated based on the surface area of the equivalent cylinder $S^c_{env,S}$ by considering a circularity Φ^c_{circ}.

$$\boldsymbol{S^c_{env,D} = S^c_{env,S}/\Phi^c_{circ}} \quad \textbf{(II.61)}$$

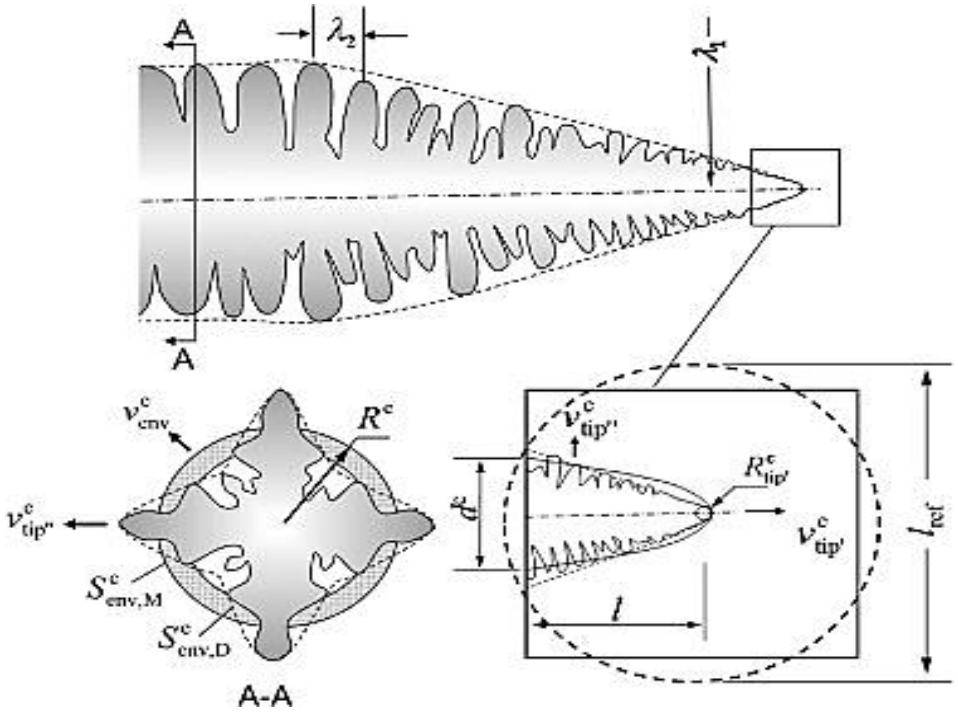

Fig.II. 5*: *The shape of the columnar dendrite trunk is simplified as a step-wise cylinder with the cross-section area equivalent to the fictitious tree-trunk envelope connecting the secondary and tertiary dendrites. The parabolic shape of the columnar envelope near the primary dendrite tip is also simplified as an equivalent cylinder with an averaged diameter and explicitly-tracked length [40].

Both Φ^c_{env} and Φ^c_{circ} are morphological parameters (≤ 1). When the envelope of columnar trunk (dashed line in Fig.II.5) is identical to an ideal circle (cross section of a cylinder), they are equal to one. If cross section of the dendrite trunk envelope is close to a quadrate, then $\Phi^c_{env} = \frac{\sqrt{2}}{\pi}$, $\Phi^c_{circ} = \frac{\sqrt{\pi}}{2}$. For any other complicated envelopes, both morphological parameters are smaller than the values mentioned above. With these

morphological parameters, any arbitrary cross-section of the dendrite trunk envelope can be approximately described with an equivalent circle, [40]. The parabolic envelope is represented as an analogous cylinder with an averaged diameter d^c and length l in the columnar dendrite tip area (Fig.II.5). A method previously described [44] is used to track the cylinder's length. The dendritic morphology of the primary dendrite tip area is modeled using the corresponding shape factor and circularity.

2.1.3.1 Growth kinetics

a. Equiaxed growth

There are two types of growth: globular growth and dendritic growth. Solute partitioning happens at the solid-liquid phase boundary during globular growth (identical to the grain envelope). Diffusion around the spherical grain controls grain growth, and its growth velocity v_{glob}^{e} may be calculated analytically

$$\boldsymbol{v_{glob}^{e} = \frac{D_l}{R^e}.\Omega} \quad \textbf{(II.62)}$$

where Ω is the constitutional undercooling $(C_l^* - C_l)/(C_l^* - C_S^*)$. For the dendritic growth, the growth velocity of the dendrite tips v_{tip}^{e}, can be determined by the LGK model, [42]. With Eq.II.58 the growth velocity of the equivalent sphere of dendritic grain is obtained $v_{env,S}^{e}$. The globular-to-dendritic transition (GDT) is determined by comparing the two growth velocities, v_{glob}^{e} and $v_{env,S}^{e}$.

$$\boldsymbol{v_{env}^{e} = \max\left(v_{glob}^{e}, v_{env,S}^{e}\right)} \quad \textbf{(II.63)}$$

The growth surface area concentration $S_{env,M}^{e}$ of the equivalent spheres is calculated

$$\boldsymbol{S_{env,S}^{e} = \Phi_{lmp}^{e}.(36\pi.n)^{\frac{1}{3}}.f_e^{\frac{2}{3}}} \quad \textbf{(II.64)}$$

where n is number density of the grains, and Φ_{lmp}^{e} is an impingement factor for the growing grains. With the v_{env}^{e} and $S_{env,S}^{e}$, the volume averaged mass transfer rate from the l-phase to the e-phase can be calculated.

b. Columnar growth

Again, there are two types of growth: cellular (non-dendritic) and dendritic. The diffusion governs cellular growth and its radial growth velocity v_{cell}^{c}:

$$v_{cell}^{c} = \frac{D_l}{R^c}.\Omega.ln^{-1}\left(\frac{\lambda_1}{\sqrt{3}R^c}\right) \quad \textbf{(II.65)}$$

Here a staggered arrangement of the cellular trunks is assumed. The actual cellular diameter is $2R^c$, and the far field reference diameter is $(\frac{2\lambda_1}{\sqrt{3}})$. The radial growth velocity of the secondary dendrite tip $v_{tip'}^{c}$ is determined by the LGK model for the dendritic growth, [42]. With Eq.II.60 the growth velocity of the equivalent cylinder of the columnar dendrite trunk is obtained $v_{env,C}^{c}$. Comparing the above two growth velocities, v_{cell}^{c} and $v_{env,C}^{c}$, determines the cellular-to-dendritic transition (CDT).

$$v_{env}^{c} = \max\left(v_{cell}^{c}, v_{env,C}^{c}\right) \quad \textbf{(II.66)}$$

The growth surface area concentration $S_{env,C}^{c}$ of the equivalent cylinder is calculated as follow:

$$S_{env,C}^{c} = \Phi_{lmp}^{c}.\frac{2\pi R^c}{\lambda_1^2} \quad \textbf{(II.67)}$$

where Φ_{lmp}^{c} is an impingement factor for the growing columnar trunks. With v_{env}^{c} and $S_{env,C}^{c}$, the volume averaged mass transfer rate from the *l*-phase to the *c*-phase in the volume elements, which contain the fully over-grown columnar trunks, can be calculated.

Some particular considerations and assumptions must be made in volume elements that contain columnar tips. The same technique as Eqs. II. (65) and (66) is used to produce v_{env}^{c} for the radial growth of the equivalent cylindrical envelope, but the length of the columnar trunks "*l"*, which is contained in the volume element, and the corresponding diameter, $d^c/2$, must be monitored explicitly, [46]. Additionally, the contribution of the growth of the primary tips themselves $(v_{tip'}^{c}.\pi R_{tip'}^{c}2)$ to the total volume averaged mass transfer in the considered volume element must also be taken into account. Kurz and Fisher [45] estimated the tip radius $R_{tip'}^{c}$, and the primary tip growth velocity $v_{tip'}^{c}$ was calculated using the KGT model, [46]. The solidification of the interdendritic melt is treated in the same way for both equiaxed and columnar growth and is described elsewhere, [41].

2.1.4. Mushy zone instability model

A new numerical model of mushy zone instability is proposed [47], which describes the relation between mush zone instability and mush permeability (see Fig. II.6). The ability of the new instability criterion to characterize and predict channel segregation is illustrated by

comparing the possible channel locations estimated from the developed standard with numerically simulated channel segregation in casting. In addition, the number and location of segregated channels estimated by the new instability model will be compared with the number and location estimated using the remelting criterion.

Fig. II. 6 shows schematically a liquid-solid mushy region in a rectangular cavity solidifying from the left wall. Liquid near the roots of the dendrites is highly segregated, *i.e.*, enriched in solute, and this is shown by the darker shading (see Fig.II.6 a). In the dendritic columnar mushy zone, the average distance between the side branches, i.e., the secondary dendritic arm spacing (λ_2) is used as the characteristic length scale of the porous structure in the permeability model (Fig.II.6b). As an example, a typical width of the mushy zone is of the order of 10 mm. Spacing of dendrite arms in such a mushy zone would be the order of ~0.01-0.1 mm, as shown in Fig. II. 6 (b) [48]. The scale of the REV used for the description of such a mushy zone is of the order of few d_2 (see Fig.II.6c). The channel segregates form due to the perturbation in the liquid fraction field (shown by isolines of the liquid fraction field in Fig.II.6d) near the high- f_l region of the mushy zone as the solidification progresses (see Fig.II.6d). The length scale of the channel type segregation is approximately 1- 10 mm. We can precise the length of a channel is 10 mm while the width is 1 mm. These dimensions are at least 10 times larger than the characteristic size of the porous structure, λ_2 (0.1 mm). The channel width is of the same order of magnitude as the REV size. The analysis presented in this work is conducted at the scale of the REV whose size is in the order of few d_2 . It is important to notice that the only characteristic size given as an input to the averaged model is that used for the permeability, i.e., λ_2 . What can be also said is that the channel width we obtained from the simulation results is of the same order of magnitude as the REV dimension. The analysis conducted by Mehrabian *et al.* [48] was exactly at the same scale as in the present work.

Assuming dendritic columnar solidification with rigid solid dendrites, constant physical properties of the mixture, and Boussinesq approximation, the momentum conservation for the liquid phase using one-domain and volume averaging modelling approach is given as follows [49]:

$$\rho \frac{\partial(f_l \vec{v}_l)}{\partial t} + \rho \nabla.(f_l \vec{v}_l \vec{v}_l) \quad = f_l \nabla P + f_l \mu \nabla^2 \vec{v}_l - f_l^2 \frac{\mu}{K} \vec{v}_l + \rho_0 f_l \vec{g}[\beta_T (T - T_0) + \beta_C (C_l - C_0)] \qquad \textbf{(II.68)}$$

The mushy zone is considered as a porous medium, of permeability K, saturated with liquid. The third term on R.H.S of the Eq.II.68 accounts for the drag force of the solid skeleton on the interdendritic liquid [50-54]. To assess the role of permeability on the instability in the mushy

zone, we consider fluid flow in this region. In the mushy zone, the inertial and viscous terms of Eq.II.68 can be neglected and it reduces to the Darcy equation [48] .

$$\frac{\mu}{K(f_l)} \boldsymbol{f_l \vec{v}_l} = -\boldsymbol{\nabla P} + \boldsymbol{\rho_0 \vec{g}}[\boldsymbol{\beta_T}(\boldsymbol{T - T_0}) + \boldsymbol{\beta_C}(\boldsymbol{C_l - C_0})] \quad \textbf{(II.69)}$$

For the simplest mushy zone permeability model, K is a function of f_l and the characteristic size in the microstructure (secondary dendritic arm spacing λ_2, a constant value of λ_2 is assumed in this study). If locally, we perturb the liquid fraction (porosity) field by δf_l, one observes a corresponding perturbation $\delta \vec{v}_l$ caused in the velocity field.

$$\frac{\mu}{K(f_l+\delta f_l)}[\,(\boldsymbol{f_l} + \boldsymbol{\delta f_l})(\boldsymbol{\vec{v}_l} + \boldsymbol{\delta \vec{v}_l})] = -\boldsymbol{\nabla P} + \boldsymbol{\rho_0 \vec{g}}[\boldsymbol{\beta_T}(\boldsymbol{T - T_0}) + \boldsymbol{\beta_C}(\boldsymbol{C_l - C_0})] \quad \textbf{(II.70)}$$

One can notice that a perturbation in liquid can occur for different reasons like instability in the fluid flow. The analysis that we present corresponds to a classical linear perturbation analysis in which the goal is to determine conditions corresponding to an amplification of the instability. If it is possible to get such conditions, this analysis will introduce a new way to understand phenomena like channel formation as we will illustrate later.

The perturbations in the liquid fraction and the velocity field can of course trigger further perturbations in pressure, temperature and concentration fields. In the following analysis, these perturbations are neglected. It is based on the following assumptions:

- We assume that the temperature field in the mushy zone is mainly controlled by diffusive heat transfer. Therefore, the influence of a flow perturbation on the temperature field is negligible.
- We further assume that the time scale of the evolution of perturbation is large with respect to the time scale of solute diffusion at the scale of the secondary dendrite arm spacing. There- fore, we can assume that the local liquid composition in the mushy zone is at thermodynamic equilibrium and closely follows the temperature field. Similarly, the perturbation of liquid concentration can thus be considered negligible.
- The strongest assumption is that of negligible perturbation of the pressure field, its validity is shown in the results.

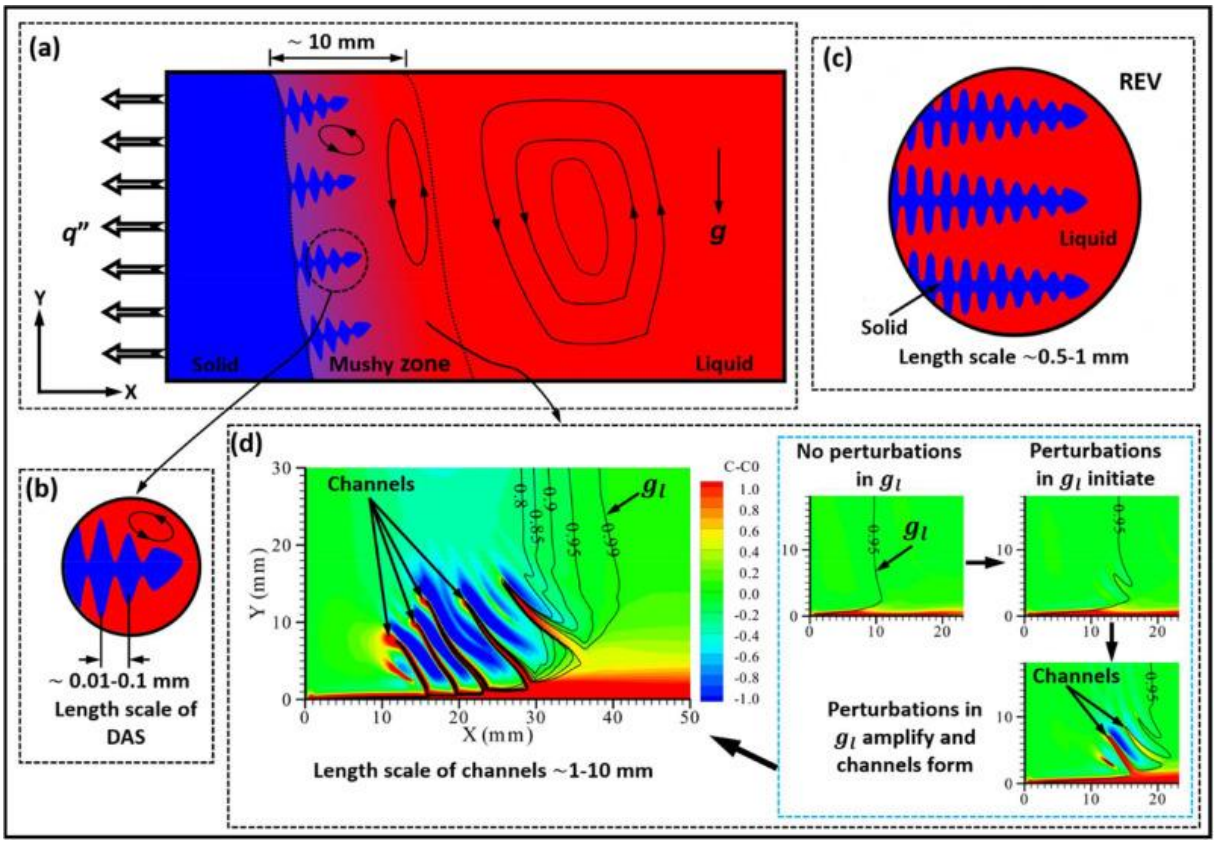

***Fig.II. 6*:** *Schematic illustrating the physical scales and the formation of channel segregates phenomena during columnar solidification (a) system (macroscopic) scale (dendrites in the mushy zone are exaggerated, they will be seen at high magnification), (b) grain scale, (c) representative elementary volume (REV), (d) formation of channel segregates (isolines in black colour show the liquid fraction field). [47]*

In Eq.II.70, $K(f_l)$ will become $K(f_l + \delta f_l)$ after the perturbation. On subtracting Eq.II.69 from Eq.II.70 one gets

$$\frac{\mu}{K(f_l+\delta f_l)}[\,(f_l + \delta f_l)(\vec{v}_l + \delta\vec{v}_l)] = \frac{\mu}{K(f_l)} f_l \vec{v}_l \qquad \textbf{(II.71)}$$

which can be rearranged to:

$$\vec{v}_l + \delta\vec{v}_l = \vec{v}_l \frac{K(f_l+\delta f_l)}{K} \frac{f}{f_l+\delta f_l} \qquad \textbf{(II.72a)}$$

$$\vec{v}_l + \delta\vec{v}_l = \left[K(f_l) + \frac{dK}{df_l}\delta f_l\right] \frac{f_l \vec{v}_l}{K} \left[\frac{1}{f_l}\left(1 + \frac{\delta f_l}{f_l}\right)^{-1}\right] \qquad \textbf{(II.72b)}$$

Since the perturbation δf_l is small, the second and higher order terms of $\frac{\delta f_l}{f_l}$ will be very small and hence can be neglected while expanding Eq.II.72b as:

$$\vec{v}_l + \delta\vec{v}_l = \left[K(f_l) + \frac{dK}{df_l}\delta f_l\right]\frac{f_l\vec{v}_l}{K}\left[\frac{1}{f_l}\left(1 - \frac{\delta f_l}{f_l}\right)^{-1}\right] \quad \textbf{(II.72c)}$$

Again, while expanding Eq.II.72c the terms containing the square of δf_l (as they will be small) can be neglected, which give us:

$$\vec{v}_l + \delta\vec{v}_l = \vec{v}_l - \frac{\vec{v}_l}{f_l}\delta f_l + \frac{\vec{v}_l}{K}\frac{dK}{df_l}\,\delta f_l \quad \textbf{(II.73a)}$$

$$\delta\vec{v}_l = \vec{v}_l\left[\frac{1}{K}\frac{dK}{df_l} - \frac{1}{f_l}\right]\delta f_l \quad \textbf{(II.73b)}$$

Eq.II.73b suggests that the perturbation in velocity $\delta\vec{v}_l$ is proportional to the perturbation in liquid fraction δf_l and the velocity $\vec{v}_l$, which suggests that the higher the interdendritic velocity, the higher will be the extent of perturbation. It is also interesting to note that $\delta\vec{v}_l$ depends on a bracketed term $\left[\frac{1}{K}\frac{dK}{df_l} - \frac{1}{f_l}\right]$ which consists of permeability and its derivative with respect to f_l. To understand whether the perturbation in f_l (*i.e.*, δf_l) will amplify or dampen with time, one needs to evaluate the sign of $\frac{\partial(\delta f_l)}{\partial t}$. It needs consideration of the coupling of phase change with the transport of heat and solute.

We consider the averaged solute conservation equation for the solid and liquid phases and assume infinite diffusion in the liquid phase and zero diffusion in the solid phase (Scheil's assumption) at the scale of the secondary dendrite arms (microscopic scale) [48]. The averaged solute conservation equation can be expressed as [48]:

$$\frac{\partial(f_l C_l)}{\partial t} + C_s^*\frac{\partial(f_s)}{\partial t} + f_l\vec{v}_l.\nabla(C_l) = 0 \quad \textbf{(II.74)}$$

In Eq.II.74, C_l is the volume-averaged concentration in the liquid phase and C_s^* is the concentration in the solid phase at the solid-liquid interface. The liquid phase is at the thermodynamic equilibrium composition due to infinite diffusion, thus we can express the temperature by $T = T_m + mC_l$, where T_m is the melting temperature of the pure solvent and m is the liquidus slope. The solid-liquid interface is at thermodynamic equilibrium, and thus $C_s^* = k_p C_l$, where k p is the binary partition coefficient. Eq.II.74 transforms to:

$$f_l\frac{1}{m}\frac{\partial T}{\partial t} + (1 - k_p)C_l\frac{\partial(f_l)}{\partial t} + \frac{1}{m}f_l\vec{v}_l.\nabla T = 0 \quad \textbf{(II.75)}$$

Expressing $\frac{\partial T}{\partial t} = \vec{v}_T\nabla.T$ (where $\vec{v}_T$ is the velocity of the isotherm), Eq.II.75 becomes:

$$\left(\mathbf{1}-\boldsymbol{k_p}\right)\boldsymbol{C_l}\frac{\boldsymbol{\partial(f_l)}}{\boldsymbol{\partial t}}+\frac{\mathbf{1}}{\boldsymbol{m}}\,\boldsymbol{f_l}(\vec{\boldsymbol{v}}_{\boldsymbol{l}}-\vec{\boldsymbol{v}}_{\boldsymbol{T}}).\boldsymbol{\nabla T}=\mathbf{0} \quad \textbf{(II.76)}$$

We again impose an infinitesimal perturbation δf_l in f_l in Eq.II.76 which causes an infinitesimal perturbation $\delta\vec{v}_l$ in $\vec{v}_l$. As considered earlier the influence of this perturbation on $\vec{v}_T$, ∇T and C_l is assumed to be negligible. The perturbed form of Eq.II.76 becomes:

$$\frac{\mathbf{1}}{\boldsymbol{m}}\,(\boldsymbol{f_l}+\boldsymbol{\delta f_l})[(\vec{\boldsymbol{v}}_{\boldsymbol{l}}+\boldsymbol{\delta}\vec{\boldsymbol{v}}_{\boldsymbol{l}})-\vec{\boldsymbol{v}}_{\boldsymbol{T}}]\,.\boldsymbol{\nabla T}+\left(\mathbf{1}-\boldsymbol{k_p}\right)\boldsymbol{C_l}\frac{\boldsymbol{\partial(f_l+\delta f_l)}}{\boldsymbol{\partial t}}=\mathbf{0} \quad \textbf{(II.77)}$$

Subtracting Eq.II.76 from Eq.II.77 and keeping only the first order term of δf_l (as δf_l is small), we obtain:

$$\frac{\mathbf{1}}{\boldsymbol{m}}\boldsymbol{f_l}\,\boldsymbol{\delta}\vec{\boldsymbol{v}}_{\boldsymbol{l}}\,.\boldsymbol{\nabla T}+\frac{\mathbf{1}}{\boldsymbol{m}}\boldsymbol{\delta f_l}\,(\vec{\boldsymbol{v}}_{\boldsymbol{l}}-\vec{\boldsymbol{v}}_{\boldsymbol{T}})\,.\boldsymbol{\nabla T}+\left(\mathbf{1}-\boldsymbol{k_p}\right)\boldsymbol{C_l}\frac{\boldsymbol{\partial(\delta f_l)}}{\boldsymbol{\partial t}}=\mathbf{0} \quad \textbf{(II.78)}$$

Using the relation for $\delta\vec{v}_l$ from Eq.II.73b, we get:

$$\frac{\mathbf{1}}{\boldsymbol{m}}\boldsymbol{f_l}\,\vec{\boldsymbol{v}}_{\boldsymbol{l}}\left[\frac{\mathbf{1}}{\boldsymbol{K}}\frac{\boldsymbol{dK}}{\boldsymbol{df_l}}-\frac{\mathbf{1}}{\boldsymbol{f_l}}\right]\boldsymbol{\delta f_l}\,.\boldsymbol{\nabla T}+\frac{\mathbf{1}}{\boldsymbol{m}}\boldsymbol{\delta f_l}\,(\vec{\boldsymbol{v}}_{\boldsymbol{l}}-\vec{\boldsymbol{v}}_{\boldsymbol{T}})\,.\boldsymbol{\nabla T}+\left(\mathbf{1}-\boldsymbol{k_p}\right)\boldsymbol{C_l}\frac{\boldsymbol{\partial(\delta f_l)}}{\boldsymbol{\partial t}}=\mathbf{0} \quad \textbf{(II.79a)}$$

$$\frac{\mathbf{1}}{\boldsymbol{m}}\left[\boldsymbol{f_l}\,\vec{\boldsymbol{v}}_{\boldsymbol{l}}\frac{\mathbf{1}}{\boldsymbol{K}}\frac{\boldsymbol{dK}}{\boldsymbol{df_l}}-\vec{\boldsymbol{v}}_{\boldsymbol{T}}\right]\,.\boldsymbol{\nabla T}\boldsymbol{\delta f_l}+\left(\mathbf{1}-\boldsymbol{k_p}\right)\boldsymbol{C_l}\frac{\boldsymbol{\partial(\delta f_l)}}{\boldsymbol{\partial t}}=\mathbf{0} \quad \textbf{(II.79b)}$$

Rearrangement of Eq.II.79b gives:

$$\frac{\boldsymbol{\partial(\delta f_l)}}{\boldsymbol{\partial t}}=-\frac{\mathbf{1}}{\boldsymbol{m}(\mathbf{1}-\boldsymbol{k_p})\boldsymbol{C_l}}\left[\boldsymbol{f_l}\,\vec{\boldsymbol{v}}_{\boldsymbol{l}}\frac{\mathbf{1}}{\boldsymbol{K}}\frac{\boldsymbol{dK}}{\boldsymbol{df_l}}-\vec{\boldsymbol{v}}_{\boldsymbol{T}}\right]\,.\boldsymbol{\nabla T}\boldsymbol{\delta f_l} \quad \textbf{(II.79c)}$$

For k_p value less than one and negative value of the slope *m*, it gives a condition for perturbation δf_l to amplify with time as:

$$\frac{\boldsymbol{\partial(\delta f_l)}}{\boldsymbol{\partial t}}>\mathbf{0}\ \textbf{if}\ \vec{\boldsymbol{v}}_{\boldsymbol{l}}.\boldsymbol{\nabla T}>\frac{\boldsymbol{K}}{\boldsymbol{f_l}}\left(\frac{\boldsymbol{dK}}{\boldsymbol{df_l}}\right)^{-\mathbf{1}}(\vec{\boldsymbol{v}}_{\boldsymbol{T}}.\boldsymbol{\nabla T}) \quad \textbf{(II.80)}$$

It may be noted that the new criterion is derived in terms of amplification of the local perturbations in the mushy zone i.e., $\frac{\partial(\delta f_l)}{\partial t}>0$, which is different from a remelting criterion i.e., $\frac{\partial(f_l)}{\partial t}>0$. The derived criterion for amplification of perturbation involves a local permeability term (and hence the local liquid fraction) which makes it different from the existing remelting criterion such as, Flemings' criterion of remelting, $\vec{v}_l.\nabla T>\vec{v}_T.\nabla T$ [48]. From Eq.II.80 it can be seen that the mush instability depends on the interdendritic velocity, the isotherm velocity and the temperature gradient. Also, it explicitly depends on the dynamically changing characteristic of the mushy zone during solidification *i.e.,* on the

permeability. It is evident that for a given cooling rate the two favourable conditions for amplification of perturbation are a higher interdendritic velocity ($\vec{v}_l$) in the direction parallel to ∇T and / or a lower value of $\frac{K}{f_l}\left(\frac{dK}{df_l}\right)^{-1}$.

A widely used approach in modelling the mushy zone permeability is to use the Blake-Kozeny permeability model [55-60], which is given as:

$$\boldsymbol{K = \frac{\lambda_2^2 f_l^3}{180(1-f_l)^2}} \qquad \textbf{(II.81)}$$

In the dendritic columnar mushy zone, the interdendritic characteristic arm spacing is used to describe the mushy zone permeability. The average distance between the side branches *i.e.,* the secondary dendritic arm spacing (λ_2) is used as the interdendritic characteristic arm spacing in the permeability model. The above expression is very schematic and a more realistic description, accounting for the microstructure of the dendrites, would be necessary. However, this challenging and very important point is out of the scope of the present study. Since our main objective is to discuss the relationship between the mushy zone instability and the mush permeability, a simplified expression for mushy zone permeability law (Blake-Kozeny permeability model) is used. It is important to notice at this stage that as we use the Scheil's assumption, the characteristic size λ_2 introduced in Eq.II.81 is the only characteristic size appearing in the whole set of equations of the model. Which means in other words that the size of the REV used for the averaging procedure is in the order of magnitude of λ_2.

This model can be summarized as the following:

- The interdendritic velocity, the isotherm velocity, the temperature gradient, and, most importantly, the mush permeability are all factors in the new instability criterion devised for amplification of perturbations in the mushy zone.
- The new instability criterion suggests two favourable conditions for amplification of perturbation, a lower value of $\frac{K}{f_l}(\frac{dy}{dx})^{-1}$and/or a higher interdendritic velocity (v_l).
- The permeability and its derivative with respect to liquid fraction (the $\frac{K}{f_l}(\frac{dy}{dx})^{-1}$ function) in the outer part of mushy zone (high- f_l regions, liquid fraction more than 0.9) plays a key role in the amplification of the mush instability. The part of the mushy region near the liquidus is more prone to the initiation of such instabilities.

- The new instability criterion very well describes and predicts the placements of segregated channels observed in the numerical simulations. It characterizes these segregated channels better than that by the previously available remelting criterion. The predictions of segregated channels based on remelting severely under characterize these defects (e.g., their number and length) in the casting. [47]

2.1.5. Phase-field method

The phase-field method has recently emerged as a powerful computational approach to modelling and predicting mesoscale morphological and microstructure evolution in materials. It describes a microstructure using a set of conserved and non-conserved field variables (or order parameters) that are continuous across the interfacial regions. The temporal and spatial evolution of the field variables is governed by the Cahn-Hilliard nonlinear diffusion equation and the Allen-Cahn relaxation equation. With the fundamental thermodynamic and kinetic information as the input, the phase-field method is able to predict the evolution of arbitrary morphologies and complex microstructures without explicitly tracking the positions of interfaces.

2.1.5.1 Sharp interface approach

In conventional modelling technique for phase transformations and microstructural evolution, i.e the sharp interface approach, the interfaces between different domains are considered to be infinitely sharp, and a multi-domain structure is described by the position of the interfacial boundaries. The kinetics of microstructure formation is then modeled by a set of partial differential equations that describe the release and diffusion of heat, the transport of impurities, and the complex boundary conditions that govern the thermodynamics at the interface for each domain. As a concrete example, in the solidification of a pure material the advance of the solidification front is limited by the diffusion of latent heat away from the solid-liquid interface, and the ability of the interface to maintain two specific boundary conditions; flux of heat toward one side of the interface is balanced by an equivalent flux away from the other side, and the temperature at the interface undergoes a curvature correction known as the Gibbs–Thomson condition. These conditions are mathematically expressed in the following sharp interface model, commonly known as the Stefan problem:

$$\begin{cases} \frac{\partial T}{\partial t} = \nabla.(\alpha \nabla T) \ \ with \ \alpha = (k/\rho Cp) \\ \rho L_f V_n = ks\nabla T.\, n|_{int}^{S} - kL\nabla T.n|_{int}^{L} \\ T_{int} = T_m - (\gamma T_M/L_f)_\kappa - (V_n/\mu) \end{cases} \quad \textbf{(II.82)}$$

where T =T(x, t) denotes temperature, k thermal conductivity (which assumes values k_s and k_L in the solid and liquid, respectively), ρ the density of the solid and liquid, cp the specific heat at constant pressure, α the thermal diffusion coefficient, L_f the latent heat of fusion for solidification, γ the solid-liquid surface energy, T_M the melting temperature, κ the local solid liquid interface curvature, V_n the local normal velocity of the interface, and μ the local atomic interface mobility. Finally, the subscript "int" refers to interface and the superscripts "S" and "L" refer to evaluation at the interface on the solid and liquid side, respectively.

Like solidification, there are other diffusion-limited phase transformations whose interface properties can, on large enough length scales, be described by specific sharp interface kinetics. Most of them can be described by sharp interface equations analogous to those in Equation 1. Such models often referred to as sharp interface models operate on scales much larger than the solid-liquid interface width, itself of atomic dimensions. As a result, they incorporate all information from the atomic scale through effective constants such as the capillary length, which depend on surface energy, the kinetic attachment coefficient, and thermal impurity diffusion coefficient.

2.1.5.2 Details of phase field modelling

Imagine the growth of a precipitate which is isolated from the matrix by an interface. There are three distinct entities to consider: the precipitate, matrix and interface. The interface can be described as an evolving surface whose motion is controlled according to the boundary conditions consistent with the mechanism of transformation. The interface in this mathematical description is simply a two-dimensional surface; it is said to be a sharp interface which is associated with an interfacial energy σ per unit area. In the phase field method, the state of the entire microstructure is represented continuously by a single variable known as the order parameter ϕ. For example, ϕ = 1, ϕ = 0 and 0 < ϕ < 1 represent the precipitate, matrix and interface respectively. The latter is therefore located by the region over which ϕ changes from its precipitate value to its matrix value, as shown in figure below.

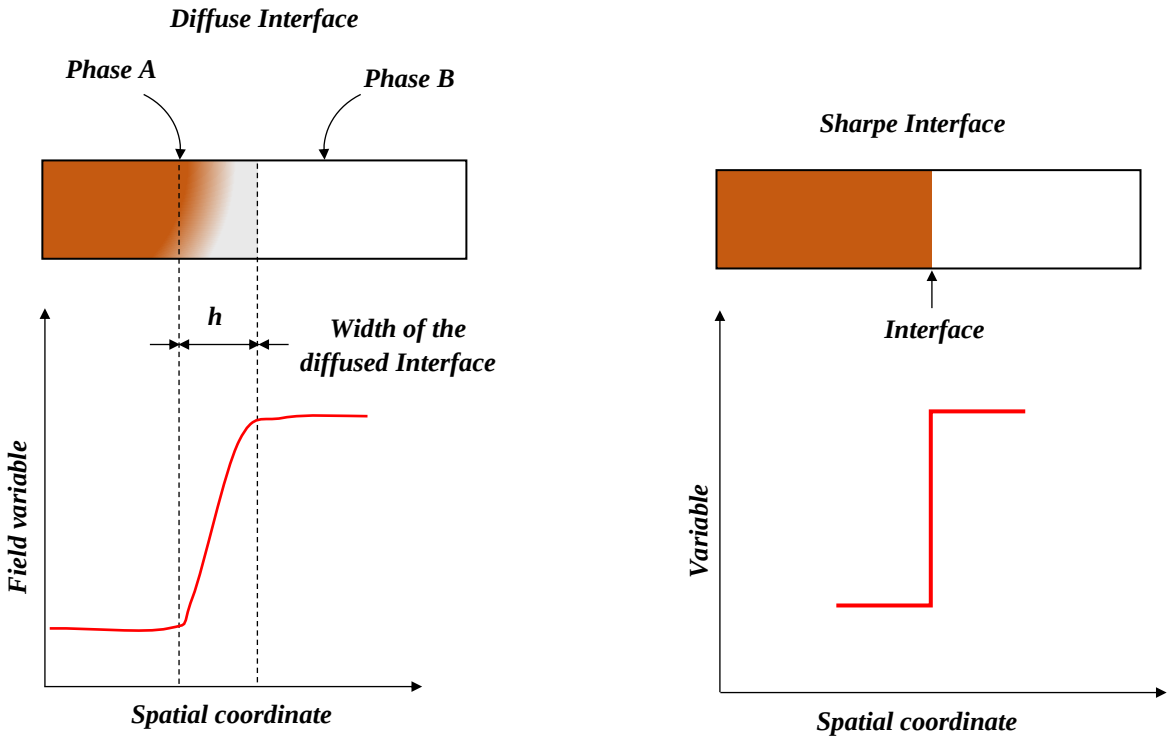

***Fig.II.7* :** *Illustrative diagram of diffusive interface and sharp interface*

The range over which it changes is the width of the interface. The set of values of the order parameter over the whole volume is the phase field. The total free energy "G" of the volume is then described in terms of the order parameter and its gradients, and the rate at which the structure evolves with time is set in the context of irreversible thermodynamics, and depends on how G varies with ϕ. It is the gradients in thermodynamic variables that drive the evolution of structure.

Consider a more complex example, the growth of a grain within a binary liquid (Fig.II.8). In the absence of fluid flow, in the sharp interface method, this requires the solution of seven equations involving heat and solute diffusion in the solid, the corresponding processes in the liquid, energy conservation at the interface and the Gibbs-Thomson capillarity equation to allow for the effect of interface curvature on local equilibrium. The number of equations to be solved increases with the number of domains separated by interfaces and the location of each interface must be tracked during transformation. This may make the computational task prohibitive. The phase field method clearly has an advantage in this respect, with a single functional to describe

the evolution of the phase field, coupled with equations for mass and heat conduction, i.e., three equations in total, irrespective of the number of particles in the system. The interface illustrated in Fig.II.8b simply becomes a region over which the order parameter varies between the values specified for the phases on either side. The locations of the interfaces no longer need to be tracked but can be inferred from the field parameters during the calculation.

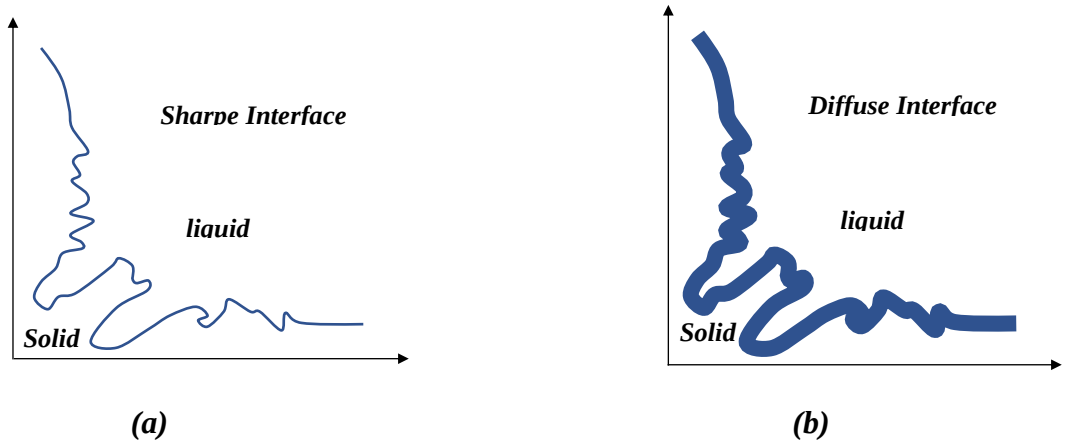

Fig.II.8 *:growth of a grain within a binary liquid: (a) sharp interface, (b) diffuse interface*

Notice that the interface in Fig.II.8b is drawn as a region with finite width, because it is defined by a smooth variation in ϕ between $\phi = 0$ (solid) and $\phi = 1$(liquid). The order parameter does not change discontinuously during the traverse from the solid to the liquid. The position of the interface is fixed by the surface where $\phi = 0.5$.

2.1.5.3 Order parameter

The order parameter in phase field modelling is a function of space and time which may or may not have macroscopic physical interpretations. For two-phase materials, ϕ is typically set to 0 and 1 for the individual phases, and the interface is the domain where $0 < \phi < 1$. For the general case of N phases present in a matrix, there will be a corresponding number of phase field order parameters ϕ_i with I =1 to N. ϕ_i=1 then represents the domain where phase i exists, $\phi_i = 0$ where it is absent and $0 < \phi_i < 1$, its bounding interfaces. Suppose that the matrix is represented by ϕo then it is necessary that at any location:

$$\sum_{i=0}^{N} \boldsymbol{\phi_i} = \mathbf{1}$$

It follows that the interface between phases 1 and 2, where $0 < \phi_1 < 1$ and $0 < \phi_2 < 1$ is given by $\phi_1 + \phi_2 = 1$; similarly, for a triple junction between three phases where $0 < \phi i < 1$ for i=1,2,3, the junction is the domain where $\phi_1 + \phi_2 + \phi_3 = 1$.

2.1.5.4 Governing equations and mathematics of phase field modelling

As a first requirement for any problem to be modeled by phase field modelling, a free energy functional (**for isothermal cases and for non-isothermal cases free entropy functional**) has to be defined as a function of order parameter. The general expression of a free energy functional is shown below:

$$\boldsymbol{F} = \int_v [\boldsymbol{f}(\boldsymbol{\phi}, \boldsymbol{c}, \boldsymbol{T}) + (\boldsymbol{\epsilon_c^2}/\boldsymbol{2}) \times |\boldsymbol{\nabla c}|^2 + (\boldsymbol{\epsilon_\phi^2}/\boldsymbol{2}) \times |\boldsymbol{\nabla \phi}|^2] \, \boldsymbol{dv} \qquad \textbf{(II.83)}$$

The first term in the left-hand side of the equation is free energy density of the bulk phase as a function of concentration, order parameter and temperature. The second and the third term denote the energy of the interface. The second term denotes the energy due to the gradient present in the concentration and the third term denotes the energy due to the gradient present in the order parameter.

After doing a little bit of mathematics (which is intentionally ignored here, considering the point that only the application of these equations shall be sufficient at undergraduate level study), one arrives at two kinds of equation. The first one is for conserved order parameters and the second one is for non-conserved order parameters.

- **Cahn-Hilliard Equation** – Cahn-Hilliard equation gives the rate of change of conserved order parameter with time.

$$\frac{\partial \boldsymbol{\phi}}{\partial \boldsymbol{t}} = \boldsymbol{M}.\boldsymbol{\nabla^2}[\frac{\partial \boldsymbol{f}}{\partial \boldsymbol{\phi}} - \boldsymbol{\varepsilon_\phi^2}\,\boldsymbol{\nabla^2 \phi}] \qquad \textbf{(II.84)}$$

The above equation is for constant (position-independent) mobility M. ϕ is order parameter, ∇ is divergence, *f* is free energy of the bulk, ε_ϕ is gradient energy coefficient. As one can quite clearly notice that Cahn-Hilliard equation is nothing but modified form of Fick‟s second law for transient diffusion.

Cahn-Allen Equation - Cahn-Allen equation gives the rate of change of non-conserved order parameter with time.

$$\frac{\partial \phi}{\partial t} = -M[\frac{\partial f}{\partial \phi} - \epsilon_{\phi}^{2} \nabla^{2} \phi] \quad \textbf{(II.85)}$$

Cahn-Allen equation is also known as time-dependent **Ginsburg-Landau equation**.
While deriving the Cahn-Hilliard and Cahn-Allen equation, an important expression ($\partial\phi/\partial t = M \times \partial F/\partial\phi$) was used, which clearly does makes sense because the change in free energy functional with respect to change in order parameter ϕ, must be in some relation with change in order parameter ϕ with respect to time.

2.1.6. Lattice Boltzmann procedure

Lattice Boltzmann (LB) methods are a class of mesoscopic particle-based approaches to simulate fluid flows. They are becoming a serious alternative or complementary to traditional methods for CFD. LB methods are especially well suited to simulate flows in complex geometries, and they are straightforwardly implemented on parallel machines. Historically, the LB approach is developed from lattice gases, although it can also be derived directly from the simplified Boltzmann BGK equation. In lattice gases, particles live on the nodes of a discrete lattice. The particles jump from one lattice node to the next, according to their (discrete) velocity. This is called the propagation phase. Then, the particles collide and get a new velocity, the collision phase. Hence the simulation proceeds, alternating between particle propagations and collisions. The two phases can be clearly distinguished. It can be shown that lattice gases lead to the Navier-Stokes equations of fluid flow [61,62]. The major disadvantage of the lattice gases method for common fluid dynamics applications was the exponential complexity of the collision rules which was overcome in previous works (see for instance [64-65]). If the main interest is a smooth flow field, one needs to average over a very large lattice and over a long time period. The LB method solves this problem by pre-averaging the lattice gas. It considers particle distributions that live on the lattice nodes, rather than the individual particles. In the setting up, the velocity and thermal field have to receive a different treatment when considering the lattice approach [63]

2.1.6.1 LB equation for the velocity field

The Lattice Boltzmann method employed in this study uses an hexagonal lattice (Frisch-Hasslacher-Pomeau model) (Fig.II.9), leading to the form:

$$\boldsymbol{f_i(x + c_i\Delta t, t + \Delta t) - f_i(x, t) = \Omega_i} \quad \textbf{(II.86)}$$

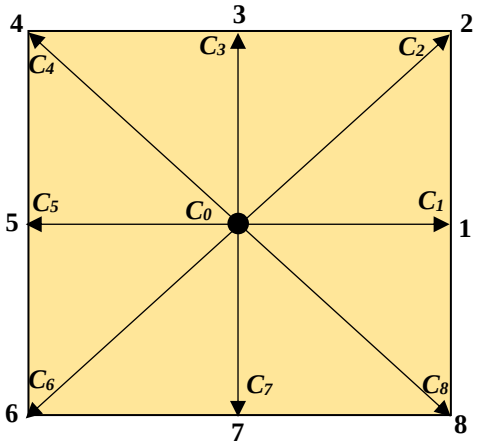

Fig.II.9 *:Example of LB grid (D2Q9).*

where f_i is the particle distribution defined for the finite set of the discrete particle velocity vectors c_i. The collision term Ω_i on the right-hand side of Eq. (II.86) uses the so called Bhatangar-Gross-Krook (BGK) approximation. The essence of this approximation for LB method is that the collision term Ω_i will be replaced by the well-known classical single relaxation time

$$\boldsymbol{\Omega_i = \frac{f_i - f_i^{eq}}{\tau} + \delta_i F_i} \quad \textbf{(II.87)}$$

where τ is the relaxation time and f_i^{eq} is the local equilibrium distribution function that has an appropriately prescribed functional dependence on the local hydrodynamic properties. $\delta_i F_i$ is the external force field. The equilibrium distribution can be formulated as in [62]:

$$\boldsymbol{f_i^{eq} = \omega_i \rho \left(1 + \frac{3(c_i.u)}{c^2} + 9\frac{(c_i.u)^2}{(2c^4)} - 3u.u/(2c^2)\right)} \quad \textbf{(II.88)}$$

where u and ρ are the macroscopic velocity and density, respectively, and the ω_i are the weights that are given by the length of the velocity vector:

$$\boldsymbol{\omega_i = \begin{cases} 4/9 & i = 0 \\ 1/9 & i = 1,2,3,4 \\ 1/36 & i = 5,6,7,8 \end{cases}} \quad \textbf{(II.89)}$$

The set of discrete velocities ci for the two dimensional and nine connected nodes (D2Q9) are defined as follows:

$$\boldsymbol{c_i} = \begin{cases} (\mathbf{0},\mathbf{0}) & \boldsymbol{i = 0} \\ \left(\cos\left[\frac{(i-1)}{2}\pi\right], sin\left[\frac{(i-1)}{2}\pi\right]\right) & \boldsymbol{i = 1,2,3,4} \\ \sqrt{2}\left(\left[\frac{(i-1)}{2}\pi + \frac{\pi}{4}\right], sin\left[\frac{(i-1)}{2}\pi + \frac{\pi}{4}\right]\right) & \boldsymbol{i = 5,6,7,8} \end{cases} \quad \textbf{(II.90)}$$

where δx, δt and $c = \delta x/\delta t$ are the lattice size, time step and the lattice constant which depend on the lattice sound speed, respectively. The basic hydrodynamic quantities, such as density ρ and velocity u, are obtained through moment summations in velocity space:

Flow density: $\boldsymbol{\rho(x,t) = \sum_i f_i(x,t)}$ **(II.91)**

Momentum: $\boldsymbol{\rho u(x,t) = \sum_i f_i(x,t)\, e_i}$ **(II.92)**

The Chapman-Enskog expansion for the density distribution function can recover the continuity and Navier-Stokes equations. The detailed derivation of this procedure is given in [66,67]. The lattice viscosity [61] is determined by:

$$\boldsymbol{\nu = \frac{1}{3}\left(\tau_v - \frac{1}{2}\right)} \quad \textbf{(II.93)}$$

where τ_v is the relaxation time.

2.1.6.2 LB equation for temperature field

In general, LB methods for a fluid flow involving heat transfer in a plain medium can be classified into two categories, the multi-speed models [61] and the double distribution function approach [62]. In the doubled population, the flow and the temperature fields are solved by two separate equations. To derive the LBGK model for Eqs. (II.86)-(II.88), two LBGK equations are used to solve the velocity and temperature fields, respectively. In this context, the evolution equation for the internal energy is given as follows:

$$\boldsymbol{g_i(x + e_i\Delta t, t + \Delta t) = g_i(x,t) - \frac{1}{\tau_T}\left[g_i(x,t) - g_i^{eq}(x,t)\right] - \omega_i \frac{L_f}{C_p}\left[f_l^{n,j} - f_l^{n-1}\right]} \quad \textbf{(II.94)}$$

where g_i is the energy distribution function, τ_T is the dimensionless relaxation time for the temperature field, and the equilibrium temperature distribution function is given by:

$$\boldsymbol{g_0^{eq} = -\frac{2}{2}\rho e\frac{u.u}{c^2}; g_{2k+1}^{eq} = \frac{\rho e}{9}\left(\frac{3}{2} + \frac{3}{2}\frac{c_{2k+1}.u}{c^2} + \frac{9}{4}\frac{(c_{2k+1}.u)^2}{c^4} - \frac{3}{2}\frac{u.u}{c^2}\right);} \quad \textbf{(II.95)}$$

$$g_{2k}^{eq} = \frac{\rho e}{36}\left(3 + 6\frac{c_{2k}.u}{c^2} + \frac{9}{2}\frac{(c_{2k}.u)^2}{c^4} - \frac{3}{2}\frac{u.u}{c^2}\right) \qquad \text{for } k= 1, 2, 3, 4$$

the macroscopic temperature is calculated from:

$$\rho e = \sum_i g_i \qquad \textbf{(II.96)}$$

The temperature and internal energy are related through the state equation, $e = RT$. The Chapman-Enskog expansion for the density distribution function recovers the macroscopic energy equation. This gives the thermal diffusivity α in term of the thermal single relaxation:

$$\alpha = \frac{1}{3}\left(\tau_T - \frac{1}{2}\right) \qquad \textbf{(II.97)}$$

2.1.6.3 Phase change treatment with LBM

To solve the phase change problem, a fixed grid approach is used, similar to the principle used for enthalpy formulation when considering continuum media [68-70]. The melting process takes place over a temperature range $T_m \pm \varepsilon$, where ε is a small quantity (typically 5% of ΔT). The principle of the enthalpy method is to separate the sensible and latent heat components in the vicinity of the solid–liquid interface ($T_m - \varepsilon < T < T_m + \varepsilon$). The latent heat component is expressed in term of the latent heat and liquid fraction, Fl, which is defined as:

$F_l = 1$ **for** $T > T_m + \varepsilon$ **;**

$F_l = 0$ **for** $T < T_m - \varepsilon$ **;**

$F_l = (T - Tm + \varepsilon)/2\varepsilon$ **for** $T_m - \varepsilon < T < T_m + \varepsilon$

Dynamically, the phase change zone is treated like a porous medium. The flow penetration into the medium depends on its permeability. With the LB approach, this basic concept is introduced by assuming that the population densities are uniformly distributed throughout the volume of each node. Each particle moves a total distance of 1 or √2 lattice spacing in one time step, depending on its speed. If the node is totally solid, $f_\alpha^*(x,t)$ is completely reflected. $f_\alpha(x,t) = f_\alpha(x, t + \Delta t)$. If the node contains a fraction of fluid $F_l \neq 1$, only a part of $f_i^*(x,t)$ is propagated, the other part is reflected and returned to the initial cell. We note f^{**} the result of the collision step given by:

$$f_\alpha^*(x, t + \Delta t) = f_\alpha^*(x,t) + \frac{1}{\tau}\left[f_\alpha^{eq}(x,t) - f_\alpha^*(x,t)\right] \qquad 0 \leq \alpha \leq 8 \qquad \textbf{(II.98)}$$

The streaming process in the porous media can be written as:

$$\boldsymbol{f_\alpha(x,t+\Delta t) = f_\alpha^{**}(x,t) + \lambda[f_{\bar{\alpha}}^{**}(x + c_\alpha \Delta t, t+\Delta t) - f_\alpha^{**}(x,t+\Delta t)] \quad 0 \le \alpha \le 8} \quad \textbf{(II.99)}$$

Where $\bar{\alpha}$ is the index of the direction opposite c_α and $\lambda = 1 - F_l$ a factor to take account of the permeability of the medium depending on the liquid fraction of the material in each node. If $\lambda = 1$, there is no effect on streaming processes. if $\lambda = 0$, the streaming processes is reduced to the usual free fluid LBM.

2.2.Numerical models based on multi-domain approach

2.2.1. A $2D^{1/2}$ model for natural convection and solidification in a narrow enclosure

$2D^{1/2}$ models for the simulation of natural convection and pure material solidification in a horizontal differentially heated slender cavity were presented by I. Hamzaoui et al. The configuration is based on the AFRODITE experimental setup, which is a reference solidification benchmark. The $2D^{1/2}$ models are obtained by averaging the equations of mass, momentum and heat conservation in the transverse z direction. The integration is performed on the assumption of a constant temperature along the z-axis, which seems realistic in such a confined cavity and for low values of the Prandtl number corresponding to liquid metals and metallic alloys. A well-defined velocity profile has also to be assumed. Two velocity profiles have been considered, the usual parabolic Poiseuille profile ($2D_P^{1/2}$ model) and the Hartmann-type profile featuring two boundary layers of adjustable size δ on the sides of a uniform bulk ($2D_H^{1/2}$model). The first assumption stating the uniformity of the temperature along the transverse z direction has been checked to be valid in a large range of the control parameters *Pr* (the Prandtl number) and *Gr* (the Grashof number). [71]

In this part, we are interested in cases of solid-liquid phase equilibrium. These cases are obtained when the hot wall of the crucible is at a constant temperature above the melting temperature and the cold wall at a constant temperature below the melting temperature. We will then have, in steady-state, coexistence of solid and liquid phases separated by a front whose shape and position are fixed. The relevance and reliability of the different *2D* models (*2D*, $2D_P^{1/2}$, and $2D_H^{1/2}$) to predict well the *3D* results, on the position and the shape of the solid-liquid fronts obtained, are examined.

The geometry corresponds to the crucible of the experimental device 'Afrodite' and present in Fig.II.10. the numerical simulations, this geometry is taken in its dimensional form. In the 3D models, the crucible is represented by a parallelepiped cavity with length L = 0.1m, height H = 0.06 m and depth W = 0.01 m. The side walls are adiabatic, while the left and right walls are at constant but different temperatures depending on the case considered. In the 2D models, the cavity is reduced to a rectangular cavity of length L = 0.1 m and height H = 0.06 m. The material chosen for the simulations is pure tin. Its melting temperature is Tm = 505 K. Two cases of phase equilibrium are reported. In the first one, named case (1), the temperature of the hot wall is T_h = 512 K and that of the cold wall is T_c = 502 K. In the second, named case (2), T_h = 507.5 K and T_c = 503.5K.

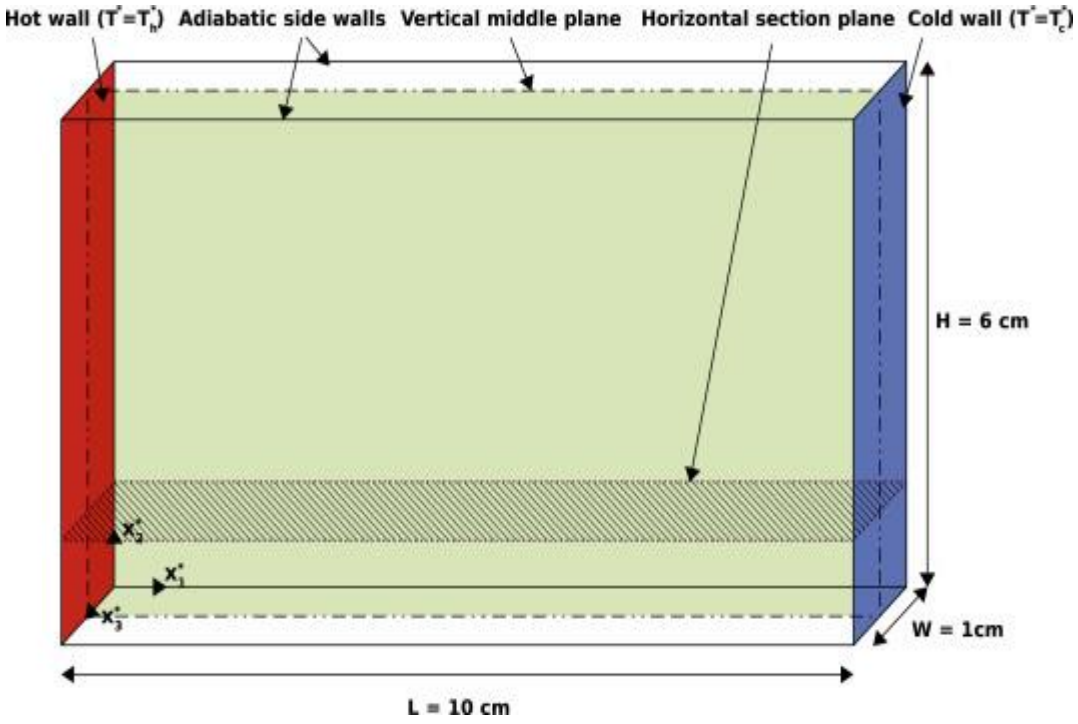

Fig.II. 10: *Geometrical configuration of the study: Differentially heated parallelepipedic cavity with left and right end walls held at constant temperatures T_h^* and T_c^*, respectively. The other walls are adiabatic. Characteristic planes are shown: the vertical middle plane (green plane) and a horizontal section plane (hatched plane) [71].*

The study of these cases with solid-liquid phase change requires the consideration of convective-diffusive heat exchange in the liquid phase and diffusive heat exchange in the solid phase. In the latter, only the heat equation is solved and it is summarized in the heat conduction equation:

$$\frac{\partial T^*}{\partial t} = \frac{\lambda_s}{\rho C_{p_s}} \nabla^{*2} T^* \quad \textbf{(II.100)}$$

In the liquid phase, the energy conservation equation is coupled to the conservation equations for momentum and mass. Based on the results of Assael *et al* [72] indicating a linear variation of the density over a wide range of temperature variation above the melting temperature T_m, the Boussinesq approximation is applied in the liquid domain to describe the variation of the density in the buoyancy term. The conservation equations in the liquid phase for the $2D^{1/2}$ models are as follows [71]:

- **The momentum equation conservation**

$$\frac{\partial \overline{u}_i^*}{\partial t} + \overline{u}^*.\nabla \overline{u}_i^* = -\frac{1}{\rho}\frac{\partial \overline{P}^*}{\partial x_i^*} + \nu \nabla^{*2} \overline{u}_i^* + g\beta_T(\overline{T}_l^* - T_m)\delta_{i,2} + S_i^* \text{ for } i = 1 and\ 2 \quad \textbf{(II.101)}$$

for the model $2D_H^{1/2}$

$$S_{H,i}^* = \left\{1 - F^2\left[\frac{3}{2} - \frac{1}{2}tanh^2\left(\frac{W}{2\delta^*}\right) - \frac{3\delta^*}{W}\tanh\left(\frac{W}{2\delta^*}\right)\right]\right\}\overline{u}^*.\nabla \overline{u}_i^* - F\left[\frac{2}{\delta^* W}tanh\left(\frac{W}{2\delta^*}\right)\right]\nu \overline{u}_i^* \quad \textbf{(II.102)}$$

With $F = \left[1 - \frac{2\delta^*}{W}tanh\left(\frac{W}{2\delta^*}\right)\right]^{-1}$ **(II.103)**

for the model $2D_p^{1/2}$

$$S_{P,i}^* = -\frac{1}{5}\overline{u}^*.\nabla \overline{u}_i^* - \frac{12}{W^2}\nu \overline{u}_i^* \quad \textbf{(II.104)}$$

- **The energy conservation equation**

$$\frac{\partial \overline{T}_l^*}{\partial t} + \overline{u}^*.\nabla \overline{T}_l^* = \frac{\lambda_l}{\rho C_{p_l}} \nabla^{*2} \overline{T}_l^* \quad \textbf{(II.105)}$$

- **The mass conservation equation**

$$\nabla^*.\overline{u}^* = 0 \quad \textbf{(II.106)}$$

The S_i^* term in Eq.II.101 refers to the source term of the $2D^{1/2}$ models but is expressed in its dimensional form. By removing it, we find the classical *2D* conservation equations and by letting the index *i* vary from 1 to 3 and by removing the bars on the velocity, pressure and

temperature variables (these bars mean that they are values averaged over the thickness of the cavity), we obtain the *3D* conservation equations.

The solid and liquid regions are separated by the solid-liquid phase change front. The energy balance on this front is expressed by the Stefan condition [73]:

$$\boldsymbol{\rho \Delta H_m v_m^* . n^* = (\phi_l^* - \phi_s^*) . n^*} \quad \textbf{(II.107)}$$

where ΔH_m is the latent heat of melting, v_m^* is the velocity of the solid-liquid front, ϕ_l^* and ϕ_s^* are the heat fluxes from the liquid and solid regions, respectively, and n^* is the normal vector to the phase change front.

This model is implemented with the COMSOL Multiphysics 5.2 software. In addition to the "Laminar Flow" and "Heat Transfer in Fluid" models used for the hydrodynamic and thermal resolutions, the "Deformed Geometry" model of the deformable mesh branch proposed by COMSOL is now used. This physics allows both the deformation of the mesh and the tracking of the solid-liquid front once the condition at the interface is well set. With this approach, the defined domain, corresponding to the chosen geometry, is divided into two regions, a liquid region and a solid region. Fig. II.11(a) shows the initial mesh used in the *2D* models. Two domains are distinguished, the liquid domain represented in red and the solid domain represented in blue. The proportions occupied by each of the domains within the cavity, and that in the two cases of phase equilibrium studied, are determined with the temperature diffusive solution. This solution is used as an initial condition for the temperature field. In the initial state, the solid-liquid interface separating the two subdomains is thus perfectly vertical (Fig. II. 11(a)). For case (2), at t = 0 s, this boundary is at x_1 = 0:07 m, because it corresponds to the isotherm $T = T_m$, which is the melting temperature [71].

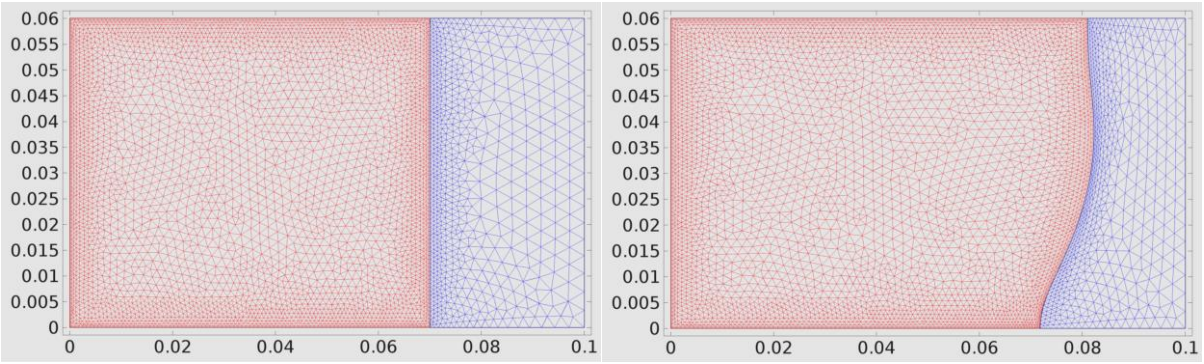

Fig.II.11: *2D mesh used for the study of phase equilibrium cases. The domain is divided into two regions, the liquid region (in red) and the solid region (in blue).* ***(a):*** *the mesh of the 2D models,* $2D_p^{1/2}$ *and* $2D_H^{1/2}$ *at the initial instant for case (1).* ***(b):*** *the stationery mesh obtained for case (1) with the 2D model [75].*

PARTIAL CONCLUSION

This bibliographic review of the different possible approaches to model the solid-liquid phase change of pure metals and metal alloy shows the variety of methods and models available, as well as the complexity of the numerous physical phenomena involved. This field of study remains vast (encompassing many aspects and multi-physical phenomena), topical (recent studies and projects are still dealing with this problem) and with at stake not only the understanding but also various and very competitive industrial applications. The need for efficient numerical tools, facilitating the resolution and the simulation of various processes, is present.

In the light of the above, it concluded that the numerical modelling can be done with two main approaches, different from each other, and which present, each, its own advantages but remain appropriate to a certain type of study. The first one is the multi-domain method, which allows the explicit tracking of the solid-liquid of the solid-liquid interface. It is suitable for the study of isothermal phase changes of pure bodies. It will therefore be used to simulate the solid-liquid phase change of pure tin within the benchmark 'Afrodite', [71]. The second method, the enthalpic method, allows the resolution of a unique system of equations over the whole studied domain (containing both solid and liquid phases), is better adapted to the study of phase changes non-isothermal phase changes with the mushy zone. It will be used to model the phase changes of the studied binary alloys. In this context, segregation models will be associated with it, with a certain number of hypotheses and assumptions that will be discussed on a case-by-case basis.

An important observation that was mentioned by Hachani *et al* [74] concerns the reproducibility of the solidification experiments. Indeed, a statistical study, concerning the solidification of 8 identical ingots of Sn-Pb alloy under the same experimental conditions, allowed us to conclude that, although the global results of the solidification are identical (in terms of global macrostructures), not lesser differences remain between the 8 ingots. Fluctuations of the temperature in the liquid bath at the end of the solidification as well as differences between the distributions of the segregated channels are observed.

In the following this work, chapters III and IV are devoted to the expression of two-phase model of the Sn-10wt.%Pb solidification under the effect of thermousolutal and forced convection based on enthalpy approach. These models are intended to be reliable tools, with a high ease/speed of resolution to lend themselves to parametric and/or statistical studies.

References

[1] Boussaa, R., 2014. Etude de l'influence de la convection naturelle lors de la solidificationdes métaux purs et des alliages métalliques binaires : expériences et simulations. PhD thesis, Université Claude Bernard Lyon 1.

[2] N. R. Eyres, D.R. Hartree, J. Ingham, R. Jackson, R.J Sarjant and J.B Wagstaff, Philosophical Trans. R. Soc. Lond. Ser. A, Math. Phys. Sci. 240 (1946) 1-57.

[3] M.E Rose, Math. Comput. 14 (1960) 249-256.

[4] V.R. Voller and C. Prakash, Int. J. Heat Mass. Transfer 30 (1987) 1709-1719.

[5] A. K. Haagen, E. Franquet, E. Pernot, and D. Brüggemann, Int. J. Thermal Sciences 118 (2017) 69-103.

[6] F. Rösler and D. Brüggemann, Heat Mass Transfer 47 (2011) 1027-1033.

[7] V. D. Fachinotti, A. Cardona and A. E. Huespe, Int. J. Num. Meth. Eng. 44 (1999) 1863-1884.

[8] V. Voller and C. Swaminathan, Numer, Heat Transf. Part B Fundam 19 (1991) 175-189.

[9] P. Lamberg, R. Lehtiniemi and A. M. Henell, , Int. J. Thermal Sciences 43 (2004) 277-287.

[10] E. Franquet, A. K. Haagen, and D. Brüggemann, invited talk, Coupled problems conference 2017, VII International Conference on Coupled Problems in Science and Engineering, Rhodes Island, Greece, 12-14 June 2017.

[11] A. D. Brent, V. R. Voller and K. J. Reid, Numerical Heat Transfer 13 (1988) 297-318.

[12] D. K. Gartling, Computer Methods in Fluids, K. Morgan, C. Taylor, and C. A. Brebbia, eds., Pentech, London, (1980) 257-284.

[13] M. H. Avnaim, A. Levy, B. Mikhailovich, O. Ben-David, and A. Azulay, J. Heat Transfer 138 (2016) 112301.

[14] R. R. Kasibhatla, A. König-Haagen and F. Rösler, Heat Mass Transfer 53 (2017) 1735-1744.

[15] K. Morgan, Comput. Meth. Appl. Mech. Eng. 28 (1981) 275-284.

[16] F.Wolf and R. Viskanta, Int. J. Heat Mass Transfer 31 (1988) 1735-1744.

[17] V. Tavernier, S. Millet, D. Henry, V.Botton, G. Boutet,and J.-P.Garandet, Int. J. Heat Mass Transfer 110 (2017) 209-218.

[18] R. Boussaa, L. Hachani, O. Budenkova, V. Botton, D. Henry, K. Zaidat, H. Ben Hadid, Y. Fautrelle, International Journal of Heat and Mass Transfer 100 (2016) 680-690.

[19] M. Ishii and N. Zuber: AIChE J., 1979, vol. 25, pp. 843-55.

[20] J. Ni and C. Beckermann: Metall. Trans.B, 1991, vol. 22B, pp. 349-61.

[21] A. Ludwig, M. Wu,Metall. Mater. Trans. A 33 (2002) 3673-3683.

[22] M. Wu, A. Ludwig, A. B¨uhrig-Polaczek, P.R. Sahm,Inter. J. Heat Mass Transfer 46 (2003) 2819-2832.

[23] M. Wu, A. Ludwig,Adv. Eng. Mater. 5 (2003) 62-66.

[24] M. Wu, A. Ludwig, J. Luo,Mater. Sci. Forum 475-479 (2005)2725-2730.

[25] M. Wu, A. Ludwig, L. Ratke,Model. Simul. Mater. Sci. Eng. 11 (2003)755-769.

[26] M. Wu, A. Ludwig, L. Ratke,Metall. Mater. Trans. A 34 (2003)3009-3019.

[27] A. Ludwig, M. Wu, M. Abodano, L. Ratke, Mater. Sci. Forum 508-509 (2006) 193-198.

[28] J.D. Hunt,Mater. Sci. Eng. 65 (1984) 75-83.

[29] C.Y. Wang, C. Beckermann,Metall. Mater. Trans. A 25 (1994) 1081-1093.

[30] M. Martorano, C. Beckermann, Ch.-A. Gandin, Metall. Mater. Trans. A34 (2003) 1657-1674.

[31] M. Wu, A. Ludwig, Materials Science and Engineering. A 413–414 (2005) 109-114.

[32] M. Wu, A. Ludwig, Metall. Mater. Trans. A 37A (2006) 1613-1631.

[33] W. Kurz, D.J. Fisher, Trans Tech Publications , Aedemannsdorf, Switzerland, 1989.

[34] J. Lipton, M.E. Glicksman, W. Kurz,Mater. Sci. Eng. 65 (1984) 57-63.

[35] J.P. Gu, C. Beckermann,Metall. Trans. A 30 (1999) 1357-1366.

[36] C. Y. Wang and C. Beckermann,Metall. Mater. Trans., 1993, 24A, 2787-2802.

[37] C. Y. Wang and C. Beckermann,Metall. Mater. Trans., 1996, 27A,2754-2764.

[38] M. Rappaz and Ph. The´voz, Acta Metall., 1987, 35, 1478-1497.

[39] M. Rappaz and Ph. The´voz, Acta Metall., 1987, 35, 2929-2933.

[40] M. Wu, A. Ludwig, International Journal of Cast Metals Research (2009) 1-4.

[41] M. Wu and A. Ludwig, Proc. 5th Decennial Intern. Conf. on Solidification Processing, July 23-25, 2007, Sheffield, UK. Ed. H.Jones., University of Sheffield, 130-135.

[42] J. Lipton, M. E. Glicksman and W. Kurz, Mater. Sci. Eng., 1984,65, 57-63.

[43] Ø. Nielsen, B. Appolaire, H. Combeau and A. Mo, Metall. Mater.Trans., 2001, 32A, 2049-2060.

[44] M. Wu and A. Ludwig: Metall. Mater. Trans., 2007, 38A, 1465-1475.

[45] W. Kurz and D. J. Fisher, Trans Tech Publications, Aedemannsdorf, Switzerland, 1989.

[46] W. Kurz, B. Giovanola and R. Trivedi, Acta Metall., 1986, 34, 823-834

[47] Alok Kumar, Miha Založnik, HervéCombeau, Gérard Lesoult, Arvind Kumar, International Journal of Heat and Mass Transfer 164 (2021) 120602.

[48] R. Mehrabian, M. Keane, M.C. Flemings, Metall. Mater. Trans. 1 (1970) 1209–1220, doi: 10. 10 07/BF0290 0233.

[49] S. Ganesan, D.R. Poirier,Metall. Trans. B. 21 (1990) 173–181, doi: 10.1007/BF02658128.

[50] C. Prakash, V. Voller, Numer. Heat Transf. Part B. 15 (1989) 171–189, doi: 10.1080/10407798908944899.

[51] W.D. Bennon, F.P. Incropera, Int. J. Heat Mass Transf. 30 (1987) 2161–2170, doi: 10.1016/ 0 017-9310(87)90 094-9.

[52] I. Vannier, H. Combeau, G. Lesoult, Mater. Sci. Eng. A. 173 (1993) 317–321, doi: 10.1016/0921- 5093(93)90236- 8.

[53] S. Chakraborty, P. Dutta, Int. J. Heat Mass Transf. 46 (2003) 2115–2134, doi: 10.1016/S0017- 9310(02)00530- 6.

[54] N. Ahmad, H. Combeau, J.-.L. Desbiolles, T. Jalanti, G. Lesoult, J. Rappaz, M. Rappaz, C. Stomp, Metall. Mater. Trans. A. 29 (1998) 617–630, doi: 10.1007/s11661-998- 0143- 9.

[55] A. Kumar, B. Dussoubs, M. Založnik, H. Combeau, J. Phys. D. Appl. Phys. 42 (2009) 105503, doi: 10.1088/0022-3727/42/10/105503.

[56] M. Kumar, M. Založnik, H. Combeau, B. Goyeau, D. Gobin, Model. Simul. Mater. Sci. Eng. 21 (2013) 045016, doi: 10.1088/0965-0393/21/4/ 045016.

[57] D.R. Poirier, Metall. Trans. B. 18 (1987) 245–255, doi: 10.1007/BF02658450.

[58] A.K. Singh, B. Basu, A. Ghosh, Metall. Mater. Trans. B Process Metall. Mater. Process. Sci. 37 (2006) 799–809, doi: 10.1007/s11663-006-0062-3.

[59] R. Nasser-Rafi, R. Deshmukh, D.R. Poirier, Metall. Trans. A. 16 (1985) 2263–2271, doi: 10.1007/BF02670426.

[60] B. Goyeau, T. Benihaddadene, D. Gobin, M. Quintard, Metall. Mater. Trans. B. 30 (1999) 613–622, doi: 10.1007/s11663- 999- 0022- 9.

[61] F.J. Alexander, S. Chen, J.D. Sterling, Phys. Rev. E 47 (1993) R2249.

[62] X. He, S. Chen, G.D. Doolen, , J. Comput. Phys. 146 (1998) 282-300.

[63] M. Jami, A. Mezrhab, M. Bouzidi, P. Lallemand, Physica A: Statist. Mech. Appl. 368 (2) (2006) 481-494.

[64] F.J. Higuera, J. Jimenez, Europhys. Lett. 9 (7) (1989) 663-668.

[65] F.J. Higuera, S. Succi, R. Benzi, Europhys. Lett. 9 (1989) 345-349.

[66] S. Hou, Q. Zou, S. Chen, G. Doolen, A.C. Cogley, J. Comput. Phys. 118 (1995) 329-347.

[67] B.I. Pavel, A.A. Mohamad, in: R. Bennacer, M. El Ganaoui, A.A. Mohamad, J. Sicard (Eds.), Progress in Computational Heat and Mass Transfer, vol. I, Lavoisier-Tec & Doc., 2006, pp. 411-416.

[68] M. El Ganaoui, A. Lamazouade, P. Bontoux, D. Morvan, Int. J. Comput. Fluids 31 (4–7) (2002) 539–556.

[69] E. Semma, Thèse de doctorat Franco-Marocaine, Université de la Méditerranée/Université Mohamed V, 2004.

[70] J. Kaenton, E. Semma, V. Timchenko, M. El Ganaoui, E. Leonardi, G. de Vahl Davis, Int. J. Heat Mass Transfer 47 (2004) 3403–3413.

[71] I. Hamzaoui, S. Millet, V. Botton, A. Benzaoui, D. Henry, L. Hachani, R. Boussaa, K. Zaidat, Y. Fautrelle, , 140 (290) 167-193.

[72] M. J. Assael, A. E. Kalyva, K. D. Antoniadis, R. M. Banish, I. Egry, J.Wu, E. Kaschnitz, and W. A.Wakeham, J. Phys. Chem. Reference Data 39 (2010) 033105.

[73] F.Wolf and R. Viskanta, Int. J. Heat Mass Transfer 31 (1988) 1735-1744

[74] L. Hachani, K. Zaidat, Y. Fautrelle, International Journal of Thermal Sciences, 110 (2016) 186-205.

[75] I. Hamzaoui, Thèse de Mécanique des Fluides, L'UNIVERSITE DE LYON, 2019.

CHAPTER III

Numerical Simulation of Metallic Alloy Solidification Under Thermosolutal Convection

This chapter is mainly inspired from my paper [1], published in "Journal of Heat Transfer (ASME)", which is based on the description of fully 3D enthalpy approach that applied on the solidification of binary metallic alloy under the effect of thermosolutal convection. A three-phases columnar solidification model that takes into account the growth of columnar grains, their motions and the formation of macrosegregation, will be detailed. Special attention is given to the treatment of remelting phenomenon and consequently segregation mechanism is considered.

1. Introduction

The both experimental and numerical studies presented in this chapter are derived from a solidification benchmark experiment called "AFRODITE" performed at the SIMAP Laboratory in Grenoble, France. The main goal of this devise is to investigate the formation of as-cast structure and macro- and mesosegregation, as presented in the works of Hachani et *al.*, [28]. The AFRODITE configuration is mainly inspired from the previous work of Hebditch and Hunt [2], which studied the effect of thermosolutal convection on the solidification process. In this work, by promoting the directional horizontal solidification of lead-tin and tin-zinc alloys (that is, perpendicular to the gravity vector), a significant mesoscopic and macrosegregation were observed. The experiment setup was designed as quasi-2D and has been considered as a reference for many numerical studies, including benchmark problems [3,4] and studies of the effect of microsegregation modelling [5], local growth kinetics [6-9], shrinkage-induced segregation [5, 7] and three-dimensional effects [9-12]. The prediction of segregations, particularly at the macro scale, has shown a strong sensitivity to several factors, the most relevant is the permeability modelling, through the effect of the general permeability level [11], anisotropy [5], fluid inertia (Forchheimer correction term) [13] and numerical discretization [14]. Although the Hebditch and Hunt experiment has proven to be a useful reference, true quantitative comparisons with numerical simulations are hampered by uncertainties in heat transfer modelling. In an effort to address these problems, the SIMAP/EPM laboratory developed AFRODITE benchmark experiment, which considered as a new experimental design that allows for precise control of the cooling rate and horizontal temperature gradient through closed-loop control and detailed measurements, [15]. The AFRODITE setup can be also considered as a reference experiment that represents a key tool for the validation of numerical models in comparison with detailed quantitative and qualitative measurements obtained with

fully controlled initial and thermal boundary conditions and post-mortem analysis, [16]. The redesign has revealed the effects of cooling rate and horizontal temperature gradient on microstructure, macro, and mesosegregation, [17, 18].

This chapter will be focused on the study of the effect of thermosolutal convection on the solidification processes of Sn-10*wt*.%Pb alloy using a numerical model describing the coupled heat, mass and momentum transport phenomena based on a volume-averaged approach. In particular, we demonstrate that such model can predict the solute stratification in the liquid phase during the solidification process. This stratification is obtained by considering the direction of the flow with regard to the thermal gradient in the mushy zone. The numerical model is applied only to simulate the solidification processes, and is validated by in-situ measurements of thermal fields and post-mortem analysis. The second objective is to evaluate the main factors that have a direct effect on segregation phenomenon, namely the macrosegregation corresponding to the last liquid solidified and channels segregation (or freckles) which developed during the solidification process.

2. AFRODITE setup

The AFRODITE benchmark experiment, performed in the SIMAP/EPM laboratory and described elsewhere [19-21], is a key tool for the validation of numerical models by comparing with detailed measurements obtained with thoroughly controlled initial and thermal boundary conditions. In its principle, the experiment is similar to the well-known Hebditch and Hunt experiment [2], with a special emphasis on obtaining reproducible quantitative measurements. The Sn-Pb binary alloy pre-sample is enclosed in a parallelipedic cavity of 100 mm in length, 60 mm in height and 10 mm in width. The sketch of the experiment is shown in Fig. III.1. All walls except for two narrow vertical ones are held at approximately insulating conditions during the whole process via a Kirchhoff box. The alloy is solidified by two temperature controllable heat exchangers, shown in Fig. III.1.

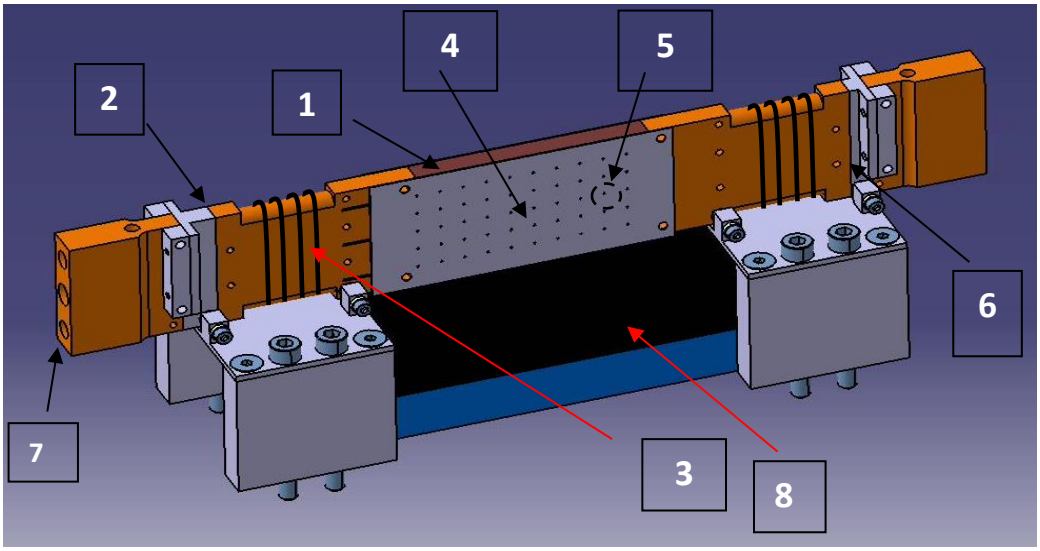

(a)

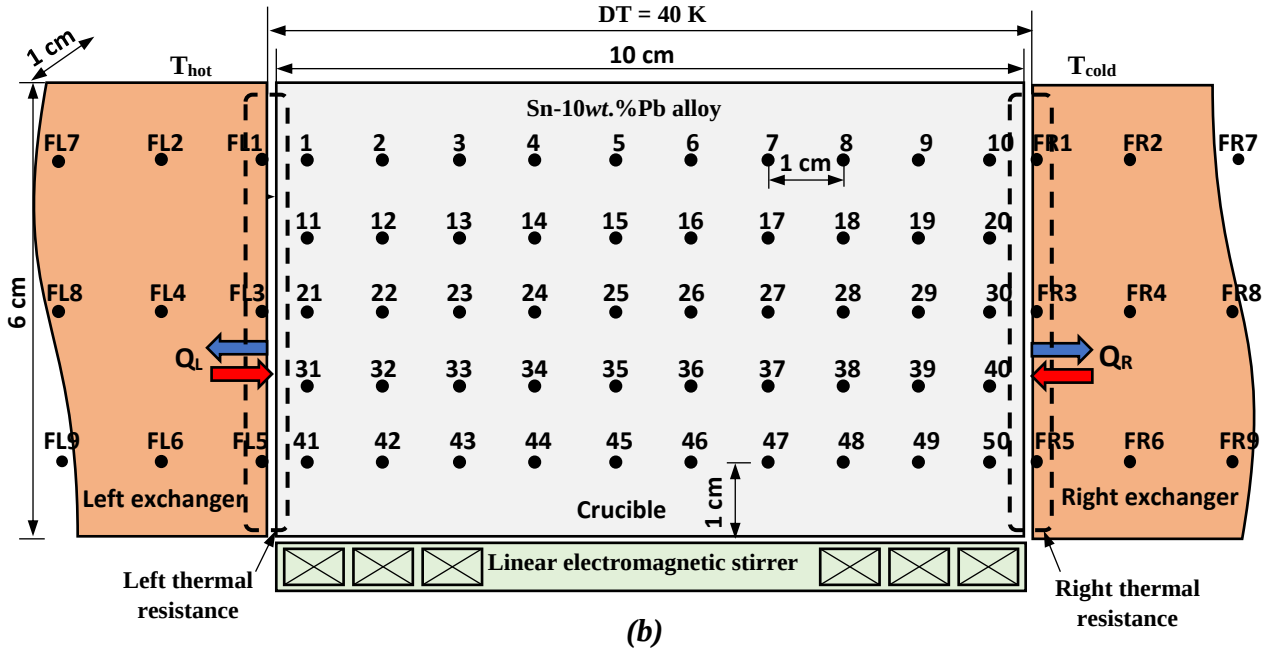

(b)

Fig.III.1 **:** *(a) Schematic view of the experimental facility. 1. Sn-Pb sample, 2. Left "cold" heat exchanger, 3. Resistance, 4. Stainless steel crucible, 5. Thermocouple position matrix, 6. Right "hot" heat exchanger, 7. Water cooling system, 8. Linear motor. (b) Sketch of the sample surrounded by the two lateral heat exchangers and the location of the lateral thermocouple lattice (L1 to L50) welded on one of the largest surfaces of the crucible. Contact resistances between the two heat exchangers (left and right) and the solidifying volume indicated by dashed black line rectangles, is also shown.*

An array of fifty K-type thermocouples, placed on the largest surfaces of the stainless-steel crucible, is used to record the temperature field, and therefore the evolution of solidification. A linear stirrer is placed beneath the sample in order to homogenize the sample after the melting

process prior to the beginning of solidification. The procedure of the experiments includes 5 separate stages, illustrated in Fig. III.2:

Stage 1. *Melting*: The sample is melted by applying a constant heating rate (0.03 K/s) to the left and the right heat exchangers.

Stage 2. *First holding stage*: The two heat exchangers are maintained at the same constant temperature (T = 260 °C), to produce a homogeneous temperature field.

Stage 3. *Setting a mean horizontal temperature difference*: A mean horizontal temperature gradient is created by setting a temperature difference between the left and the right heat exchanger.

Stage 4. *Second holding stage*: The two heat exchangers are maintained at constant temperature with applied DT (i.e., Tleft = 280 °C and Tright = 240 °C).

Stage 5. *Solidification*: A constant cooling rate of -0.03 K/s is applied on the two heat exchangers while maintaining the horizontal temperature difference from stage 4.

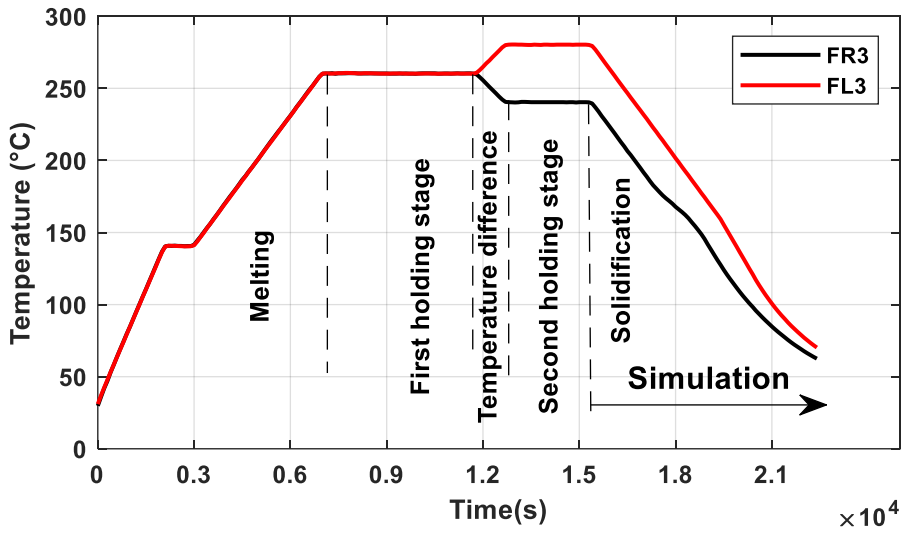

Fig.III. 2 **:** *Time evolution of measured temperature during solidification of thermocouples FR3 and FL3 placed in the contact interfaces between the two heat exchangers right and left, respectively*

3. Model Description and Numerical Details

3.1. Geometric configuration

The geometrical configuration considered in this study is presented in Fig. III.3. It is a differentially heated parallelepiped cavity. The dimensions are chosen to correspond to the crucible of the experimental benchmark 'Afrodite'. where L is the length along the x direction (L = 100 mm), H is the height along the y direction (H = 60 mm) and W is the width along the z direction (W = 10 mm). The top, bottom, and side walls are considered as adiabatic faces, while the two vertical end walls at x = 0 cm and x = 10 cm are at imposed temperatures (Dirichlet boundary conditions) . The end wall on the left is at a hot temperature T_h and the end wall on the right is at a cold temperature T_c, that varying over time.

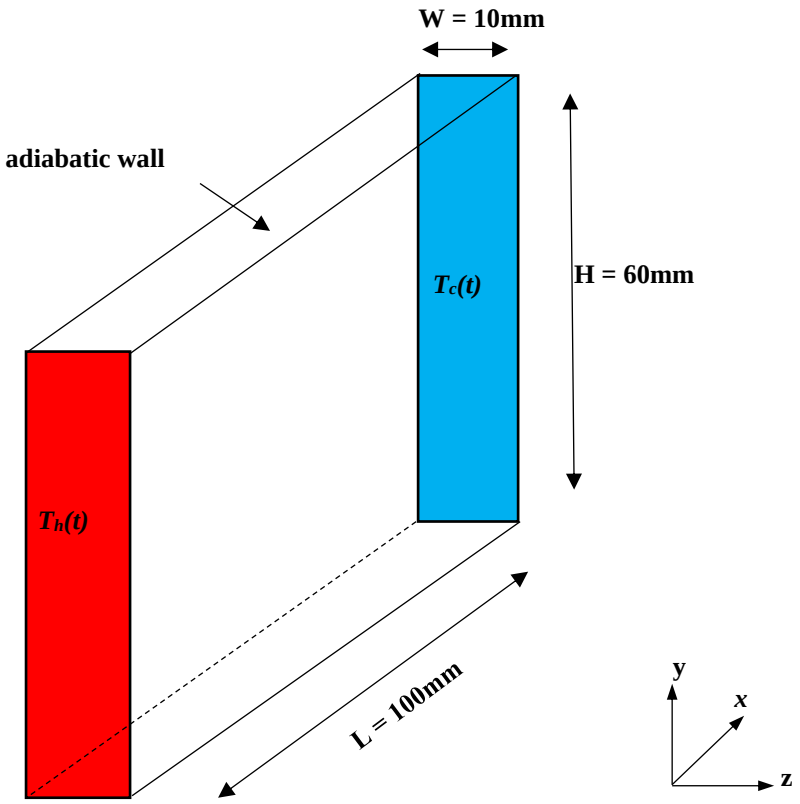

Fig.III.3*: *Geometrical configuration of the study: Differentially heated parallelepipedic cavity with left and right end walls held at variant temperatures Th(t) and Tc(t), respectively.

3.2.Mesh

In order to capture all the process details in terms of flow configuration, heat and mass transfer, namely solute transport and meso and macro segregation, it is important to choose an adequate

mesh that will be adapted to the problems considered. Indeed, creating a high-quality mesh is one of the most critical factors that must be considered to ensure simulation accuracy. While increasing the fineness will typically yield a higher quality mesh, the computational cost will significantly increase as well. A high-quality mesh also means that there is an optimal balance between the computational cost and the level of fineness achieved. A low-quality mesh will not only result in inaccurate simulation results but might even cause the solver to produce an error due to instability. Such instability is typically caused by poor-quality or illegal cells. Actually, it important to stress a specific and rigorous study on the mesh sensitivity to predict segregated channels, which is highly sensitive to the mesh size. Indeed, the columnar numerical model cannot be accurate enough to reflect the actual physics of the entire phenomenon. Unfortunately, due to the very long computation time required, it has not been able to investigate this effect in 3D computation. For the same reason, the variability of the numerical solution for various other computation approaches has not been tested, in particular the anisotropic mushy zone permeability model and grid size sensitivity. However, numerous mesh refinements were used to examine the accuracy of the model implemented and the minimal refinement to ensure the convergence of solution, was used. Moreover, the applied numerical approach treats hydrodynamic motion in the liquid phase and columnar grains whose growth is taken into account and a double time step scheme to accelerate solution, was used. Thus, in this study, we have chosen a uniform structured mesh at the level of the walls presented in Fig.III.4, with quadrilateral form contains 48×10^4 cells and 510741 nodes

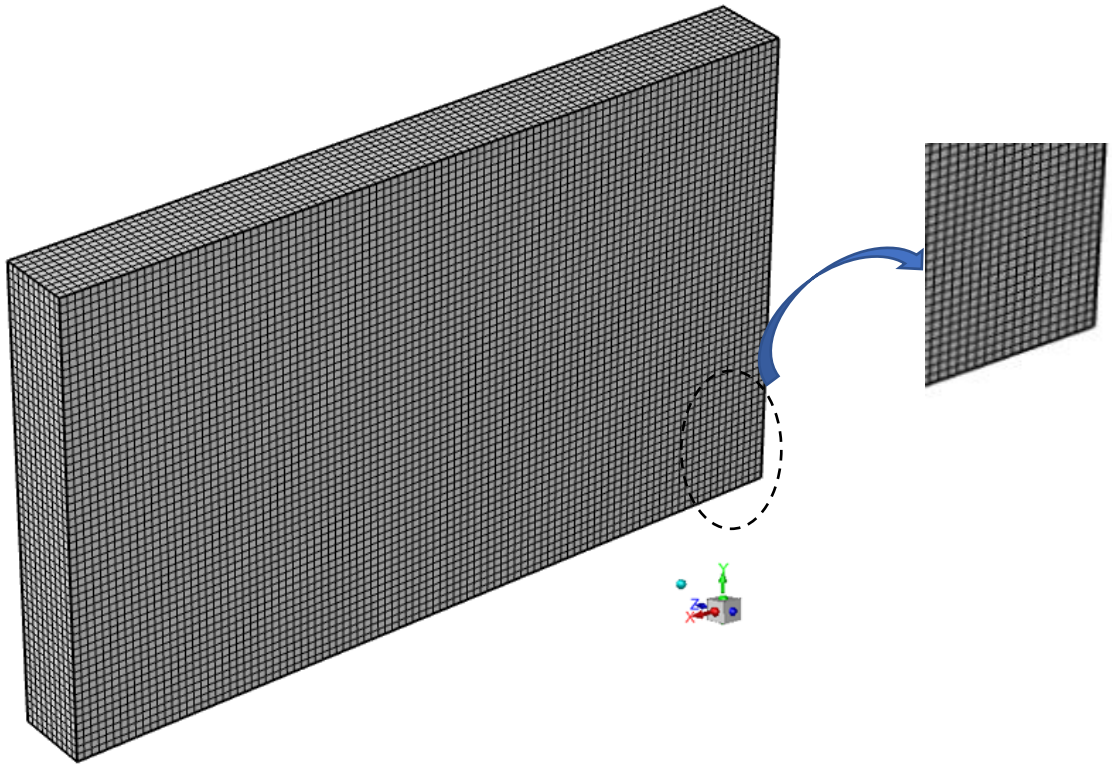

Fig.III.4*: *Schematic of the mesh used (48×10^4 cells, 510741 nodes)

3.3.Simplifying assumptions

The formulation of this problem is based on a number of simplifying assumptions. These assumptions are related to the geometry, the type of flow, the transfer mechanisms and the phase change problems. In the case considered, we have adopted the following assumptions:

- The liquid is assumed to be Newtonian and incompressible.
- Heat transfer by radiation is assumed to be negligible (Kirchhoff box).
- Shrinkage or volume variations due to the phase change are negligible.
- Columnar dendritic solidification (*no equiaxed grain growth*)
- mushy zone equivalent to an isotropic porous medium of permeability defined by the Carman-Kozeny relation

3.4. Equations system

The simulation of the previously presented solidification process requires the resolution of a system comprising both the conservation equations of the desired quantities and the consideration of the segregation phenomena induced by solute transport during the phase change and predicted by the phase diagram. The resolution is restricted here for the variables

sought at a macroscopic scale. This model assumes only the columnar dendritic growth, i.e., the appearance and growth of equiaxed grains are therefore not considered, although experimentally these growth structures can appear in solidified ingots. This system includes the conservation equations involving the modelling of the physical phenomena. The mass, heat and solute conservation equations are averaged over both liquid and solid phases, while the momentum conservation equations are averaged only in the liquid phase. For this purpose, conservation equations for three physical properties (mass, heat and solute) plus the Navier-Stokes average for the momentum equation are available. However, three more scalar relationships are necessary, those between $\langle H \rangle$ and (T, C_s), $\langle C \rangle$ and (C_l, f_s), and T and C_l, more particularly in the mushy zone (i.e., $0 \leq f_s \leq 1$).

The principal first relationship can be written as:

$$\langle \boldsymbol{H} \rangle = \boldsymbol{f_s H_s} + (\mathbf{1} - \boldsymbol{f_s})\boldsymbol{H_l} \ \boldsymbol{with} \begin{cases} \boldsymbol{H_l = Cp_l T + L} \\ \boldsymbol{H_s = Cp_s T} \end{cases} \quad \textbf{(III.1)}$$

Where f_s is the solid fraction, Cp_s and Cp_l are the volumetric specific heat of solid and liquid phases, respectively and L is the volumetric latent heat. The necessary physical properties for the calculation are reported in Table (1).

Assuming that the simple level rule approach applies at the microscopic scale of the Dendrite Arm Spacing (DAS) illustrated in the second chapter, based on the case of full local thermodynamic equilibrium, the second relationship can be written as:

$$\langle \boldsymbol{C} \rangle = \boldsymbol{f_s C_s} + (\mathbf{1} - \boldsymbol{f_s})\boldsymbol{C_l} = \boldsymbol{C_l}[\mathbf{1} - \boldsymbol{f_s}(\mathbf{1} - \boldsymbol{k})] \quad \textbf{(III.2)}$$

The concentrations in the liquid phase and the solid phase in the mushy zone are given using the rule of levers which assumes that there is a thermodynamic and chemical equilibrium between the two phases with instantaneous diffusion of the solute in them. This means that ($C_s = kC_l$), where k is the partition coefficient. This parameter is given by the phase diagram which is assumed constant in our calculation (k = 0.0656). In addition, it is assumed that the concentration in the liquid is related to temperature via the linearization of the phase diagram. Thanks to this approach, we can define a constant slope "m", thus given in the mushy zone, above the eutectic temperature

$$\boldsymbol{T = T_f + mC_l} \quad \textbf{(III.3)}$$

Where T_f is the melting temperature of pure solvent (Sn).

It is assumed that the volumetric mass of the Sn-10*wt*.%Pb alloy is constant in the solid phase and the liquid phase, except for the buoyancy term of the Navier-Stokes equation with respect to the Boussinesq approach. Based on these appropriate assumptions, the volumetric mass of the liquid phase can be expressed as:

$$\boldsymbol{\rho = \rho_0[1 - \beta_T(T - T_0) + \beta_C(C_l - C_0)]} \quad \textbf{(III.4)}$$

Where ρ_0 and C_0 are the referential density and initial mass concentration of the alloy, respectively. β_T and β_C are the thermal and solutal expansion coefficients obtained by polynomial fitting, as follows:

$$\boldsymbol{\beta_T = \frac{1}{\rho_0}(0.742841 + 5.8927 \times 10^{-3} C_l)} \quad \textbf{(III.5)}$$

$$\boldsymbol{\beta_C = -\frac{1}{\rho_o}(47.6554 - 2 \times 0.10063 \times C_l - 5.8927 \times 10^{-3} T)} \quad \textbf{(III.6)}$$

The liquid viscosity is taken from H. Thresh and A. Crawley, [23] and shown in Eq. III.7, where the constants *A* and *B* have been fitted also with a polynomial expression.

$$\boldsymbol{\mu_l(C_l[wt.\%], T[K]) = A(C_l)\rho_0^{1/3}\, exp\left(\frac{B(C_l)\rho_0}{T}\right)} \quad \textbf{(III.7)}$$

With:

$$\begin{cases} A(C_l[wt.\%]) = 2750 \times 10^{-4} - 2934 \times 10^{-6} C_l + 1.212 \times 10^{-7} C_l^2 - 1.56 \times 10^{-9} C_l^3 \\ B(C_l[wt.\%]) = 8849 + 0.9411 C_l - 4.193 \times 10^{-2} C_l^2 - 5.3 \times 10^{-4} C_l^3 \end{cases}$$

The thermal conductivities of the solid and liquid phases are taken from V.P. Osipenko, [24] and have been fitted with the polynomial expressions given in Eq. III.8 and 9 . The diffusion coefficient for Pb in the liquid is taken from R.A. Khairulin et *al.* [22] and is shown in Eq. III.10, while the solid diffusion coefficient is assumed constant and given in Table 1.

$$\boldsymbol{\lambda_l(C_l[wt.\%]) = 25 + 0.02T - 0.35C_l + 0.002C_l^2} \quad \textbf{(III.8)}$$

$$\boldsymbol{\lambda_s(C_l[wt.\%]) = 64.74 - 0.016T - 0.543C_s + 0.0023C_s^2} \quad \textbf{(III.9)}$$

$$\boldsymbol{D_l(T[K]) = 1.4 \times 10^{-7}\, exp\left(-\frac{2.29 \times 10^4}{RT}\right)} \quad \textbf{(III.10)}$$

3.4.1. Mass and momentum conservation equations:

This part models the hydrodynamic aspect occurring during solidification. It includes the consideration of the buoyancy force terms. Indeed, the liquid part is subject to the thermo-subjective convection induced by the variations of the density of the liquid phase ρ_l. These density variations can be caused by the thermal expansion of the liquid as a function of its temperature (ΔT) or by the change in its alloying element composition (ΔC). Since lead has a higher density than tin, variations in lead concentration within the liquid phase cause variations in density. This hydrodynamic modelling also includes a braking term from the solid phase which has assumed zero velocities. This braking term also exists in the mushy zone assimilated to an isotropic porous medium. The equations of conservation are:

- Mass conservation equation:

$$\boldsymbol{div\, V = div\,(f_l V_l) = 0 \quad with \quad f_l = (1 - f_s)} \qquad \textbf{(III.11)}$$

- Momentum conservation equation for the liquid phase

$$\boldsymbol{\rho_0 \left[\frac{\partial (f_l V_l)}{\partial t} + (f_l V_l . grad) V_l\right] - \nabla . (\mu_l . \nabla . f_l V_l) + f_l^2 \frac{\mu}{K} V_l =}$$
$$\boldsymbol{\rho_0 [1 - \beta_T (T - T_0) + \beta_C (C_l - C_0)] f_l g - f_l grad(p)} \qquad \textbf{(III.12)}$$

Where K is the permeability of the mushy zone which is approximated by the well-known Carman-Kozeny relationship, based on the basic isotropic assumption that the specific surface of the solid is equal to that of uniform spheres whose diameters are equal to the secondary dendrite arm spacing (λ_2).

$$\boldsymbol{K = \frac{f_l^3}{(1 - f_l)^2} \frac{\lambda_2^2}{180}} \qquad \textbf{(III.13)}$$

3.4.2. Heat conservation equation

The modelling of convective-diffusive heat transfers occurring within the domain, as well as the rejection of latent heat during phase change, is done via the energy conservation equation. In this model, an enthalpic approach is used. It allows the resolution of a single equation describing the variation of the temperature variable T over the entire domain comprising the two liquid and solid phases. The interfaces separating the solid and liquid phases are not followed. The local state of the material is described by the value of the liquid fraction f_l and

solid fraction f_s. As the density is assumed to be invariant between the solid and liquid states, no distinction is made between the mass fractions and volume fractions. They are equal and noted f_l for the liquid and f_s for the solid. The energy conservation equation is expressed as follows:

$$\frac{\partial \langle H \rangle}{\partial t} + (f_l Cp_l) f_l V_l . grad(T) = (f_l \lambda_l + f_s \lambda_s) div[grad(T)] \quad \textbf{(III.14)}$$

3.4.3. Solute conservation equation

The solute conservation equation is expressed in terms of the averaged concentration which define in Eq.III.2, and is written as follows:

$$\frac{\partial \langle C \rangle}{\partial t} + f_l V_l . grad(C_l) = 0 \quad \textbf{(III.15)}$$

It is important to note that the solutal diffusion term has been omitted because it is negligible compared with the solutal transport.

Table. III-1. Thermophysical data and parameters used in the calculation

	Unit	**Sn-10*wt*.%Pb**
Phase diagram data		
Initial concentration, C_0	wt pct	10
Melting temperature, T_f	K	505
Liquidus temperature, T_{Liq}	K	492
Eutectic temperature, T_E	K	456
Liquidus slope, m	K.wt pct^{-1}	-1.286
Distribution coefficient, k	----	0.0656
Eutectic mass fraction, C_E	wt pc	38.1
Thermal data		
Specific heat, Cp_s, Cp_l	J.kg^{-1}.K^{-1}	209, 243
Thermal conductivity, λ_s (373 K), λ_l (513 K)	W.m^{-1}.K^{-1}	63, 30
Latent heat, L	J.kg^{-1}	6.1×10^3
Other Characteristics		
Reference volumetric mass, ρ_0	Kg.m^{-3}	7×10^3

Thermal expansion coefficient, β_T	K^{-1}	$\approx 6.6\times10^{-5}$
Solutal expansion coefficient, β_C	wt pct^{-1}	$\approx -4.2\times10^{-4}$
Dynamic viscosity, μ	$kg.m^{-1}.s^{-1}$	1×10^{-3}
Primary dendrite arm spacing, $\boldsymbol{\lambda_1}$	µm	$\approx 3.75\times10^{-4}$
Secondary dendrite arm spacing, $\boldsymbol{\lambda_2}$	µm	$\approx 1\times10^{-4}$
Calculation parameters		
Physical time, t	s	3×10^{3}
Time step, Δt	s	5×10^{-3}
Grid size, $N_x\times N_y\times N_z$	cells	48×10^{4}

3.5.The implementation of the mathematical model in ANSYS/FLUENT

The formulation of the two-phase equations proposed by Fluent is very similar to the formulation of the system equations. Thus, the mass conservation and momentum equations for the solid and fluid phase can be entered directly into Fluent. On the other hand, it is necessary to specify in Fluent, through the User Defined Functions (*UDF*), the sources and the corresponding transfer coefficients: the mass sources Γ, the momentum equations transfer coefficients at the interface and the transfer coefficients of momentum equations at the interface K_f and the electromagnetic ($F_{e.m}$) or gravity volume forces. As for the energy and solute conservation equations, these are introduced in Fluent using the scalar transport equations. Indeed, in Fluent we have the possibility to define, in addition to the classical transport equations (mass, momentum equations), additional scalar transport equations (the "User Defined Scalars"). The general form of a scalar equation is the following:

$$\frac{\partial(m\psi)}{\partial t} + \boldsymbol{div}(\boldsymbol{\varphi\psi}) = \boldsymbol{div}(\boldsymbol{D^*\nabla\psi}) + \boldsymbol{S} \qquad \textbf{(III.16)}$$

Where ψ represents the transported physical field, m the accumulation term, φ the mass flux, D^* the diffusivity and *S* the possible sources. We note that *m*, φ, D^* and *S* are parameters to be defined by the user. These can be easily particularized using user defined functions. Thus, the energy equation, the solute conservation equations in solid and fluid can be easily implemented in Fluent by articulating ψ, *m*, φ, D_k^* and k S as follows:

	ψ	m	φ	D^*	S
The energy equation	T	$\rho_s f_s cp_s + \rho_l f_l cp_l$	$\rho_s f_s cp_s v_s + \rho_l f_l cp_l v_l$	$f_s\lambda_s + f_l\lambda_l$	$L\Gamma_s$
The solute conservation equation in solid	C_s	$\rho_s f_s$	0	$f_s\rho_s D_s$	$C_s^*\Gamma_s$
the solute conservation equation in the fluid	C_l	$\rho_l f_l$	$\rho_l f_l v_l$	$f_l\rho_l D_l$	$-C_s^*\Gamma_s$

3.6.The resolution algorithm

We remind that the discretization method is the finite volume method. Thus, all the partial differential equations of the model are solved by integrating them on the cells of the discretization domain. The spatial discretization method used is the 2nd order UPWIND method with a fully implicit treatment. The temporal discretization is the implicit first order Euler discretization. The system of equations is solved according to a segregated algorithm which means that all equations are solved in a sequential and iterative manner.

4. Results and discussion

In this part, we will compare the numerical simulation results with those of experiment obtained with the AFRODITE setup on the solidification of Sn-10wt.%Pb alloy.

It should be underlined that in the experiment temperature distribution as well as cooling rate during solidification are programmed and controlled via temperature measurements at the heat exchangers. As discussed elsewhere [30], a contact resistance may exist between the wall and the sample and be dependent on the wettability of the walls by melt, on motion of liquid and on distribution of liquid fraction in the volume because of shrinkage during solidification. That means that actual temperature difference across the bulk should be smaller compared to that imposed on the heat exchangers and vary with transition from liquid to solid state. Furthermore, the lateral cooling rate in the experiment can deviate from programmed one if intense solidification accompanied by a large amount of heat release occurs or if the water cooling is not sufficient. To take these effects into account, temperature at the inner side of the lateral walls is recalculated using temperature measurement made by the thermocouples placed on the

heat exchangers and those on the frontal side of the cavity near their lateral sides. According to the scheme in Fig. (III.1-b), if convective heat transfer is neglected near the lateral wall, the heat flux should conserve along the horizontal axis x.

Indeed, the boundary temperatures are extrapolated using in-situ measurements of each series of the three thermocouples at the same height; (L_{01}, L_{21}, L_{41}). in left side and (L_{10}, L_{30}, L_{50}) in the right side. Accordioning to the scheme presented in Fig. III.1, these conditions can be written as:

$$\boldsymbol{\lambda_{Sn-Pb}.S.\frac{\left(3T_{Ext-Left}(t)-(L_{01}(t)+L_{21}(t)+L_{41}(t)\right)}{3e}=\emptyset_L(t)} \quad \textbf{(III.17)}$$

$$\boldsymbol{\lambda_{Sn-Pb}.S.\frac{\left(L_{10}(t)+L_{30}(t)+L_{50}(t)-3T_{Ext-Right}(t)\right)}{3e}=\emptyset_R(t)} \quad \textbf{(III.18)}$$

With:

$$\boldsymbol{\phi_R(t)=\frac{\lambda_{Cu}.s}{h_\xi}(-\frac{FR1(t)}{2}+\frac{2}{3}FR2(t)-2FR3(t)+\frac{8}{3}FR4(t)-\frac{1}{2}FR5(t)+\frac{2}{3}FR6(t)-\frac{1}{6}FR7(t)-\frac{2}{3}FR8(t)-\frac{1}{6}FR9(t))} \quad \textbf{(III.19)}$$

$$\boldsymbol{\phi_L(t)=\frac{\lambda_{Cu}.s}{h_\xi}(\frac{FL1(t)}{2}-\frac{2}{3}FL2(t)+2FL3(t)-\frac{8}{3}FL4(t)+\frac{1}{2}FL5(t)-\frac{2}{3}FL6(t)+\frac{1}{6}FL7(t)+\frac{2}{3}FL8(t)+\frac{1}{6}FL9(t))} \quad \textbf{(III.20)}$$

Where λ_{Sn-Pb}, λ_{Cu} are the thermal conductivities of the Sn-10*wt*.%Pb alloy and the copper, respectively. *S* the heat exchange surface ($S = 6.10^{-4}m^2$) and h_ξ is the step calculation in the horizontal direction ($h_\xi = 15mm$). "*e = 5 mm*", is the horizontal distance between the thermocouples L_{21} and $T_{Ext\text{-}Left}$ in the left side and between the thermocouples L_{30} and $T_{Ext\text{-}Right}$ in the right side. (FL1, FL2, ...FL9) and (FR1, FR2, ..., FR9), are the thermocouples of the left and right exchanger, respectively, (see Fig. III.1).

The extrapolated boundary temperature profiles ($T_{Num\text{-}Right}$, $T_{Num\text{-}Left}$), are presented in Fig III.5. Thus, these extrapolated temperatures are used as a uniform Dirichlet boundary condition at the thermal boundary of our calculation domain.

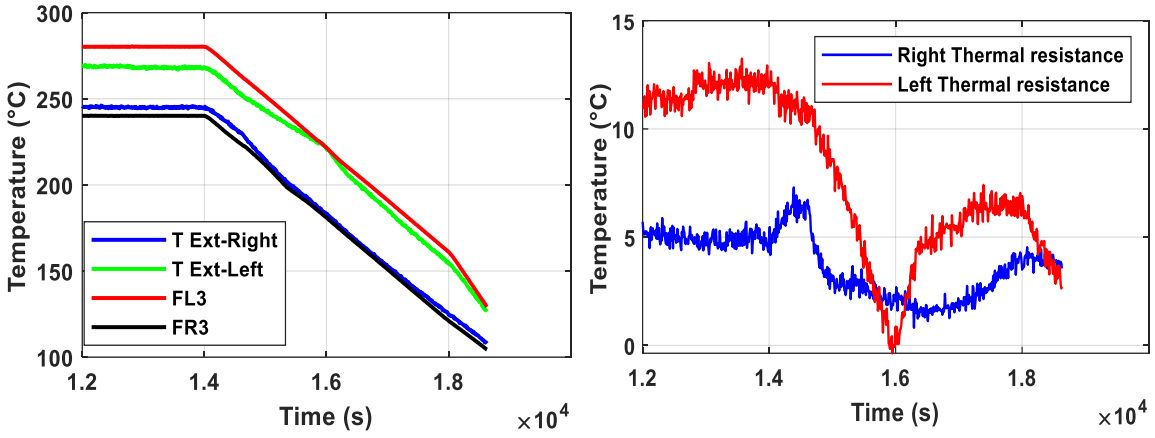

(a) ***(b)***

Fig.III. 5**:** *(a) Extrapolated boundary temperature profiles during the solidification of Sn-10wt.%pb alloy. The figure also shows the time profile of right (FR3) and left (FL3) exchangers (see Fig.1). (b) Profiles of thermal contact resistances from the second thermal holding stage to end of solidification.*

4.1.Temperature profile comparison between experiment and simulation

In our comparative study, the experimental time 15500 s is taken as the initial time (t = 0 s) for the numerical simulation, i.e., at the application of the cooling rate (solidification step). The initial "Pb" concentration is set as uniform and equal to 10 *wt.*%.

Fig.III.6 shows the measured and numerical temperature fields at three different times during the solidification stage's total period. The corresponding numerical values of the instantaneous temperature field are given in Appendix (A). The numerical results appear on the left side, while the experimental measurement results appear on the right side. In both cases, the temperature maps are recorded at the lateral wall of the crucible (z = 0), which carries all the acquisition thermocouples.

The first snapshots (Fig.III.6 (a) at t = 1820 s) correspond to a completely liquid sample. Due to the horizontal temperature gradient between the two vertical walls, a buoyancy force is generated and acts in the cavity. The melt flows upward near the hotter vertical side and downward near the colder vertical side, creating a convective loop (vortex) that is disseminated across the cavity and forms a positive temperature gradient in the upward direction. It should be underlined that, despite the low value of the Prandtl number ($Pr = 7\times10^{-3}$), The temperature fields obtained from numerical simulations and experimental measurements show clearly that

the flow strength is sufficient to distort the isotherm, with a maximum velocity obtained by simulation of v_{max} = 1.12 cm/s.

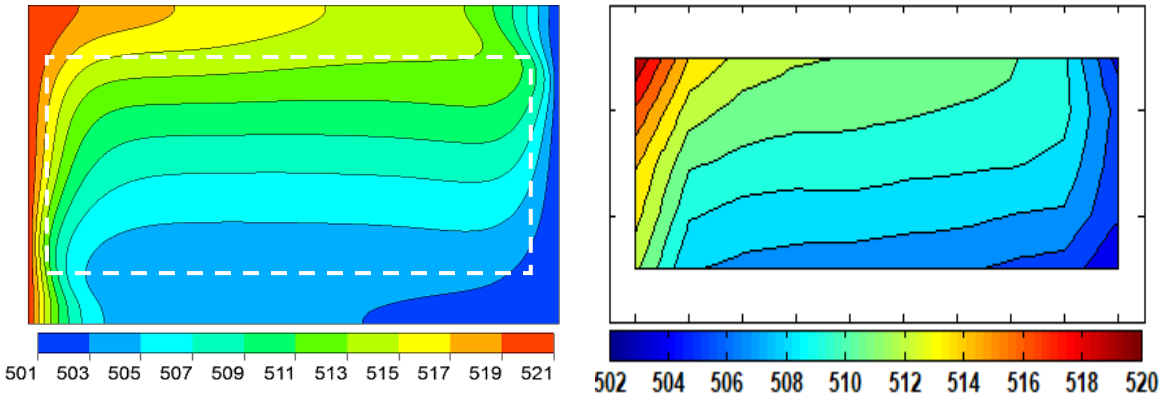

(a) t = 1820 s

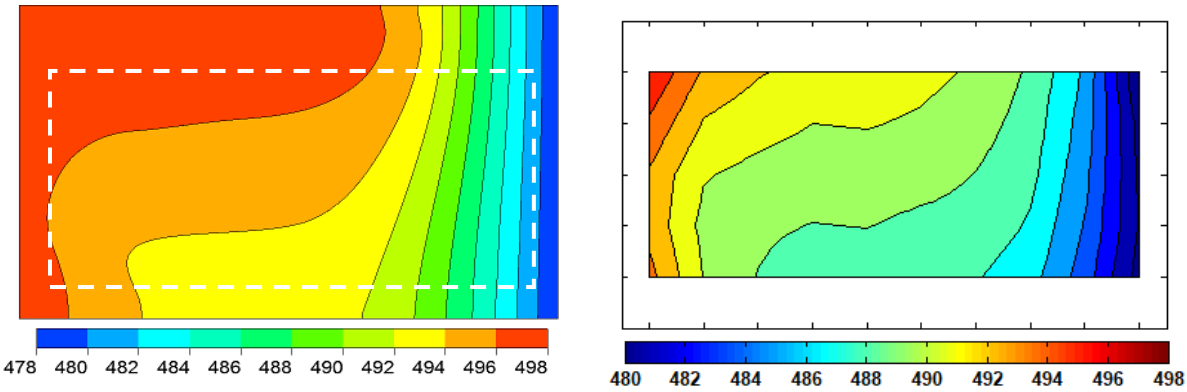

(b) t = 2650 s

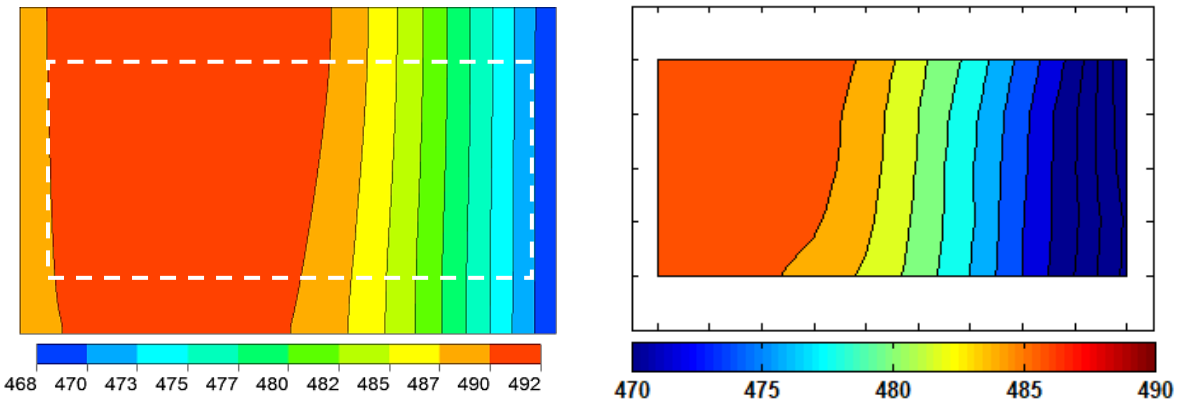

(c) t = 3220 s

Fig.III. 6**:** *Temperature maps recorded at selected times during the solidification of a Sn-10wt.%Pb alloy: (a) t = 1820 s, (b) t = 2650 s and (c) t = 3220 s, after the initial simulation time (t = 0 s) which corresponds to the time 1400 s of the experimental process. The numerical*

calculations are presented on the left side and the experimental data on the right side. The experimental measurement area in which thermocouples are present is indicated by a white dashed rectangle on the numerical snapshots presented in the left column. Conversely, the white strip framing the coloured temperature map on the experimental snapshots corresponds to the part of the domain in which no thermocouple is present.

In order to compare the solutal buoyancy forces with thermal ones, it is important to introduce relevant dimensionless parameters involve, namely the buoyancy number N_b, express as follows:

$$\boldsymbol{N_{buoy} = \frac{\beta_c}{\beta_T}.\frac{\delta C}{\delta T},} \qquad \textbf{(}\boldsymbol{\delta T}\textbf{: is the thermal variations in the melt)} \qquad \textbf{(III.21)}$$

Assuming that the mushy zone is in thermodynamical equilibrium, the buoyancy number N_{buoy}^{mush} takes the following adapted form:

$$\boldsymbol{N_{buoy}^{mush} = \frac{1}{m}.\frac{\beta_c}{\beta_T},} \qquad \textbf{(}\boldsymbol{m}\textbf{: is the liquidus slope)} \qquad \textbf{(III.22)}$$

If we take δT = 20 K, which is an estimated value taken from an extrapolate calculation given by Eqs. (17 and 18) for the effective temperature difference between the two lateral ingot walls and δC = 10*wt*.% as estimated value for solutal gradients, the numerical values of N_{buoy} and N_{buoy}^{mush} are 3.18 and 4.95, respectively. This indicates clearly that solutal buoyancy effects are dominant during solidification, in the present case.

Fig.III.6(b) shows the temperature field corresponding to time 16650 s, i.e. 2650 s after the beginning of the solidification. As the superheated melt is cooled from both sides, while maintaining a constant temperature difference, and the temperature of the cold wall (right side) gradually decreasing below the liquidus temperature (T_L = 492.K), the columnar dendrites begin to grow, thus forming a columnar liquid mushy zone. The isotherms in the right side of the sample gradually become vertical compared with the previous selected time (t = 1820 s), with a mainly conductive heat exchange mode. The maximum melt velocity is now about 0.98 cm/s, which indicates a decrease of around 47% from the previous value at the beginning of the solidification (t = 1820 s).

The last time (t = 3220 s) is shown in Fig.III.6 (c). The solidification front continued to advance from the right to the left in both maps. A significant decrease of the temperature gradient occurs due to the ripening of the solid phase, which leads to a drop in the fluid volume in the mushy

zone. The numerical results predict the appearance of a second solidification front on the sample's left side at this time, since the temperature applied on this side is now below the liquidus point of the alloy. However, at this time, the temperature maps obtained from experimental measurements do not indicate the existence of a second front. This difference can be attributed to the fact that the distribution of the thermocouples does not cover the entire surface of the crucible (see Fig.III.1-b). Furthermore, the last liquid phase, confined between the two solidification fronts, gradually disappears to be replaced by a global mushy zone. In this region, Low residual velocities remain, forming two counter-rotating loops because the velocity is relatively higher in the central part, which is hotter than the nearby sides. Heat transfer is mainly conductive with quasi-vertical isotherms at this time, and consequently, the last liquid does not solidify at the left wall (hot side), but at a distance from it.

4.2.Discussion on main factors responsible for segregated channels

In order to identify the main factors that can directly affect the segregation mechanism, especially at the meso- and macro-scales, the Pb concentration maps coupled with velocity vectors (left column) and the maps of the solid fraction evolutions (right column), are shown in Fig.III.7 at three selected times. As mentioned previously, the solidification is asymmetric due to the applied mean horizontal temperature gradient and starts from the right-side. When the solidification progresses, if the liquid velocity is opposite to the temperature gradient, a negative segregation will be formed in the upper part of the cavity (Fig.III.7(a)), and against a positive segregation will be occurred near the bottom of the crucible (Fig.III.7(b)). Among a several factors, we believe that the development of segregated channels is the result of the interaction of two specific mechanisms in the regions which characterised by a columnar structure. The first mechanism is the onset of high-potential sites for the appearance of mesosegregation zones, which is closely related to the instability of the solidification front caused by overall convection and the movement of the interdendritic liquid, that is controlled by its permeability in the mushy zone. At present, it is difficult to accurately predict the time and location of the initiation mechanism of mesosegregation, but the dimensionless Rayleigh number may be a relevant parameter that can provide an indication of the onset. C. Beckermann *et al*. [25], estimate that if the Rayleigh number of the mushy zone, developed specifically for freckles forming in Ni superalloys during upward directional solidification (with a temperature gradient opposite to gravity, and for small grain inclination angles), is greater than a certain critical value, which

ranging between 0.12 and 0.24, there is a high chance that a segregated channel would start up. In order to determinate the adequate value of the Rayleigh number corresponding to our configuration (directional horizontal solidification of Sn-10*wt*.%Pb alloy), the approach developed in M. Worster *et al.* [26], is used:

$$Ra_{L_c} = \frac{\left(\frac{\Delta\rho}{\rho_0}\right).g.K_{aver}.L_c}{\alpha.\nu} \qquad \textbf{(III.23)}$$

Where L_c is the characteristic length scale related to the local temperature by $L_c = \frac{T_L - T}{G}$ with T corresponds to a temperature range of about 14 K below the liquidus temperature whereas G is temperature gradient taken identical to our average experimental temperature difference (G = 4 K/cm), α the thermal diffusivity, ν is the kinematic viscosity of the melt in the mush. The relative liquid density inversion $(\Delta\rho/\rho_0)$ over the mush of height L_c is given by $\left(\frac{\Delta\rho}{\rho_0}\right) = \frac{\rho(T) - \rho(T_{Liq})}{\rho(T)}$. K_{aver} is the mean permeability K (Eq.13) corresponding to the average liquid fraction f_l in the mush length Lc. Although our configuration is a solidification perpendicular to the gravity vector, the calculation gives an estimated value of 0.125, which is in good agreement with the critical interval given in [25].

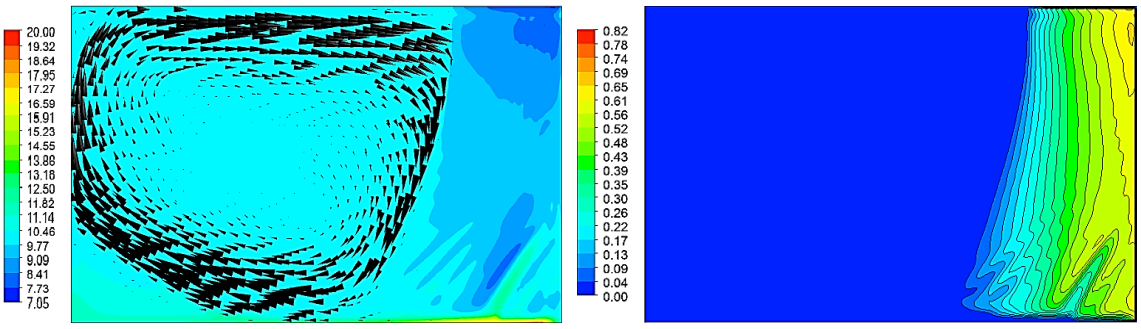

v_{max} = 0.9 cm/s

(a) t = 818 s

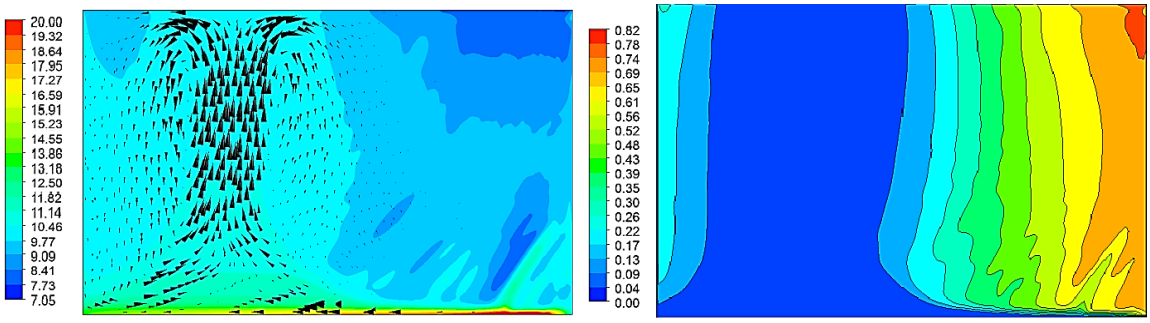

v_{max} = 0.1cm/s

(b) t = 1115 s

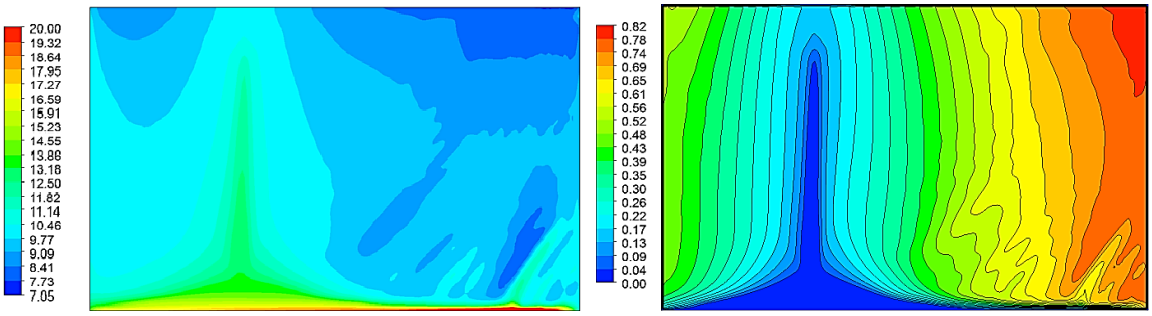

$v_{max} \approx 0$ *cm/s*

(c) t = 1355 s

Fig.III.7**:** *Right column: Map of average Pb concentration coupled with the velocity vectors (black). Left column: Solid fraction evolution. Three selected times are shown: (a) 818 s, (b) 1115 s and (c) 1355 s.*

The second factor is the growth stability of the segregated channel resulting in the ripening of the solid phase in the mushy zone and the configuration of the existing interdendritic flows. The results show that the development of the segregated channel is always accompanied by a suppression solidification mechanism in the lower part of the columnar structure front region, as indicated in the maps of solid fraction evolution in the right column of Fig.III.7.

An increase in local interdendritic flow induced by a flow perturbation is favoured by the resulting suppressed solidification. It's also worth noting that this latter mechanism only happens when the interdendritic flow $(\vec{u}_l)$ is in the opposite direction of the liquid concentration gradient $(\vec{\nabla} c)$, as will be discussed below and shown in Fig.III.8. However, there seems to be a characteristic time to stability the segregated channel, because the channels do not appear in the case of accelerated solidification, which prevents the increase in local interdendritic flow driven by flow disturbances.

We assume that the fluid-solidification interaction is a stabilizing factor on the flow perturbation and instability of the solidification front, so channel segregation will not occur. This can be confirmed by the fact that in the upper right part of the sample, although the dominance of the columnar structure and the critical Rayleigh number conditions are fully

satisfied, the experimental results obtained from the X-ray radiographic analysis shown in Fig.III.10 clearly shows that no channel occurred there.

Fig.III.7(b) and (c) also show that the transport of the enriched liquid from the inside of the mushy zone leads to a significant positive segregation towards the bottom of the cavity and induces or expands the solute stratification in the bulk liquid. due to the stratification in the melt. Furthermore, comparing the overall macrosegregation pattern in Fig.III.7(c), shows a negative segregation towards the top of the sample and a 'peak' of positive segregation where the two solidification fronts meet.

Fig.III.8 shows the suppressed solidification region in its early stages, where channels develop. Segregated channels appear in the zones which are characterized by a relatively high concentration corresponding to the lower solid fraction. As explained previously, the positive direction of $(\vec{\nabla}c)$ represented by red vectors during this stage of solidification is almost right-downward, whereas the liquid flow (black vectors) in the channel is left-downward, as shown in Fig.III.7. It can be seen that the sign of $\vec{u}_l$ and $\vec{\nabla}c$ in the channel is negative, which confirms that the solidification process will be slowed. In the neighbouring region (channel surroundings), the fluid has a tendency to orient itself towards the channel, which is characterized by a relatively high permeability compared with its surroundings (drainage effect).

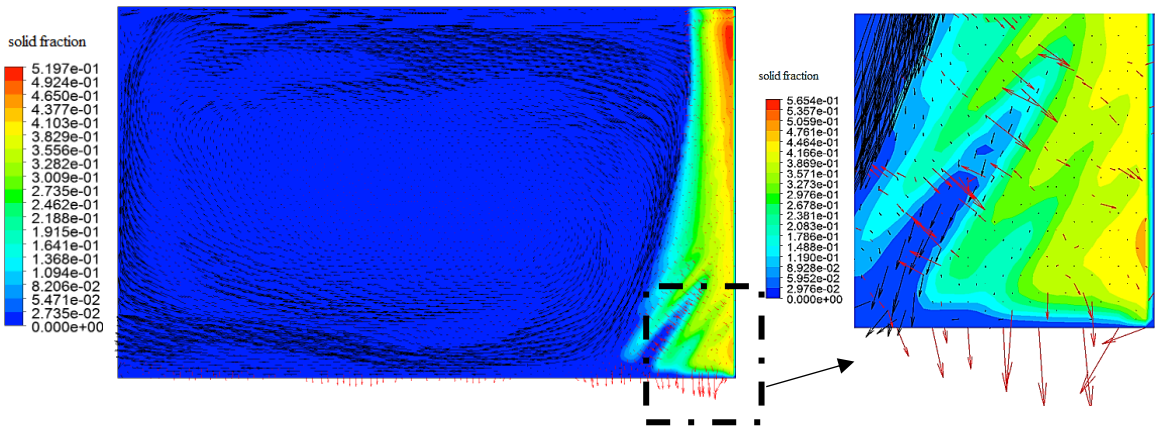

(a) ***(b)***

Fig.III.8**:** *(a) Map of solid fraction at time 600 s, coupled with the velocity vectors (black); (b) zoomed-in view of the area bounded by a discontinuous black line with the liquid velocity* $\vec{u}_l$ *(black) and concentration gradients* $\vec{\nabla}c$ *(red).*

Conversely, the sign of $\vec{\nabla}c$ and $\vec{u}_l$ in the neighbouring zone (surrounding the channel) is actually positive, which provides clear indications that the solidification might be accelerated there. The channel can be stable with this particular situation of flow-solidification interaction. In addition, in the mushy zone, the flow is influenced by the intensity and direction of the convective vortex acting in the liquid phase. However, the fluid flow in the channel surroundings is primarily influenced by the concentration gradients$(\vec{\nabla}c)$.

Moreover, during the solidification process, there is a potential possibility of remelting in mushy zone that has formed. The literature shows that there are two main mechanisms in which remelting can occur: local reheating due to the hot bulk transported by convection and/or concentration increase in liquid that surrounding the dendrites due to the flow of solute-rich liquid into these regions. Indeed, the remelting issue has been investigated by both numerical and experimental studies, A. kumar *et al.* [27] and M.G. Worster [28]. The theoretical details and numerical model related to the phenomenon are not highlighted this latter, namely its impact on the segregation development. It is clear that this phenomenon needs further examined, in order to explain its effect on the segregated channels formation, in terms of morphology and level of concentration, we have followed the history of the thermal and concentration fields as well as their corresponding liquid fraction of three different points: point 1 (*x = 95 mm, y = 20 mm, z = 0.5 mm*), point 2 (*x = 91 mm, y = 10 mm, z = 0.5 mm*) and point 3 (*x = 88 mm, y = 0.5 mm, z = 0.5 mm*), located in the same channel segregation (freckle), presented in Fig.III.9(a).

Fig.III.9 shows the time-evolution of temperature and their corresponding liquid fraction and average concentration for each point selected. It is easy to note that due to the decrease of temperature in these points (Fig.III.9(b)), which becomes lower than the liquidus temperature (T_L = 492 K), the liquid fraction has decreased from initial value f_l = 1 to 0.8 and 0.74 for point 1 and 2, respectively, which corresponding to the solidification progress. However, the third point which located almost at the crucible bottom, presents a little decrease of liquid fraction of about 7% (f_l = 0.93), because of the effect of heavy solute sedimentation, as shown in Fig.III.9(c). Fig.III.9(c) shows also an increase in the liquid fraction of about 10%, 20% and 7% in points 1, 2 and 3, at the instants 563 s, 623 s and 660 s, respectively after the start of the cooling stage. This behaviour that corresponds to a remelting phenomenon of the solid in the mushy zone, is accompanied by a major increase in the level of concentration due

to the transport of solute rejected within the mushy zone, which reaches 24*wt*%. These factors are the favourable conditions for the creation of a segregated channel.

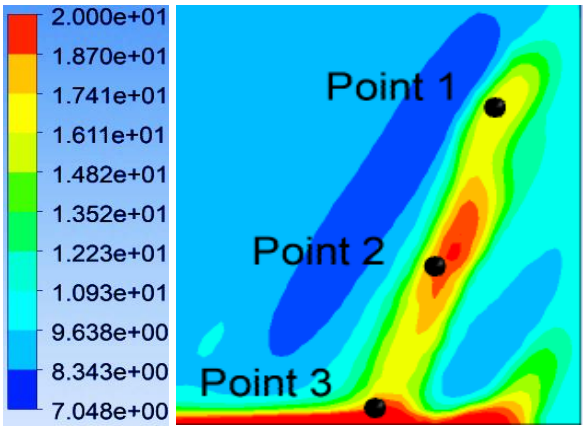

(a) Position of the three points selected

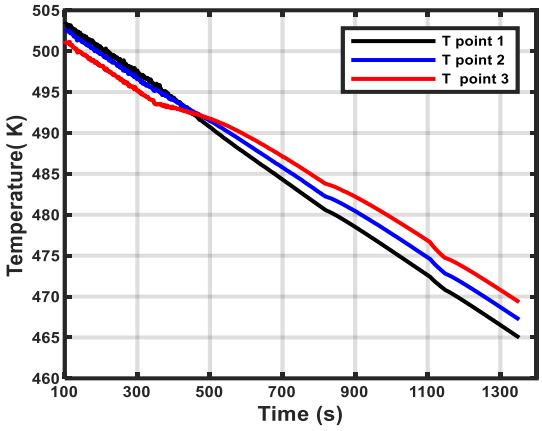

(b) Temperature

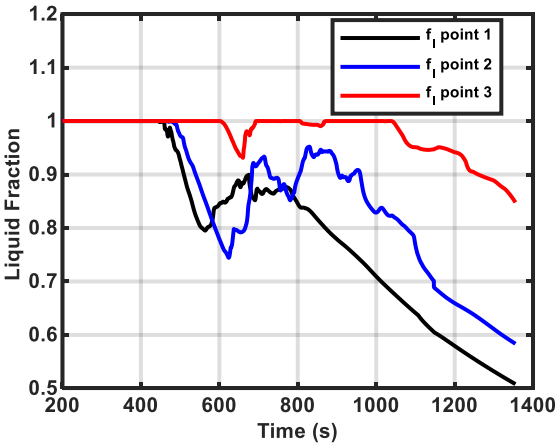

(c) Liquid fraction

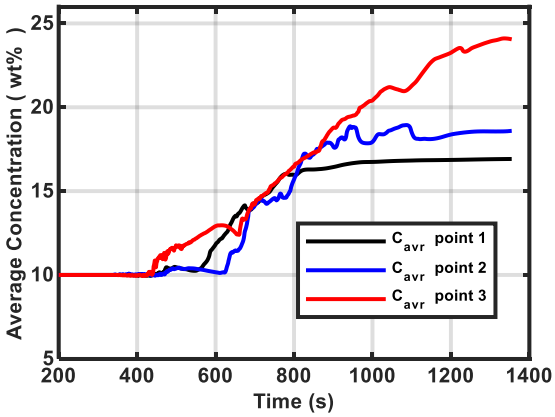

(d) Average concentration

Fig.III.9**:** *Time-evolution of temperature, average concentration and liquid fraction for three points, located in the same segregated channel (freckle): point 1 (x = 95 mm, y = 20 mm, z = 0.5 mm), point 2 (x = 91 mm, y = 10 mm, z = 0.5 mm) and point 3 (x = 88 mm, y = 0.5 mm, z = 0.5 mm).*

A fluctuating values of these concentrations and relatively less in the corresponding temperatures, were observed just in the time before and during remelting. Fig.III.8(d) shows clearly an increase in the solute concentration in the points 2 and 3 located to the identified remelting sites, which correspond to the zone of channels segregation formation. Thence, these analyses clearly show that the remelting is a direct result of the local increase in the concentration of a solidified sites because of the inflow of solute-rich liquid in the mushy zone.

Indeed, due to the relatively large liquidus slope of Sn-10*wt*.%Pb alloy, small gradients of concentration induce a significant drop in liquidus temperature and thereby remelting is strongly affected by solutal variations.

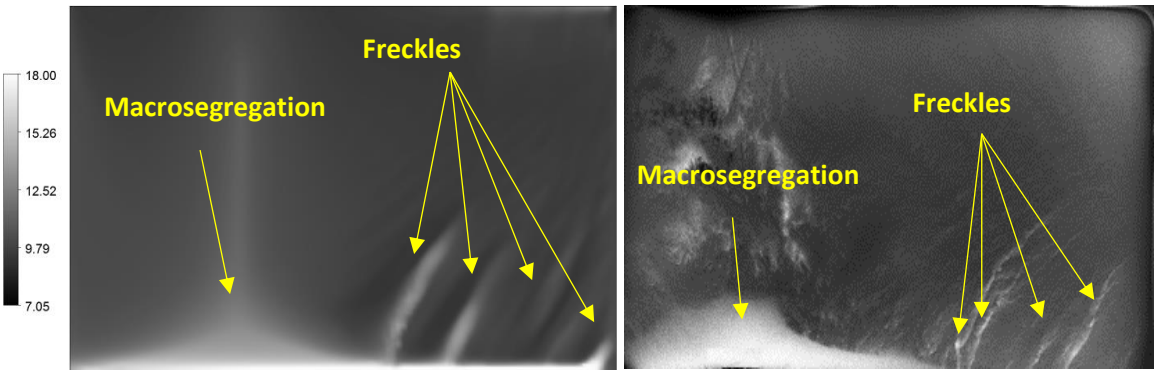

(a) ***(b)***

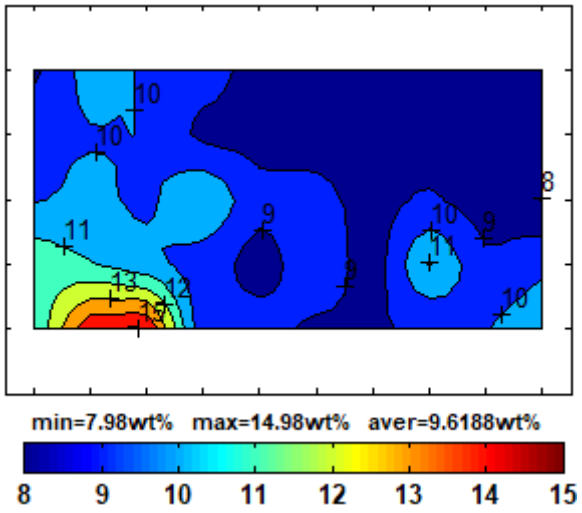

8.78	10.37	9.89	9.43	8.64	8.62	8.61	8.74	8.51	8.93
9.70	9.95	9.97	8.78	8.66	8.68	8.63	8.62	8.51	8.64
9.93	10.22	9.81	10.91	9.33	9.22	8.73	9.12	8.54	7.98
11.67	11.08	10.34	9.53	8.60	9.68	8.54	11.04	9.21	9.76
11.08	14.78	14.98	9.25	9.38	8.80	8.92	9.13	9.96	10.76

(c)

Fig.III.10**:** *(a) Photo of X-ray radiography of the solidified sample (b) Lead concentration map averaged over the sample thickness calculated by numerical simulation, at the end of the solidification process (in wt.%) and (c) Lead concentration map measured by the chemical method coupled with the inductively coupled plasma technique (left) and corresponding numerical values (right).*

In fact, when the solidification accelerates, the area around each channel reject lead, thus leading to enrich the solute in the channel, which induces a pumping effect by solutal buoyancy. Locally, the resulting flow happens from the zones with a relatively high solid fraction to the more liquid zones, which continues to drain the solute into the segregated channels.

Fig.III.10(a) presents the overall macrosegregation pattern obtained numerically by averaging the concentration field over the sample thickness "*e"*, as expressed by Eq. 22, compared with the experimental analysis obtained by X-ray radiography, shown in Fig.III.10(b). The concentration variations are mainly in the vertical direction, and the 'peak' seen in the simulation result is not apparent in the experiment. However, the X-ray radiograph does not give quantitative information for the variations of concentration, therefore, the segregation level is uncertain. The X-ray radiographs in Fig.III.10(b), also uncover information about the mesosegregation localisation. The results show several channels in the lower-right portion of the sample, which is very consistent with the numerical simulations.

$$\bar{C}_{aver}(x,y) = \frac{1}{e}\int_0^e C(x,y,z)dz \qquad \textbf{(III.24)}$$

The isotropic Carman-Kozeny law adopted in our model shows a very consistent with the experiment, both with respect to channels location and the relative channels number between experiment and simulation. According to the numerical results, the lead concentration in the segregation channels and macrosegregation region, which corresponds to the last liquid solidified, can reach 18 wt.%.

Fig.III.10(c) illustrates the results the experimental solute distribution obtained by a chemical method based on dissolution in an HNO_3/HCl ($1\text{-}2\times10^{-3}$) acid mixture and coupled with the ICP (Inductive Coupled Plasma) technique for determining a quantitative analysis of lead distribution. The ingot chips analysed, weighing approximately 200 mg, are obtained by core-drilling 50 holes correspond to the thermocouple positions, as mentioned previously [28, 29]. As expected, the results show clearly that the solute rejection process starts from the cold aspect (right) of the ingot, therefore there is a lead-enriched zone on the bottom-left at the end of solidification. This region corresponding to the last solidified liquid has a concentration exceeding 14*wt*.%. However, a macrosegregation region with the highest concentration of up to 18 *wt*.% was observed in the right-hand corner of the sample. This concentration peak provides clear indications of the segregated channels formation at this location. Conversely, one disadvantage of this technique is that it cannot detect all other segregated channels predicted by simulation. This may be due to the core size (1 mm), which may be too large to capture the phenomenon that is developing at mesoscopic scale.

4.3.Segregation morphology

In this part, we focus on the morphology of the segregated channels as well as the plume of macrosegregation correspond to the last liquid solidified in the ingot. To characterise this morphology, both numerical results and specific post-mortem analysis will be used. Snapshots of averaged lead concentration maps over the sample thickness obtained by numerical simulation are shown in Fig.III.11. In all cases, the mesosegregation is on the right side of the ingot, appearing in the form of several solute-enriched channels. Fig.III.11(a) (1-3) shows a time/space follow-up of the segregated channels development in this zone. Their morphologies correspond, generally, to a tubular structure distributed over the thickness of the sample and more particularly along the front or back walls. These structures are initiated close to the cold right endwall, and in the vicinity of the side walls at a certain height, (see Fig.III.11(a1). As the solidification-flow interaction activates during the advance of the solidification front, the stable channels develop in the mushy zone with a descending quasi-arc shape, affected by the descending convective motion and the suppressed solidification in this zone, (Fig.III.10(a2 and a3). Their lead concentration varies between 11.5 and 28 *wt.*%. Furthermore, the dimensions of the tubular segregated channels vary widely. In general, their diameter varies between 0.8 and 2.2 mm and their arc-length between 4 and 24 mm.

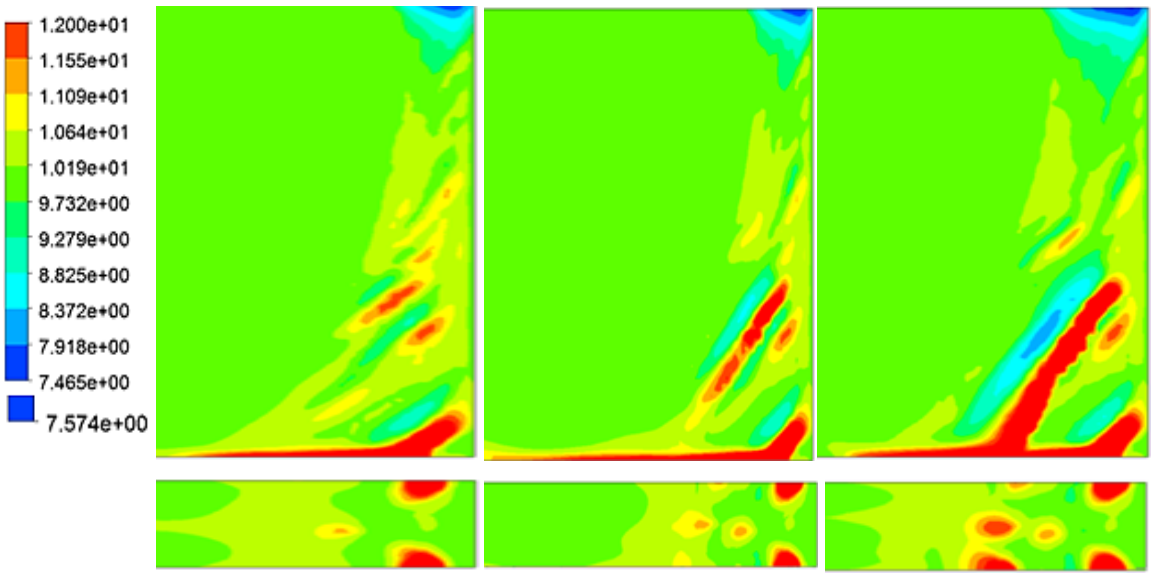

(a1) 550 s ***(a2) 600 s*** ***(a3) 650 s***

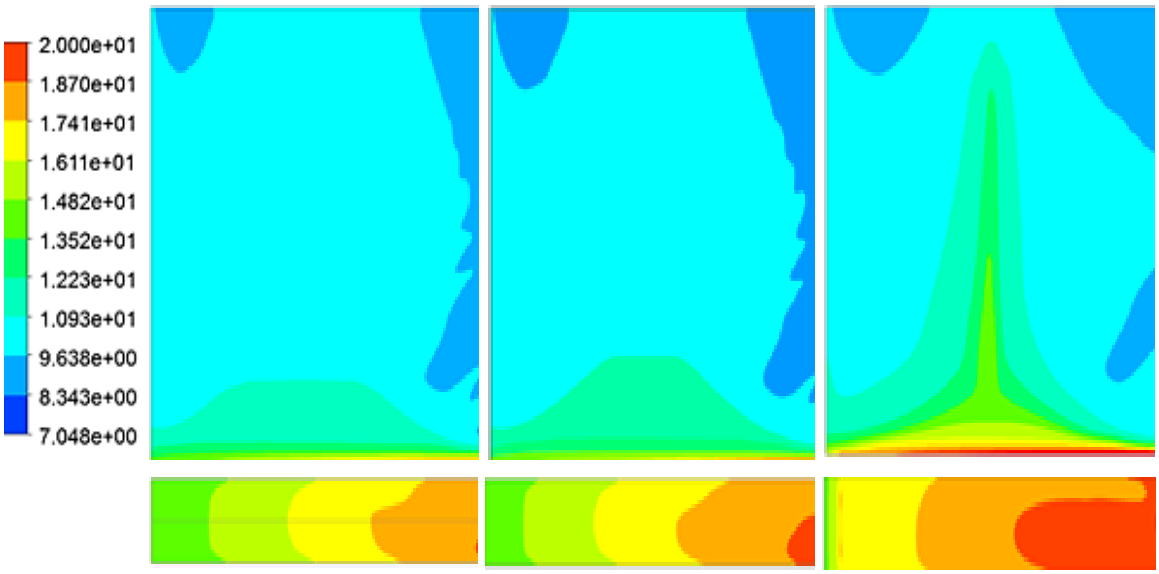

(b1) 1115 s ***(b2) 1144 s*** ***(b3) 1355 s***

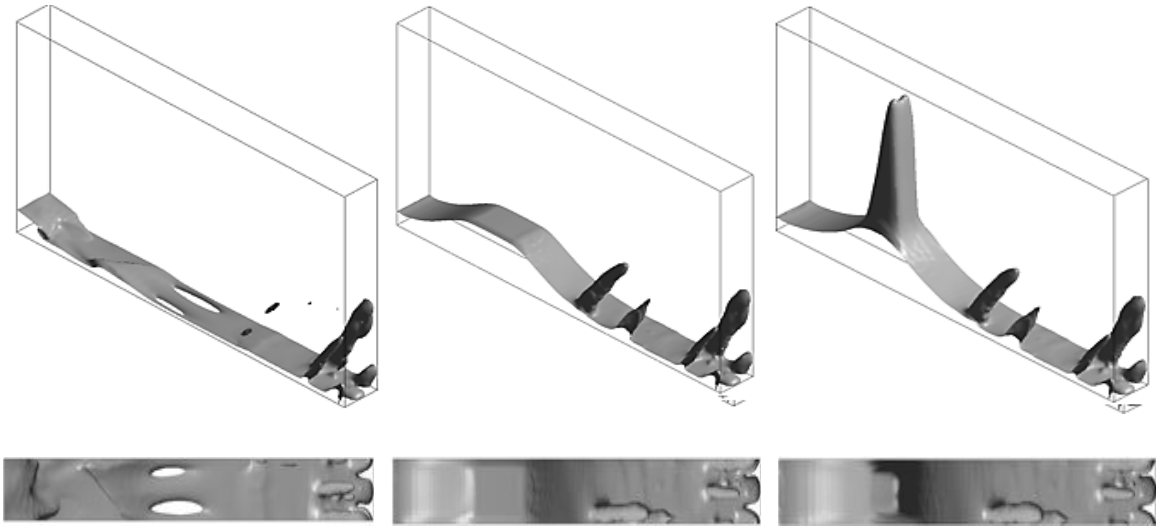

(c1) 818 s ***(c2) 1115 s*** ***(c3) 1355 s***

Isoconcentration $\langle C \rangle = 12wt.\%$

Fig.III.11: *Snapshots tracking: segregated channel development (a.x.); development of macrosegregation corresponding to the last liquid solidified (b.x.); 3D views of lead isoconcentration of 12 wt.% Pb, shown in greyscale (c.x).*

Fig.III.11(b) (1-3) represents the development of macrosegregation corresponding to the last liquid solidified. As predicted, it has a plume shape, indicating a zone richer in solute at the bottom of the column near the left side of the sample. Simultaneously to the stratification effect, this morphology is a direct result of the transported solute caused by the action of the two convective loops resulting from the advance of the two solidification fronts and which stay

active in the last solidified liquid. This plume has a significantly high concentration, ranging between 12.3% and 20 wt.%. It has a height of 53 mm and a base length of 44 mm (see Fig.III.11). (b3).

Fig.III.11(c) (1-3) shows 3D views of the lead isoconcentration surfaces at 12 *wt*% in the solidified ingot obtained by numerical simulation (displayed in grey). The figure shows a focus on the lead rich zones, i.e. principally solute stratifications in the bottom of the ingot, the segregated channels (right part), and the solidification-end plume. The lateral-side walls of the crucible present potential privileged areas for the development of segregated channels. Some small discontinuous channel parts are found halfway up the right third of the sample. It is important to note that a dissymmetry is observed in the shape and location of the segregated channels, despite the symmetrical boundary conditions imposed at the back-side walls. This may be explained by the effect of the solidification front instabilities due to fluctuations of the temperature field, which create asymmetries. In real situations similar to the one studied here, the flow is fluctuating and the existence of the fluctuations is generally accompanied by a destabilization of symmetry, which will affect both the flow configuration and the temperature field.

In order to evaluate these observations, a new view of macrosegregation presented as a set of slices perpendicular to the front/back was studied numerically and experimentally. The ingot is cut into nine slices parallel to the (yz) plane, corresponding to 10, 20, 30, 40, 50, 60, 70, 80, and 90 mm from the right (cold side) to left (hot side), which are analysed by X-ray radiophotography carried out in the perpendicular x-direction. The slices are between 5 and 5.6 mm thick, and their height varies between 55 and 60 mm (effect of shrinkage in the later solidified part). The corresponding X-ray photographs are shown in Fig.III.12, compared with lead concentration maps in (yz) planes obtained from the numerical simulation at the same locations as the ingot slices. It is important to emphasize that the comparison can only be done qualitatively, because each X-radiograph of the slices in Fig.III.12(a) is obtained by integration of the X-ray signal over its thickness, (5-6 mm), while the numerical results in Fig.III.12(b), are the segregation map of the corresponding sections. Generally, the comparison illustrates good agreement between experiment and simulation. The bright zones observed by X-radiography correspond to the positions predicted by simulation for lead enrichment regions. On the simulation plots (Fig.III.12(b)), The segregated channels can be seen clearly in the first

four isoconcentration maps (right part of the sample), with quasi-circular cross-section forms distributed over the thickness of the ingot, but with the majority near to the side walls.

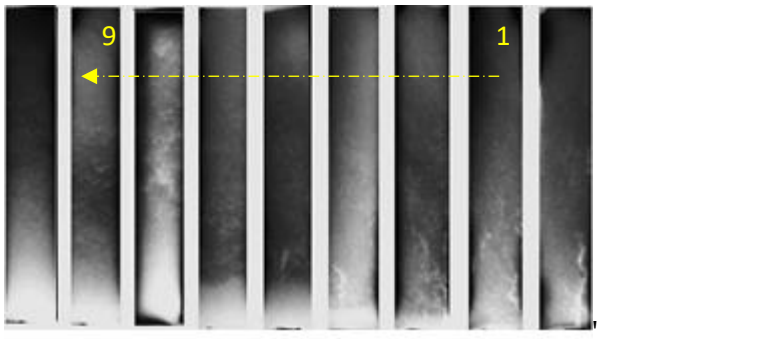

(a)

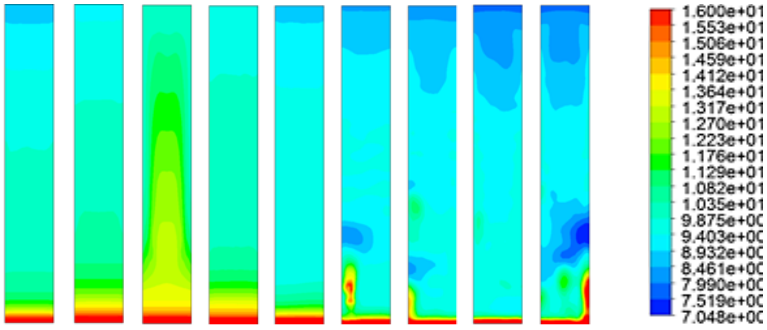

(b)

Fig.III. 12**:** *(a) X-radiography photos of the slices and (b) contour maps of the iso-concentrations obtained by numerical simulation. The positions of the slices (1-9) are 10, 20, 30, 40, 50, 60, 70, 80, and 90 mm from the cold wall (right side).*

Apparently, tubular forms with elongated shapes, sometimes a little blurred, can also be detected in the X-ray radiography, in particular in the first four slices. Note that due to the significant thickness of the ingot slices analysed by X-ray radiography in this direction, i.e., perpendicular to the (*yz*) plane, the segregated channels will describe a path.

It is important to note that, due to the effect of the projection of these kinds of analysis techniques, the X-ray photographs show elongated forms of channels with an attenuation in terms of intensity by averaging over the slice thickness. The X-ray photographs show clearly the high level of lead segregations around the zones in the left side where the end of solidification occurs, more particularly in the last three slices (see Fig.III.12(a)). The position of the solidification-end plume appears quite symmetrical in the seventh iso-concentration map with respect to the vertical (xy) plane in simulation (Fig.III.12(b)), but does not show such

symmetry in the experiment (see the seventh and eighth slices in Fig.III.12(a)), except approximately in the lower part. The level of lead segregation in the lower-left corner region (slices 7, 8 and 9 in Fig.III.12(a)), is actually overestimated by the simulation, and the transition from the lower Pb-enriched regions to the high concentration is predicted more explicitly numerically than shown by the experimental analysis (X-radiographs). Some average sizes and locations of the segregation channels which are not precisely matched in the experimental results (effect of projection), are also overestimated by the numerical simulation.

4.4.Macrostructure

The macrostructure of the ingot is shown in Fig.III.13(a). Macrostructure is obtained after post mortem analysis, which consists of several passes of polishing and chemical attack with a mixture of 75% Vol HCL (37 mol%/v) and 25% Vol HNO3 (69.5%). A distinct columnar zone is observed, which originates at the right side of the sample, grows at an angle approximately 45 degrees from horizontal and extends over half the length of sample. The direction of natural convection has direct consequence on the upwind tilting of the columnar grains. Furthermore, a smaller columnar region is observed in the top and bottom left corner which corresponds to the solidification front emerging from the left-hand side of the sample. In the lower part of the sample, below the two columnar regions, a more equiaxed microstructure is observed which roughly corresponds to the region of positive segregation seen in Figs.III.10 and 12.

To understand the formation of the as-cast structure, another analyses than X-rays and ICP were conducted in order to establish grain structure and verify the effect of solute stratification on the final crystal structure. Fig.III.13(b) gives a graphic representation of the number of grains in terms of their size. The geometric forms specific characteristics of the macrostructure are summarized in Appendix (B). The results clearly show that the stratification in lead significantly favours the mechanism of columnar-to-equiaxed transition (CET), and consequently refining equiaxed grains. This is observed by the dominance of the number of grains less than 40 mm^2, in particular in the region where the two solidification fronts meet. These results are in good coherence with the experimental parametric study on the effect of the average cooling rate and alloy composition on the CET in directionally solidified in Pb-Sn alloys in the range 2-40%Sn, performed by Ares and Schvezov, [31]. The results showed a correlation similar to that given by Hunt's model. Indeed, we believe that the predominant mechanism responsible for blocking progress of the columnar front, and consequently the onset

of CET, is solutal-driven remelting, due to flow of interdendritic enriched-solute liquid during columnar growth (solidification), as proposed by Zheng et *al.* [32]. The authors have shown that there is a specific angle between the two vectors (interdendritic flow in mushy zone $\overrightarrow{u_l}$ and concentration gradient $\vec{\nabla} c$) which can give indications about the possibility of fragmentation. Indeed, they suggest that when it is larger than π/2, fragmentation may occur, and consequently no fragments can be produced when it is smaller than π/2.

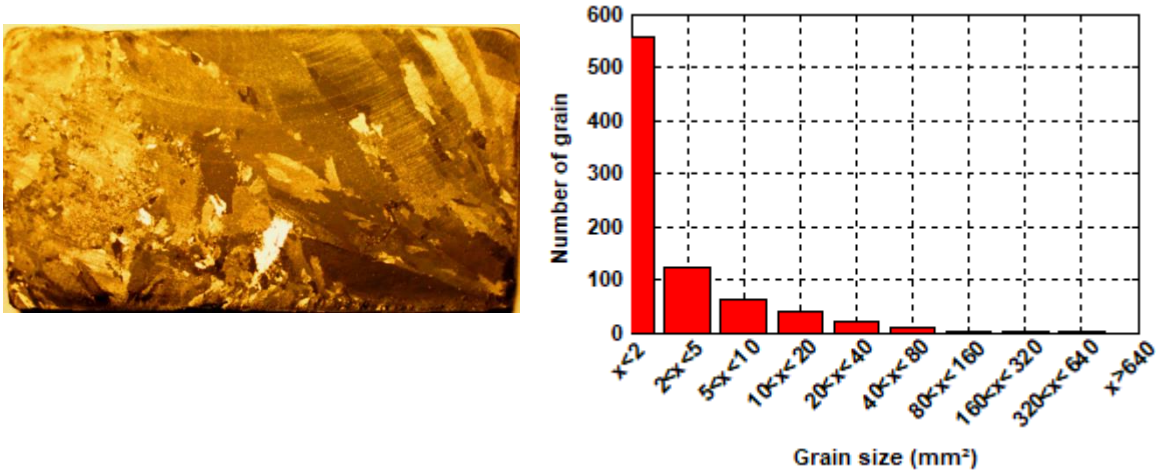

(a) **(b)**

Fig.III.13: *Macrostructure of Sn-10wt. %Pb alloy (a) and its distribution of grain size (b). [28]*

Otherwise, as the rejected solute enriches the interdendritic liquid, the concentration gradient, which is the driving growth force, will gradually decrease. Grains, which are transported by convection out mushy zone, will grow under certain conditions and then slowly stop growing without coming into direct contact with one another, Martorano et *al.* [33].

5. PARTIAL CONCLUSION

A full 3D numerical model, implemented in ANSYS/Fluent software, is used to reproduce the solidification of the Sn-10*wt.*%Pb alloy in a benchmark solidification experiment. The model is based on a two-phase volume-averaged approach assuming perfect microscopic mixing (lever rule). The corresponding instantaneous temperature distributions and final post-mortem characterizations are available, allowing a detailed comparison between the numerical and experimental results. The agreement between experiment and simulation in terms of temperature evolution and macro- and meso segregation morphology and behaviour further

verified the numerical model used. Rigorous processing of the experimental temperature data has been applied to define appropriate unsteady thermal boundary conditions for the numerical model, which enable buoyancy convection to be taken into account correctly in this 3D simulation. We can deduce some findings and general conclusions about the effect of thermosolutal convection on the solidification process, particularly concerning the solute stratification, segregation morphology and CET mechanism.

- Globally, three different mechanisms are responsible for the movement of fluid in the mushy zone, and consequently the development of segregation at different scales and with different morphologies:
    - convection in the mushy zone, which transports the solute within and outside the mush,
    - solidification front instabilities driven by the convection in the bulk and the motions of the interdendritic liquid and controlled by its permeability in the mushy zone,
    - interdendritic local flow induced by a flow perturbation resulting in the suppressed solidification mechanism, which occurs only when the interdendritic flow $(\vec{u}_l)$ is in the opposite direction to the liquid concentration gradient $(\vec{\nabla} c)$.
    - remelting results to the local increase in concentration due to inflow of solute-rich liquid in the mushy zone and/or reheating due to the hot bulk transported by convection, is a favourable condition to the development of a segregated channels.
- Both numerical simulations and experimental characterisations show that the segregated channels are distributed over the ingot thickness and have a tendency to exhibit a curved shape. Most of them have a complex 3D morphology and tend to have tubular forms.
- A columnar-to-equiaxed transition (CET) was observed in the experiment, which was discussed in our previous work [28, 39]. This result can be attributed to convective motions that exert two main effects. First, the buoyancy force generates liquid convection that homogenizes the melt and decreases the temperature gradients, therefore creating favourable conditions for onset of a CET. Second, hot flow currents impinging the mushy zone can enhance fragmentation/remelting of the secondary arms. The solute-enriched melt transported by the interdendritic flow, under certain conditions

which depend on the flow configuration (in the columnar-growth direction or against the $\vec{\nabla}c$ direction), promotes remelting and consequently fragmentation, and the resulting fragments are a predominant factor in the formation of equiaxed grains.

Appendix A Instantaneous temperature maps recorded for three selected times corresponding to the experiments Sn-10*wt*.%Pb. Experimental conditions: DT = 40K, CR = - 0.03K/s.

	Temperature maps (K)
1820s	**514.27 509.96 509.46 509.16 509.06 508.96 508.56 508.27 507.96 505.84** **515.76 511.26 510.65 510.46 510.56 510.27 510.16 509.76 509.65 507.26** **516.76 512.56 512.06 511.76 511.86 511.65 511.36 511.26 510.84 507.96** **519.06 514.46 513.27 512.76 512.96 512.56 512.46 512.26 511.56 508.27** **521.96 516.56 514.65 513.96 513.84 513.56 513.16 512.56 511.46 506.65**
2650s	**494.27 490.65 489.46 488.96 488.76 488.86 488.46 487.76 485.36 481.16** **493.76 490.65 489.84 489.65 489.76 489.56 489.46 488.46 486.16 481.86** **494.06 491.36 490.76 490.56 490.56 490.36 489.96 489.16 486.56 481.76** **495.65 492.56 491.76 491.36 491.36 491.06 490.76 489.65 487.06 481.46** **497.56 494.16 492.76 492.26 492.16 491.76 491.36 489.96 487.27 480.56**
3220s	**491.76 490.36 489.27 488.36 487.84 486.86 484.36 481.16 477.46 472.96** **491.46 490.16 489.26 488.76 488.65 487.56 485.27 481.56 477.96 473.26** **490.96 489.84 489.36 489.06 488.96 488.06 485.65 482.27 478.06 472.84** **491.36 490.26 489.76 489.27 489.16 488.36 486.06 482.56 478.27 472.46** **491.84 490.86 490.36 489.76 489.56 488.56 486.56 483.06 478.96 471.65**

Appendix B. Geometric characteristics of the macrostructure of Sn-10*wt*.%Pb. Experimental conditions DT = 40K, CR = - 0.03K/s.

Grain size mm²	**Area µm²**	**Area percentage** (%)	**Number of grains**

x < 2	319.0	4.21	558
2> x >5	384.9	5.08	121
5>x>10	469.4	6.20	64
10>x>20	573.3	7.57	40
20>x>40	508.0	6.71	19
40>x>80	522.1	6.90	10
80>x>160	991.7	1.31	1
160>x>320	437.5	5.78	2
320>x>640	620.5	8.20	1
x>640	0	0	0

References

[1] Ab. Abdelhakem, Ab. Nouri, L. Hachani, Y. Fautrelle, K. Zaidat, Journal of Heat Transfer (ASME), 2022, 144(4): 042401.

[2] D.J. Hebditch, J.D. Hunt, Metallurgical transactions B, 5 (1974) 1557-1563.

[3] M. Bellet, H. Combeau, Y. Fautrelle, D. Gobin, M. Rady, E. Arquis, O. Budenkova, B. Dussoubs, Y. Duterrail, A. Kumar, C.A. Gandin, B. Goyeau, S. Mosbah, M. Zaloznik, International Journal of Thermal Sciences, 48 (11) (2009) 2013-2016.

[4] N. Ahmad, H. Combeau, J.L. Desbiolles, T. Jalanti, G. Lesoult, J. Rappaz, M. Rappaz, and C. Stomp, Metallurgical and Materials Transactions A, 29(2) (1998) 617-630.

[5] M.C. Schneider and C. Beckermann, International Journal of Heat and Mass Transfer, 38(18) (1995) 3455-3473.

[6] C. Beckermann, International Materials Reviews, 47 (5) (2002) 243–261.

[7] M. Založnik, and H. Combeau, conference paper, The Minerals, Metals & Materials Society (2015).

[8] S. Chakraborty and P. Dutta, International Journal for Numerical Methods in Fluids,38 (9) (2002) 895-917.

[9] T. Carozzani, C.A. Gandin, H. Digonnet, M. Bellet, K. Zaidat, And Y. Fautrelle, Metallurgical and Materials Transactions A, 44(2) (2013) 873-887.

[10] S. Gouttebroze, V.D. Fachinotti, M. Bellet, H. Combeau, International Journal of Forming Processes, 8 (2005) 203-217.

[11] V.F. De Felice, K.O. Tveito, M. Založnik, H. Combeau, M. M'Hamdi, IOP Conference Series: Materials Science and Engineering, 33 (1) (2012) 012088.

[12] J. Li, M. Wu, J. Hao, A. Ludwig, Computational Materials Science, 55 (2012) 407-418.

[13] A. Kumar, M. Založnik, H. Combeau, B. Goyeau, D. Gobin, Modelling and Simulation in Materials Science and Engineering, 2013. **21**(4): p. 045016.

[14] A. Kumar, B. Dussoubs, M. Založnik and H. Combeau, IOP Conference Series: Materials Science and Engineering, 27 (2011) 012039.

[15] X.D. Wang, P. Petitpas, Ch. Garnier, J-P. Paulin, Y. Fautrelle, Comptes Rendus Mécanique, 335(2007) 336-341.

[16] X.D. Wang. and Y. Fautrelle, International Journal of Heat and Mass Transfer, 52 (23) (2009) 5624-5633.

[17] P.J. Prescott, F.P. Incorpera, JOURNAL OF HEAT TRANSFER-TRANSACTIONS OF THE ASME, 1994 116 (3), 735-741.

[18] S. Mosbah, PhD Thesis in Sciences et Génie des Matériaux, 2008, CEMEF - Centre de Mise en Forme des Matériaux, ENSMP Paris.

[19] Wang, X.D., et al., Comptes Rendus Mécanique, 2007. **335**(5-6): p. 336-341.

[20] Wang, X. and Y. Fautrelle, International Journal of Heat and Mass Transfer, 2009. **52**(23-24): p. 5624-5633.

[21] Hachani, L., et al., Int. J. Heat and Mass transfer, 2011.

[22] J.N. Koster, and R. Derebail, Heat and Mass Transfer, 32 (6) (1997) 489-498.

[23] H. Thresh and A. Crawley, Metallurgical and Materials Transactions B, 1 (6) (1970) 1531-1535.

[24] V.P. Osipenko, Russian Physics Journal, 13 (12) (1970) 1570-1573.

[25] C. Beckermann, J. Gu, W. Boettinger, Metallurgical and Materials Transactions A, 31 (2000) 2545-2557.

[26] M.G. Worster, Journal of Fluid Dynamics, 237 (1992), 649-69.

[27] A. Kumar, P. Dutta, S. Sundarraj, M.J. Walker, Numerical Heat Transfer, Part A, (2014) 59-83.

[28] M. Worster, J. Wettlaufer, Journal of Physical Chemistry B, 101 (1997) 6132-6136.

[29] L. Hachani, K. Zaidat, B. Saadi, X. Wang, Y. Fautrelle, International Journal of Thermal Sciences, 91 (2015) 34-48.

[30] L. Hachani, K. Zaidat, Y. Fautrelle, International Journal of Heat and Mass Transfer, 85 (2015) 438-454.

[31] A.E. ARES and C.E. SCHVEZOV, Solidification Parameters during the Columnar-to-Equiaxed Transition in Lead-Tin Alloys, 31A, (2000)1611.

[32] Y. Zheng, M Wu, E Karimi-Sibaki, A Kharicha, A Ludwig, 122 (2018) 939-953.

[33] M.A. Martorano, C. Beckermann, Ch.-A. Gandin, Metallurgical and Materials Transactions A, 25 (2003) 1657.

CHAPTER IV

Numerical Simulation of Metallic Alloy Solidification Under Forced Convection Driven by External Travelling Magnetic Field

Preamble

Both the numerical and experiments results presented previously in the third chapter, clearly showed the ~~need~~ necessity to introduce an external force, allowing the control of melt during the solidification process in terms of thermal and solute homogenization and hydrodynamic morphology stabilization. In order to satisfy these conditions, electromagnetic stirring is proposed as a promising technical solution. The objective of this chapter is to examine the effect of forced convection driven by a Travelling Magnetic field on the solidification process. Two solidification cases for a binary Sn-10wt.%Pb alloy were examined (under natural convection and under forced convection). A 3D numerical simulation using a modified model which is previously detailed in the third chapter with an additional term containing the Lorentz force which represents the electromagnetic stirring contribution in the momentum equations. The case of forced convection driven by electromagnetic stirring in the opposite direction to natural convection stirring was examined. All numerical results are compared to those of experiments, which are well described in the work of Hachani et *al.* [1].

1 Proposed electromagnetic inductor

1.1 System Description

The structure of the proposed electromagnetic inductor is shown in Fig.IV.1. It consists of six coils which distributed along the ferromagnetic head placed at the bottom. Such distributed coils make a better use of the core, copper and also improve the magnetomotive force (mmf) waveform, defined by a direct current of one ampere flowing in a single-turn loop. The linear coil distribution in fact, provides a vector of magnetic field which pointed upward and moves linearly over the pad.

Since the inductor is a three-phase system with six coils, each two coils are connected to one phase of the power supply providing a phase winding. For instance, (a and a') forming phase-A, and similar to that (b and b') and (c and c') forming the other two phases B and C as illustrated in Fig.IV.2.

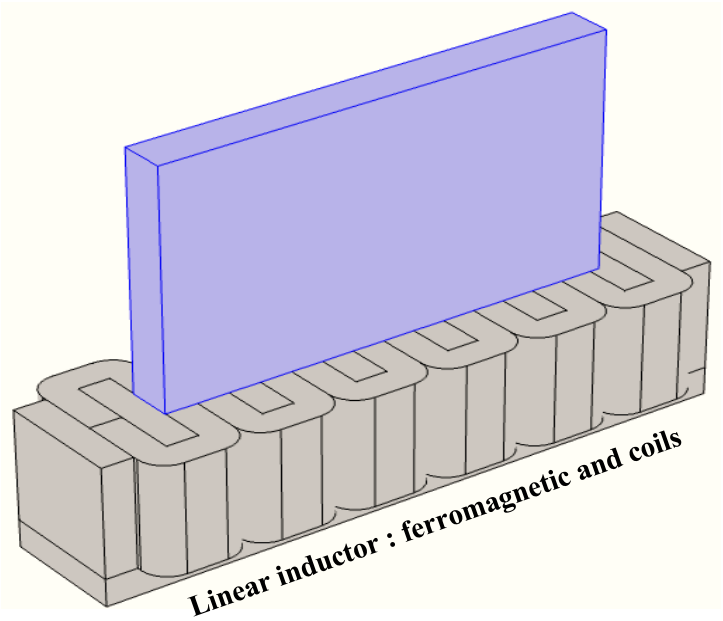

Fig.IV.1 **:** *3D Geometry of the proposed electromagnetic inductor*

The coils distribution between the three phases is made in a way that assures a reasonable constant magnetic flux density as a resultant of the three phases travelling above the charging pad, [2].

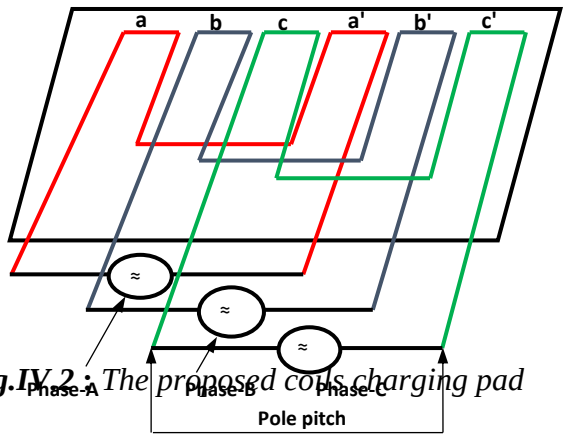

Fig.IV.2 **:** *The proposed coils charging pad*

1.2 Travelling magnetic field principle

If an alternating current flows through the phase coil, it produces a pulsating mmf wave, whose amplitude and direction depends on the instantaneous value of the current flowing through the coil. Fig.IV.3 illustrates the mmf distribution in space at various instants due to an alternating current flow in inductor. Each phase coil produces similar sinusoidally distributed mmf waves, but displaced by 120 electrical degrees in space from each other (see Fig.IV.3). The balanced

three-phase instantaneous currents flowing through the three-phase coils of the charging pad can be expressed as,

$$\begin{cases} I_A = I_0 \cos(\omega t) \\ I_B = I_0 \cos(\omega t + 2\pi/3) \\ I_C = I_0 \cos(\omega t + 4\pi/3) \end{cases} \quad \textbf{(IV.1)}$$

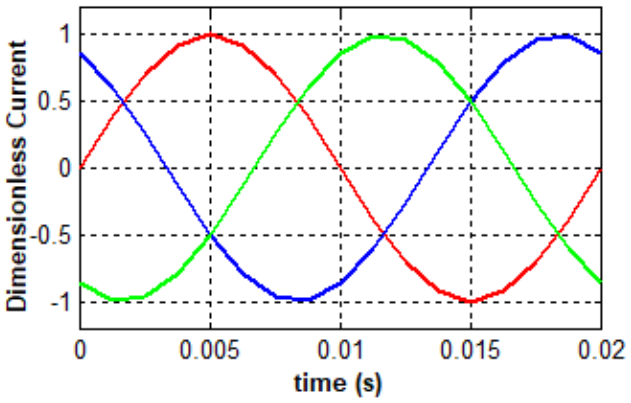

Fig.IV.3 **:** *Three phase current varying with time*

When the currents presented by the system of equations (IV.1) flow through the respective phase coil (phase-A, B and C), each produces a sinusoidally distributed mmf wave in space, pulsating along its magnetic axis and having a peak located along the axis. Indeed, when current vary with time a magnetic field will come forth as shown in Fig.IV.4. When θ = 0°, the point with the maximum magnetic field density is on winding A.

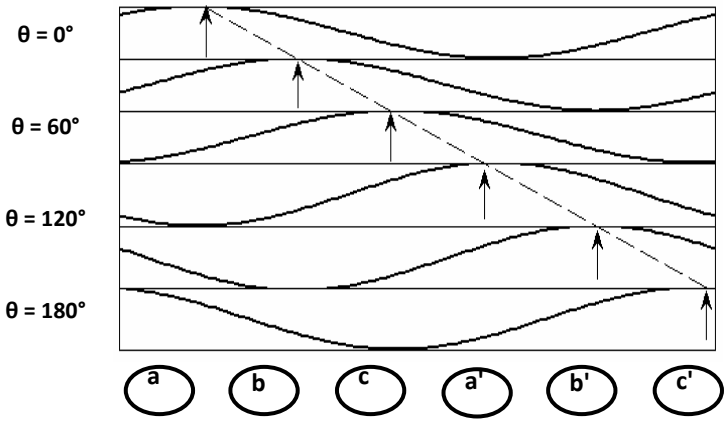

Fig.IV.4 **:** *Production of travelling magnetic field with three phase currents.*

As θ increases, the point will travel on the core from *A* to *B* and to *C*, namely a travelling magnetic field is produced. The induced current in the melt interacting with the travelling magnetic field. Each mmf wave can be represented by a space vector along the axis of its phase with magnitude proportional to the instantaneous value of the current. The resultant mmf wave is the net effect of the three component mmf waves at any point in the air above the pad defined by a distance *x*. The origin of *x* can be chosen to be the axis of phase-A. At any instant of time; all the three phases contribute to the air gap mmf along the path defined by *x*. The resultant magnetic flux density wave above the pad at a distance ***x*** from the chosen origin can be obtained as:

$$\boldsymbol{B(x,t) = B_{max} \cos\left(\omega t - \frac{\pi x}{\tau}\right)} \quad \textbf{(IV.2)}$$

Where τ, is the pole pitch, *i.e.* the distance between two neighbouring poles on the axial length of the pad as shown in Fig.IV.2), ω is the pulsation ($\omega = 2\pi f$) and *f* is the frequency of the primary power supply. It can be seen from Fig.IV.2 that if the mmf wave travels a complete pitch pole, the displacement *x* is equal to τ, at the same time θ completed a half cycle (π) of a period.

$$\boldsymbol{\frac{x}{\theta} = \frac{\tau}{\pi} \; or \; x = \theta \frac{\tau}{\pi}} \quad \textbf{(IV.3)}$$

As $\theta = 2\pi ft$, the synchronous velocity of the travelling wave can be given as:

$$\boldsymbol{U_s = \frac{dx}{dt} = \frac{dx}{d\theta} \times \frac{d\theta}{dt} = \frac{\tau}{\pi} \times \omega = 2\tau f} \quad \textbf{(IV.4)}$$

Note that the synchronous velocity does not depend on the number of poles and only depend on the pitch pole, [4]. The Fig.IV.5 gives a 3D graphical representation of the streamlines as well as the spatial distribution of the magnetic field in the cavity for a frequency of ($f = 50Hz$) and a current intensity of ($I = 8A$), obtained by numerical simulation.

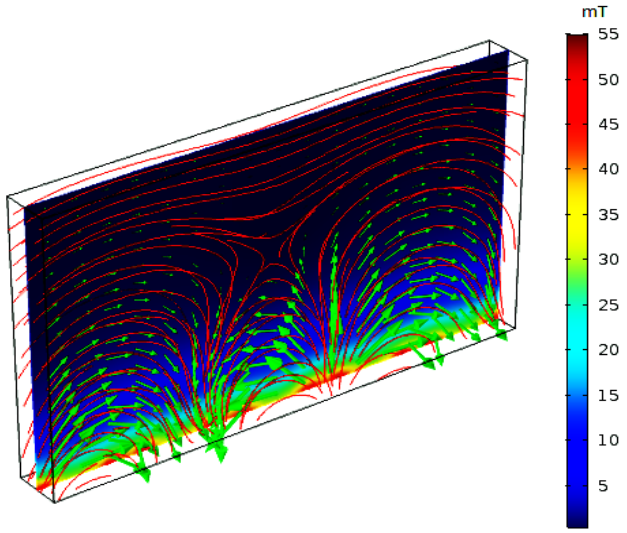

Fig.IV.5 : *Spatial evolution of the travelling magnetic field intensity. The red lines correspond to the streamlines and volume vectors are the magnetic field for the conditions:* f_0 *= 50Hz and* $J_0 = 10^6$ *A/m*^{2}.

2 Electromagnetic body force

In order to determine the body force responsible for the electromagnetic stirring, it is necessary to technically characterize the inductor used. Indeed, the wavelength λ and the pole pitch τ are $\lambda = 2\tau = 96$ mm, so that the wave number is $k = 2\pi/\lambda = 65.45$ m^{-1}. The synchronized velocity of the moving magnetic field is $U_S = f_0\lambda = \omega/k = 4.8$ m/s. It is worth noticing that the width and length of both the inductor and the cavity are rather short; it will be seen later that this strongly affects the strength of the effective driving force. In spite of the moderate aspect ratios (L/e = 20 and L/H = 5/3), the fluid flow model is based on the assumption that these ratios are large enough to justify the existence of a central region in which the flow can be considered to be quasi-parallel to the x axis.

The expression of the electromagnetic force when the fluid domain is infinite in the z direction is detailed in Reference [2]. The vector potential $A = A(x, y, t)e_z$ has only one nonzero component; according to the Maxwell equations, the current density and magnetic field obey the relations:

$$\begin{cases} \boldsymbol{J} = -\left(\boldsymbol{\nabla\varphi} + \frac{\partial \boldsymbol{A}}{\partial \boldsymbol{t}}\right) \\ \boldsymbol{B} = \boldsymbol{\nabla} \times \boldsymbol{A} = \left(-\frac{\partial \boldsymbol{A}}{\partial \boldsymbol{y}}, \boldsymbol{0}, \frac{\partial \boldsymbol{A}}{\partial \boldsymbol{x}}\right) \end{cases} \qquad \textbf{(IV.5)}$$

Moreover, the periodic *x* and *t* dependences yield:

$$\boldsymbol{A = A_0 M(y) exp[i(kx - \omega t)]} \quad \textbf{(IV.6)}$$

The *z* dependence is quite classic:

$$\boldsymbol{M(y) = exp\left[-\left(k + i\frac{\mu\sigma\omega}{2k}\right)y\right]} \quad \textbf{(IV.7)}$$

In these expressions, μ and σ stand for the permeability and conductivity, respectively, of the melt.

The expression of the electromagnetic force $\boldsymbol{F = J \times B}$ was developed in the reference [3], for a confined configuration identical to that of our case, as follows:

$$\boldsymbol{F_x = \frac{\sigma\omega k^*}{2} A_0 \exp(-2k^* y) + \frac{k^* A_0^2}{2} \exp(-2k^* y)\left[\left(\frac{\pi}{2e}\right)^2 \frac{\sin(2X^*)}{\mu} - \sigma\omega \cos(2X^*)\right]} \quad \textbf{(IV.8)}$$

$$\boldsymbol{F_z = -\frac{\pi k^* \beta^* A_0^2}{2\mu e} exp(-2k^* y)\cos(2X^*) + \frac{\pi A_0^2}{4\mu e}\beta^{*2} exp(-2k^* y)\sin(2X^*)} \quad \textbf{(IV.9)}$$

$$\boldsymbol{F_y = \frac{A_0^2}{2}\left[\sigma\omega\beta^* - \left(\frac{\pi}{2e}\right)^2 \frac{k^*}{\mu}\right] exp(-2k^* y) - \frac{A_0^2}{2}\left[\sigma\omega\beta^* - \left(\frac{\pi}{2e}\right)^2 \frac{k^*}{\mu}\right] exp(-2k^* y)\cos(2X^*) - \frac{A_0^2}{2}\left[\sigma\omega\beta^* - \left(\frac{\pi}{2e}\right)^2 \frac{k^*}{\mu}\right] exp(-2k^* y)\sin(2X^*)} \quad \textbf{(IV.10)}$$

with $k^{*2} = k^2 + (\frac{\pi}{2e})^2$, $\beta^* = -\frac{\mu\sigma\omega}{2k^*}$ and $X^* = k^* x - \frac{\pi z}{2e} + \beta^* y - \omega t$. Throughout this article, the upper index ()* refers to quantities that take into account the narrowness of the fluid domain.

The two components of the active averaged electromagnetic force in the melt can be expressed as follows:

$$\begin{cases} \langle \boldsymbol{F_x} \rangle = \frac{\sigma\omega k^*}{2} \boldsymbol{A_0^2 exp(-2k^* y)} \\ \langle \boldsymbol{F_y} \rangle = \frac{\boldsymbol{A_0^2}}{2}\left[\boldsymbol{\sigma\omega\beta^* - \left(\frac{\pi}{2a}\right)^2 \frac{k^*}{\mu}}\right] \boldsymbol{exp(-2k^* y)} \end{cases} \quad \textbf{(IV.11)}$$

As expected, the component F_z has a zero-time (or x) average. In addition, all terms are proportional to $sin(2X^*)$ or $cos(2X^*)$, which are periodic functions of *t* and *x*, respectively, as can be discerned in the Fig.IV.6. Thus, both F_x and F_y have a nonzero average that decreases exponentially with *z* and exhibits the classic skin depth of thickness $1/k^*$, (see Fig.IV.7). Clearly,

the average of F_x is the driving force; the average of F_y is a kind of z-dependent extra-gravity, which affects the pressure distribution.

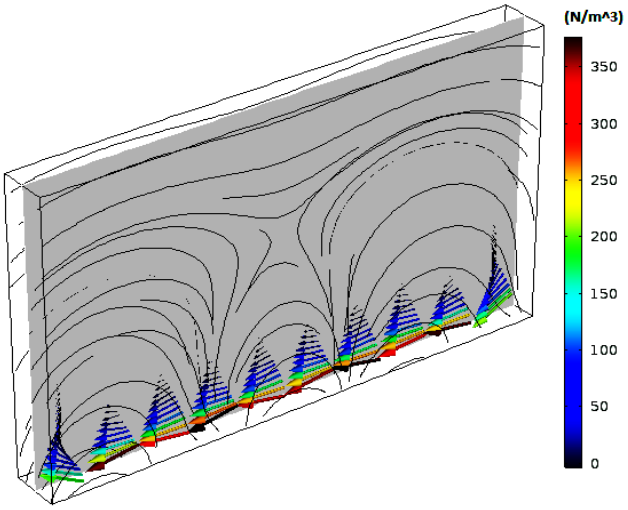

***Fig.IV.6* :** *3D spatial evolution of electromagnetic forces: the black lines correspond to the streamlines of magnetic field and volume vectors are the Lorentz forces.*

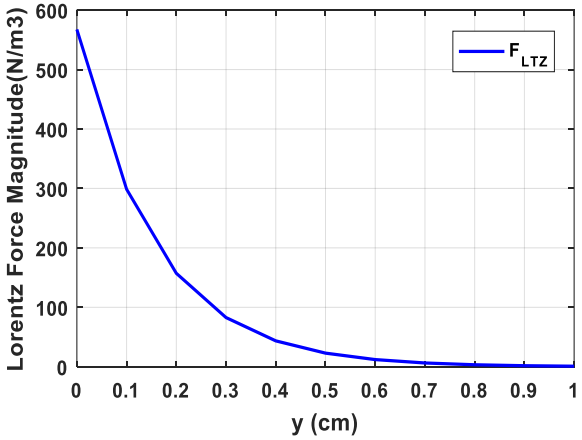

***Fig.IV.7* :** *Spatial evolution of the electromagnetic force magnitude in the vertical direction (x = 5cm, z = 0.5 cm and y varies between 0 and H= 6 cm). Results obtained for the condition: f_0 = 50Hz and I = 8 A.*

However, this inductor also has a finite length; this generates a magnetic field reduction. Indeed, at a given time, over the total length L_{IN} = *24.4 cm*, which is smaller than 3 times the wavelength $\lambda = 2\tau = 96$ *mm*, only two full pairs of magnetic poles can be found. The corresponding reduction of the electromagnetic force can also be estimated as being on the order of 1/5, [3]. As a consequence, a reduction characterised with global factor C ≈ 0.05, such that the typical value of the effective force is:

$$F_{em} = CA_0^2 \frac{\sigma\omega k^*}{2} \quad \textbf{(IV.12)}$$

The scaling law for the driving force, namely, the way it depends on the physical parameters of the inductor, remains independent of *C*. This is a very important point, because it means that *C* can be determined once for any given inductor.

3 Numerical simulation of metallic alloy solidification under forced convection

A 3D numerical simulation of the solidification process under the effect of forced convection in the opposite direction of thermosolutal convection was performed and compared the results obtained numerically with the experimental results for highlighting the influence of forced convection on the solidification process in terms of velocity, thermal, and solute distribution. We propose a 3D numerical model which is described in chapter 3. However, we add the Lorentz force term in Eq (III.12) to express the contribution of the forced convection. The same boundary conditions used in the case of the solidification process under thermosolutal convection are adopted, as shown in the following equation:

$$\rho_0 \left[\frac{\partial(f_l V_l)}{\partial t} + (f_l V_l . grad) V_l\right] - \nabla.(\mu_l . \nabla . f_l V_l) + f_l^2 \frac{\mu}{K} V_l = \rho_0[1 - \beta_T(T - T_0) + \beta_C(C_l - C_0)] f_l g - f_l grad(p) + f_l F_{LTZ} \quad \textbf{(IV.13)}$$

With :

$$\beta_T = \frac{1}{\rho_0}(0.742841 + 5.8927 \times 10^{-3} C_l)$$

$$\beta_C = -\frac{1}{\rho_o}(47.6554 - 2 \times 0.10063 \times C_l - 5.8927 \times 10^{-3} T)$$

$$\nabla.(f_l V_l) = 0$$

$$\frac{\partial\langle H\rangle}{\partial t} + (f_l Cp_l) f_l V_l . grad(T) = (f_l \lambda_l + f_s \lambda_s) div[grad(T)]$$

$$\frac{\partial\langle C\rangle}{\partial t} + f_l V_l . grad(C_l) = \nabla.(f_l D_l \nabla C_l) + \nabla.(f_l D_l \nabla C_l), \langle C\rangle = f_s C_s + f_l C_l$$

$$K = \frac{f_l^3}{(1-f_l)^2} \frac{\lambda_2^2}{180}$$

Where $$F_{LTZ}\begin{cases}\langle F_x\rangle = \frac{\sigma\omega k^*}{2}A_0^2 exp(-2k^*z)\\ \langle F_z\rangle = \frac{A_0^2}{2}\left[\sigma\omega\beta^* - \left(\frac{\pi}{2a}\right)^2\frac{k^*}{\mu}\right]exp(-2k^*z)\end{cases}$$

3.1 Effect of electromagnetic stirring on hydrodynamic configuration

In this part, we present the hydrodynamic field in the case of electromagnetic stirring in the opposite direction of natural convection. Noting that the natural convection is created by the application of an average horizontal temperature gradient equal to 20 K. However, forced convection is generated by the application of an external travelling magnetic field (TMF).

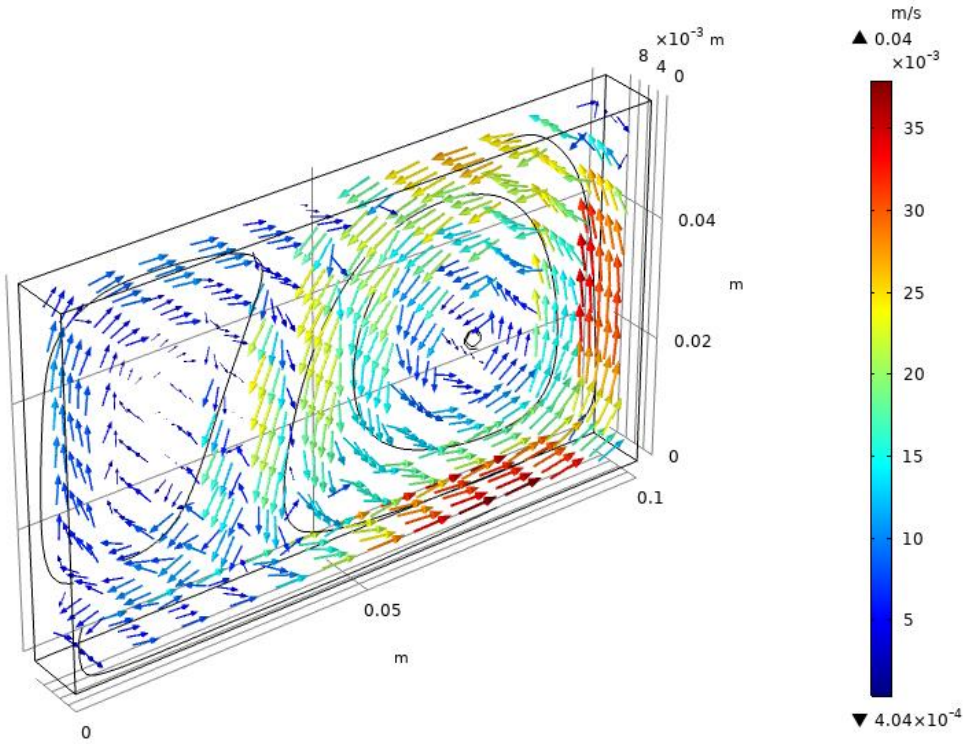

Fig.IV.8 : *3D numerical simulation of the dynamic configuration of the stirring in the opposite direction*

Fig. IV.8**,** clearly shows the development of two vortices, one rotates inversely to the other. The small vortex on the left wall of the cavity, which corresponds to the effect of natural convection, rotates clockwise. In the left base part of the cavity, we notice the development of a second vortex with a counter-clockwise rotation direction. This behavior is due to the existence of forced convection which acts against the natural convective flow direction. A competition effect

between the two vortices is created in the cavity. We notice an explicit dominance of the forced convection with an order of magnitude of speed of 4 cm/s, compared to the thermosolutal convection.

It is interesting to compare electromagnetic forces with buoyancy. We have introduced a non-dimensional interaction parameter *N*, defined as the ratio between Lorentz force F_{LTZ} and buoyancy, namely:

$$\boldsymbol{N = \frac{F_{LTZ}}{g\rho\beta_c\Delta C}} \qquad \textbf{(IV.14)}$$

In the case of electromagnetic stirring in the opposite direction of natural convection, the value of *N* is equal to 9.7. Thus, the electromagnetic forces are usually predominant compared to buoyancy. Finally, before solidification, the Reynolds number based on the maximum velocity *U* is:

$$\boldsymbol{R_e = \frac{U\left(\frac{H^2}{L}\right)}{\nu} = 10080} \qquad \textbf{(IV.15)}$$

The value of R_e indicates that the bulk flow regime is likely to be turbulent. This is consistent with the significant turbulent fluctuations.

3.2 Effect of EM stirring on the temperature field evolution

We present in this section the numerical simulation results of the studied solidification process under the effect of the forced convection in the opposite direction to natural convection. The evolution of the temperature fields over time is shown in Fig. IV.9.

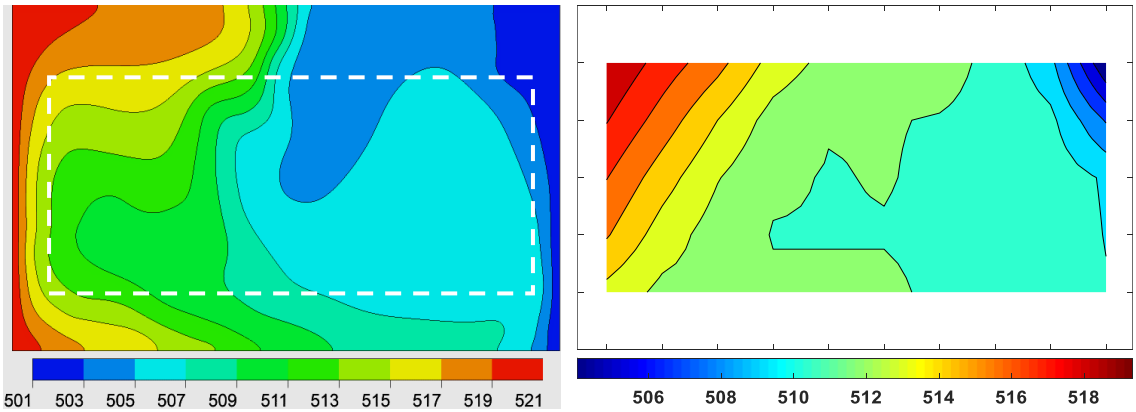

(a)t = 2000 s

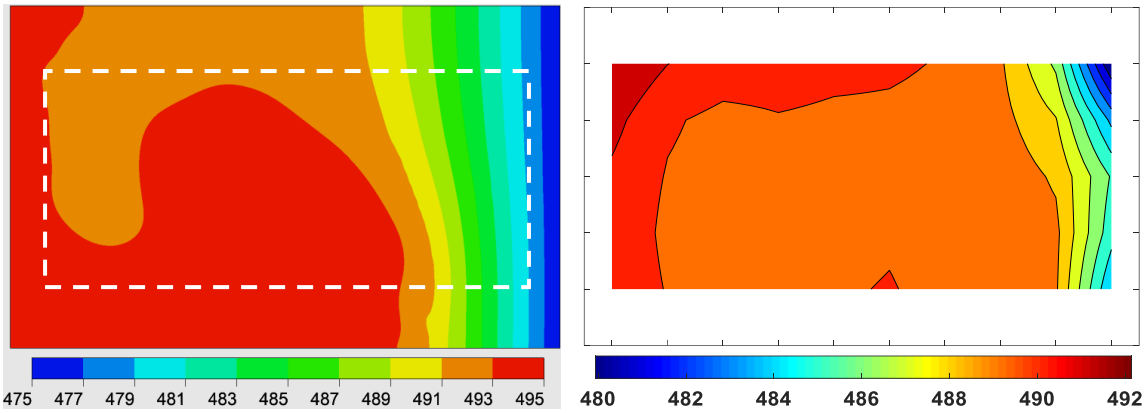

(b) t = 2950 s

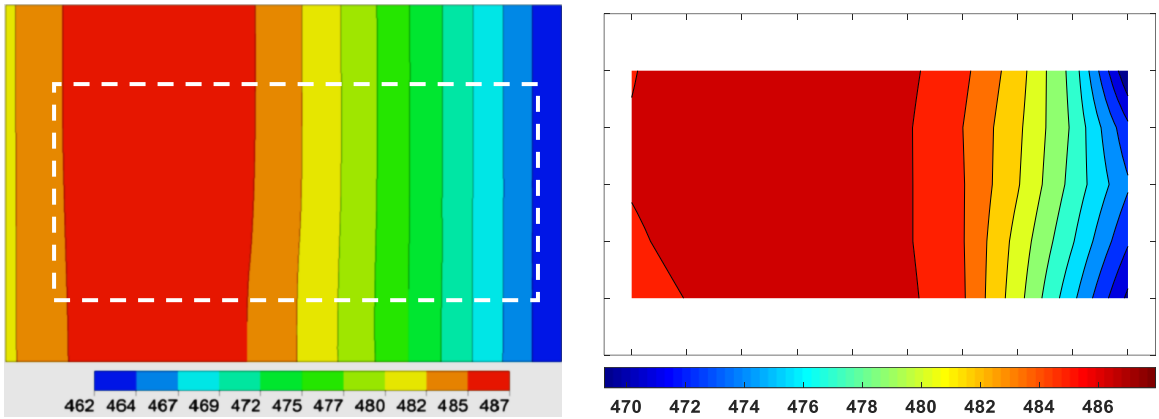

(c) t = 3500s

Fig.IV.9 **:** *Temperature maps recorded at selected times during the solidification of a Sn-10wt.%Pb alloy: (a) t = 2000 s, (b) t = 2950 s and (c) t = 3500 s, after the initial simulation time (t = 0 s) which corresponds to the time 1400 s of the experimental process. The numerical calculations are presented on the left side and the experimental data on the right side. The experimental measurement area in which thermocouples are present is indicated by a white dashed rectangle on the numerical snapshots presented in the left column. Conversely, the white strip framing the coloured temperature map on the experimental snapshots corresponds to the part of the domain in which no thermocouple is present.*

Selected instantaneous colourmaps at t =2000 s, 2950 s,3500 s of the temperature field is given in Fig. IV. 9 to illustrate the thermal evolution during the solidification process. The results in the left column have been obtained numerically and those in the right column have been obtained experimentally. A buoyancy force occurs in the cavity due to a temperature difference between the side walls. In the absence of other forces, the melt on the hotter lateral side would flow upward, while the melt near the cooler wall would flow downward, producing

a vortex and a positive temperature gradient in the vertical direction (discussed previously in Chapter 3). The application of electromagnetic force on the cavity bottom toward the colder side also leads to the creation of two vortexes which makes liquid goes upward near a colder side and the same behaviour near the hotter side.

The first snapshot (Fig. IV. 9(a) at t = 2000s) correspond to a completely liquid sample. we noticed that the stirring mode in the opposite direction of the natural convection changed the flow morphology. This is indicated by the deformation of the isotherms in this case with a negative slope which means the appearance of a vortex in the opposite direction of the thermosolutal convection called natural. The thermal fields obtained from numerical simulation and experimental measurements clearly reveal that the flow is effective enough to deform the isotherm lines, with a maximum magnitude of velocity of v_{max} = 4.27 cm/s obtained by simulation.

Fig. IV. 9(b) shows the temperature field corresponding to time 2950 s, i.e. after the beginning of the solidification. The isotherms gradually become vertical and less distorted. due to the decrease of the temperature of the cold wall (right side) below the liquidus temperature (T_L = 492 K), the liquid flow becomes feeble thus the heat is transferred mainly by a dominant conduction mode. Although, the temperature difference between the right and the left walls exists, the temperature is mostly uniform in the cavity.

Fig. IV. 9(c) corresponds to the instant t = 3500 s. We noticed the same behavior as in the previous selected instants. Deformation of the isotherms in the stirred cases and the low values of local temperature gradients clearly indicate the effect of electromagnetic stirring in the last liquid. However, temperature maps show clearly on the left side the existence of isotherms which signal a temperature level ranging from 484 to 488 K, that corresponds to a level of undercooling below of the liquidus temperature (T_L = 492 K) of 8 and 6 K respectively. Indeed, an estimated calculation of the undercooling of this alloy, presented in the work Hachani *et al*. [5], gives a new range between 0.5 and 10 K. So, we attribute the progress of these isotherms to the advancement of a second solidification front on the left side. This conclusion is very consistent with the positions of the shrinkage that correspond to the last liquid solidified.

3.3 Macrostructure

To evaluate the effect of forced convection generated by the chosen electromagnetic stirring mode on the grain size and the final metallographic structure, macrostructures of samples obtained from both solidification experiments described previously have been revealed. Macrostructures are obtained after post mortem analysis, which consists of several passes of polishing and chemical attack with a mixture of 75% Vol HCL (37 mol%/v) and 25% Vol HNO3 (69.5%).

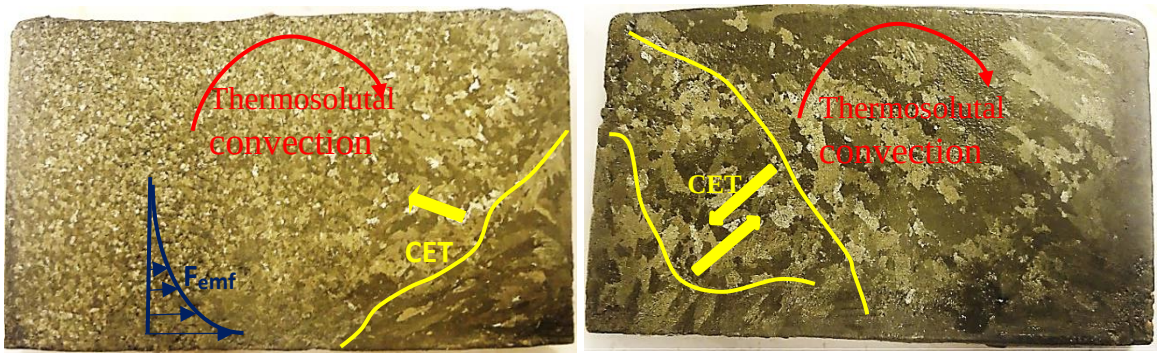

(a) **(b)**

Fig.IV.10 : *Macro structure on the lateral plane of Sn-10wt.%Pb ingot. The experimental conditions are temperature difference DT = 40 K, cooling rate CR = 0.03 K/s and the applied current intensity I = 8.2 A. (a)The case of stirring in the opposite direction of thermosolutal convection. (b) The case of thermosolutal convection.*

Fig.IV. 10(a) presents the macrostructures of Sn-10wt.%Pb solidification under the effect of The stirring in the opposite direction of thermosolutal convection. A zone of predominantly equiaxed grains of fine size on almost 85% of the ingot, has been observed. A columnar structure is located in the lower right corner (cold side) of the ingot, unlike the case of solidification under the effect of thermosolutal convection, we observe that the dominant morphology of the macrostructure is columnar with an equiaxed zone corresponding to the last liquid at the end of solidification. This macrostructure refinement is the direct consequence of electromagnetic stirring, which has two main effects. First, the activated forced convection in the bulk driven by Lorentz force, which homogenizes the pool concentration and reduces the temperature gradients, thereby creating favourable conditions for the appearance of the CET. Second, a hot flow impinging the solid-liquid interface can promote remelting, and

consequently dendrite fragmentations. These fragments that transported by convection can create equiaxed grains under specific conditions.

Moreover, this stirring mode has confirmed its effectiveness for homogenizing temperature in the liquid by reducing the gradients of temperature. We noticed that in this stirring mode, the area extension of the undercooling liquid in front of the solidification is almost twice that of solidification under the effect of thermosolutal convection. Maintaining this high degree of undercooling greatly promotes remelting mechanism of dendrites . It is important to note that the efficiency of this kind of electromagnetic stirring to refine the structure is significantly improved compared to that of the case of the solidification under the effect thermosolutal which presented Fig.IV. 10(b) and described in chapter 3. In parallel with the mechanical effect of fragmentation called neck effect (separation of secondary or tertiary dendrite arms from the main trunks in the channels during solidification), this mode of stirring allowed a significant penetration of the liquid in the mushy zone and could reinforce the effect of the remelting of the dendritic arms. These results are in good agreement with Fleming's criterion on dendrite arm remelting. This criterion is based on the comparison between the velocity of the interdendritic liquid u_l^d, and the advancement velocity of the isotherms V_T, $\frac{u_n}{V_T} > 1$ (re-flow criterion). It has been shown that the remelting of dendrite arms can be attributed to two main factors:

- Either the increase in the temperature or the concentration of the surrounding liquid, which is induced by the penetration of the hot liquid from the liquid bath into the mushy zone (entrance velocity).
- Or the increase in the average concentration caused by the convection of the interdendritic liquid in the direction of the thermal gradient (outgoing velocity of the mushy zone).

Moreover, it is important to mention that, the remelting phenomenon of the dendritic arms becomes predominant if the velocity of the interdendritic liquid is faster than the velocity of isotherms advancement in the direction of the solidification front progression. Remelting is effective when $u_l^d > V_T$, (see Fig. IV. 11).

This phenomenon is expressed in the following equation:

$$\frac{\partial f_L}{\partial c_L} = -1\left(\frac{1-\beta}{1-k_p}\right)\left(1+\frac{u_l^d.\nabla T}{CR}\right)\frac{f_L}{c_L} \qquad \textbf{(IV.16)}$$

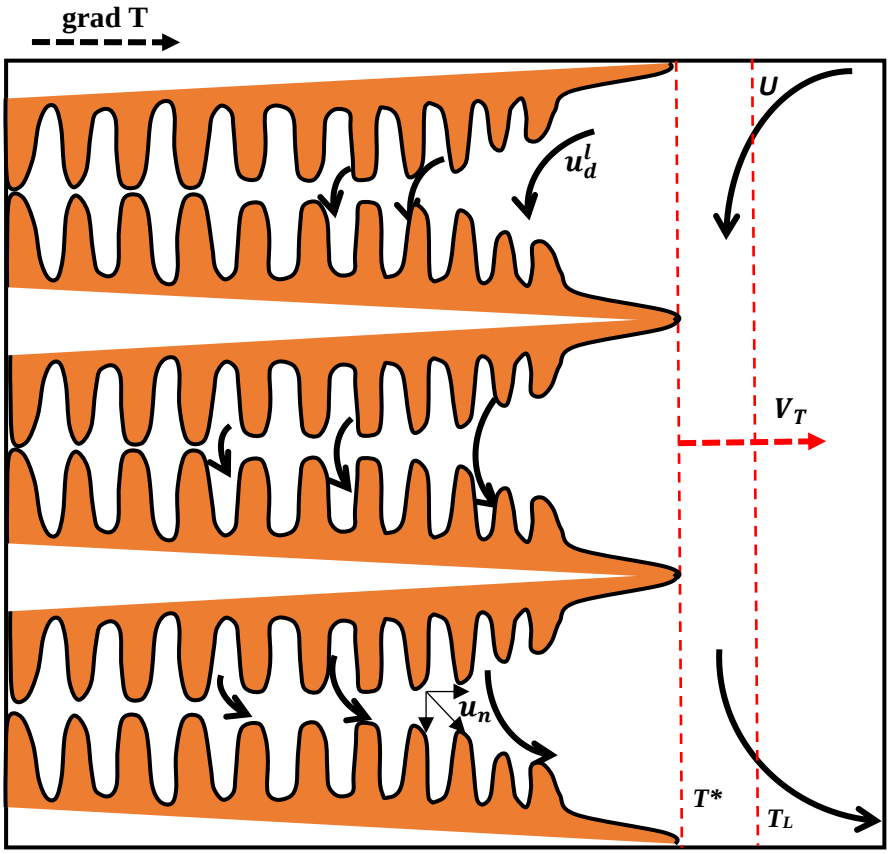

Fig.IV.11 **:** *Schematic representation of the convection velocities: U in the liquid, in the interdendritic regions, and un its projection on the temperature gradient, parallel to the direction of advancement of the isotherms. The velocity of advancement of the isotherms is noted.[6]*

Where β is the shrinkage coefficient ($\beta = \rho_l/\rho_s - 1$), u_l^d is the velocity of the interdendritic liquid, CR is the cooling rate, f_L is the liquid fraction and c_L is the liquid concentration. ρ_l and ρ_s are the specific masses of the liquid and solid phases, respectively. However, the cooling rate can be expressed as a function of the advancement velocity of the isotherms V_T, according to the relation:

$$|\boldsymbol{CR}| = \boldsymbol{V_T}.\boldsymbol{\nabla T}$$

Equation (IV.16) becomes:

$$\frac{\partial f_L}{\partial c_L} = -\left(\frac{1-\beta}{1-k_p}\right)\left(1+\frac{u_l^d.\nabla T}{V_T.\nabla T}\right)\frac{f_L}{c_L} \qquad \textbf{(IV.17)}$$

And by projection on the direction of advancement (direction parallel to isotherm lines) we obtain:

$$\frac{\partial f_L}{\partial c_L} = -\left(\frac{1-\beta}{1-k_p}\right)\left(1+\frac{u_l^d}{V_T}\right)\frac{f_L}{c_L} \qquad \textbf{(IV.18)}$$

In the case where the specific mass considered constant (the same specific mass in both phases), β becomes zero. After integration of the relation (IV.18), a Scheil-Gulliver type relation (case for which there is no interdendritic convection, $u_n = 0$) is obtained, according to the isotherms advance and the interdendritic liquid velocity:

$$f_L = \left(\frac{c_L}{c_0}\right)^{-\left(\frac{1}{1-k_p}\right)\left(1-\frac{u_l^d}{V_T}\right)} \qquad \textbf{(IV.19)}$$

A second phenomenon can probably take place, favouring in turn the process of fragmentation of the dendritic arms. This is the increase in the viscosity of the interdendritic liquid due to the high presence of these fragments, which could certainly reduce the velocity of the flow in the mushy zone but favoured the entrainment of the fragments transported by the movements of forced convection. This phenomenon has been mentioned in previous works as J. W. Gao et al [7], J. P. Gu et al. [8], and Q. Li et al [9].

Moreover, at the scale of a secondary dendrite arm, if the velocity of the outgoing interdendritic liquid is greater than the velocity of the isotherm-lines advancement, in the direction of the temperature gradient, there will be a supply of the coldest liquid and more solute (Fig. IV. 11). We can then consider that the lower temperature of the surrounding liquid will have no influence compared to the effect of the solute concentration. The diffusion of the heat becomes faster compared to that of the solute, i.e., quick homogenize of the temperature. On the other hand, the increase of the average concentration of the surrounding liquid causes the refusion of the dendrite arm until complete remelting of its "neck", allowing the fragment to be detached. Indeed, the formation of segregated channels is a direct consequence of this phenomenon in the case of forced convection, in which the fragments of remelted dendrites are carried away by the convection going to the direction of the temperature gradient (Hellawell et al. [10]). We can estimate the Lewis number defined by the ratio between the thermal diffusivity and chemical diffusion, which is equal to 6.05×10^3 for Sn-Sn-10wt.%Pb alloy.

The experimental analysis conducted show that the position of the electromagnetic stirrer with respect to the position of the isotherm, which corresponds to the liquidus (TL = 219.46 °C), is an important parameter regarding the remelting of the dendrite arms, since this remelting depends directly on the velocity of the interdendritic liquid. In particular, we can estimate the necessary minimum distance to induce the remelting, by determining the order of magnitude of the velocity of the interdendritic liquid for a Darcy flow by neglecting the gravitational effect:

$$\boldsymbol{u_n = -\frac{K}{\rho\nu}\frac{dp}{dz}} \quad \textbf{(IV.20)}$$

Where *K* and *p* are the permeability of Sn-10*wt*.%Pb and pressure, respectively. We can then estimate the order of magnitude of the pressure gradient induced by the action of the magnetic field, R. Moreau [11]: $(B_0^2/\mu_0.L)$. In our case, we define *L* as δ, the electromagnetic skin depth. The equation (IV.18) becomes:

$$\boldsymbol{u_n \sim \frac{K}{\rho\nu}\frac{B_0^2}{\mu_0 H}} \quad \textbf{(IV.21)}$$

Therefore, for the reflow to take place, the condition (IV.21) must be satisfied and the following relation for the remelting criterion R_C, is thus obtained:

$$\boldsymbol{R_c \sim \frac{1}{V_T}\frac{K}{\rho\nu}\frac{B_0^2}{\mu_0 H} > 1} \quad \textbf{(IV.22)}$$

General conclusions can be deduced:

- An increase in the induction power (i.e., a high intermittent electromagnetic field) which increases the rate of liquid convection in the melt and the mushy zone (interdendritic liquid).
- High permeability improves remelting. A relative high permeability of the mushy zone favours the penetration of the liquid therein. The convection of the interdendritic liquid can therefore be important enough to break up the dendrites, which causes the refinement of the structure.
- Increasing the cooling rate, has two distinct effects, first, the remelting of the dendrite arms is not favoured because the velocity of the isotherms advancement is increased. This does not allow the solute-rich liquid to reach the poorest regions in order to remelt the dendrite arms. Second, the extent of super cooling region ahead of the solidification front is greater, so the survival of the fragments is thus improved. To obtain the

fragmentation of the dendrites, the cooling rate must be large enough, so that the fragments are not instantaneously remelted, but it must also be lower than the convection velocity of the interdendritic liquid.

- Decreasing the stirrer-crucible distance promotes remelting. In fact, intensifying the convection movements (EM stirring) on the solidification front enhances the liquid penetration into the mushy zone, which has the impact of increasing the convection velocity of the interdendritic liquid.[6]

3.4 Effect of electromagnetic stirring on meso and macrosegregation

Following the comparison of temperature maps during the solidification process between simulation and experiment, post-mortem analysis comparisons are shown. Two experimental techniques were performed on the final ingot to get the distribution of the elements of the solidified alloy, which is the purpose of this study. Firstly, there's X-ray imaging, which involves taking a snapshot in greyscale with distinct areas indicating the presence of the heaviest element (in our case lead). The second technique involves coring samples of 3 mm in diameter at the 50 positions corresponding to the thermocouples, then determining the local composition averaged throughout the volume of the sample using chemical analysis ICP (Inductively Coupled Plasma).

Fig.IV.12 presents the X-ray photograph of the solidified Sn- 10 %pds Pb ingot and the corresponding distribution of the lead concentration obtained by numerical simulation, averaged over the thickness and presented in grey levels, in order to have a qualitative comparison.

We notice that macrosegregation zone is smaller than in the case of the solidification under the thermosolutal convection which presented in chapter 3 and is shifted from the left side to the centre of the ingot. This can be attributed to the second solidification front developed from the left side of the ingot (see the temperature maps at time t = 3500 s). This segregation zone has a lower concentration level than in the case of the solidification under the thermosolutal convection chapter 3.

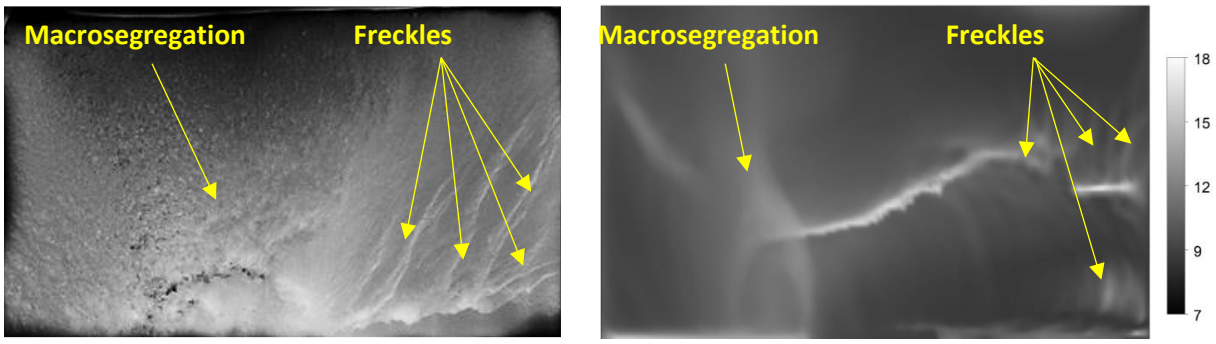

(a) (b)

Fig.IV.12 **:** *(a) Photo of X-ray radiography of the solidified sample, (b) Lead concentration map averaged over the sample thickness calculated by numerical simulation, at the end of the solidification process (in wt.%).*

A significant number of segregated channels were noticed on the right side of this ingot. Numerically, in Fig.IV.12(b), we can find these channels in the right part of the ingot in the form of arcs. However, their number and position do not exactly reproduce those observed in the experiment. In order to have an acceptable comparison, it is necessary to carry out a series of reproducibility of the same experiment in order to know if these channels will certainly be located at the same positions. Hachani [12] conducted such a study for the same experimental conditions. Preliminary results tend to show that the number of segregated channels and their position is not obtained deterministically, and vary from one experiment to another, with similarities in the shape of the channels and the end of the solidification chimney. In our numerical results, we still manage to have segregated channels in the same part of the ingot as the experiment. We also obtain an end-of-solidification chimney, but it is offset from the experiment presented here.

In the light of the resulted obtained, we believe that the application of electromagnetic stirring in the opposite direction of thermosolutal convection, has several effects on segregation:

1- The creation of a force opposing the lead stratification mechanism, which significantly reduces the size and density of the segregation in the last liquid.
2- A competition between the downward gravitational drainage forces and the one from the convective flow in the opposite direction upward. Indeed, it is clear that there is a detachment effect of the segregation zone compared to the case of solidification under the effect of natural convection and the case stirred in the same direction of the latter.

3- The fragmentation of the dendritic arms due to the reflow leads to a microsegregation in the zone characterized by the formation of equiaxed grains.

3.5 Effect of electromagnetic stirring on the morphology of segregated channels

A 3D view of solute distribution exceeding the nominal concentration (C0 = 10 wt %) is presented in Fig.IV.13 in order to study the effect of this mode of electromagnetic stirring, which attempts to correct the defects linked to segregation. The main objective is to examine the efficiency of the stirring in the opposite direction of thermosolutal convection, on the segregation behaviour in terms of the level of concentration, size, position, and morphology, namely segregated channels which are difficult to track.

As expected, the numerical results demonstrate that segregated channels are formed during the solidification process, which appear at the right side of the sample characterized by a columnar structure with a non-regular morphology (a complex geometric shape), However, there are segregated channels developed near the side walls with a curved tubular structure (see Fig.IV. 13(a-c)). These channels are initiated close to the cold right side, at a certain height due to the effect of EM stirring in the opposite direction of thermosolutal convection where the Lorentz force prevents sedimentation of the solute. As the mushy zone ripens, they develop inside it with a descending quasi-arc shape, in connection with the descending convective flow acting in this solidification area, while a chimney of macrosegregation was developed in the lower left part of the sample corresponding to the last liquid solidified. It is very noticeable that this stirring method significantly favours the development of segregated channels in terms of number, However, it reduces its dimensions. On the other hand, we discover that it plays a positive role in reducing macrosegregation by lowering the level of concentration inside it, as well as in reducing the sedimentation rate at the bottom of the cavity ($C_{max} \leq 12\%$).

As mentioned earlier in chapter three, there is a potential possibility of remelting in the mushy zone during the solidification process, which is mainly related to two main mechanisms: local remelting due to a hot flow transported by convection and/or concentration increase in the liquid surrounding the dendrites due to the transported flow of solute-rich liquid into these regions (inter-dendritic region). In this part, we focus on studying the effect of forced

convection in the opposite direction to thermosolutal convection, on the formation of the segregated channels at morphology and concentration level.

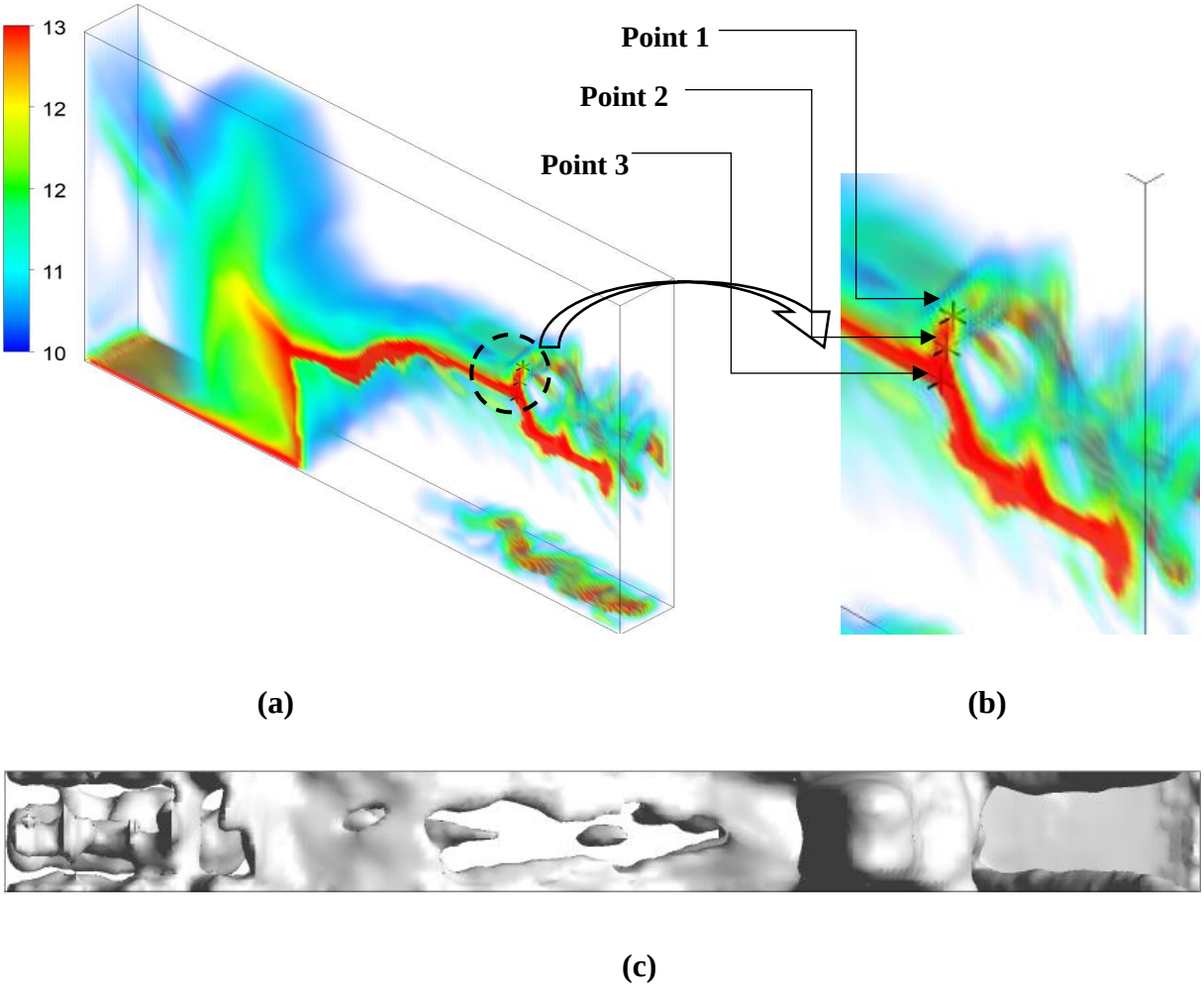

Fig.IV.13* :view of the lead concentration in the solidified ingot (numerical simulation) that exceeding the nominal concentration (C_0 =10wt%), in order to highlight the size, number and shape of the segregated channels. (a) and (b) represent a side view and c) represents a top view of the ingot in order to see the local position of the different channels.*

In order to analyze this phenomenon, the evolution of the thermal and concentration fields was tracked as well as their corresponding liquid fraction of three different points: point 1 (x = 81.1 mm, y = 39 mm, z = 9.2 mm), point 2 (x = 80.5 mm, y = 36 mm, z = 9.2 mm), and point 3 (x = 80 mm, y = 33 mm, z = 9.2 mm) in the same segregated channel (see zoom view in Fig.IV.13(b).

Fig.IV.14 presents the time evolution of liquid fraction, as well as the temperature and average concentration for each selected point. The liquid fraction has dropped from initial value f_l = 1 to 0.91, 0.82 and 0.8 for point 1, 2 and 3, respectively, this is due to the temperature

decrease in these points Fig.IV.14(b), which becomes lower than the liquidus level (T_l = 492 K), and referring to the solidification progress. Then, we notice an increase in the liquid fraction of about 4%, 3% and 4% in points 1, 2 and 3, at the instants 750 s, 830 s and 860 s, respectively after the beginning of the cooling stage. This behaviour which corresponds to a remelting phenomenon of the solid in the mushy zone, is accompanied by a significant increase in the level of concentration due the transport of solute rejected within the mushy zone, which reaches 12.8*wt*%. These factors are the favourable conditions to the development of a segregated channels. Moreover, due to the effect of EM stirring in the opposite direction of thermosolutal convection, a fluctuating value of these concentrations and relatively less in the corresponding temperatures were observed just in the time before and during remelting.

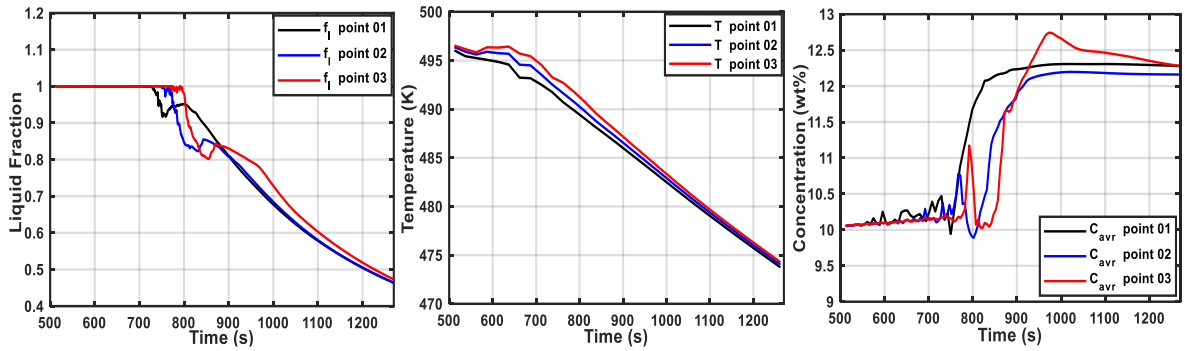

(a) **(b)** **(c)**

Fig.IV.14:*Time evolution of (a) Liquid fraction, (b) Temperature and (c) average concentration of the three selected points within the segregated channel during the solidification process of Sn-10wt.%Pb alloy under the effect of EM stirring in the opposite direction of thermosolutal convection*

Fig.IV.14(c) shows a clear increase in solute concentration in the identified remelting locations at points 1, 2, and 3, which corresponds to the freckle formation zone. This high lead concentration areas results in a decrease in the liquidus temperature leads to a local remelting. As a result, these analyses demonstrate that remelting is a direct consequence of a local increase in concentration of solidified locations due to the inflow of solute-rich liquid in to mushy zone. Small concentration gradients cause a significant decrease in liquidus temperature and hence remelting is strongly influenced by solutal variations, due to the relatively large liquidus slope of Sn-10wt. % Pb alloy.

X-ray photographs of the cross-sections of the ingot allowed the characterization of the effect of the electromagnetic stirring on the general morphology of the segregation and in particular that of the segregated channels in the transverse direction of the ingots.

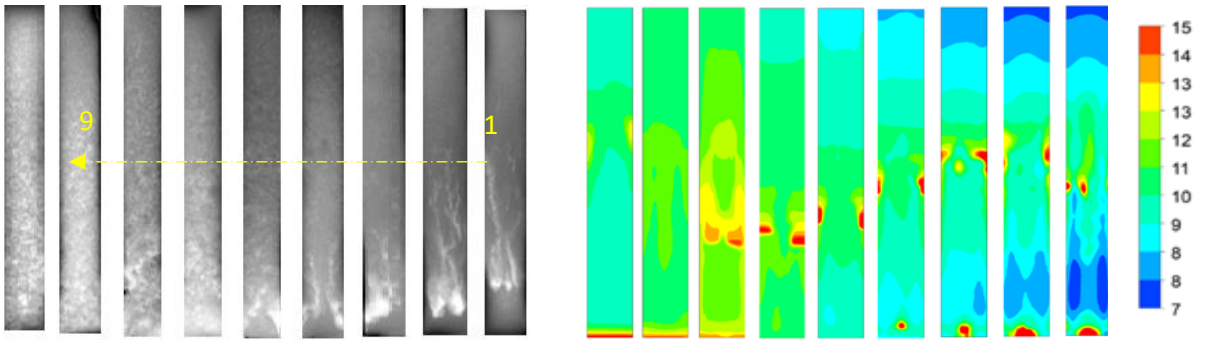

(a) (b)

Fig.IV.15 : *(a) X-ray of cross sections on the left and, (b) contour maps of iso-concentrations on the right for the solidification of the Sn-10wt% Pb alloy under the effect of forced convection.*

The cross-sections of the solidified ingot under the effect of forced convection in the opposite direction of convection are shown in Fig.IV.15. Generally, the comparison illustrates good agreement between experiment and simulation. Especially, if the comparison is qualitative in the first place. This case presents a peculiarity with respect to the morphology, as well as the size of the segregated channels along the transverse direction. The channels are explicitly localized in the first four slices, with a non-regular morphology (complex geometrical shape), and present large size channels in the lower part that can reach about 4mm. The Height of segregated channels in the lower-right corner region (slices 1, 2,3, and 4 in Fig.III.15(b)), is actually overestimated by the simulation. A macrosegregation detachment mechanism is well spotted from the fifth slice to the first slice due to the effect of the reversal of the mixing direction with respect to the natural convection. Microsegregation corresponding to the formation of equiaxed grains in all the last five slices was observed. We noticed a very significant decrease of the lead stratification effect in the base of the ingot, except in the seventh and ninth slice. A macrosegregation chimney is quite clear in the last slice, probably created by the formation of a double vortex in the last liquid due to the advancement of the two solidification fronts.

PARTIAL CONCLUSION

3D numerical simulation of Sn-10wt.%Pb alloy solidification under the effect of the electromagnetic stirring in the opposite direction to natural convection was performed. In the light of the experimental and numerical study presented in this chapter, we can deduce some general findings and conclusions concerning the morphology of the segregation, as well as the effect of electromagnetic stirring applied on the solidification process.

We have analyzed the effect of electromagnetic stirring on solidification process of Sn-10*wt*.%Pb alloy, namely the final grain structure as well as the elimination of defects related to segregation at different scales. The analyzes carried out on the experimental measurements and the numerical simulation have provided quantitative and qualitative data on the thermal behavior and dynamic configuration, as well as the solidification front dynamics. Based on the post-mortem analysis, various types of macrostructures were obtained, i.e., columnar and equiaxed. The columnar-to-equiaxed transition was observed for experiment carried out. The results have clearly shown the existence of two types of segregation: the first takes the form of segregated channels located in the first layers of solids formed, while the second, known as a normal segregation zone, corresponds to the last liquid at the end of solidification, which has assumed, in most cases, a panache form due to macrosegregation. The analysis has shown a strong influence of the EM stirring, compared to the solidification under the effect of the thermosolutal convection (Chapter 3), in particular on the development of the columnar-equiaxed transition mechanism (CET). A significant reduction of the solutal sedimentation and consequently on macrosegregation, was observed in this case. Indeed, it has shown that the electromagnetic stirring leads to a considerable increase of velocity in the melt, in their turn changing heat transfer conditions in terms of large undercooling zone, which is considered as an optimal environment for the development of homogenously distributed metallic grains with a decreased size. Stirring in the opposite direction to natural convection has shown its effectiveness in achieving the finest equiaxed structures. This stirring mode combines both the remelting and the mechanical fragmentation mechanisms. The numerical model used proven its effectiveness in terms of examining the dynamic and thermal fields, as well as studying the segregation phenomenon since it produced results that were qualitatively and quantitatively extremely similar to those obtained experimentally.

References

[1]L. Hachani, K. Zaidat, Y. Fautrelle, I. J. of Heat and Mass Transfer 85, 438-454.

[2] R. Moreau, Kluwer Academic Publishers, Dordrecht, Netherlands, (1990), pp. 250_51.

[3] X.D. Wang, Y. Fautrelle, J. Etay, and R. Moreau, Metall. Mater. Trans. B, (2009), pp. 104-113..

[4] A. Abdolkhani and A. P. Hu, in ECCE/IEEE (2012), pp. 1796-1803.

[5] L. Hachani, B. Saadi, X.D. Wang, A. Nouri, K. Zaidat, A. Belgacem-Bouzida, L. Ayouni-Derouiche, G. Raimondi and Y. Fautrelle, International Journal of Heat and Mass Transfer, 55 (7-8) (2012) 1986-1996.

[6] Ab. Abdelhakem, L. Hachani, K. Zaidat, I. Sari, Y. Fautrelle, JOURNAL OF HEAT TRANSFER-TRANSACTIONS OF THE ASME, 2021 143 (6), 062401.

[7] J. W. Gao, C. Y. Wang, JOURNAL OF HEAT TRANSFER-TRANSACTIONS OF THE ASME. May 1999, 121(2): 430-437 (8 pages).

[8] J. P. Gu, C. Beckermann and A. F. Giamei, Metall. Mat. Transaction A. V28, (1997), p 1533.

[9] Q. Li and C. Beckermann, J. of crystal growth, V. 236, (2002), p. 432.

[10] A. Hellawell, J. R. Sarazin and R. S. Steube, Phil. Trans. R. Soc. Lond. A, 345, (1993), p. 507.

[11] R. Moreau, Progress in crystal growth and characterization of materials, (1999), P.161.

[12] L. Hachani, Thèse de doctorat en Mécanique, INPG-Grenoble et l'Université de Batna-Algérie, 2013.

.

General Conclusions

General Conclusions

In recent years, numerical methods are considered as an effective tool to identify the important phenomena related to the solidification process, more particular the segregation defects which occur at different scales and specifical times. Both numerical analysis and experimental investigations have been interested on the exact description of this multidisciplinary process from dendrite growth at microscopic scale to grain motions and their ripening at macroscopic scale. The present work is mainly focused on the numerical simulation for columnar solidification of binary alloy under the effect of convective flow, using a volume average approach. For this purpose, solidification experiments were conducted using a benchmark experimental setup developed in the SIMAP/EPM laboratory, named AFRODITE. The principle of these experiments was the solidification of a rectangular ingot of dimensions $100\times60\times10$ mm^3 inside a parallelepiped crucible heated on both end vertical walls.

After comprehensive literature review of different numerical approaches and solutions proposed for some crucial issues, a three-dimensional (3D) model was developed and implemented in ANSYS/Fluent software to simulate the solidification of a binary alloy by a two-phase columnar numerical model, based on the resolution of momentum, energy and solute equations, considering the mushy zone as a porous medium taken into account by a Darcy term. This later term contains a permeability factor "*K*" expressed from the liquid fraction and the secondary inter dendritic spacing λ_2. In additional, an enthalpy method based on fixed-grid techniques which allows the resolution of a unique system of equations on the same studied domain (containing both the solid and liquid phases), was adopted in the algorithm of solution. This model was tested in simulations of two benchmark solidification experiments in order to study of solidification process and macrosegregtaion formation at laboratory scales.

First, a rigorous treatment of the experimental temperature data was applied to define the appropriate unsteady thermal boundary conditions for the numerical model, which allow buoyancy convection to be properly taken into account in this 3D simulation. The agreement between simulation and experiment in terms of temperature evolution and segregation morphology and behavior whether the chimney of macrosegregation corresponding to the last liquid solidified or even the segregated channels characterizing the columnar regions, further verified the numerical approach used.

The main conclusions are summarized below.

1. For the case of solidification under the effect of thermosolutal convection we can conclude that among the several factors which are responsible for the movement of fluid in the mushy zone, and consequently the development of segregation at different scales and with different morphologies, there are four dominant mechanisms:
    - convection in the mushy zone, which transports the solute within and outside the mush,
    - instabilities of solidification front driven by the convection in the bulk and the movement of the interdendritic liquid controlled by its permeability in the mushy zone,
    - interdendritic local flow created by a flow perturbation resulting in the suppressed solidification mechanism, that happens only when the interdendritic flow ($\vec{u}_l$) is in the opposite direction to the liquid concentration gradient $(\vec{\nabla}c)$.
    - remelting results to the local increase in concentration due to inflow of solute-rich liquid in the mushy zone and/or reheating due to the hot bulk transported by convection, is a favourable condition to the development of a segregated channels.

2. For the case of solidification under forced convection driven by an external travelling magnetic field (electromagnetic stirring in the opposite direction in regards to natural convection), both experimental and numerical results showed that:
    - The electromagnetic stirring in the liquid phase created by the coupling between the induced currents and the presence of the inductive magnetic field, has shown its effectiveness in homogenizing the temperature by significantly reducing the thermal gradient and also the concentration by preventing the sedimentation effect,
    - The columnar-equiaxial transition is observed in the ingot solidified under electromagnetic stirring. It is important to note that in general, electromagnetic stirring not only promotes equiaxial columnar transition but can also very significantly refine the equiaxed grains.
    - We believe that the predominant phenomenon responsible for the CET mechanism was the dendritic arms fragmentation by remelting effect. It was shown that the forced convection induced by the Lorentz force was about ten times more important than the natural convection created by the thermal and

solute gradients. Indeed, the penetration of hot liquid with high level of concentration in the mushy zone is more important, which subsequently create a favourable environment for remelting and consequently fragmentation.

- The refusion of the dendrite arms strongly depends on the velocity of the interdendritic liquid, which itself is a function of the permeability of the mushy zone. This remelting leading to the formation of fragments, favours the growth of equiaxed grains if the fragments survive.

3. Although, 3D numerical simulations are the most reliable to the real physics of the solidification phenomenon, but it remains expensive (in terms of computational time) for such processes of solidification, with so many coupled physical phenomena.

The envisaged extension of this work would be, in terms of numerical modelling (more particular 3D models), to introduce the three-phase solidification model or even five-phase model (in the case where the equiaxed structure exist), in order to predict the equiaxed-columnar transition. On other hand, it is interesting to study the effects of forced convection driven by another different magnetic field configurations (in the direction of natural convection to promote it, in the opposite direction, an alternating field with a variable frequency) as it has shown its effectiveness to control the solidification process of binary alloys. This offers the opportunity to avert defects due to segregation (concentration heterogeneity). These new calculations could allow a comparison with the solidification experiments under magnetic field that have already performed with AFRODITE. Another perspective would be to change the nominal concentration in order to see its influence on the formation of segregated channels and on the sedimentation of lead.

An application of this model on another geometrical configuration (for example a Bridgman experiment with a vertical temperature gradient) would also be interesting to validate it. There is a multitude of experiments done at the industrial or laboratory scale with variable geometries and different alloys that could be simulated.

Abstract

This work aims to contribute to the development of a numerical model that predicts the effect of natural and forced convection on the phase change of metallic alloys. The geometrical configuration considered throughout this study was chosen to correspond to the crucible of an experimental benchmark called 'AFRODITE', developed at the SIMAP-EPM laboratory in Grenoble/France. A 3D numerical model was proposed based on the enthalpy approach (to treat cases of solidification of metal alloys with the segregation phenomenon) under the influence of natural convection and forced convection caused by electromagnetic stirring. This model has been applied in order to better understand, master and control the solidification process of metallic alloys, in terms of defects that occur during the solidification, particularly segregation at the meso and macroscopic scale. The developed numerical model was validated by in-situ and real-time measurements of temperatures at any point of the solidification system, which allows quantitative and qualitative validation.

Résumé

Ce travail vise à contribuer au développement d'un modèle numérique qui prédit l'effet de la convection naturelle et forcée sur le changement de phase des alliages métalliques. La configuration géométrique considérée tout au long de cette étude a été choisie pour correspondre au creuset d'un banc d'essai expérimental appelé 'AFRODITE', développé au laboratoire SIMAP-EPM à Grenoble/France. Un modèle numérique 3D a été proposé basé sur l'approche enthalpique (pour traiter les cas de solidification d'alliages métalliques avec le phénomène de ségrégation) sous l'influence de la convection naturelle et de la convection forcée provoquée par le brassage électromagnétique. Ce modèle a été appliqué afin de mieux comprendre, maîtriser et contrôler le processus de solidification des alliages métalliques, en termes de défauts qui se produisent lors de la solidification, en particulier la ségrégation à l'échelle méso et macroscopique. Le modèle numérique développé a été validé par des mesures in situ et en temps réel des températures en tout point du système de solidification, ce qui permet une validation quantitative et qualitative.

ملخص

يهدف هذا العمل إلى المساهمة في تطوير نموذج عددي يتنبأ بتأثير الحمل الحراري الطبيعي والقسري على تغيير الطور للسبائك المعدنية. تم اختيار الشكل الهندسي الذي تم تبنيه خلال هذه الدراسة بحيث يتوافق مع بوتقة معيار تجريبي يسمى "افروديت" الذي تم تطويره في مختبر العلوم وهندسة المواد والعمليات/المعالجة الكهرومغناطيسية للمواد في غرونوبل / فرنسا. تم اقتراح نموذج عددي ثلاثي الأبعاد القائم على مقاربة الاونثالبي (لمعالجة حالات تصلب السبائك المعدنية مع ظاهرة الانعزال الجسيمي) تحت تأثير الحمل الحراري الطبيعي والحمل الحراري القسري الناجم عن التحريك الكهرومغناطيسي. تم تطبيق هذا النموذج من أجل فهم أفضل وإتقان والتحكم في عملية تصلب السبائك المعدنية، من حيث العيوب التي تحدث أثناء التصلب، ولا سيما الانعزال الجسيمي على النطاق المتوسط والعياني. تم التحقق من صحة النموذج الرقمي المطور من خلال قياسات مباشرة في الموقع وفي الوقت الحقيقي لدرجات الحرارة في أي نقطة من نظام التصلب، مما يسمح بالتحقق الكمي والنوعي.